TECHNISCHE UNIVERSITÄT MÜNCHEN

Lehrstuhl für Technische Physik E19

Interfaces and Energy Conversion

Electron Transfer Phenomena in Interfacial Bioelectrochemistry

Claudia Baier

Vollständiger Abdruck der von der Fakultät für Physik der
Technischen Universität München
zur Erlangung des akademischen Grades eines

Doktors der Naturwissenschaften (Dr. rer. nat.)

genehmigten Dissertation

Vorsitzender:	Univ.-Prof. Dr. Ralf Metzler
Prüfer der Dissertation:	1. Univ.-Prof. Dr. Ulrich Stimming
	2. Univ.-Prof. Dr. Martin Stutzmann

Die Dissertation wurde am 12.08.2010 bei der Technischen Universität München eingereicht und durch die Fakultät für Physik am 13.12.2010 angenommen.

"Zwei Dinge sind zu unserer Arbeit nötig:
Unermüdliche Ausdauer und die Bereitschaft, etwas, in das man viel
Zeit und Arbeit gesteckt hat, wieder wegzuwerfen."
(Albert Einstein, 14.03.1879 - 18.04.1955)

Dedicated to my family

"Is there anything more beautiful than the sun?
I often watch it rise, for my restless sleep usually awakens me before dawn.
Each time I see its calm yellow light peeking above the horizon I grow a
little more determined, a little more hopeful. In a way, it is the thing that
has kept me going all this time."
from Brandon Sanderson's *Mistborn*

Contents

1. Introduction

The focus of this work is the electrochemical investigation of biomolecules at the solid-liquid interface to study their structure-function relation down to a single molecule level depending on the electron transfer process, the investigation technique and the electrode material. In order to be able to investigate biomolecules electrochemically the molecules have to be electroactive and there must be the possibility for an electrical interaction of the biomolecule with an electrode surface [1].

In nature there exist several biomolecules such as proteins and enzymes which are naturally redox-active. These biomolecules are characterized by bearing redox-active centers, e.g. heme, quinones, flavins, iron-sulfur clusters, in their active sites, whose oxidation state can reversibly change, thus being the basis of their ability to exchange electrons. These biomolecules play important roles in biological processes central to sustaining life on earth, such as respiration and photosynthesis, since they involve as a crucial step electron transfer reactions between molecular partners [2, 3]. Gaining fundamental understanding of the structure-function mechanism of such redox proteins and enzymes one can learn useful lessons from the study of biological electron transfer systems which have evolved over millions of years and which might be helpful to design new electrochemical systems for innovative technical applications. For example, in polymer electrolyte membrane fuel cell (PEM FC) research the electrocatalysis of the oxygen reduction to water at neutral pH is still a main issue, whereas in the mitochondrial electron transport chain it is achieved using non-noble metal catalytic sites from NADH and $FADH_2$ [4]. Furthermore, biochemical electron transfer reactions can be utilized in biosensor devices for biomedical analysis and applications, e.g. for glucose detection in the blood. Amperometric electrochemical biosensors can be constructed based on the measurement of hydrogen peroxide concentration produced within the oxidation of glucose to D-gluconic acid in the presence of the redox enzyme glucose oxidase [5, 6]. Therefore, major driving forces for fundamental research in the field of bioelectrochemistry include the development of innovative functional devices in biosensor technology, bioelectronics and bioelectrochemical fuel cells. However, one of the main problems in bioelectrochemistry still is the electronic communication between the biomolecule and the electrode. Beside embedding of biomolecules into conductive polymers [7], in principle there are other possibilities to provide electron transfer between the electrode and the redox-active site. Either the biomolecules are attached to the electrode surface so that direct interfacial electron transfer is possible or the biomolecules are in solution and the electron transfer with the electrode is maintained using small electron mediators to relay electrons between the electrode and the active site of the biomolecule. However, it was shown in the past that mediated electron transfer is disadvantageous in several points. Since the biomolecules are in solution their behavior, which

is often diffusion controlled, can only be investigated using integral measurement techniques such as cyclic voltammetry. Structure-function relation studies down to the single molecule level can not be performed. Detailed studies of mediated electron transfer mechanism can become quite complex as side reactions and additional reaction products due to undefined mediator interactions with the electrode and the reaction educts/products have to be taken into account. Furthermore, adsorption and subsequent denaturation of the biomolecules on the electrode surfaces leading to electrode fouling might occur.

In order to avoid these disadvantages and to enable single-molecule studies using high resolution SPM techniques, the biomolecules were stably immobilized onto the electrode surface in this thesis. Since it is well known from literature that biomolecules easily denaturate when they are in direct contact with metallic electrode surfaces [8, 9] a carbon material electrode, highly oriented pyrolytic graphite (HOPG), was chosen as substrate material for model electrode studies. Due to its atomically flat surface HOPG also offers the possibility to identify and to investigate the electrochemical behavior and structure-function relation of a single biomolecule attached to the surface using electrochemical scanning tunneling microscopy (EC-STM). However, as the HOPG surface is hydrophobic and only contains a few defect site the surface has to be functionalized to make it suitable for biomolecule immobilization. In order to provide electrochemical investigation of biomolecules the surface functionalization and the immobilization mechanism have to fulfill three requirements: 1. fast interfacial electron transfer, i.e. high conductivity from the electrode to the biomolecule or vice versa, 2. stable, if possible, covalent binding of the biomolecules to the electrode surface and 3. immobilized biomolecules should maintain their activity.
A commonly used method to chemically functionalize carbon materials is the electrochemical anodization of the surface in order to form oxygen-containing functional groups and to enhance interfacial electron transfer [10–13]. Recent studies on the electrocatalytic activity of the redox enzymes horseradish peroxidase (HRP) [14] and glucose oxidase (GOx) [15], both chemisorbed on oxidized HOPG, towards the reduction of hydrogen peroxide and the oxidation of glucose, respectively, have shown that enzymes immobilized by this procedure maintain their functionality. Wang et al. [15, 16] also confirmed good electronic coupling between the oxidized HOPG electrode and the enzyme by visualizing the electron transfer by a potential dependent EC-STM study. Gating the tunneling current in the EC-STM by the redox level of a protein has so far only be achieved for covalently immobilized azurin [3, 17, 18]. Compared to chemisorption or adsorption due to electrostatic, covalent immobilization has the advantage of strong bonds between the electrode surface and the biomolecule [19]. Furthermore, it offers the possiblity for specific immobilization, i.e. by chosing an adequate immobilization chemistry the biomolecules can be bound onto the electrode surface in a certain orientation. In the group of Ulstrup azurin was specifically bound to Au(111) modified by thiolate self-assembled monolayer using the cysteine within the protein structure as anchor [17].
The new approach aspired here is to combine covalently immobilization of biomolecules onto the HOPG and benefit from the large atomically smooth surface of the basal plane for high-resolution EC SPM studies on single biomolecules. By electrochemical reduction of a carboxyphenyl layer [20, 21] and subsequent EDC/NHS coupling the biomolecules will be covalently bound to the

graphite surface. This method was already utilized to bind enzymes such as laccase onto glassy carbon supports and to study their catalytic activity electrochemically [22]. These electrodes were electrochemically characterized and studied using bulk measurement techniques such as cyclic voltammetry. However, the degree of coverage of the surface, the orientation of the enzymes i.e. the position of the active site and the activity of a single enzyme are still a question of dispute; they can not be extracted from such integral electrochemical measurements. Within this work it will be shown that this immobilization technique is also suitable for single molecule studies using EC-STM providing fast electron transfer.

Again, the focus of this work is the electrochemical investigation of biomolecules in order to study their structure-function relationship down to a single molecule level. Independent from the immobilization mechanism the biomolecules still have to be electroactive so that one is able to study them electrochemically. However, a lot of enzymes playing important roles in physiological reactions are naturally redox-inactive and, thus, can neither be studied by electrochemical techniques nor detected by possible electrochemical biosensors. Among these redox-inactive enzymes proteases represent a large group. Proteases are enzymes that conduct proteolysis, i.e. protein break down, by hydrolysis of the peptide bonds that link amino acid residues. Proteases occur naturally in all organisms and are part of several metabolic processes and physiological reactions from e.g. digestion of food proteins to highly-regulated cascades such as the blood-clotting cascade [23] or the apoptosis pathways [24]. Furthermore, proteases are significantly involved in the metastasis of malign tumors and the reproductive cycle of viruses such as Hepatitis C [25] and HIV [26]. Therefore, proteases are important pharmaceutical targets providing high potential in the field of cancer and HIV diagnostics and therapy. For example, by preventing the function of the protease by an adequate inhibitor, the reproduction of cancer cells and viruses can be decelerated or even be completly disturbed [27, 28]. Understanding the reaction mechanism of these proteases using suitable investigation and detection methods and being able to design applicable inhibitors is of great interest in the field of clinical diagnostics, as well as medical and pharmaceutical research. Since electrochemistry offers specific and highly sensitive low-cost investigation tools, which are at the same time user-friendly and have the potential to minituarization and microarray technology using high-throughput screening (HTS), it would be the method of choice for enzyme investigation and analysis. Therefore, a possibility for electrochemical detection of redox-inactive proteases has been developed in this work based on the affinity label concept known from optical detection. Recently, fluorescently tagged affinity labels were synthesized in order to establish on-chip determination of the catalytic activity of microarrayed proteases [29, 30]. Here, for the first time, it is attempted to transfer the optical detection to the electrochemical detection of enzymes by applying redox-active markers instead of fluorophores. From literature it is known that encouraging approaches to construct active molecular circuits involve ferrocene-based systems since the ferrocene/ferrocenium interconversion is fast and the redox couple is stable in a variety of environments [31, 32]. Therefore, the first step of the bottom-up approach was to synthesize watersoluble affinity labels suitable for cysteine proteases where a ferrocene moiety serves as redox-active tag, so-called ferrocene affinity labels (FcAL) [33]. In the second step, two promising ferrocene affinity labels and enzymes labeled with these two

FcALs were electrochemically characterized in order to verify the functionality of the FcALs using cyclic voltammetry (CV), which is often the method of choice when starting with an unknown system [34]. In order to provide a detailed proof-of-principles, the electrochemical properties of unlabeled and labeled enzymes are characterized from bulk enzyme electrodes down to a single molecule level using in-situ electrochemical scanning tunneling microscopy (EC-STM). EC-STM images are always a convolution of the "true" surface topography and its conductivity and show therefore contrasts between high and low conductive surface features e.g. adsorbed molecules. This has already been theoretically proposed by Schmickler [35] in 1990 and was confirmed experimentally by Tao [36] six years later. Tao [36] investigated Fe(III)-protoporphyrin (FePP) and protoporphyrin (PP) molecules adsorbed on HOPG by EC-STM and was able to distinguish between the ion-containing and the ion-free conformation of the molecule due to their different electrochemical properties. Since EC-STM allows to map changes in the nanoscopic chemical environment the binding process of the electroactive ferrocene affinity label to the immobilized enzymes will be studied in-situ directly on the electrode surface. In the third step, the FcALs will be used in order to investigate the catalytic activity of the enzyme electrodes in the absence and presence of inhibitors. Only if it is possible to detect changes in the enzymatic behavior caused by the inhibitors, the FcAL concept and the electrochemical detection method using FcALs is interesting for future applications in electrochemical biosensors and biomedical analysis.

As already mentioned, in order to electrochemically characterize enzymes attached to electrode surfaces EC-STM was used throughout this work since it allows to perform electrochemical studies on a single molecule level. In general one can say that the invention of scanning probe microscopy (SPM) [37–39] has had a tremendous impact on the field of nanoscience and nanoelectronics during the last decades and has made significant contributions to the analysis of protein/enzyme–surface interactions. Especially the EC-STM has offered the possibility of attaining a so far, unmatched level of comprehension of the electron transfer mechanisms through redox-active metalloproteins and -enzymes. In-situ EC-STM provides a direct means of associating tunneling behaviour with specific environmental and molecular parameters down to a single molecule level, enabling in-situ to resolve tunneling pathways through individual molecules [36, 40–42] and biomolecules [3, 18, 43, 44] and thus has the potential to study structure and reactivity of enzymes down to a single molecule level [15, 16]. However, experimental problems remain. In order to avoid any interference of the STM tip with the protein structure only small tunneling currents can be applied. Therefore, a technique which just measures the potential (at $I = 0$), still under full potantial control of the electrode and in electrochemical environment, may be advantageous. Thus, the technique, scanning electrochemical potential microscopy (SECPM) [45], where the tip is used as potential probe to map the potential distribution of the surface may be able to accomplish this. Since no electrons tunnel through the sample, SECPM appears to be especially suited for the investigation of organic and biological molecules adsorbed on electrode surfaces in their natural environment, but under electrochemical conditions. However, so far the SECPM was only utilized to either map the electrochemical double layer perpendicular to an electrode surface [46, 47] or to image the distribution of tungsten in a carbon-like diamond film [48]. In this work enzymes of different size, chemical composition and electrochemical properties

will be studied applying constant potential mode SECPM. A comparison of SECPM images and constant current mode EC-STM images of the same electrode area shows that SECPM has a great potential for the non-invasive investigation of single molecules at the solid-liquid interface [49].

In this work functionalized HOPG mainly served as a model carbon support in order to study the electrochemical behavior of biomolecules attached to electrode surfaces. However, to exploit biological electroactive proteins and enzymes an understanding of the principles which govern efficient biological electron transfer is essential. Besides the immobilization technique and an optimal electronic communication between the biomolecule and the electrode, the electronic and electrochemical properties of the support material also play an important role [50]. Graphitic (sp^2-bonded) carbon materials, such as glassy carbon or HOPG, are susceptible to corrosion and might therefore be disadvantagous in technical applications. Due to its unique properties such as electrochemical inertness, low background current, its large potential window and its biocompatibility, boron-doped (sp^3-bonded) diamond is a promising alternative carbon material for bioelectronical applications. However, enzyme and protein immobilization, as well as a fast electron transfer are still challenging. Depending on the surface termination of the diamond electrode (hydrogen- or oxygen-terminated), different techniques in order to functionalize and immobilize biomolecules are known in literature. The functionalization of hydrogen-terminated diamond is often based on a photochemical treatment to bind amine-terminated hydrocarbon chains onto the surface [51], whereas oxidized diamond can be for example modified by silane groups [52]. Here, the approach to functionalize the diamond surface applying producing oxygen containing groups by different oxidation procedures and immobilize biomolecules without further linker molecules directly onto these oxygen-terminated surfaces is investigated. Therefore, the well-known metalloprotein azurin is used to study and compare the electrochemical behavior of oxygen-terminated diamond and oxidized HOPG protein electrodes.

To summarize, in order to study the electrochemical behavior of biomolecules at the solid-liquid interface the thesis contains the following subtopics:
HOPG is chosen as model electrode material which will be functionalized via different methods to optimize the direct electron transfer between the surface and the biomolecule.
To be able to also study naturally electroinactive enzymes electrochemically, the affinity label concept will be adopted to the electrochemical detection.
In addition to the established investigation techniques such as cyclic voltammetry and EC-STM, which allows single molecule studies, the SECPM will be introduced as suitable imaging tool for biological samples.
Furthermore, oxygen-terminated boron-doped diamond will be tested as alternative carbon support material for bioelectrochemistry.

The thesis is structured in 6 chapters. An introductory part containing the focus and the outline of this work is given here in Chapter 1.
In Chapter 2 a fundamental background of interfacial electrochemistry, biophysical and biochemical fundamentals, and scanning probe microscopy is given. The section on interfacial electro-

chemistry focuses on the solid-liquid interface and a detailed description of the electrochemical double layer (EDL) occuring at every electrode/electrolyte interface. Furthermore, different electrode reactions, the principles of electron transfer and their investigation by cyclic voltammetry will be introduced. The section on biochemistry and biophysical fundamentals includes an insight into electron transfer in biological structures and an overview of the biochemical structure and function of the proteins and enzymes used within this work, as well as an insight into peptide synthesis, enzyme kinetics, and biosensor technology. Since the scanning tunneling microscope (EC-STM) is the technique of choice within this thesis to study the electrochemical behavior of single biomolecules, the third section describes in detail the principle of the scanning tunneling microscopy (STM), its various applications under electrochemical conditions (EC-STM), and its applications in bioelectrochmistry. Furthermore, the latest modification of the EC SPM the scanning electrochemical potential microscope (SECPM) will be introduced.

Chapter 3 includes information about chemicals, experimental procedures and setups, describes the electrochemical glass cell and potentiostats. Furthermore, the setup of the EC-STMs and the SECPM, tip preparation, and insulation are explained. Different electrodes, the electrode preparation for different experiments, and the labeling of enzymes will be specified.

The main part, Chapter 4, presents the results of this work according to the subtopics mentioned above and can be subdivided into five sections. In Section 4.1 different approaches to functionalize highly oriented pyrolytic graphite (HOPG) for biomolecule immobilization are introduced. Section 4.2 presents two synthesized electroactive ferrocene affinity labels (FcAL) for the new approach of electrochemical biosensing of redox-inactive enzymes such as the cysteine protease papain, which serves as test-enzmye. The more promising FcAL is studied in detail in Section 4.3 where also a comprehensive electrochemical STM investigation of FcAL labeled and unlabeled papain down to a single molecule level is presented. Furthermore, the detection of the enzyme labeling in solution and on the electrode surface will be verified by cyclic voltammetry and EC-STM. Section 4.4 includes the results obtained for the investigation of biomolecular electrodes using the new electrochemical scanning probe technique, the SECPM. Section 4.5 shows preliminary results of oxygen-terminated diamond as possible support material for biomolecule electrodes.
Although all results are discussed and compared to literature data within the sections, in Chapter 4, an overall discussion of the experimental results regarding electron transfer phenomena in bioelectrochemistry will be given in Chapter 5.

A summary and conclusions also containig an outlook on further possible investigations and experiments are given in Chapter 6.

2. Fundamentals

2.1. Interfacial Electrochemistry

Interfacial Electrochemistry can be defined as "the study of structures and processes at the interface between an electronic conductor (the electrode) and an ionic conductor (the electrolyte)" [34]. The structure of the interface and the reactions that occur are of great interest to electrochemists. They can be investigated with electrochemical methods by monitoring potential, current, charge and/or capacitance. This chapter gives an introduction of fundamental prinicples in electrochemistry, the structure of the solid/liquid interface and possible electrochemical reactions including electron transfer processes between the electrode and an electroactive species either in the electrolyte or adsorbed to the electrode.

2.1.1. The Solid-Liquid Interface and the Electrochemical Double Layer

At any interface between two phases and particularly between an electrode and an electrolyte solution, i.e. at the solid-liquid interface, there exists a separation of positive and negative charge in a direction perpendicular to the phase boundary. This charge separation occurs in order to establish equilibrium at the interface and forms a double layer, the so-called electrochemcial double layer (EDL) [53, 54]. According to Grahame [55] the electrochemical double layer "is the array of charged particles and oriented dipoles which is thought to exist at every interface". Therefore, the double layer consists on the one side of the ionic excess charges of the electrolyte and on the other side of the electrode charges which compensate each other. In the early twentieth century Gouy, Chapman, and Stern developed a classical model of the electrochemical double layer which was mainly based on the pioneering work of Helmholtz. The theory of the electrochemical double layer describes the charge distribution and the electrical potentials arising as a consequence of the charge separation.

2.1.1.1. The Helmholtz Model

In 1853, Helmholtz [56] modelized the solid-liquid interface as a rigid double layer comparable to a parallel plate capacitor considering the electrode (metal) surface as one plate and the electrolyte as the other plate holding the counter-charge. This simple model of two layers of opposite charge was the origin of the term "electrochemical double layer". According to Helmholtz, the double layer has a differential capacitance C_H which is given by

$$C_H = \frac{\varepsilon \cdot \varepsilon_0}{d} \tag{2.1}$$

where $\varepsilon > 1$ is the dielectric constant modulating the permittivity of free space ε_0 and d is the distance between the two virtual plates. This distance is given by the closest approach of the centers of the ions solved in the electrolyte to the electrode surface, i.e. d is equal to the ionic radius. Adopting a value of d of 1 Å to 2 Å and a value of $\varepsilon = 4.5$ (the water molecules in the layer between the plates are oriented, and the value of ε is much lower than that in the bulk solution, $\varepsilon \approx 80$ for dilute aqueous solution), values of C_H lie between 20 to 40 $\mu\mathrm{F} \cdot \mathrm{cm}^{-2}$, which corresponds to values experimentally observed. However, the Helmholtz Model only characterizes the close proximity of the solid-liquid interface. According to Equation 2.1 the differential capacitance C_H is a constant which is not the case in real systems. Experimental results have shown that C_H varies with the applied potential and the concentration of the electrolyte. Therefore, either ε or d have to depend on these variables. Furthermore, one has to account for mobile charge carriers (ions or other charged molecules) that may diffuse to and away from the electrode surface called the diffuse double layer.

2.1.1.2. The Gouy-Chapman Theory

In the beginning of the 1920s, the thermal motion of the ions in the EDL was included in the theories developed independently by Gouy [57, 58] and Chapman [59] in France and England, respectively. They proposed the idea of a diffuse layer within the electrolyte and followed a statistical mechanical approach. Therefore, the diffuse layer in the electrolyte near the electrode surface can be approximated by a series of laminae, parallel to the electrode. Although all laminae are in thermal equilibrium with each other, the ions of any species i are not at the same energy in different laminae due to the fact that the electrostatic potential φ varies with the distance from or to the electrode. Furthermore, each ion species is treated as a population of charged point particles following a Boltzmann distribution. The energy needed to bring the ion from outside the double layer to its actual position in the EDL defines its energy. The concentration n_i of the species i with the ionic charge z_i in an infinitely small laminae with respect to the bulk concentration n_i^0 is:

$$\frac{n_i(x)}{n_i^0} = \exp\left(-\frac{z_i e \varphi(x)}{k_B T}\right) \tag{2.2}$$

e is the electron charge, T is the absolute temperature and k_B is the Boltzmann constant. The total charge per volume is then

$$\rho(x) = \sum_i n_i^0 z_i e \cdot \exp\left(-\frac{z_i e \varphi(x)}{k_B T}\right) \tag{2.3}$$

where $\rho(x)$ is related to the potential at distance x by the one-dimensional Poisson equation:

$$\rho(x) = -\varepsilon(x)\varepsilon_0 \frac{d^2\varphi(x)}{dx^2} \tag{2.4}$$

Combining Equation 2.3 and Equation 2.4 considering the boundary conditions $\varphi(x = \infty) = 0$, i.e. the potential in the bulk solution is 0, and $\frac{d\varphi}{dx} = 0$, i.e. there is no potential change within the bulk region, yields the Poisson-Boltzmann equation.

$$\left(\frac{d\varphi}{dx}\right)^2 = \frac{2k_BT}{\varepsilon\varepsilon_0}\sum_i n_i^0\left[\exp\left(\frac{-z_ie\varphi}{k_BT}\right) - 1\right] \tag{2.5}$$

Equation 2.5 is valid for the assumption that the dielectric constant of the solvent is independent of distance and ion concentration. For a symmetrical electrolyte (z:z) where each ion species has an absolute charge magnitude z the Poisson-Boltzmann Equation 2.5 can be simplified. Further integration between the electrode surface ($x = 0$) where the potential is φ_0 and an arbitrary location x results in [53]:

$$\frac{\tanh\frac{ze\varphi}{4k_BT}}{\tanh\frac{ze\varphi_0}{4k_BT}} = \exp(-\kappa x) \tag{2.6}$$

Where

$$\kappa = \left(\frac{2n^0z^2e^2}{\varepsilon\varepsilon_0k_BT}\right)^{1/2} \tag{2.7}$$

is the reciprocal of the characteristic diffuse layer thickness, the so called Debye-Hückel length given by κ^{-1} in cm if c^* is the bulk $z:z$ electrolyte concentration in moll^{-1}. For dilute aqueous solutions ($\varepsilon = 78.49$) at 25°C:

$$\kappa = (3.29 \cdot 10^7)zc^{*1/2} \tag{2.8}$$

For small φ_0, i.e. $\varphi_0 \leq \frac{50}{z}$ mV, at 25°C, $\tanh\frac{ze\varphi}{4k_BT} \approx \frac{ze\varphi}{4k_BT}$ and Equation 2.6, the potential of the electrochemical double layer can be approximated by

$$\varphi(x) = \varphi_0\exp(-\kappa x) \tag{2.9}$$

By calculating φ from Equation 2.6 or Equation 2.9 several useful quantities such as the electrode surface charge density and the charge density in the solution phase σ at the interface, the concentration profile of each ion species or the differential capacitance C_d can be obtained from a thermodynamics formalism.

2.1.1.3. Stern's improvement

While Gouy and Chapman considered the ions as point charges Stern improved the model by taking the finite size of the ions into account, i.e. the ions can not approach the electrode surface closer than their ionic radius added, if they are solvated, the radius of the solvation shell. This distance of closest approach for the centers of the ions is x_2 which defines the outer Helmholtz plane (OHP), where φ_2 is the potential in the OHP. The ions closest to the electrode which form the OHP and which are held in position by purely electrostatic forces are termed "nonspecifically adsorbed" ions. These are mainly solvated cations. The considerations of the Gouy-Chapman theory, especially the Poisson-Boltzmann equation in 2.5 are still valid at distance $x \geq x_2$. Stern's interfacial model can be treated as an extension for $x \leq x_2$ where no charge between the electrode surface (x_0, φ_0) and the OHP (x_2, φ_2) is present. Thus, according to the Poisson equation 2.4, the potential drops linearly from φ_0 to φ_2. The potential profile in the diffuse layer of a $z:z$ electrolyte (see Equation 2.6) is then given by:

$$\frac{\tanh\frac{ze\varphi}{4k_BT}}{\tanh\frac{ze\varphi_2}{4k_BT}} = \exp(-\kappa(x - x_2)) \tag{2.10}$$

The differential capacitance C_d can be obtained from the thermodynamics formalism (for detailed information see [53]).

$$\frac{1}{C_d} = \frac{x_2}{\varepsilon\varepsilon_0} + \frac{1}{\varepsilon\varepsilon_0\kappa\cosh(\frac{ze\varphi_2}{2k_BT})} = \frac{1}{C_H} + \frac{1}{C_D} \tag{2.11}$$

This model is known as the Gouy-Chapman-Stern (GCS) model schematically shown in Figure 2.1. As can be seen in Equation 2.11, the double layer capacitance consists of two contributions: C_H and C_D. C_H is the contribution of the rigid Helmholtz layer which does not depend on the potential whereas C_D is the contribution of the diffuse layer. Of special interest is the point of zero charge (PZC) where the electrical charge density on the surface is zero ($\sigma_M = 0$). For dilute electrolytes and φ_0, and therefore φ_2, being close to the PZC, C_D is dominant in C_d. For higher concentrated electrolytes and φ_0 values significantly different from the PZC charges are located close the electrode, the diffuse part becomes negligible and C_d can be derived from the Helmholtz model.

Although being a good approximation for the electrochemical double layer the Gouy-Chapman theory only describes electrostatic effects disregarding polarization effects within the electrolyte, i.e. the dependence of the dielectric constant on the distance to the electrode or the dependence of C_H on the potential. Furthermore, the model neglects ion-ion interactions or strong nonspecific interactions of the ions with the electrode surface. Another important issue, which will be shortly

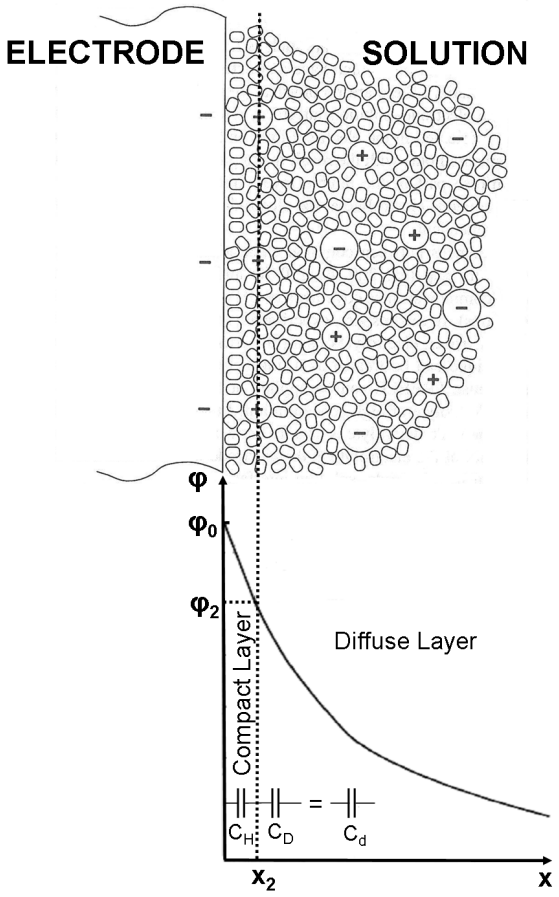

Figure 2.1. Scheme of the composition and the potential profile of the electrochemical double layer according to the GCS model, based on [60] (upper part) and [53] (lower part)

discussed in the next paragraph, is the adsorption of charged or uncharged species by chemical interactions with the electrode.

2.1.1.4. Specific adsorption

As already mentioned the ions that form the OHP are mainly solvated cations which are non-specifically adsorbed by electrostatic forces. Most anions however loose part of their solvation shell when entering the double layer and forming a chemical bond with the electrode surface. These ions are termed "specifically adsorbed". While the nonspecific adsorption is due to long range electrostatic effects, chemical interactions which cause specific adsorption of ions are short range in nature and occur very close to the electrode at distances x_1 smaller than the OHP ($x = x_2$). The centers of the specifically adsorbed ions form the so-called Inner Helmholtz Plane (IHP) at $x = x_1$. Specific adsorption of charged species can easily be detected experimentally since specific adsorption results in a shift of the PZC.

Therefore, the currently accepted model for the structure of the electrochemical double layer by Grahame [55] splits the interface into three regions:

- $x \leq x_1$: Inner Helmholtz Plane (IHP) caused by chemical interactions between ions and the electrode;
- $x_1 < x \leq x_2$: Outer Helmholtz Plane (OHP) caused by electrostatic interactions between ions and the electrode;
- $x > x_2$: Diffuse Layer, exponential decay of the potential of the electrochemical double layer according to equation 2.9.

.

2.1.2. Fundamentals of Electrode Reactions

An electrode reaction is a process that involves the transfer of electrons from an electrode to a chemical species, or vice versa. In the following, only the simple case is considered where an electrode is immersed in an electrolyte which contains the electroactive species O with its two different oxidation states, oxidized O and reduced R, where n is the number of the transferred electrons within the reaction. A simple electrode reaction that converts O to R and vice versa can be described by

$$O + ne^- \leftrightharpoons R \tag{2.12}$$

and consists of three steps: 1) the reagent O must reach the electrode surface, 2) the heterogeneous electron transfer process from the electrode to the species O takes place and 3) the reaction product R must leave the electrode surface. The overall reaction rate will be limited by the slowest elementary step either caused by mass transport (crucial in step 1 and step 3) or

electron transfer (crucial in step 2). Electrode reactions can involve multiple electron transfers, e.g. metal deposition, corrosion or coupled chemical reactions.

2.1.2.1. Transition State Theory and Interfacial Electron Transfer

The transition state theory describes the kinetics of electrode reactions and the factors controlling the corresponding reaction rates. Thereby, within the reaction, the reactant first reaches a transition state, also called activated complex, before the reaction product is formed. The changes in the standard free energy during the reaction pathway is shown in Figure 2.2. The electron transfer, occuring within the electrode reaction can be described as a quantum process. The basic model for electron transfer reactions was developed by Marcus, Hush, Levich and Dogonadze in several contributions starting in the 1950s [61–66]. These models are based on fast electronic motion and slow nuclear motion, the Franck-Condon principle, i.e. electron transfer occurs via tunneling between reactant and product nuclear vibational surfaces.

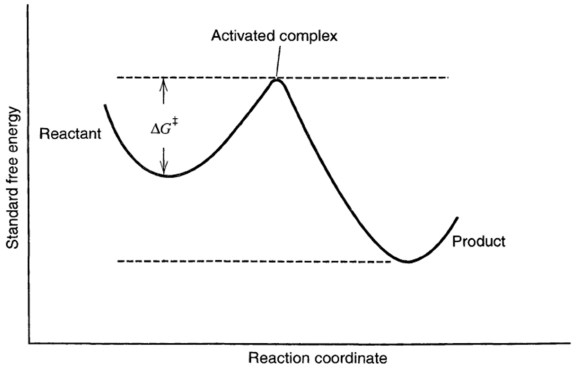

Figure 2.2. Scheme of the changes in free energy during a reaction, the transition state is the configuration of maximum free energy, taken from [53]

Assuming that all activated complexes are transmitted into the product via an electron transfer process, the reaction rate constant k [s^{-1}] can be expressed as

$$k = \kappa_{el} \frac{k_B T}{h} \exp\left(-\frac{\triangle G^{\ddagger}}{RT}\right) \tag{2.13}$$

where κ_{el} is the electronic transmission coefficient which can take values between zero and unity and mainly depends on the electronic coupling matrix element which describes the strength of coupling between the reactant, the product and the transition states. k_B is the Boltzmann's constant, T the absolute temperature and h the Planck constant. Equation 2.13 is a general expression for a system at equilibrium. It shows that the rate constant for an elementary process is fixed for a given temperature and pressure and does not depend on the reactant and product concentrations. Treating the reactant and product energy surfaces as parabolic (Fig. 2.3), the Gibbs free energy of activation $\triangle$ $G^{\ddagger}$ can be written as

$$\triangle G^{\ddagger} = \frac{\lambda}{4}\left(1 + \frac{\triangle G^0}{\lambda}\right)^2 \tag{2.14}$$

R is the gas constant, λ the reorganization energy, $\triangle$ G^0 is the thermodynamic driving force for the reaction, also called standard Gibbs free energy change in the chemical reaction. From Figure 2.3 it is clear that broad parabolic free energy surfaces and/or small values of λ will give larger values of the electron transfer rate constant k.

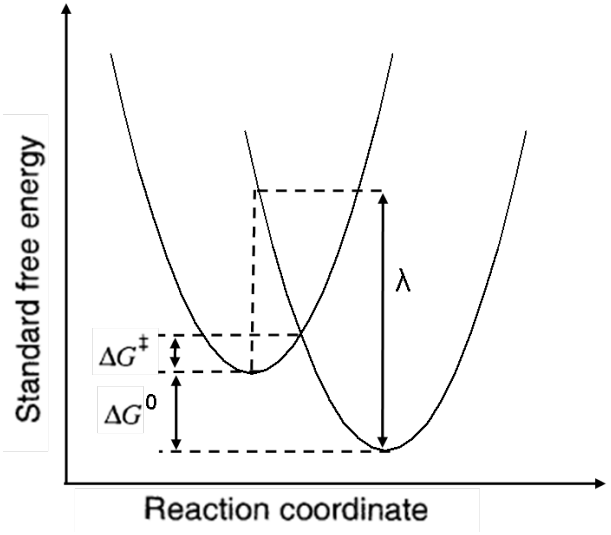

Figure 2.3. Scheme of the standard free energy surface for an electron transfer reaction, $\triangle$ $G^{\ddagger}$ is the Gibbs free energy of activation, $\triangle$ G^0 is the thermodynamic driving force for the reaction and λ is the reorganization energy.

2.1.2.2. Potentials and Currents

Since an electrode reaction always implies a transfer of electrons, the rate of the electrode reaction can be measured by the current flow in the electrochemical cell. According to Faraday's law the reduction of m mole O requires the total charge Q [67]

$$Q = n \cdot F \cdot m \tag{2.15}$$

where F is the Faraday constant (96 485 CM^{-1}). Therefore, the current, i.e. the variation of charge with time is equal to:

$$I = \frac{dQ}{dt} = n \cdot F \cdot \frac{dm}{dt} \tag{2.16}$$

Currents originating from chemical processes that obey Faraday's law are called Faradaic currents. Hence, if we are considering heterogeneous processes, the current is proportional to the

area of the electrode. One can normalize with respect to the electrode area, A, and obtain the current density j

$$j = \frac{I}{A} = n \cdot F \cdot \frac{1}{A} \cdot \frac{dm}{dt} \tag{2.17}$$

The variation of the mole number with time and per area, $\frac{dm}{dt \cdot A}$, reflects the variation of concentration per unit time and area ν (in $\mathrm{Ms^{-1}m^{-2}}$):

$$\nu = \frac{1}{A} \cdot \frac{dM}{dt} = \frac{j}{n \cdot F} \tag{2.18}$$

The rate constant ν only depends on the rate constant k of the electron transfer and the concentration c of the redox active species

$$\nu = k \cdot c \tag{2.19}$$

Therefore, the Faradaic current density can be written:

$$j = n \cdot F \cdot \nu = n \cdot F \cdot k \cdot c \tag{2.20}$$

Assuming fast electron transfer, the concentrations of O and R at the electrode surface are considered to be at equilibrium with the electrode potential, as governed by the Nernst equation

$$U_0 = U_{00} + \frac{RT}{nF} \ln \frac{c_O}{c_R} \tag{2.21}$$

where U_{00} is the standard potential of the O/R couple, R the gas constant 8.314 $\mathrm{JK^{-1}M^{-1}}$, T the absolute temperature, n the number of electrons transferred within the reaction, F the Faraday constant, c_0 concentration of the oxidized species and c_R the concentration of the reduced species. At equilibrium no net current is flowing, however, the equilibrium is dynamic, i.e. both reactions, the reduction of O and the oxidation of R, take place, but are of equal rate $-j_c = j_a = j_0$, where $-j_c$ and j_a are the cathodic and anodic partial current densities for the reduction and oxidation reactions and j_0 is the exchange current density at equilibrium, i.e. the current density that flows at U_0.

The electrons inside the electrode populate the conduction band which is called the Fermi level E_F. Applying the potential U_0 to the electrode, the Fermi level of the electrode lies in between the energy states of the molecular orbitals of the redox species, i.e. between the highest occupied molecular orbital (HOMO) and the lowest unoccupied molecular orbital (LUMO). In this case no electron transfer between the molecule and the electrode takes place (see Fig. 2.4). Applying a potential more negative than U_0 to the electrode leads to an adjustment of the surface concentration of O on the surface in order to reestablish equilibrium. The energy of the Fermi level is raised to a level at which the electrons of the electrode flow into the lowest unoccupied

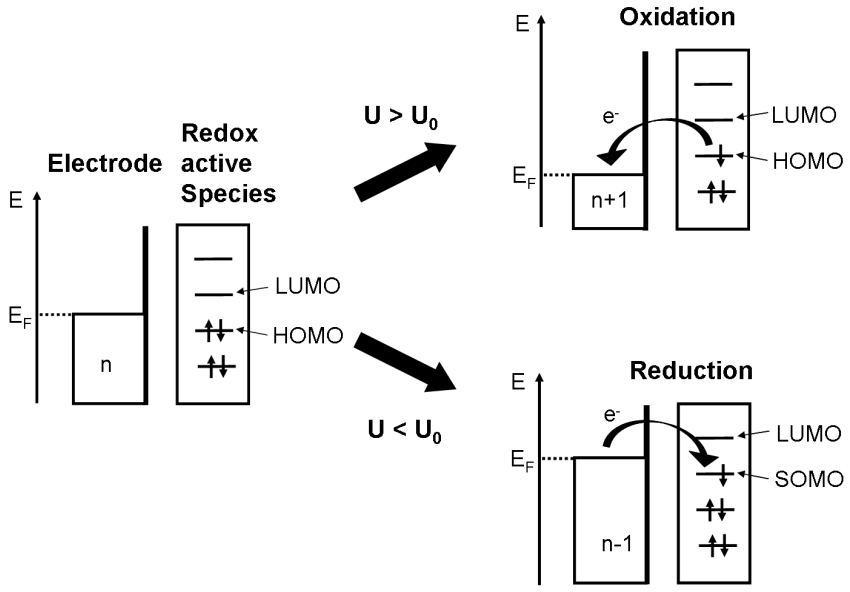

Figure 2.4. The potential applied to the electrode can trigger oxidation and reduction processes. n: number of electrons, E_F Fermi level, based on [68].

molecular orbital (LUMO) of the electroactive species. Thus, a reduction process takes place and current flows through the electrode/solution interface. Analogously, imposing an electrode potential more positive than U_0, the Fermi level is decreased and the electroactive species donates electrons from its highest occupied molecular orbital (HOMO) to the electrode. An oxidation process takes place. A single occupied molecular orbital is called SOMO.

The correlation between the applied electrode potential U and the current density j is described by the Butler-Volmer equation

$$j(\eta) = j_0 \left[\exp\left(\frac{\alpha_a n F}{RT} \eta \right) - \exp\left(-\frac{\alpha_c n F}{RT} \eta \right) \right] \tag{2.22}$$

where η is defined as the overpotential, i.e. the deviation of the potential from the equilibrium potential:

$$\eta = U - U_0 \tag{2.23}$$

and α_a and α_c are the transfer coefficients (between 0 and 1) for the anodic and the cathodic reactions, respectively. The Butler-Volmer equation is the fundamental equation of electrode kinetics and can be reduced to three limiting forms, depending on the conditions:

- high positive overpotentials: $\mid j_a \mid >> \mid j_c \mid$

$$\log j = \log j_0 + \frac{\alpha_a n F}{2.3RT} \eta \tag{2.24}$$

- high negative overpotentials: $\mid j_c \mid >> \mid j_a \mid$

$$\log|-j| = \log j_0 - \frac{\alpha_c nF}{2.3RT}\eta \tag{2.25}$$

- very low overpotentials: $\eta << \frac{RT}{\alpha_c nF}$ and $\eta << \frac{RT}{\alpha_a nF}$

$$j = j_0 \frac{nF}{RT}\eta \tag{2.26}$$

Equations (2.24) and (2.25) are known as Tafel equations and are used to determine the exchange current density and the transfer coefficient.

Furthermore, in an electrochemical cell also non-Faradaic currents exist which arise from processes of a strictly physical nature, e.g. the properties of the electrodes. As already discussed in Section 2.1.1 the solid-liquid interface of the working electrode in an electrochemical cell can be described as a double layer and thus, is comparable to a capacitor with the capacitance C

$$C = \frac{Q}{U} \tag{2.27}$$

where Q is the charge on the electrode surface and U the potential of the electrode. By applying a potential the capacitor is charged and a current, the so called capacitive current flows, according to the relation:

$$I_c = \left(\frac{U}{R}\right)\exp\left(-\frac{t}{RC}\right) \tag{2.28}$$

While Faradaic currents are a function of the square root of time $j \propto t^{-\frac{1}{2}}$, the capacitive currents decrease exponentially with time $j \propto (\exp(t))^{-1}$. Therefore, time dependent measurements can be used to discriminate between Faradaic and non-Faradaic currents.

2.1.3. Cyclic Voltammetry

Potential sweep techniques, such as linear sweep voltammetry (LSV) and especially cyclic voltammetry (CV), have become very popular techniques for initial electrochemical studies of new systems and thus, have been applied to an ever increasing range of systems [53, 68]. With both techniques the cell current I is recorded as a function of the applied potential U. Usually, the excitation signal is a potential ramp between different potentials U_i, i.e. the potential is varied linearly with time at a known sweep rate v. While LSV involves sweeping the electrode potential between two potentials U_1 and U_2 before halting the potential sweep, CV switches the direction when reaching the potential U_2. The potential sweeps back to U_1, then the potential sweep can either be stopped, again reversed towards U_2, or alternatively continued further to a value U_3. The electrochemical spectrum obtained in such experiments gives information about the potentials at which processes occur.

Figure 2.5 shows a typical triangular waveform of the excitation signal in a CV experiment. The response of an electrochemical system with an electroactive species O in solution which can

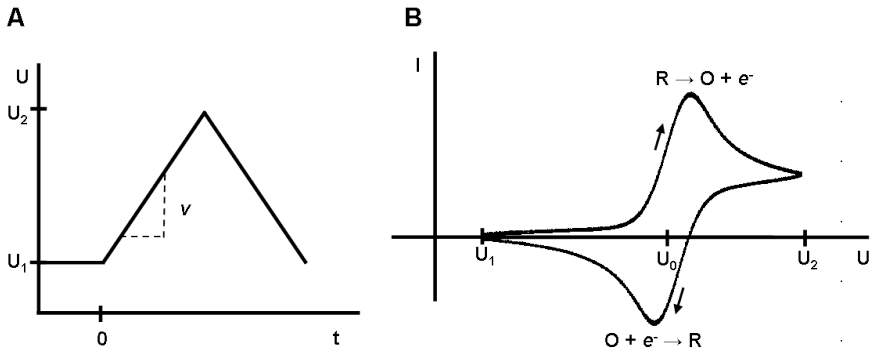

Figure 2.5. A) Cyclic potential sweep and B) resulting cyclic voltammogram.

be reduced to R is given in Fig. 2.5. Since the mathematical description of these techniques has been developed sufficiently, kinetic parameters can be determined for a wide variety of mechanisms even of fairly complicated electrode reactions. From the sweep rate dependence the involvement of coupled homogeneous reactions can be identified and processes such as adsorption can be recognized.

2.1.3.1. Redox Species in Solution

Nernstian System

An electrochemical system with an electroactive species O in solution which can be reduced to R and reoxidized to O can be described by Equation 2.12.

The cyclic voltammogram of this system has a typical reversible current-voltage response shown in Figure 2.5B. The current response recorded when sweeping the potential to negative values and thus, reducing the electroactive species, is called cathodic current with a peak value I_{cp}, the positive counterpart is defined as anodic current with a peak value I_{ap}. The corresponding peak potentials are named U_{cp} and U_{ap}, respectively. The electrochemical redox potential is given as $U_0 = \frac{1}{2}(U_{cp} + U_{ap})$.

For Nernstian systems, the kinetics at the electrode surface is rapid and the concentration of O and R adjust to the ratio given by the Nernst equation. The solution of the diffusion equations (Fick's 2nd Law) under the appropriate boundary conditions leads to a mathematical description of the voltammetric curves. The peak current I_P at 25°C can be calculated by the so called Randles-Sevičk equation [69, 70]

$$I_p = -(2.69 \cdot 10^5) n^{\frac{2}{3}} c D^{\frac{1}{2}} v^{\frac{1}{2}} A \tag{2.29}$$

where n is the number of electrons according to Equation 2.12, c is the analyte concentration in $\mathrm{Mcm^{-3}}$, D is the diffusion coefficient of the analyte in $\mathrm{cm^2 s^{-1}}$, v is the sweep rate in $\mathrm{Vs^{-1}}$ and A is the electrode area in $\mathrm{cm^2}$.

Non-Nernstian System

In contrast to a Nernstian system where redox active species can reversibly be oxidized and reduced an one-step reaction can be described by

$$O + ne^- \rightarrow R \tag{2.30}$$

i.e. a reverse reaction does not take place. For a such an irreversible process the shape of the cyclic voltammogram can again be obtained mathematically by solving the diffusion equations with adjusted boundary conditions. This yields the following equation for the peak current at $25°C$

$$I_p = -(2.99 \cdot 10^5)\alpha^{\frac{1}{2}} c D^{\frac{1}{2}} v^{\frac{1}{2}} A \tag{2.31}$$

where α is the transfer coefficient. Therefore, the peak current is proportional to the concentration and to the square root of the sweep rate as for reversible reactions, but additionally to the square root of the transfer coefficient.

Systems with Electron Transfer Kinetic Limitations

Systems where the electron transfer kinetic is limited show a Nernstian behavior at low sweep rates and a non-Nernstian behavior at higher sweep rates. This transition occurs when the relative rate of the electron transfer with respect to that of mass transport is insufficient to maintain Nernstian equilibrium at the electrode surface. This change in electrochemical behavior can be seen from a plot of the peak current I_p as a function of the square root of the sweep rate $v^{\frac{1}{2}}$, i.e. I_p increases with $v^{\frac{1}{2}}$ but is not proportional to it.

2.1.3.2. Redox Species adsorbed on the Surface

Cyclic voltammetry is a useful technique for the quantitative investigation of reactions involving adsorption processes. In this section we consider the simplest case where only the adsorbed forms of O and R are electroactive in the investigated potential range. Furthermore, we assume an adsorption so strong that the contribution of dissolved O and R to the response is negligible. Therefore, mass transport effects can be ignored. Furthermore, the electrode coverage is independent of the applied potential.

If the redox species adsorbed to the electrode surface is in good electric contact with the electrode, the cyclic voltammogram will show sharp and symmetrical peaks with no or only little peak separation (Fig. 2.6). The symmetrical peaks arise because of the fixed amount of reactant on the surface: only adsorbed O on the electrode surface can be reduced. Therefore, also the charges associated with anodic and cathodic processes are equal. If the adsorption can be described by a Langmuir isotherm, i.e. the Gibbs energy of adsorption $\triangle G_{ad}$ is considered as independent of the coverage, $U_{ap} = U_{cp}$ and the peak current is given by

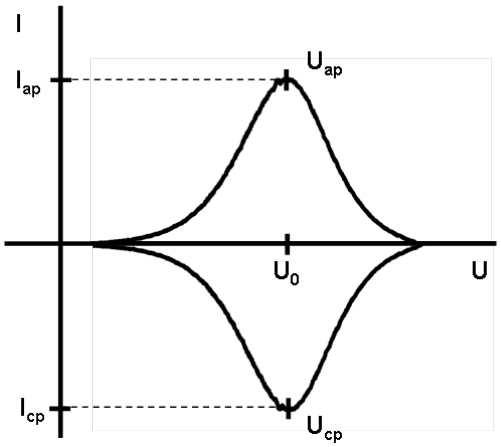

Figure 2.6. Cyclic voltammogram of a species adsorbed to the electrode surface showing Nernstian behavior.

$$\mid I_p \mid = \frac{n^2 F^2 \Gamma_0}{4RT} vA \tag{2.32}$$

where Γ_0 is the surface coverage of O before the experiment. Equation 2.32 shows that the peak current is proportional to the sweep rate v and not to its square root. The charge Q below the peaks corresponds to the oxidation or reduction of the adsorbed layer and enables the determination of the surface coverage by

$$\Gamma_0 = \mid \frac{Q}{nF} \mid \tag{2.33}$$

The shape of the cyclic voltammogram changes for non-Nernstian systems.

For such diffusionless systems Laviron [71–73] has derived an expression from the Butler-Volmer equation in order to determine the transfer coefficient α and the rate constant k. For the Nernstian systems, i.e. for small sweep rates ($v \to 0$) the cyclic voltammograms are symmetric as in Figure 2.6. The half width is independent of the transfer coefficient $\alpha \frac{90.6}{n}$ mV. For high sweep rates ($v \to \infty$), when the reaction might be limited by the kinetic of the electron transfer, the cyclic voltammogram looses its symmetrical shape.The peak currents lie at the following potentials:

$$U_{ap} = U_0 + \frac{RT}{\alpha_a nF} \ln\left(\frac{RT}{\alpha_a nF} \cdot k \cdot v\right) \tag{2.34}$$

and

$$U_{cp} = U_0 - \frac{RT}{\alpha_c) nF} \ln\left(\frac{RT}{\alpha_c nF} \cdot \frac{k}{v}\right) \tag{2.35}$$

With the help of the potential difference $\triangle U_p = U_{ap} - U_{cp}$, the transfer coefficients and the electron transfer rate can be determined when $\triangle U_p > \frac{200}{n}$mV, i.e. a irreversible system can be assumed. The slope of the graphs of $U_{ap} = f(\ln v)$ or $U_{cp} = f(\ln v)$ yields the transfer coefficients α_a and α_c, and $\triangle U_p$ results in the rate constant k.

2.2. Biophysical and Biochemical Fundamentals

2.2.1. Charge Transfer in Biomolecules

Charge transfer processes are present in almost all biological systems and are essential for capture and use of energy e.g. in the respiratory system, photosynthesis, in aerobic [74] and bacterial [75] metabolism. Thereby, energy transduction proceeds via a sequence of ordered electron transfer reactions. These processes are enabled by transition metalloproteins such as azurin and cytochrome c. Theoretically, electron transfer reaction in biological systems can be described as mentioned before in equation electrontransfer and Figure parabolic. However, for biological systems, the protein structure surrounding the redox center plays an important role since the protein shell, i.e. the "reaction medium" normally has a lower dielectric constant ($\varepsilon \approx 5$) than bulk water ($\varepsilon \approx 80$). Therefore, the interactions between the protein shell and the charge at the redox center, and the change in charge accompanying the electron transfer, are smaller than between the redox center and water. Furthermore, the constrained structure of the protein around the active site reduces the reorganization energy λ and speeds up the electron transfer reaction [76]. The kinetics of electron transfer also depends on the distance between electron donor and electron acceptor and thus on the size of the protein. Furthermore, different pathways for electron transfer e.g. through-space or through-bond, also including the possibility to change between these two electron transfer pathways, are discussed [77]. Since the peptide chain of a certain protein comprises various amino acid residues in a particular sequence and orientation, the electron transfer pathway between the electron donor and the electron acceptor is divided into a number of segments corresponding to covalently bonded parts, hydrogen bonded parts and parts where there is van der Waals contact. To sum up, the environmental reorganization Gibbs free energy as well as the function and the activity of a protein are strongly connected to its structure. Conformational modifications especially in the side chain residues of the active site often lead to changes in the functional and also electrochemical properties of the protein [78, 79]. These findings can be explained by the interplay of different interactions such as electronic-conformational interactions, combined electrostatic and hydrophobic effects, as well as possible electron tunneling pathways throughout the protein. Further details and a theoretical consideration are given in [4, 80].

2.2.2. Proteins and Enzymes

Proteins and enzymes, i.e. catalytically active proteins, are linear polymers of α-amino acids linked by peptide bonds and folded into a globular form. All amino acids contain an amine group, a carboxylic acid group and a side chain which varies between different amino acids. In the α-amino acids, the amino and carboxylate groups are attached to one carbon atom, which is called the α-carbon. The peptide bonds are formed between the carboxyl and the amino group of adjacent amino acids. The precise amino acid content and the sequence of the amino acids of a specific protein is defined by the sequence of the bases in the gene that encodes that protein. The universal genetic code specifies 20 amino acids that are naturally incorporated into proteins. In

Figure 2.7 the structures of these 20 amino acids are shown. Depending on their side chain, the amino acids have different molecular weights (MW) and chemical properties. The composition of all amino acids in a protein determines its biological activity. Proteins not only catalyze all (or most) of the reactions in living cells, they control virtually all cellular processes.

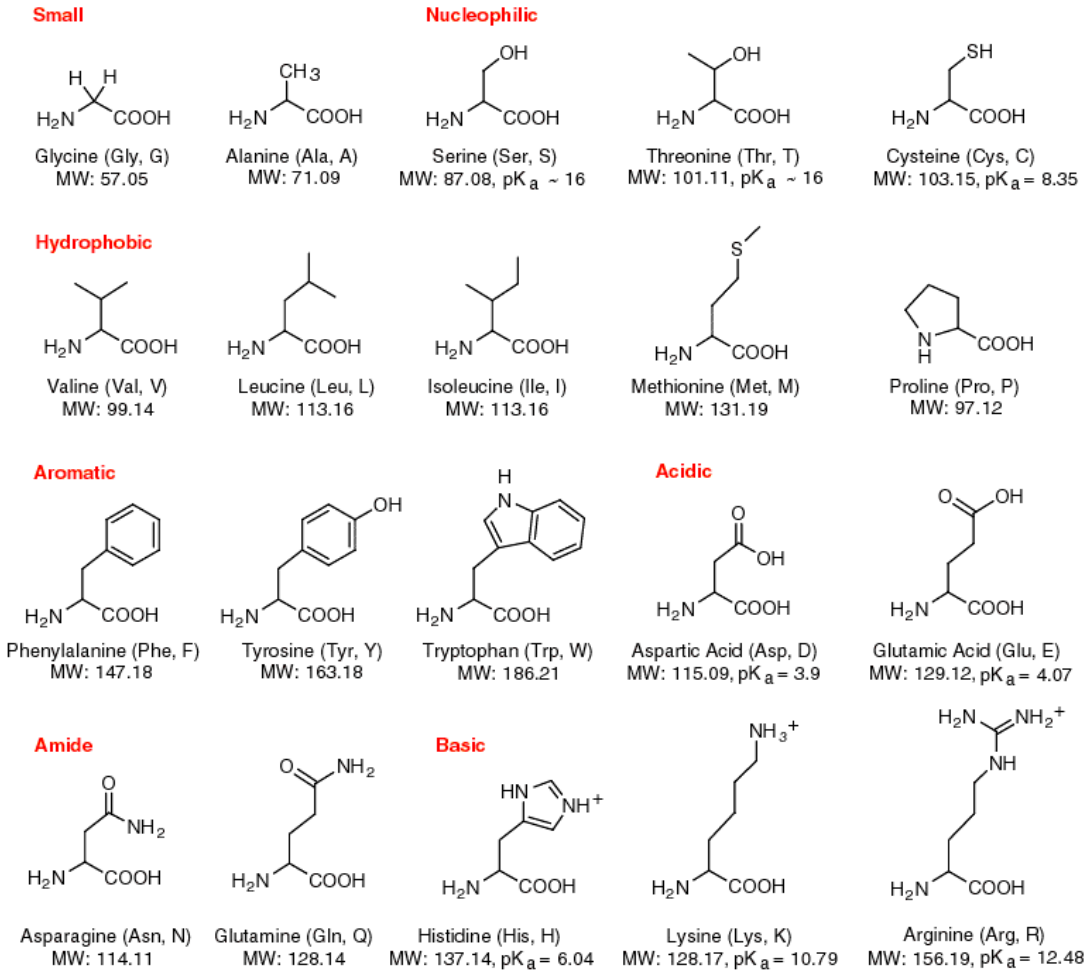

Figure 2.7. Structure of the 20 amino acids occurring in nature, together with their molecular weight (MW) and some chemical properties, taken from [81]

In this section the proteins and enzymes used in this thesis are described concerning their structure and function in biological systems. When not stated otherwise, the crystal structure of the proteins is plotted with PyMOL [82] using the corresponding accession code obtained from the Protein Data Bank (PDB) [83]. The color coding shows α-helices in red, β-sheets in yellow, and loops in green.

2.2.2.1. Ferritin and Apoferritin

Iron plays a significant role in many biological processes [84, 85] and is found in several enyzmes to transport (hemoglobin), store (myoglobin), and use (cytochromes, cytochrome oxidase) oxygen for respiration. However, since iron is toxic its concentration in living organisms has to be tightly controlled, which is maintained by the metalloprotein ferritin.
The tertiary structure of the ferritin molecule is a nearly spherical shell with a diameter of 12 nm consisting of 24 protein subunits (total molecular weight 440 kDa) that surrounds a crystalline ferrihydrite phosphate core with a diameter of up to 8 nm. At the intersections of three or four peptide subunits channels are formed. Eight hydrophilic and six hydrophobic channels link the interior of the protein shell with the exterior, providing pathways for the transfer of Fe^{2+} that passes through the hydrophilic channels into the protein shell. Therefore, ferritin is a metalloprotein that regulates the iron metabolism. It has the capacity to remove ferrous ions from serum, oxidize them to Fe^{3+} and reversibly store the resulting ferric ions in a hydrated iron oxide, forming $8FeO(OH) \cdot FeO(H_2PO_3)$ in its interior [86, 87]. When iron is needed in the organism, ferritin reduces ferric to ferrous ions. Iron becomes soluble and hydrated and exits the protein through one of the polar (hydrophilic) three-fold channels. While one ferritin molecule can contain up to 4500 Fe(III) ions, the iron free conformation apoferritin only consists of the hollow protein shell (molecular weight 18.5 kDa). The loading and unloading of iron from ferritin involves electron transfer steps which are thought to happen in the four-fold channels, however, so far the nature of the electron transfer is not clear [88, 89].

2.2.2.2. Horseradish Peroxidase

Horseradish peroxidase (HRP) is a heme-containing enzyme which belongs to the plant peroxidase superfamily. It is produced on a large scale from horseradish roots (*Armoracia rusticana*) since HRP is widely commercially used e.g. as a component of clinical diagnostic kits, for chemiluminescent assays or immunoassays, as well as treatment of waste water (for reviews see [90–92]). HRP comprises a single polypeptide of 308 amino acid residues [93]. Its structure is largely α-helical with only a small region of β-sheet [94] forming two domains, the distal and proximal domain. HRP contains two different types of metal centers, iron(III) protoporphyrin IX, referred to as the heme group, and two calcium atoms (Fig. 2.8). Both are essential for the structure and function of the enzyme. The heme group is attached to the enzyme at the proximal histidine residue (His-170) by a coordinate bond between a histidine side-chain and the heme iron atom. The heme group is located between the distal and proximal domains which each contain one calcium atom.

Most reactions catalyzed by HRP can be expressed by the following equation, in which AH_2 and AH* represent a reducing substrate and its radical product, respectively [90].

$$H_2O_2 + 2AH_2 \overset{HRP}{\rightarrow} 2H_2O + 2AH^* \tag{2.36}$$

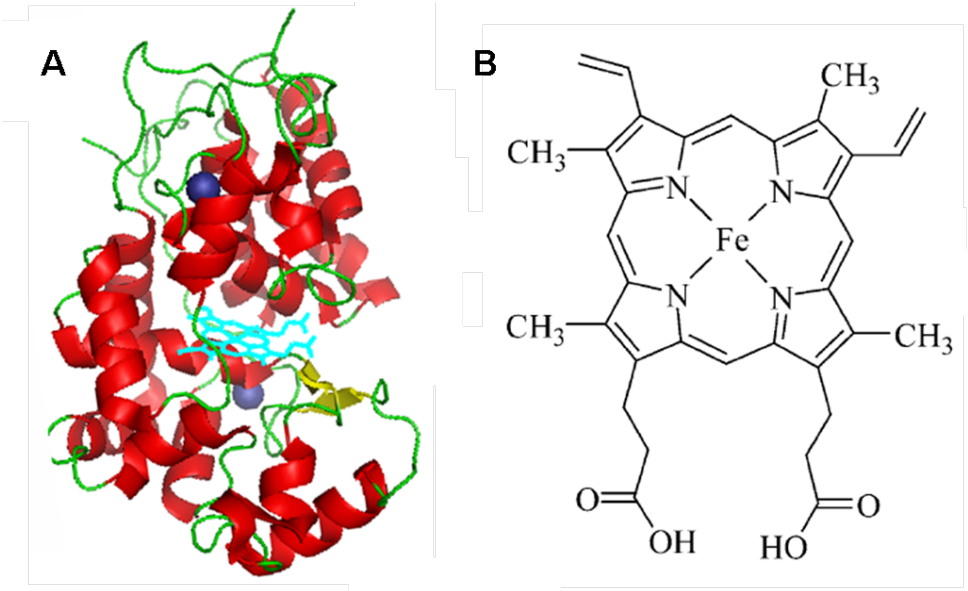

Figure 2.8. A) Crystal structure of horseradish peroxidase (PDB 1W4W). The heme group is colored in turquoise, the calcium atoms are shown in blue. B) Molecular structure of the active site of horseradish peroxidase, the Heme B, adapted from [90].

Although the conversion of hydrogen peroxide to water is not the primary function of HRP, its catalytic activity towards this reaction made HRP interesting for electrochemists and to one of the most studied members of the family of heme enzymes [95]. The electrocatalytic activity of native and genetically engineered HRP has been extensively studied on different substrate materials such as gold, silver, platinum, and different carbon materials [8, 96–100] in order to develop highly selective and efficient bioelectrocatalysts, e.g. for bioelectrochemical fuel cell applications.

2.2.2.3. Azurin

Azurin belongs to the copper-containg redox proteins (type-1) [101] which are found in several bacteria and plants and play important roles in biochemical pathways such as respiration and photosynthesis [102]. Azurin is involved in the oxidative phosphorylation of its expressing organism, where it acts as an electron transfer component, most probably shuttling electrons between cytochrome c_{551} and nitrite reductase [103]. Its functional behavior is based on the reversible oxidation of Cu^{+1} to Cu^{+2}. Azurin is a small protein (9-14 kDa) with a mononuclear copper coordinated by cysteine, two histidines, and an axial methionine [104–106]. According to crystallographic data, azurin has the dimensions of $(36 \times 25 \times 22)$ Å^3. Its structure is characterized by a globular, β-barrel conformation where the active redox site is located approximately 8 Å below the surface and a surface disulfide bridge between Cys-3 and Cys-26 is formed. Since the

disulfide offers a convenient means for anchoring azurin to gold surfaces, azurin has become an ideally suited candidate for metalloprotein investigation in bioelectrochemistry. Furthermore, a hydrophobic patch around the copper center can be exploited to confine azurin molecules on Au surfaces. The redox potentials of azurins from different sources were estimated and found to be in the range between 220 mV and 320 mV vs. NHE [44, 107, 108]. Furthermore, azurin has extensively been used in the past for single molecule scanning probe microscopy studies [3, 17, 18, 43, 109, 110]

2.2.2.4. Papain

Papain is a cysteine protease that can be extracted from the latex of the papaya fruit. It consists of a single polypeptide chain with 212 amino acid residues and has a molecular weight of 23.4 kDa [111]. In its tertiary structure, the chain is folded into two structural domains (L- and R-domain) stabilized by three disulfide bridges containing α-helices and β-sheets (Fig. 2.9). The active site is located in the cleft between these two domains containing a catalytic triad made up of the amino acids cysteine-25 (Cys-25), histidine-159 (His-159) and asparagine-158 (Asp-158). According to crystallographic data, papain has the dimensions of $(29 \times 34 \times 45)$ Å^3. Papain is proteolytic, i.e. it hydrolyzes proteins to form oligopeptides and amino acids. By breaking peptide bonds papain digests proteins. This mechanism involves the deprotonation of Cys-25 by His-159. Thereby, Asp-158 helps to orient the imidazole ring of His-159 to allow the deprotonation and enables Cys-25 to perform a nucleophilic attack on the carbonyl carbon of a peptide backbone. The free amino terminal of the peptide subsequently forms a covalent bond with the enzyme resulting in an acyl-enzyme intermediate. The enzyme is then deacylated by a water molecule, and releases the carboxy-terminal portion of the peptide. Papain is the prototype of cysteine endopeptidases, due to its homology with mammalian cysteine proteases involved in several serious diseases related to tissue degeneration [112]. Papain is often in the focus of biochemical and biophysical studies [29, 113–115] due to its easy availability and its high stability. Papain is mainly used in the pharmaceutical industry, in medicine, as well as in the food processing industry.

2.2.3. Synthesis of peptide chains

Nowadays several methods exist to synthesize amino acids [116–121] by coupling the carboxyl group of one amino acid to the amino group of another. In order to avoid unintended reactions protecting groups are necessary. Currently, the most adopted method is the solid-phase peptide synthesis (SPPS) usually performed on a polystyrene resin introduced by Merrifield in 1963 [122]. In SPPS protecting groups such as 9H-fluoren-9-ylmethoxycarbonyl (Fmoc) [123] and tert-butyloxycarbonyl (t-Boc) [124] are utilized in order to block side chain residues and therefore, avoid unwanted binding. On the other hand, activating groups such as dicyclohexylcarbodiimide (DCC) and diisopropylcarbodiimide (DIC) are commonly used to induce binding processes [125]. Synthesized chemical compounds are usually separated using high-performance liquid chromatography (HPLC) and characterized by mass spectrometry (MS) and nuclear magnetic resonance

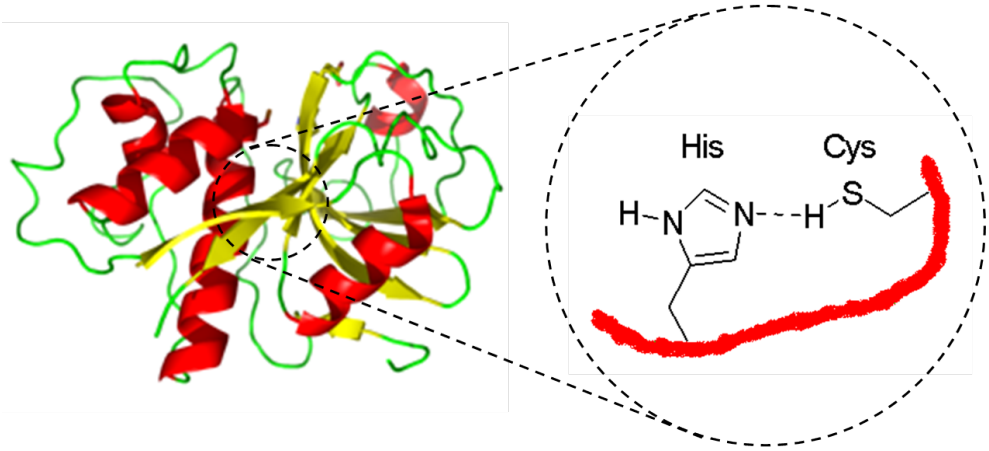

Figure 2.9. Three dimensional structure of papain based on crystallographic X-ray data (PDB 1PPD) and its active site containing the amino acids Cys-25 and His-159.

(NMR).

2.2.4. Enzyme Kinetics

2.2.4.1. Michaelis-Menten Kinectics

The kinetic of enzyme-catalyzed reactions can be described by the Michaelis-Menten kinetics (also referred to as Michaelis-Menten-Henri kinetics). In the beginning of the 20^{th} century Victor Henri supposed the formation of an enzyme substrate complex (ES) during the enzyme catalysis process [126]. Leonor Michaelis and Maud Menten extended this idea to an overall theory of the enzyme function mechanism [127]. They postulated that the formation of the reversible enzyme-substrate complex (step 1) is relatively fast before in a second step the complex dissociates again into the free enzyme E and the product P (step 2) while the product does not bind to the enzyme [128].

$$E + S \underset{k_{-1}}{\overset{k_1}{\rightleftharpoons}} ES \underset{k_{-2}}{\overset{k_2}{\rightleftharpoons}} E + P \tag{2.37}$$

Therefore, the second step is the rate limiting step of the whole process, i.e. the reaction rate v of the enzyme catalyzed reaction is proportional to the concentration of the ES complex. Assuming the enzymatic reaction to be irreversible, the product does not dissociate again into the substrate (i.e. $k_{-2} = 0$).

Furthermore, the substrate concentration [S] is often considered to be high enough to remain constant within the reaction. This is valid, when the enzyme concentration is much smaller than the substrate concentration. Briggs and Haldane [129] introduced the so-called steady state for

step 1, i.e. $k_1 = k_{-1}$. Then the initial reaction rate v_0 depends on the dissociation of ES and is given by

$$v_0 = \frac{d[P]}{dt} = k_2[ES] \tag{2.38}$$

where [ES] is not known. However, the production of the ES complex can be calculated by its formation and dissociation

$$\frac{d[ES]}{dt} = k_1[E][S] - k_{-1}[ES] - k_2[ES] \tag{2.39}$$

Then the relation of the initial reaction rate v_0 to the substrate concentration [S] is given by the Michaelis-Menten equation:

$$v_0 = \frac{v_{max}[S]}{K_M + [S]} \tag{2.40}$$

Here v_{max} describes the maximum rate and K_M is the Michaelis constant defined by

$$K_M = \frac{k_2 + k_{-1}}{k_{-1}} \tag{2.41}$$

2.2.4.2. Influence of Enzyme Inhibitors

Enzyme inhibitors are compounds which interrupt the catalysis and decelerate or even stop the enzymatic reactions. The investigation of enzyme inhibitors is essential for a better understanding of enzyme mechanisms. Since enzymes are involved in most cellular processes, enzyme inhibitors are also of great interest for drug production. In general two kinds of enzyme inhibitors have to be distinguished: the reversible and the irreversible enzyme inhibitors.

Reversible inhibitors

Common reversible enzyme inhibition is based on competitive inhibitors, i.e. the inhibitor competes with the substrate for the active site. In most cases competitive inhibitors consist of compounds similar to the substrate. The inhibitor (I) occupies the active site and, thus, avoids the binding of the substrate to the enzyme. The formed enzyme-inhibitor complex (EI) does not lead to a catalytic reaction. The Michaelis-Menten equation changes to:

$$v_0 = \frac{v_{max}[S]}{aK_M + [S]} \tag{2.42}$$

with

$$a = 1 + \frac{[I]}{K_I} \tag{2.43}$$

and

$$K_I = \frac{[E][I]}{[EI]} \tag{2.44}$$

aK_M is also called the *apparent* K_M.
Since the inhibitor only binds reversibly to the enzyme, the formation of the enzyme-substrate complex instead of the enzyme-inhibitor complex can be enhanced by increasing the substrate concentration. For $[I] \ll [S]$, the probability for the EI formation becomes negligible and, therefore, the reaction follows the "normal" Michaelis-Menten equation. In the presence of an inhibitor, when $v_0 = 0.5v_{max}$, $[S] = aK_M$, i.e. the needed substrate concentration increases by the factor a.

In addition to the competitive inhibitors there exist also the uncompetitive and the mixed inhibition. Uncompetitive inhibition takes place when an enzyme inhibitor does not bind to the active site, but only to the ES complex, forming an ESI complex. Thereby, it is not necessary that the uncompetitive inhibitor resembles the substrate. The decrease of the effective ES concentration increases the enzyme's apparent affinity for the substrate through the principle of Le Chatelier (K_M is lowered) and decreases the maximum enzyme activity (v_{max}), as it takes longer for the substrate or product to leave the active site. Uncompetitive inhibition works best when the substrate concentration is high. Mixed inhibition refers to a combination of both types of reversible enzyme inhibition - competitive inhibition and uncompetitive inhibition, i.e. the inhibitor either binds to the enzyme-substrate complex or to the active site of the free enzyme. However, in mixed inhibition, the inhibitor does not bind to the site where the substrate binds. Mixed inhibition results in a decrease of the apparent affinity of the enzyme to the substrate (*apparent* $K_M > K_M$) and in a decrease of the apparent maximum enzyme reaction rate (*apparent* $v_{max} < v_{max}$).

Irreversible inhibitors
Irreversible inhibitors either bind to functional groups of the enzyme which are crucial for its activity or even destroy them. That means they do not work by destroying the protein structure but by specifically altering the active site of the enzyme. Usually the binding between enzyme and the irreversible inhibitor is covalent. Irreversible inhibitors are generally specific for one class of enzymes and do not inactivate all proteins.

2.2.5. Biosensors

Quantification of biological or biochemical processes is of great importance for medical, biological, and biotechnological applications. Therefore, biosensor-related research has experienced immense growth over the past decades. A biosensor is generally defined as an analytical device

consisting of a recognition element and a transducer, which converts a biological response into a quantifiable and processable signal. With the invention of the first enzyme electrode by Clark and Lyons in 1962 [130], several sensing concepts and various devices have been developed. However, finding the ideal way to convert the biological information to a processable electronic signal is challenging due to the complexity of possible detection pathways and detection methods with all their advantages and disadvantages. Figure 2.10 schematically shows the basic components constituting a typical biosensor, with the biological sample where the reaction takes place, the transducer signal (which could be anything from weight or light to the current directly produced at an electrode), the appropriate detection method, and the final conversion to an electronic signal. Biosensors are typically classified by their type of recognition or transduction element. A sensor might be described as a catalytic biosensor when its recognition element (e.g. an enzyme or a series of enzymes) is able to recognize the analyte and to undergo a chemical reaction in order to form a detectable product. A sensor might be described as a bioaffinity sensor when its operation is based on the specific binding of the recognition element (e.g. an affinity label) to the analyte forming a specific complex, e.g. the reaction of an antibody with an antigen.

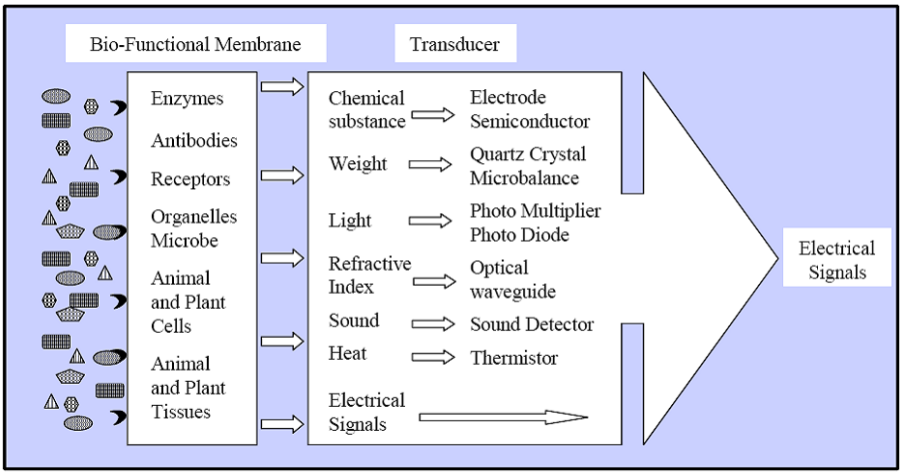

Figure 2.10. Basic components of biosensors showing the pathway from the biological sample to the electronic signal (taken from [33]).

2.2.5.1. The Affinity Label Concept

The affinity label (AL) is used to characterize the function of enzymes in biological systems. An affinity label normally consists of three parts: the recognition element, the reactive group, and the conjugation site. The property of an affinity Label (AL) to bind specifically to a certain group of enzymes is given by the recognition element. Its sequence is responsible for the selectivity and for the orientation in which the label binds to the enzyme. The recognition element and the enzyme usually form a reversible complex (anchor 1 in Fig. 2.11). Then, the reactive group of the AL reacts with the active site of the enzyme and leads to an irreversible, covalent binding

within the catalytic transformation (anchor 2 in Fig. 2.11). In Figure 2.11 the covalent binding is highlighted in yellow showing a thiol-binding. The conjugation sites function as possible binding sites for a specific marker (M) that provides the transduction signal. Depending on its physical properties the marker can be fluorescent, radio-active, magnetic, or even electroactive.

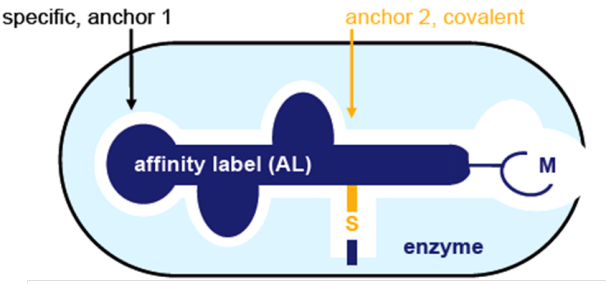

Figure 2.11. Affinity label (AL) which can bind to the active site of an enzyme.

Originally, affinity labels were developed in order to tag and localize a certain enzyme in a biological sample, e.g. tissue sample, and to analyze the specificity of the sample. Nowadays, they are mainly used to detect not only single enzymes, but whole enzyme families. Therefore, it is a challenging task to synthesize affinity labels that on the one hand can specifically react with a certain enzyme family, but on the other hand are unspecific enough to be able to react with all members of the enzyme family. Figure 2.12 shows the basic structure of the affinity label for cysteine proteases such as papain with succinic acid as the reactive group [131].

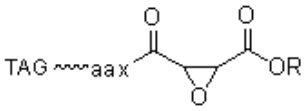

Figure 2.12. Affinity label (AL) for cysteine proteases such as papain.

2.2.5.2. Detection

In order to detect the binding of the affinity label to the active site of the enzyme a transducer (marker) must be coupled to the conjugation site of the affinity label. Depending on the properties of this marker element, e.g. a fluorophore or electroactive species, the appropriate biosensor could be based on optical or electrochemical detection methods.

Optical Detection

Optical biosensors are mainly based on measurements of absorption, reflection, or fluorescence emission in the UV, visible, or IR spectrum. Besides direct, i.e. affinity label free, detecion methods such as surface plasmon resonance (SPR) [132], the indirect fluorescence methods [133] which

function with dyes are commonly used. In 2004, Eppinger et al. [29] succeeded in measuring the catalytic activity of a papain microarray using a tailor-made fluorescently tagged affinity label (FAL) that binds in an activity-dependent manner to the active site of the enzyme (Fig. 2.13). Figure 2.13A shows an image of the microarray where 44 subarrays of 4 × 4 papain spots could be investigated for 11 different reaction times (abscissa) with four different FAL concentrations (ordinate). Quantified data corresponding to the microcarry is plotted in Figure 2.13B together with a best-fit reaction model, derived from Michaelis-Menten kinetics and indicating that FAL is a promising candidate for the on-chip determination of papain reactivity. The evaluated initial velocities (v_0) depending on the concentration of the FAL are shown in Figure 2.13. Furthermore, it was demonstrated that this method can also be used for the detection and characterization of inhibitors [29].

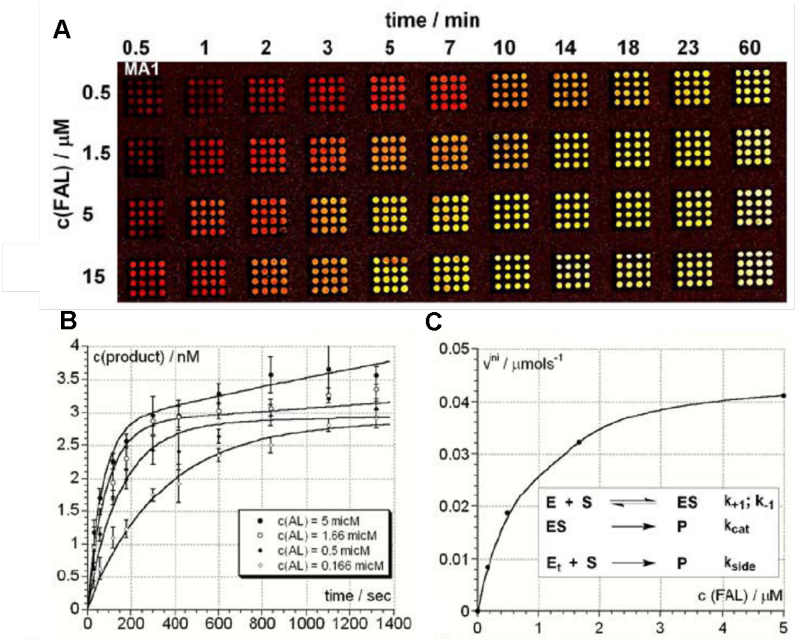

Figure 2.13. Optical detection of papain reactivity using a fluorescence affinity label. A) Microarray of 44 papain subarrays and B)corresponding quantified data according to Michaelis-Menten kinetics. C) Plot of initial velocities v_0 versus concentration of FAL, taken from [29].

Electrochemical Detection

Electrochemical sensors have received major attention in biosensing technology [6]. The most popular example is the development of a glucose biosensor, where the redox enzyme glucose oxidase is used in order to build an electrochemical glucose sensitive detector [5, 130, 134]. Compared to other biosensor architectures, electrochemical biosensors exhibit inherent advantages such as robustness, easy miniaturization and hence the design of high-density arrays, excellent detection limits, the ability to be used in turbid biofluids [135, 136] and, last but not least, from an economical point of view low-cost production of microelectronic circuits and the easy

interface with commercial electronic read-out and processing. However, electrochemical sensing of biomolecular interactions requires in general the presence of a redox-active probe as part of the detection system in order to generate a measurable current (amperometric), a measurable potential or charge accumulation (potentiometric), or measurably alter the conductive properties of a medium (conductometric). Although enzymatic transformations of substrates often serve as transduction elements in catalytic biosensors, other biorecognition elements such as antibodies, DNA, or redox-inactive enzymes in combination with an electroactive probe are used in affinity biosensors. Figure 2.14 represents some of the common electrochemical biosensor systems where the redox species is solved in solution (A), bound to an antibody which reacts with the immobilized analyte (B), or is attached to a single stranded DNA (C). Figure 2.14D shows a new approach reported by Mahmoud and Kraatz [115] which uses a ferrocene-peptide conjugate in order to detect the cysteine protease papain.

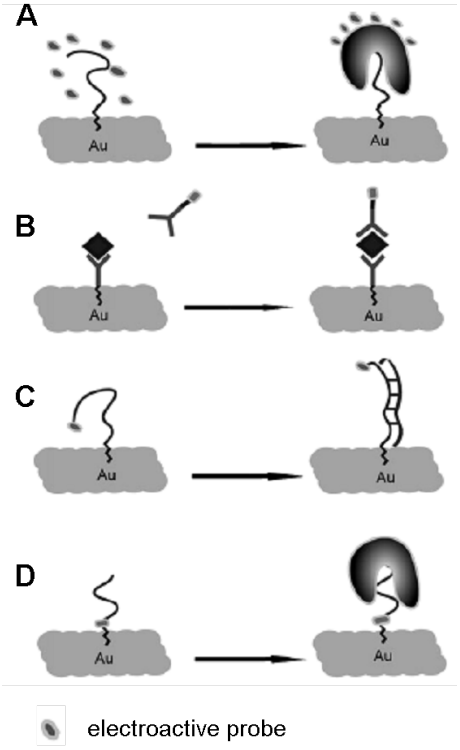

Figure 2.14. Different approaches to electrochemically detect biomolecular interactions (taken from [115])

The discovery of ferrocene in 1951 [137, 138] and the elucidation of its remarkable structure is the starting point for modern organometallic chemistry which is nowadays linked also to biology, medicine, and molecular biotechnology, leading to bioorganometallic chemistry [139]. Its unique properties such as the stability in aqueous and aerobic media, the accessibility of a variety of derivatives, and its favorable electrochemical behavior have made ferrocene groups very popular

for biological applications and for conjugation with biomolecules. Especially the redox activity and the high exchange current density which is due to a small solvent reorganization energy makes ferrocene suitable as an electroactive marker for electrochemical biosensor technology. Figure 2.15 shows the cyclic voltammogram (scan rate of 100 mVs^{-1}) of a highly oriented pyrolytic graphite (HOPG) electrode in 10 mM phosphate buffer solution (PBS, pH 7) containing 1 mM ferrocene monocarboxylic acid (FCMA) with a well-defined redox potential of 560 mV vs. NHE. The redox potential of a ferrocene-moiety can be modulated by different substituents on the cyclopentadienyl ligands. Electron withdrawing groups such as a carboxylic acid shift the redox potential in the anodic direction, whereas electron-releasing groups such as methyl groups shift it in the cathodic direction [140–142].

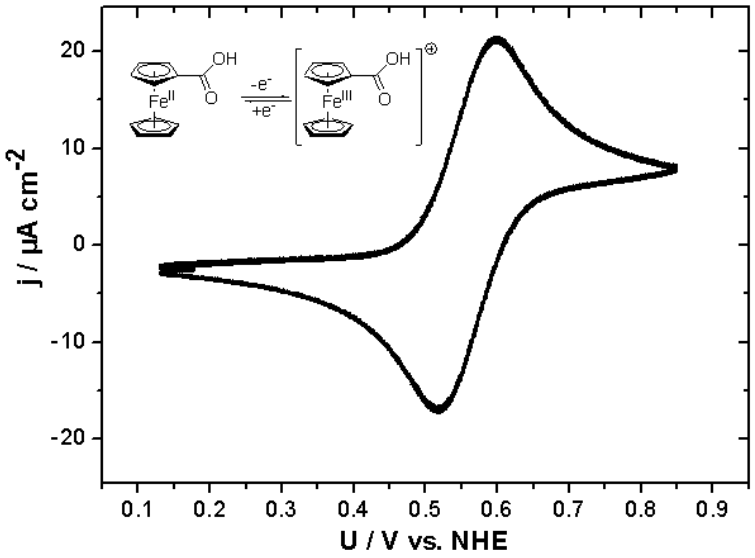

Figure 2.15. Cyclic voltammogram of a graphite electrode immersed in 10 mM PBS + 1 mM ferrocenemonocarboxylic acid, obtained at a scan rate of 100 mVs^{-1}.

2.3. Scanning Probe Microscopy

The development of the scanning tunneling microscopy (STM) by Binnig et al. [37, 38] in 1982 paved the way for a variety of scanning probe techniques and the investigation of surfaces on a nanometer scale. Since Sonnenfeld and Hansma first demonstrated that STM can also operate in electrolyte solutions [143] much progress has been made to explore the potential of this technique. The four electrode configuration in the STM allows to carry out complete in situ experiments under full potentiostatic control [144, 145] and has enabled new perspectives for studying electrochemical processes at the solid-liquid interface on a nanometer or even atomic scale. The following section will give a short introduction to the well-known electrochemical STM (EC STM) and the latest advancement of the electrochemical scanning probe microscopies (EC SPM) called "Scanning Electrochemical Potential Microscopy" (SECPM) which was introduced by Allen J. Bard et al. [47].

2.3.1. Principle of Scanning Tunneling Microscopy

2.3.1.1. Setup

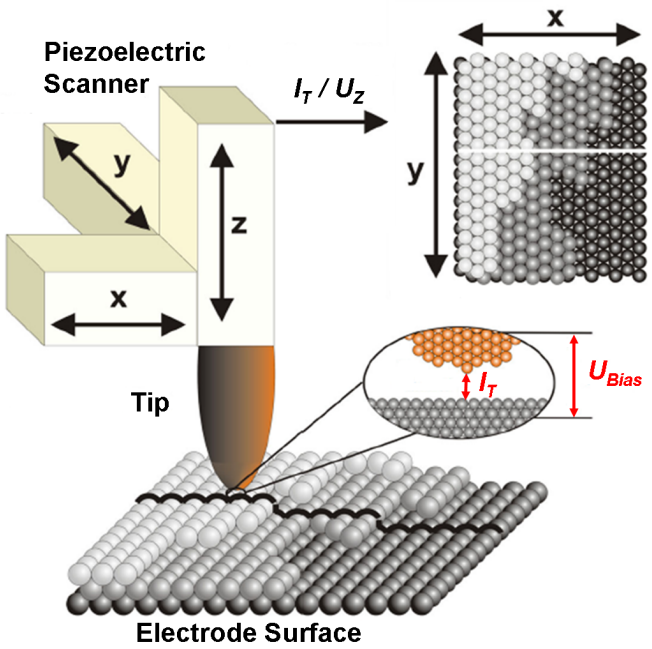

Figure 2.16. Setup of a scanning tunneling microscope (STM), based on [146]

The scanning tunneling microscope (STM) consists of a piezoelectric scanner, a conductive electrode and a sharp metal tip which is brought in close proximity to the electrode surface (Fig. 2.16). By applying a bias voltage, U_{Bias}, between tip and sample electrons can flow from the

tip to the sample or vice versa depending on the polarity of U_{Bias} and the distance between tip and sample. This mechanism is based on the quantum mechanical tunneling effect which will be described in more detail in the next paragraph. Depending on the setup, the piezoelectric scanner can either move the tip or the sample in x-, y- and z-direction with subnanometer precision in order to measure the tunneling current, I_T, and thereby the density of states of the sample with a resolution down to 0.1 Å. Since the composition of the tunneling gap is of minor importance, the STM can be operated in ultra high vacuum (UHV), in the gaseous phase or even in liquids.

2.3.1.2. Operation modi

Constant current mode

In the constant current mode I_T (Fig. 2.17A)is kept constant at a certain setpoint while the STM tip scans line by line in x- and y-direction above the electrode surface. The feedback loop compares the measured tunneling current with the chosen current setpoint and controls the current flow by adjusting the distance between tip and sample by applying a voltage U_Z to the z-piezo. Since the constant current mode adjusts the tip height, also surfaces with a higher surface roughness can be investigated in larger xy-dimension. Limitations in x-, y- and z-scan direction are given by the properties of the piezoelectric scanner.

Constant height mode

In the constant height mode (Fig. 2.17B) the STM tip scans above the electrode surface and measures the tunneling current while keeping the distance between tip and sample constant. In contrast to the constant current mode samples can be investigated with a high sampling rate due to the fact that the tunneling current has not to be controlled by the feedback loop. However, this mode is only suitable for small regions and atomically smooth surfaces. Typical distances between tip and electrode surface within scanning are between $0.2 - 2$ nm. Electrodes with a high roughness might cause danger to crush the tip into the sample surface.

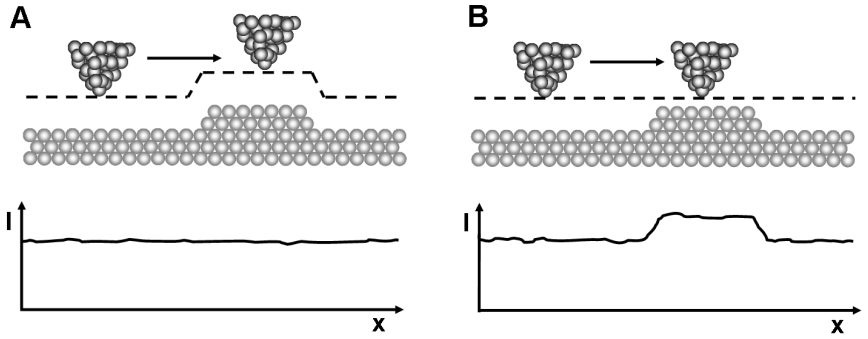

Figure 2.17. Two dimensional diagram of the STM scan modi: A, The constant current mode and B, the constant height mode, both including schematic drawings of the detected tunneling current.

Scanning Tunneling Spectroscopy

In addition to the imaging modi, the scanning tunneling spectroscopy (STS) is a very important and useful mode to explore the local electronic properties of the electrode surface and its adsorbates. Varying one of the tunneling parameters, e.g. the distance or the bias voltage (see equation 2.47), allows one to investigate the tunneling barrier properties by analyzing the I-d_T or I-U_{Bias} characteristics.

2.3.1.3. The Tunneling Effect

The tunneling current in the STM setup is attributed to the quantum mechanical tunneling effect which occurs when the wave functions of the tip and the substrate atoms overlap. In quantum mechanics the behavior of particles is governed by Schrödinger Equation.

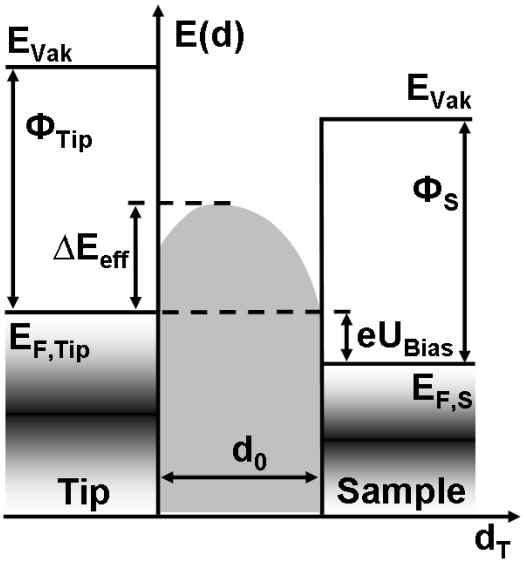

Figure 2.18. Energy-band model of the tip/tunneling barrier/sample arrangement in the STM.

The arrangement of the metal tip above a conductive electrode surface can be described quantum mechanically as a potential barrier which the electrons have to pass when flowing from the electrode to the tip (or vice versa). The potential barrier mainly depends on the conditions in the tunneling gap. Figure 2.18 shows a diagram of the energy levels of the STM tip, the sample and the potential barrier with a width of d_0 where E_{Vac} is the vacuum energy level, $E_{F,Tip}$ and $E_{F,S}$ are the Fermi levels of tip and sample, respectively. Applying a bias voltage U_{Bias} corresponds to a shift between these two Fermi levels by eU_{Bias} and results, together with the work functions of tip Φ_{Tip} and sample Φ_S, in an effective barrier height $\triangle E_{eff}$. In the shown diagram the electrons tunnel from the tip to the sample. Typical values for the tunneling barrier

are $3-4$ eV for tunneling in vacuum [147] and $1-2$ eV for tunneling in aqueous electrolytes [148].

A theoretical description of the STM tunneling current, the so called Hamilton-approach, was developed by Tersoff and Hamann [149]. Their model was based on Bardeen's formalism for electron tunneling between to metal plates [150].

According to the Wentzel-Kramer-Brillouin (WKB) approximation which provides a semiclassical, approximative solution to linear, second-order differential equations such as the Schrödinger equation, the wave function is recast as an exponential function.

$$I_T \propto \int_0^{eU} n_{tip}(E) \cdot n_{sample}(E - eU) \cdot \exp(-K(\triangle E_{eff} + \frac{eU}{2} - E)^{\frac{1}{2}} d_0) dE \tag{2.45}$$

where n_{tip} and n_{sample} are the number of states of the tip and the sample, respectively, at energy E with respect to the Fermi level. K is a constant with $K = (4\pi(2m_e)^{\frac{1}{2}}) \cdot h^{-1} = 10.25\ \mathrm{nm}^{-1} \cdot \mathrm{eV}^{-\frac{1}{2}}$.

Assuming constant densities of states, a constant distance between tip and sample and only changing bias voltage Equation 2.45 can be simplified to

$$I_T \propto const \cdot \int_0^{U} \exp(-K(\Phi - eU)^{\frac{1}{2}}) d_0) dU \tag{2.46}$$

The integration of Equation 2.46 yields the well known relation between tunneling current I_T, bias voltage U_{Bias} and tunneling barrier ($\triangle E_{eff}$, d_0) [38]:

$$I_T \propto U_{Bias} \exp(-K d_0 \triangle E_{eff}^{\frac{1}{2}}) \propto U_{Bias} \cdot R_T \tag{2.47}$$

where R_T is the effective resistance of the tunneling gap which is typically between 10^9 and 10^{11} Ω. It is obvious that the tunneling current is mainly proportional to the local density of states (LDOS). Therefore, a STM image shows an area of LDOS which for pure metallic surfaces is equal to the topography of the surface. Since the tunneling current depends exponentially on the gap width d_0, a very small change of an apparent surface height (electronic structure and surface morphology) can give rise to a large change of the tunneling current. Therefore, STM has a high z resolution (typically 0.1 Å).

2.3.2. Electrochemical Scanning Tunneling Microscopy

2.3.2.1. Setup

As already mentioned the scanning tunneling microscopy can also be operated under electrochemical conditions. While other electrochemical methods such as cyclic voltammetry (CV) or

electrochemical impedance spectroscopy (EIS) are based on measurements over large areas, the electrochemical scanning tunneling microscope provides in situ real-space imaging of electronic and structural properties of electrodes and there alteration by chemical and electrochemical processes with atomic resolution. However, in order to use the STM for electrochemical surface studies some modifications have to be implemented in the common STM setup introduced in Figure 2.16.

Figure 2.19 shows the experimental setup of the electrochemical scanning tunneling microscope (EC-STM). Following the typical arrangement in an electrochemical cell, counter electrode (CE) and reference electrode (RE) are added to measure the current and adjust the potential. Due to the limited space in the EC-STM cell, both electrodes are metallic wires typically made of Pt, Pt/Ir or Au. In addition to the sample electrode, the tip in contact with the electrolyte acts as a fourth electrode which has also to be potential controlled in order to precisely apply the bias voltage. A bipotentiostat is able to adjust the potentials at the tip U_{Tip} and the sample U_S independently versus a reference electrode. The difference $U_{Tip} - U_S$ is defined as U_{Bias} [145, 151]. While the bipotentiostat is responsible for the electrode potentials and thus for the electrochemical processes in the STM cell, the control processing unit (CPU) of the STM controls the movement of the tip and detects the measured tunneling current (data aquisition).

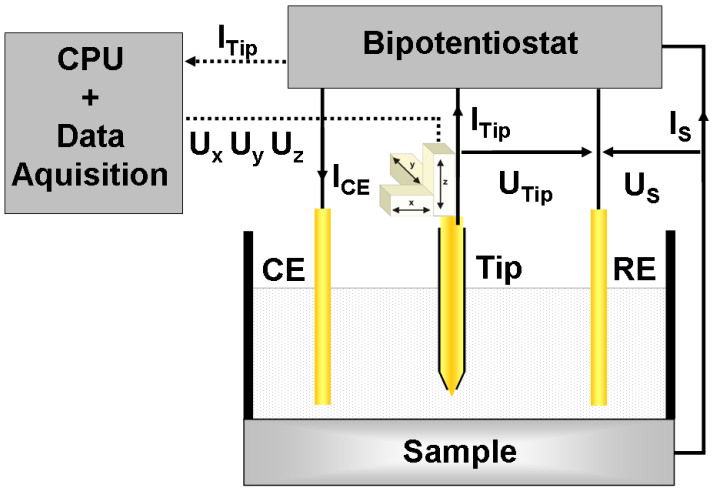

Figure 2.19. The setup of an electrochemical scanning tunneling microscope (EC-STM) is the combination of an electrochemical cell and a STM

Due to the fact that both electrodes, the sample and the tip are in contact with the electrolyte Faradaic currents may occur at both surfaces. While a small Faradaic current at the sample surface I_S does not disturb the STM measurement, a Faradaic current at the tip can easily mask the tunneling current and make the measurement impossible. Since the tunneling current is normally adjusted between 0.2 nA and 1 nA the Faradaic leakage current should not exceed

0.1 nA. In order to reduce the Faradaic current to a few pA, the metal tip is insulated up to the very apex e.g. with apiezon wax, to minimize the free surface area. Furthermore, STM tips are usually made of metals which are electrochemically inert over a large potential range such as gold or platinum. However, the measured current at the tip I_{Tip} is always a sum of the tunneling current and a Faradaic current.

2.3.2.2. EC-STM of Redox Adsorbates

Since the EC-STM offers new details about structural and electronic properties of monolayers of (bio-)molecules down to the single molecule level, theories and models of electrochemical electron transfer considering different transport mechanisms have been developed. These models give an expression of the EC-STM current as a function of the applied bias U_{Bias} and substrate potentials U_S. Thereby, the electrons tunnel from the tip to the substrate (or *vice versa*, depending on the sign of U_{Bias}) through the empty redox level of the molecule. Figure 2.20 schematically shows the energy diagram of the in-situ EC-STM system with a redox molecule located in the tunneling gap between tip and substrate (according to [44]. Performing EC-STM, the electrochemical potentials of the tip and the substrate can be varied with respect to the redox level of the redox molecule .

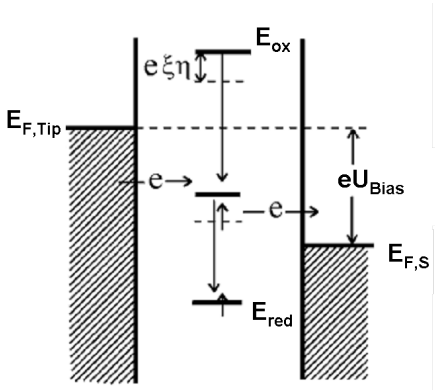

Figure 2.20. Energy diagram of in-situ EC-STM of a redox molecule showing electron tunneling from the tip to the substrate via the redox level of the molecule; taken from [44] and modified.

Resonant Tunneling Model

Already in 1992, even before the first experimental study of electron tunneling via a redox-active molecule performed by Tao [36], Schmickler and Widrig [152] proposed a model for an enhanced tunneling current when an electroactive adsorbate is present on the sample. They used the transfer hamiltonian mechanism to determine the dependence of the tunneling current on parameters such as the bias voltage, the energy of reorganization λ and electronic coupling of the redox center to the electrodes. In this model the tunneling is only effective when the starting occupied tip electron level, the intermediate molecular level and the final empty substrate level

have all the same energey; resonant tunneling model. The model hamiltonian consists of three terms: an electronic hamiltonian H_e representing the undisturbed states of the tip, the substrate and the redox center, a hamiltonian H_S for the heavy particles in the system, such as the solvent and the reactant's inner sphere, as well as their interaction with the redox center and a transfer hamiltonian H_t for the electron transfer:

$$H = H_e + H_S + H_t \tag{2.48}$$

Leading to a tunneling current expressed by

$$I_T = -\frac{e\pi}{\hbar}\int_{E_{F,S}}^{E_{F,S}-eU_{Bias}} \frac{\rho_{Tip}(E)|T_{Tip}(E)|^2\ \rho_S(E)|T_S(E)|^2}{\pi\left[\rho_{Tip}(E)|T_{Tip}(E)|^2 + \rho_S(E)|T_S(E)|^2\right]} D_{ox}(E)\mathrm{d}E \tag{2.49}$$

where $T_{Tip}(E)$ and $T_S(E)$ are the electronic couplings between the redox center and the electrodes, tip and substrate, respectively. ρ_{Tip} and ρ_S are the electronic level densities of the tip and the substrate. D_{ox} is the probability of finding an empty state of energy E within the redox couple (for further details see [3, 152]).

However, resonant tuneling implies that the electron transfer between tip and substrate is faster than typical fluctuations of the redox level energy and thus flowing electrons never get trapped on the moecule. Furthermore, this model does not consider the potentiostatic control with respect to a reference electrode.

Two-Step Model

Assuming small electronic couplings of the redox centre with the electrodes the electron transfer is normally slower than typical redox engergy fluctuations. In this case the electron transport in the EC-STM setup can be considered as a two step process, i.e. the electrons tunnel from the tip to the redox molecule located in the gap, then the electrons tunnel from the molecule to the substrate. Thereby, there is no correlation between these two processes, which means that the two electron transfer steps are independent and vibrational relaxation can occur. The two-step electron transfer theory was developed by Ulstrup and Kuznetsov et al. They calculated the tunneling current by standard chemical kinetics involving electrochemical rate constants [17, 40, 44, 153–155]:

$$I_T = e\frac{k^{o/r}k^{r/o}}{k^{o/r} + k^{r/o}} \tag{2.50}$$

where $k^{o/r}$ and $k^{r/o}$ refer to the rate constants for the electron transfer between the tip and the redox centre and between the redox centre and the substrate, respectively, and have the following forms:

$$k^{o/r} = \kappa_{el,Tip}\rho_{Tip}\frac{\omega_{eff}}{2\pi}\frac{2k_BT}{\alpha_{Tip}}\exp\left(-\frac{(\lambda - e\xi\eta - e\gamma U_{Bias})^2}{4k_BT}\right) \tag{2.51}$$

$$k^{r/o} = \kappa_{el,S}\rho_S\frac{\omega_{eff}}{2\pi}\frac{2k_BT}{\alpha_S}\exp(e\Theta\eta)\exp\left(-\frac{(\lambda - eU_{Bias} + e\xi\eta - e\gamma U_{Bias})^2}{4\lambda k_BT}\right) \tag{2.52}$$

where $\kappa_{el,Tip}$ and $\kappa_{el,S}$ are the electronic transmission coefficients for electron transfer between tip and redox center and between redox center and substrate, respectively, ρ_{Tip} and ρ_S are the electronic level densities of the tip and the substrate, ω_{eff} is the effective nuclear vibrational frequency, α_{Tip} and α_S are the electron transfer coefficients between the tip and the redox center and between the redox center and the substrate, respectively, ξ is the fraction of the substrate-solution drop and γ is the fraction of the bias voltage drop at the redox center. Θ is representative for double-layer effects and tunneling barrier-overpotential dependencies. Therefore, the tunneling current can be represented as a function of the overvoltage η and the bias voltage:

$$I_T = \frac{1}{2}e\kappa\frac{\omega_{eff}}{2\pi}\left(\mathrm{eU_{Bias}}\right)\exp\left(-\frac{\lambda + \mathrm{eU_{Bias}}}{4k_BT}\right)\left\{\cosh\left[\frac{(\frac{1}{2} - \gamma)\mathrm{eU_{Bias}} - \xi e\eta}{2k_BT}\right]\right\}^{-1} \tag{2.53}$$

2.3.2.3. Tip Induced Nanostructuring and Local Measurements

After its invention the STM was used in order to structure electrode surfaces on the nanometer and even atomic scale. In 1990 Eigler and Schweizer [156] used an UHV STM at low temperatures (4 K) to position individual xenon atoms on a single-crystal nickel surface with atomic precision. In order to pull the atoms across the surface they increased the tip-atom interaction by changing the tunnel current to a higher value and thus, lowering the tip to the atom. The invention of the electrochemical STM provided new options to use the STM tip for surface nanostructuring, an overview of different methods is given in [157, 158]. Furthermore, it was shown that the EC-STM tip can also be used as a local current sensor [159]. This technique combined the tip-induced generation of single Pd particles, the characterization of the particle and the subsequent measurement of the particle reactivity towards the hydrogen evolution reaction (HER). With this approach new insights into structure reactivity relations of Pd particles were found, e.g. with decreasing particle height an increase in the catalytic activity was observed [160]. Applying this technique to enzyme electrodes, Wang et al. [15, 16] investigated locally probed Faradaic currents induced by the redox enzyme glucose oxidase adsorbed on a graphite electrode.

SPM techniques are suitable tools for patterning electrode surfaces on the nanoscale. Especially, nanografting using contact mode AFM has been successfully applied e.g. for the formation of two-dimensional patterns within inorganic, organic or biological materials [161]. An increasing interest is also coming up in building biomolecular structures on surfaces via nanografting for the purpose of biosensor fabrication or investigating their electrical properties.

2.3.3. Scanning Electrochemical Potential Microscopy

2.3.3.1. Setup

In 2004 Woo et al. [46] reported about a modified EC-STM with a miniaturized potential probe in order to measure the local potential of solid-liquid interfaces with subnanometer spatial resolution. In 2007 this technique, now termed as scanning electrochemical potential microscopy (SECPM) was established in the group of Allen J. Bard [47] together with Veeco Instruments Inc. [45]. In order to determine the electrode surface potential in polar liquids or electrolytes, SECPM uses the potential gradient present in the electrochemical double layer formed at the solid-liquid interface (for detailed description see Section 2.1.1). The hardware is similar to an EC-STM, the modification consists in replacing the current pre-amplifier by a high input impedance potential difference amplifier (Fig. 4.4). Usually both amplifiers are embedded in the system and an internal switch allows to change between EC-STM and SECPM enabling the investigation of the same area of an electrode under in-situ conditions by both techniques for direct comparison of the topography obtained by mapping the electron density and the surface potential, respectively. The potential difference between the applied potential at the working electrode and the tip ($\triangle$U = U_S - U_{Tip}) is measured with the impedance potential amplifier and serves as feedback signal in the x-y scanning mode. Comparable to the x-y scanning modes in STM one can choose between constant potential and constant height mode SECPM.

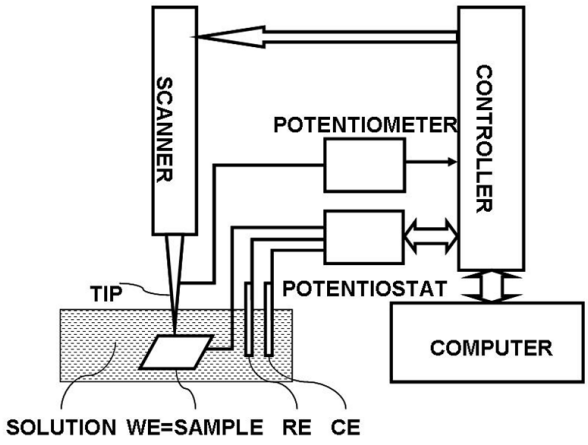

Figure 2.21. Simplified block diagram of the setup of a scanning electrochemical potential microscope (SECPM). The potential of the tip is measured and fed into a high impedance amplifier; taken from [45].

Corbella et al. [48] first used the constant potential mode of this technique to investigate the metal-distribution of electrodes by imaging the surface of tungsten-containing diamond-like carbon (DLC) films in the x-y direction. In the constant potential mode the feedback loop controls a given potential difference and adjusts the tip height while scanning over the surface. This mode is comparable to the constant current mode in STM as it also produces "topographical" images of the surface. The SECPM images of DLC films, taken with Pt/Ir tips in H_2O, showed

a granular appearance of the surface. The smallest grains that could be resolved were about 30 nm in size.

In addition, SECPM also offers the possibility to map the potential distribution of the interface in x-z direction. According to the GCS model the theoretical potential φ of an electrode/electrolyte interface changes with the distance across the electrochemical double layer (EDL)[53]. Experimentally the SECPM tip serves as a potential probe measuring the potential profile of an electrode while moving perpendicular to its surface (Fig. 2.22). Thereby, the detected signal is given by the potential difference between the applied substrate potential U_S and the tip potential U_{tip}. When tip and electrode are in contact the potential measured at the tip is equal to the applied working electrode potential U_S, i.e. $\triangle U = 0$. Whereas, far away from the surface, the potential of the EDL is equal to the potential of the bulk electrolyte φ_{bulk}, i.e. $\triangle U = \varphi_0 - \varphi_{bulk} = U_S - \varphi_{bulk}$. The decay of the EDL is characterized by the Debye length κ^{-1} as described in Section 2.1.1.

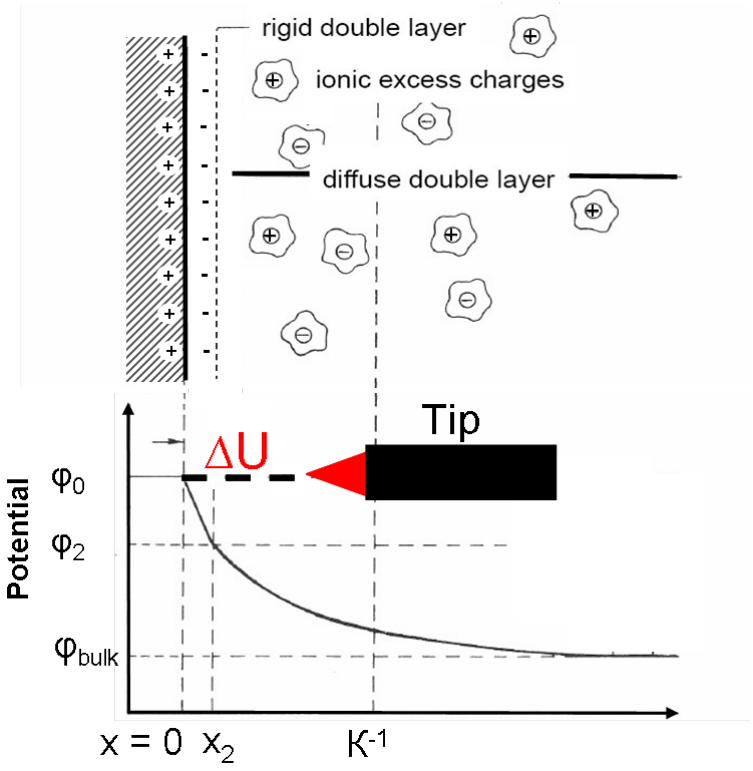

Figure 2.22. Scheme of the SECPM tip in front of an electrode probing the potential profile of the EDL by measuring $\triangle U$.

Woo et al. [46] investigated the local potential profile of an Au(111) electrode in 1 mM $NaBF_4$ in a potential range from -0.2 V to 0.4 V (vs. Au in the same solution) by moving a nanoscale gold disk tip [162] perpendicular to the surface (x-z direction). In the following the nomenclature

is taken over from the reference and thus not be listed in the attachment. The potential profiles were measured while the tip approached the electrode starting from 30 nm above the surface until a mechanical contact was made (Fig. 2.23). The potential is given as the difference of the detected potential at the tip ϕ_{pr} and the OCP of the tip ϕ^0_{pr} which is measured far away from the Au(111) surface. Figure 2.23 shows the (ϕ_{pr}-ϕ^0_{pr}) vs. distance plots for different electrode potentials, described by E_{WE}. These plots are characterized by three regions: I, between 30 and 18 nm above the surface, the probe measures the potential of the solution bulk independent of the applied potential, i.e. all curves show the same constant potential. II, when the probe further approaches the surface, the probe is located inside the EDL and the probed potential changes gradually towards the potential of the surface. The slope of the potential profile varies with the applied potential between -23 mVnm^{-1} and +20 mVnm^{-1} for different E_{WE}. III, Finally, the probe contacts the metal surface and adopts the applied potential E_{WE}.

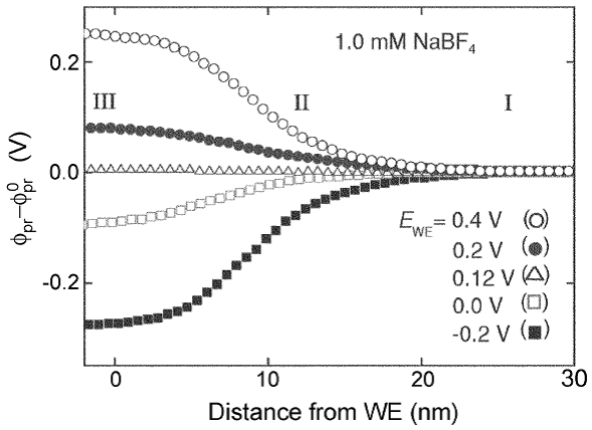

Figure 2.23. Potential measured at the probe ϕ_{pr} as it approaches the Au(111) surface; taken from [46] where ϕ^0_{pr} is the OCP of the tip far away from the electrode surface.

Hurth et al. [47] performed similar experiments with a flattened Pt/Ir-probe to investigate the influence of the surface potential and of the electrolyte concentration on the double layer profile of a Pt foil in KCl. Varying the potential of the Pt foil from 0.2 V to 0.4 V vs. a platinum polypyrrole (PtPPy) reference electrode [163], the potential profiles were measured in 10^{-5} M KCl over a distance of 60 nm showing all the same potential gradient with a decay of approximately 50 nm. In contrast, when applying 0.4 V vs. PtPPy to the foil and changing the electrolyte concentration from 10^{-5} M to 10^{-4} M the potential-distance curves showed a change in the decay length from approximately 60 nm to 30 nm. This is qualitatively in good agreement with the Gouy-Chapman-Stern theory which predicts a Debye length of 30 nm for a 10^{-4} M and 96 nm for 10^{-5} M. A 10^{-3} M concentrated KCl should theoretically result in an Debye length of 9.6 nm, however, no significant difference between the potential profiles obtained in 10^{-4} M and 10^{-3} M KCl was observed which was explained by the free apex of the tip exceeding the expected double layer size i.e. the probe was not able to resolve the double layer of higher

concentrated solutions. However, in order to interprete these potential curves measured by Woo et al. [46] and Hurth et al. [47] quantitatively, it is necessary to understand how the presence of a probe influences the original EDL at the electrode or vice versa. Since the metallic potential probe in contact with the electrolyte also forms an EDL it can interact and overlap with the EDL at the electrode at close distances. The measured interfacial potential results from the overlap of both EDLs. Although diffuse double layer interactions between two parallel plates [164], heterogeneously charged colloidal particles [165] or charged particles near surfaces [166] have already been considered in the past, a comprehensive theory for potential profiling SECPM taking real boundary conditions encountered in SECPM into account has to be developed in the future. First attempts by Hamou et al. [167] reported about an electrostatic approach directly aimed to the SECPM experiments using FEM simulation to compute the EDL potential measured with the metallic probe. Double layer interaction effects caused by the geometry of the tip apex and the free area of the tip are included in this model. They found that the shape of the metallic apex affects the ion distribution in the nanogap resulting in an electroneutral region between tip apex and electrode. Influences of the tip on the potential profiles will be discussed together with preliminary results in Section 4.4.

2.3.3.2. Scanning Electrochemical Potential Microscopy Tip as local pH Sensor

Performing spatially resolved pH measurements at the nanoscale using electrochemical SPM techniques is of great interest in the research field of crevice corrosion [168], but also in electrocatalysis [169] and even in biology. The determination of pH in tissues, pH gradients at the cell membrane or at the membrane of cell organelles would give new insights into the energy metabolism of cells and the functionality of proton pumps [170–172]. Similar to the approach shown above where the EC-STM tip was used as a local current sensor in order to measure the reactivity of single nanoparticles or the Faradaic currents produced by enzymatic reactions one might think about using a potentiometric SECPM tip as a local pH sensor. Of course pH changes could also be monitored with the amperometric response by calculating the H^+ or OH^- concentrations from their steady-state reduction or oxidation current at the tip. Although qualitatively useful, it is hard to obtain quantitative results that could be translated into absolute pH since amperometric properties of a STM tip are known to depend on their characteristic dimension. In contrast, the potentiometric properties are not thought to be size dependent, at least as long as the response of the surface surpasses that of the edges, i.e. with smaller electrodes imperfections will probably become critical and seriously affect the electrode potential [173]. Most potentiometric pH microsensors are covered with glass, liquid and polymeric membranes, or metal oxide films [174]. However, these materials are not suitable for the application as an electrochemical SECPM tip. Therefore, a pH sensitive tip material such as platinum (Pt) or palladium (Pd) is required. The primary standard for pH measurements is the reversible hydrogen electrode (RHE), Pt/H_2, H^+_{aq} [175, 176]. According to the Nernst equation (Equation 2.21) its potential is given by

$$U_0 = U_{00} + \frac{RT}{2F} \ln f_{H_2} - \frac{RT}{F} \text{ pH} \tag{2.54}$$

where the pH represents the proton concentration, U_{00} is the standard potential, by convention 0 mV at all temperatures and f_{H_2} is the fugacity of hydrogen. However, for analytical applications of the RHE the electrolyte must contain hydrogen of defined partial pressure. In contrast to platinum palladium, also being a member of the platinum group metals, possesses the ability to store hydrogen within its crystal lattice and is therefore able to function as a pH sensitive palladium hydride (Pd/H) [177–179] and can be also used in hydrogen free solutions [180]. The pH sensitivity of palladium hydride can be understood by the palladium/hydrogen phase diagram shown in Figure 2.24.

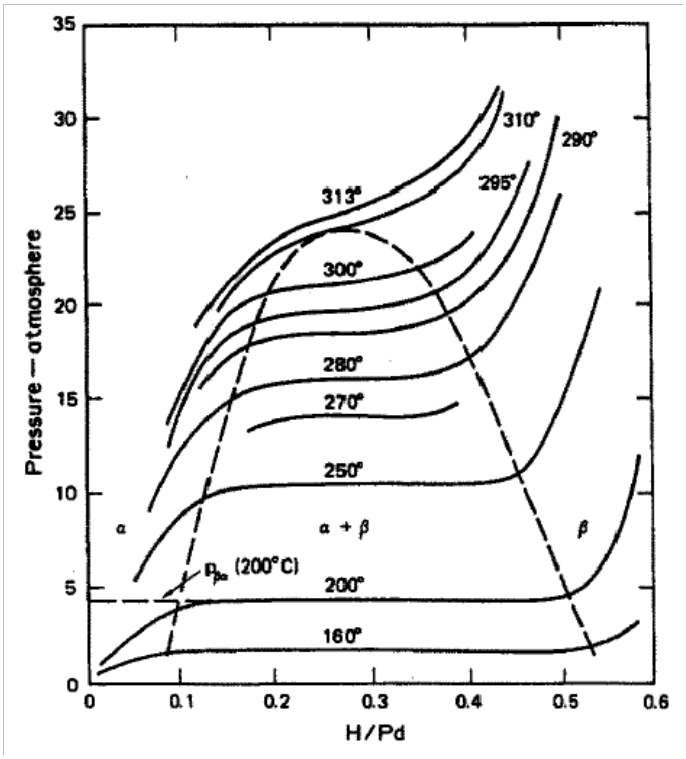

Figure 2.24. Phase diagram of palladium hydride [179]

At room temperature (red dashed line), three different phases can exist depending on the atomic ratio of H/Pd [168, 176]:

- H/Pd $\leq$ 0.025: low hydrogen containing α phase where the activity (or chemical potential) of hydrogen varies depending on the amount of hydrogen in the α phase. When the hydrogen content is increased to the edge of the miscibility gap, the system is said to have only one degree of freedom (at T = const), which fixes the hydrogen content and therefore, the hydrogen activity of the α phase.
- 0.025 H/Pd $\leq$ 0.6: intermediate miscibility gap consisting of two phases, α and β phase. According to equilibrium the activity of hydrogen in the α phase must be equal to the

activity in the β phase, i.e. within this region of hydrogen content the activity of hydrogen remains constant providing a wide-ranging and stable hydrogen activity against which the hydrogen ion activity in solution can be reliably measured. The potential of 50 mV vs. RHE was attributed to a mixed potential due to the presence of the two-phase region with the α phase predominating [181]

- H/Pd $>$ 0.6: high hydrogen-containing β phase, the potential drops to zero volt.

The potential of a Pd/H electrode is dependent on the composition in the pure α and β phases, but is independent of composition in the mixed $\alpha + \beta$ phase region. This means using a Pd/H SECPM tip electrode in the miscibility gap, a change in the proton concentration changes the equilibrium potential (Nernst potential) of the Pd/H electrode. The high impedance amplifier of the SECPM setup allows the measurement of the open circuit potential (OCP) at the SECPM tip. Therefore, the potential shift of the OCP caused by an increase or decrease in proton concentration within a catalytic reaction can be examined (schematically illustrated in Fig. 2.25).

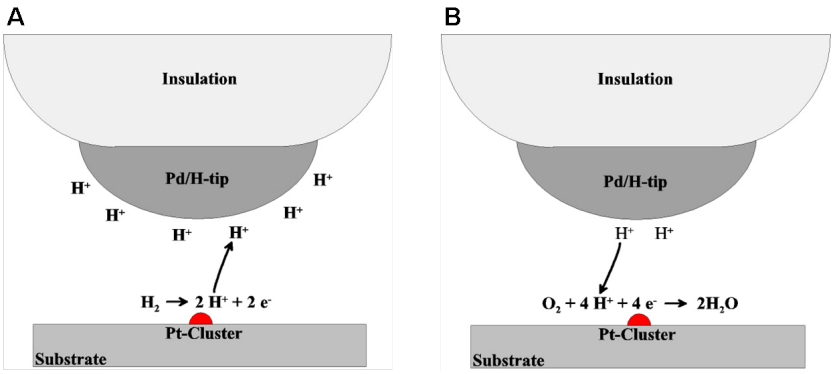

Figure 2.25. Potential shift method: Schematics of the proton concentration measurement utilizing a hydrogen-loaded palladium SECPM tip (Pd/H tip) as a local pH sensor. A) Illustrates the situation for an increasing proton concentration, whereas B) shows a catalytic reaction which results in a decrease of the proton concentration.

According to the Nernst equation, a change of the proton concentration by a decade results in a change of the measured OCP of the tip by 59 mV. This effect can be used to set up a method to directly determine the proton concentration around the SECPM tip.

3. Materials and Methods

3.1. Chemicals and Experimental Procedures

3.1.1. Chemicals

Chemicals	**Formula**	**Provider**	**Purity**
Acetonitrile	CH_3CN	Merck	pro analysi
Di-Sodium Hydrogen Phosphate-Dodecahydrate	$Na_2HPO_4 \cdot 12H_2O$	Merck	pro analysi
Ethanol	C_2H_5OH	Merck	pro analysi
Ethanolamine	$NH_2CH_2CH_2OH$	Sigma Aldrich	$\geq$90%
Hydrochloric Acid (30%)	HCl	Merck	pro analysi
Hydrogen Peroxide (33%)	H_2O_2	Merck	pro analysi
Leupeptin Triflouroacetate salt	$C_{20}H_{38}N_6O_4$	Sigma Aldrich	90%
N-Ethyl-(3-dimethylaminopropyl)-N$'$-ethylcarbodiimide Hydrochloride	$C_8H_{17}N_3 \cdot HCl$	Sigma Aldrich	98%
N-Hydroxysuciimide	$C_4H_5NO_3$	Sigma Aldrich	98%
Perchloric Acid (70%)	$HClO_4$	Merck	pro analysi
Sodium Chloride	NaCl	Merck	pro analysi
Sodium Dihydrogen Phosphate-Monohydrate	$NaH_2PO_4 \cdot H_2O$	Merck	pro analysi
Sodium Hydroxide	NaOH	Merck	pro analysi
Sodium Perchlorate Monohydrate	$NaClO_4 \cdot H_2O$	Merck	pro analysi
Sulfuric Acid (95-98%)	H_2SO_4	Merck	pro analysi
Tris(2-Carboxyethyl)phosphine HCl	$C_9H_{15}O_6P \cdot HCl$	Calbiochem	99.7%
Tetrabutylammonium Tetrafluoro-borate	$C_{16}H_{36}BF_4N$	Fluka	98%

Nobel metal wires such as gold (Au) with a diameter of 0.25 mm and a diameter of 0.5 mm, palladium (Pd, diameter 0.25 mm), platinum (Pt, diameter 0.25 mm) and platinum/iridium (Pt/Ir with a ratio Pt:Ir of 80:20, diameter 0.25 mm) were purchased from Carl Schäfer GmbH

Co.KG (Germany). The pure Au, Pd and Pt wires had a purity of 99.9%.
Throughout the experiments Argon gas (4.8) from Linde AG (Germany) was used in order to flush the electrolyte and remove dissolved oxygen from the experimental setup.

3.1.2. Proteins and Enzymes

Proteins and enzymes were dissolved in 10 mM phosphate buffer solution and stored either at 4°C or -20°C, according to their specification. The concentration and the pH of the protein solution was dependent on the experiment and will be mentioned elsewhere. All proteins and enzymes were purchased from companies and used without further purification.

Proteins and Enzymes	**Extracted from**	**Provider**
Apoferritin	Equine Spleen	Calbiochem
Azurin	*Pseudomonas aeruginosa*	Sigma Aldrich
Ferritin	Horse Spleen	Sigma Aldrich
Horseradish Peroxidase	Horseradish	Roche
Papain	Papaya Latex	Sigma Aldrich

3.1.3. Preparation of Electrolytes

All electrolytes and solutions were prepared with ultrapure water obtained from a Millipore water purification system consisting of a Elix and a Milli-Q Gradient A10 (18.2 MΩ cm, 3 ppm total organic carbon, TOC)(Millipore).
For all electrochemical experiments investigating biomolecules either in the electrochemical glass cell or in the EC SPMs phosphate buffer solution (PBS, pH 7) was used as standard electrolyte. PBS was mixed up with 10 mM di-sodium hydrogen phosphate dodecahydrate ($Na_2HPO_4{\cdot}12H_{12}O$) and 10 mM sodium dihydrogen phosphate monohydrate ($NaH_2PO_4{\cdot}H_2O$). The pH value of the solution was measured with an universal pH electrode (VWR, Germany) and a pH meter CG 804 (Schott, Germany) which was regularly calibrated with buffer solutions of pH 4.01 (Hanna Instruments, Germany) and pH 7.00 (CertiPUR, Merck, Germany). If necessary, the pH of the phosphate buffer solution was adjusted with HCl or NaOH.
Peroxymonosulfuric acid (Caro's acid) was prepared with H_2SO_4 ($95-98\%$, Merck) and H_2O_2 (33%, Merck) at a volume ratio of 1:1 for the cleaning procedure.

3.1.4. Cleaning Procedure

All glass ware, Teflon© parts and noble metals were cleaned in peroxymonosulfuric acid (Caro's acid) before use in order to dissolve and remove traces of metal ions and organic contaminations. The Caro's acid was freshly prepared every two months. Afterwards all parts were first thoroughly

rinsed with Milli-Q water and then washed in boiling Milli-Q water. After the cleaning procedure and prior to cell assembling, the gold parts were flame annealed.

3.1.5. Synthesis of Chemical Compounds

The synthesis was performed by Alice Schlichtiger during her PhD thesis in the Chemistry Department of the TU München under the supervision of Dr. Jörg Eppinger. All preparation steps were carried out in air with standard glassware and solvents unless otherwise indicated. Chemicals and solvents were purchased from Sigma-Aldrich or Novabiochem (see [33]).

3.1.5.1. 4-Carboxyphenyl Diazonium Tetrafluoroborate

In order to covalently immobilize proteins and enzymes e.g. by their lysine side chains, free carbonyl groups must be available on the electrode surface. In this work the surface of highly oriented pyrolytic graphite (HOPG) was functionalized with 4-carboxyphenyl groups. For this purpose, 4-carboxyphenyl diazonium tetrafluoroborate ($C_{15}H_{13}BF_4N_2O_4$) was obtained by diazotation of the amine together with sodium nitrite ($NaNO_2$) under acidic conditions [182]. 3.4 g 4-aminobenzoic acid ($H_2NC_6H_4CO_2H$, 25 mM) was dissolved in 15 ml fluoroboric acid (HBF_4, 50%, 100 mM) and 25 ml water. The solution was cooled down to 0 °C. 1.8 g sodium nitrite (26 mM) dissolved in 5 ml water was added dropwise to the solution. After the reaction mixture achieved room temperature it was concentrated in vacuum to half of its original volume. The precipitated product was filtered, washed with ether and dried in vacuum. One obtains the desired diazonium salt as a white solid with a yield of 89% (5.25 g, 22.25 mM).

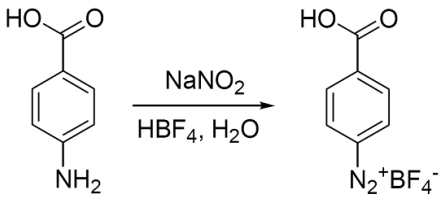

Figure 3.1. Synthesis of 4-carboxyphenyl diazonium tetraflouroborate.

3.1.5.2. Ferrocene Affinity Labels for Proteases

This section reports about the synthesis and characterization of two watersoluble ferrocene affinity labels (FcAL) for cathepsin cysteine proteases such as papain giving only a short overview, for detailed information about the development and the synthesis process it is referred to [33]. For peptide synthesis enantiomerically pure L-amino acids have been used. The peptide was synthesized on a rink amide resin using Fmoc-strategy [123] and standard coupling conditions. The ethyl-L-trans-epoxysuccinic acid [183], ferrocenylmethylamine [184] and 1-[2-[(tert-butoxycarbonyl)amino]-2-(carbonyl)ethyl]ferrocene [185] were synthesized according to

mentioned literature procedures.

The Affinity Label

The affinity label (Fig. 3.2A) was synthesized on solid phase similar to the work of Barett et al. [186] and Bogyo and co-workers [131]. Its structure is mainly based on the E-64 motive (Fig. 3.2B).

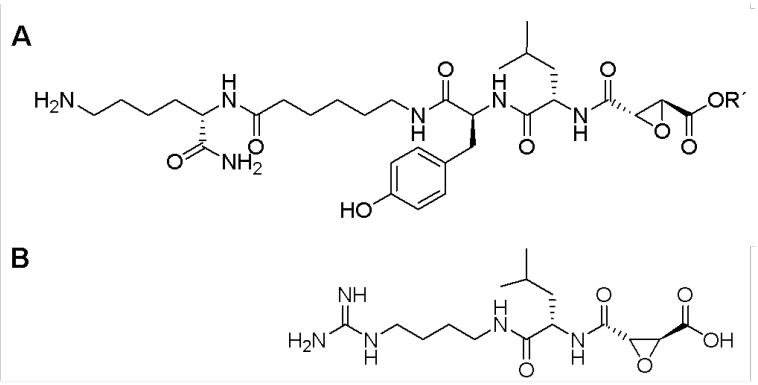

Figure 3.2. A) Structure of the affinity label (AL) for cysteine proteases ([131, 186]) B) based on the E-64 motive.

The E-64 motive is a well known irreversible inhibitor of papain and papainlike cysteine proteases which was first isolated from the bacteria *Aspergillus japonicus* by Hanada et al. [187, 188] in 1978. The reactive group of the E-64 derivatives, an epoxy succinic acid, binds to cysteine proteases by forming a thioether bond with the sulfhydryl group in the active center of the enzyme [189] (see Fig. 3.3) leading to an irreversible enzyme-AL complex. E-64 is useful for active site titration since one mole of E-64 inhibits one mole of protease, i.e. it binds in an active-dependent manner to the enzyme.

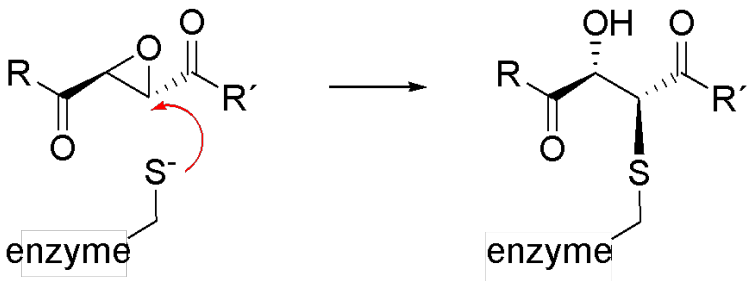

Figure 3.3. Scheme of the binding mechanism of the E-64 motive and related structures to the active site of a cysteine protease [189].

Two Ferrocene Affinity Labels

In order to receive redox active labels the affinity label was modified with ferrocene derivatives. Ferrocene was chosen as electroactive probe due to its unique electrochemical properties. Ferrocene is a redox system with high exchange current density due to its low solvent reorganization energy λ. The difference between the two ferrocene affinity labels is the position of the redox marker, i.e. the ferrocene moiety (see Figure 3.4). In one case, the "classical" way, the ferrocene moiety attached to a linker molecule is positioned at the N-terminus of the affinity label (Fig. 3.4 left). Therefore, ferrocenylalanine, first prepared by Osgerby and Pauson [190], was synthesized by a modified procedure described by Carlstrom and Frejd [185]. Thereby, the amino function should mediate the solubility of the FcAL. In the other case the ferrocene group is located at the so called carboxyl terminus (Fig. 3.4 right). Ferrocenylmethylamine was chosen for the coupling with the carboxylic group of the label due to the straightforward synthesis as described by Beer and Smith [184].

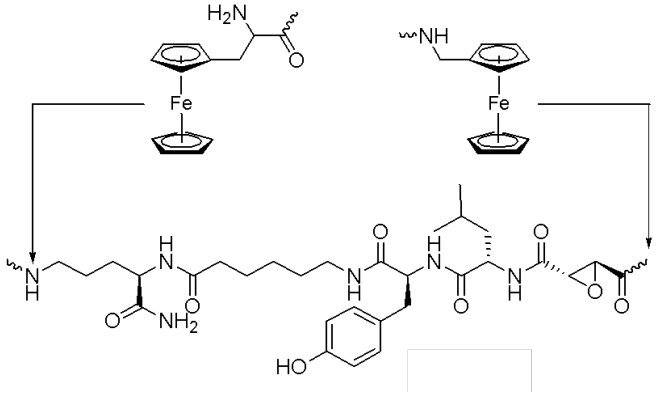

Figure 3.4. Scheme of the affinity label and the redox markers ferrocenylalanine (left) and ferrocenylmethylamine (right) for coupling to the N-terminus and the carboxyl terminus, respectively.

Fe(Cp)(η-C_5H_4-CH_2-$CH(NH_2)$-CO-Lys-Ahx-Tyr-Leu-Epx-COOEt)

1-[2-[(tert-butoxycarbonyl)]-amino-2-(carbonyl)ethyl]-ferrocene was synthesized according to literature procedure [185]. 37 mg (0.1 mM) was dissolved in dimethylformamide (DMF, 1 ml) and a solution of the peptide (17 mg, 0.025 mM), 1-hydroxybenzotriazole hydrate (15 mg, 0.1 mM), N,N,N',N'-Tetramethyl-O-(benzotriazol-1-yl)uronium tetrafluoroborate (32 mg, 0.1 mM) and diisopropylethylamine (17.4 μl, 0.1 mM) in DMF (2 ml) was added. After stirring for 2 h the solvent was evaporated in vacuo and the crude product was purified by high-performance liquid chromatography (HPLC, 10-90 %, 30 min, with a retention time, i.e. time between injection and maximum detected response t_R =13.10 min) to get 11 mg (43 %) of the pure compound. However, only acidic deprotection of the product leads to a watersoluble ferrocene affinity label. Therefore, the protected ferrocene affinity label (11 mg, 0.011 mM) is stirred in a solution of 20%

trifluoroacetic acid (TFA) in dichlormethane (DCM) at room temperature for 1 h. The solvent is removed in vacuo and the crude product is purified by HPLC ($10-90\%$, 30 min, $t_R = 9.54$ min) to get 9 mg (92%) of the unprotected watersoluble label Fe(Cp)(η-C_5H_4-CH_2-CH(NH_2)-CO-Lys-Ahx-Tyr-Leu-Epx-COOEt) also named FcAL(out).

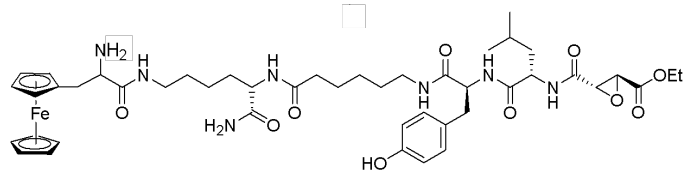

Figure 3.5. Ferrocene affinity label FcAL(out) based on the E-64 motive where the ferrocenylalanine is coupled to the N-terminus of the label.

Fe(Cp)(η-C_5H_4-CH_2-NH-CO-Epx-Leu-Tyr-Ahx-Lys)

Saponification of the ethylester achieved on the rink amide resin (300 mg of the loaded resin, loading 0.64 mmol $\cdot$ g^{-1}) by addition of a solution of potassium hydroxide (150 mg) in dry ethanol (5 ml) (2 x 1.5 h). After filtration the resin was washed several times with CH_2Cl_2 and DMF. For coupling a solution of ferrocenemethylamine (215 mg, 1 mmol), benzotriazolyloxytris(dimethylamino)phosphonium hexafluorophosphate (BOP) (442 mg, 1 mmol) and diisopropylethylamine (0.35 ml, 2 mM) in DMF (5 ml) was added to the resin. After 2 h the solution was filtered and the resin was washed twice with DMF. Cleavage from the resin was achieved using a mixture of TFA (95%), water (2.5%) and triisopropylsilane (2.5%). The solution was filtered and dried in vacuo. The labeled peptide was purified by HPLC ($10-90\%$, 30 min, t_R=9.60 min) to get 21 mg (15% calculated from the maximum loading of the resin) of the pure compound Fe(Cp)(η-C_5H_4-CH_2-NH-CO-Epx-Leu-Tyr-Ahx-Lys) also named FcAL(in).

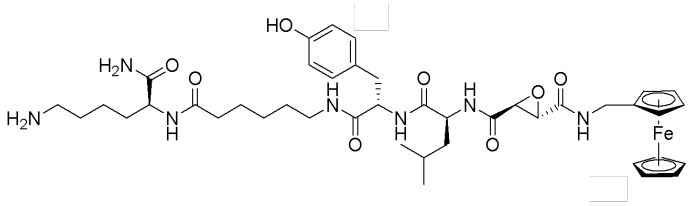

Figure 3.6. Ferrocene affinity label FcAL(in) based on the E-64 motive where the ferrocene moiety is located at the carboxyl terminus of the label.

3.1.5.3. Characterization

Analytical and preparative high-performance liquid chromatography (HPLC) of the peptides was performed by a Varian ProStar 210 system using a Vydac MS C-18 column (10 μ, 250mm $\times$ 10 mm,

preparative) and a Polaris 10 C18-A250 (250 mm × 4.6 mm, analytical), respectively. All synthesized compounds were investigated and characterized in the Chemistry Department of the TUM using nuclear magnetic resonance (NMR, not shown here, further details [33]) and mass spectrometry (only shown when necessary). Depending on the compound either electrospray ionization (ESI) or matrix-assisted laser desorption/ionization time of flight (MALDI-TOF) mass spectrometry was performed. ESI mass spectra were recorded using a LCQ classic from Thermo Electron by B. Cordes. Thereby, an electrospray disperses the liquid containing the analyte of interest into a fine aerosol. The ions observed by mass spectrometry may be quasimolecular ions created by the addition of a proton and denoted $[M + H]^+$. Corresponding HPLC/MS separation was performed by a HP 1100 from Hewlett Packard (method: HPLC 10-90% (H_2O/Acetonitrile containing 0.1 % HCOOH), 15 min, 0.3 mL/min, YMC ODS-A(C18), 125 × 2.1 mm, 120A, S-3 um).

Labeled and unlabeled proteins were characterized by MALDI-TOF mass spectrometry using a Bruker Biflex III instrument. Due to its soft ionization technique MALDI-TOF is often used for the analysis of fragile biomolecules (proteins, peptides, sugars) and large organic molecules (dendrimers, macromolecules). The analyte (e.g. protein sample) is embedded in a crystallized matrix (often containing of 3,5-dimethoxy-4-hydroxycinnamic acid, α-cyano-4-hydroxycinnamic acid or 2,5-dihydroxybenzoic acid). Fireing laser at the crystal the matrix absorbs the laser energy and is ionized. Part of its charge is transferred to the analyte molecule (e.g. the proteins) which is then also ionized. In the TOF mass spectrometer the ions are accelerated by an electric field. Measuring their time of flight their mass-to-charge ratio ($\frac{m}{z}$) can be calculated by

$$t = b\sqrt{\frac{m}{z}} \tag{3.1}$$

where b is a proportionality constant representing factors related to the instrument settings and characteristics (e.g. the strength of the accelerating electric field).

3.2. Electrochemical Setup and Instruments

3.2.1. The Electrochemical Glass Cell

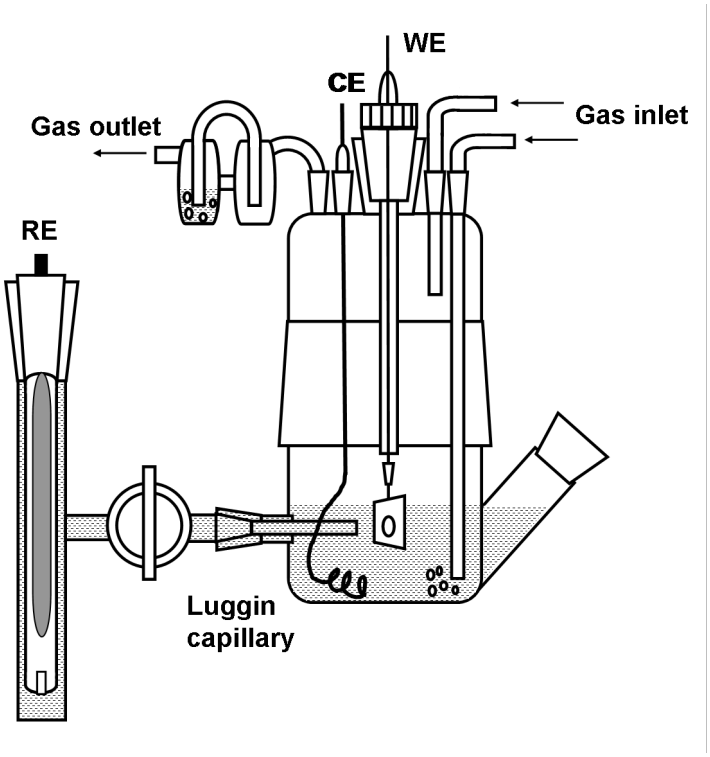

Figure 3.7. Two compartment electrochemical glass cell in a standard three electrode arrangement.

All electrochemical measurements were performed in glass cells in a standard three electrode arrangement consisting of the working electrode (WE), at which the electrochemical process of interest occurs, the reference electrode (RE) and the counter electrode (CE). The glass cell is made up of two compartments where the reference electrode is separated from the working electrode and the counter electrode. In order to minimize the potential drop in the electrolyte, the reference electrode is placed very close to the working electrode through a Luggin capillary (see Fig. 3.7). The headspace of the cell and the electrolyte can be purged with inert gas through two gas inlets made up of glass tubes in order to remove the oxygen from the electrolyte. The gas outlet passed through a small glass reservoir filled with water (the bubble counter), in order to prevent the diffusion of air back into the cell.

Commercial mercury/mercury sulfate electrodes ($Hg|Hg_2SO_4$, B 3610, Schott, Germany) were used as reference electrodes (RE) in all experiments. In order to keep diffusion overpotentials as small as possible, mercury/mercury sulfate electrodes stored in different solutions were used for different experiments depending on the pH of the electrolyte. For all experiments performed in

acidic solution (0.1 M or 1 M $HClO_4$) mercury/mercury sulfate electrode stored in 0.1 M H_2SO_4 were used. (Hg | Hg_2SO_4 | 0.1 M H_2SO_4) with a constant potential of 660 mV vs. NHE). In the case of the enzyme experiments which were performed in neutral buffer solution pH 7 the mercury/mercury sulfate electrode was stored in neutral K_2SO_4 solution (Hg | Hg_2SO_4 | K_2SO_4) with a constant potential of 650 mV vs. NHE). Due to the different charge carriers in the used electrolyte and the mercury/mercury sulfate electrode soltuion diffusion potentials $\triangle U_{diff}$ arise at the liquid-liquid phase boundary caused by the different chemical potentials of the charge carriers. The diffusion potentials can be calculated by the Henderson equation [191]:

$$\triangle U_{diff} = -\frac{RT}{F} \cdot \frac{\sum\limits_i \frac{[a_i(I)-a_i(II)]u_i|z_i|}{z_i}}{\sum\limits_i [a_i(I)-a_i(II)]\, u_i|z_i|} \cdot \ln \frac{\sum\limits_i a_i(I)u_i|z_i|}{\sum\limits_i a_i(II)u_i|z_i|} \tag{3.2}$$

where R is the gas constant, T the absolute temperature, F the Faraday constant. Furthermore, a_i(I), a_i(II) and u_i(I), u_i(II) are the activity and the ion mobility, respectively of the ion species i in the liquid phase I or phase II. z_i(I) and z_i(II) give the number of charges of the accordant ions. According to Equation 3.2 the diffusion potential at the 0.1 M $HClO_4$ | 0.1 M H_2SO_4 phase boundary is calculated to be $\triangle U_{diff} = 1.08$ mV and can therefore be neglected. For the 1 M $HClO_4$ | 0.1 M H_2SO_4 phase boundary a diffusion potential $\triangle U_{diff} = 39.9$ mV was considered.
For all experiments the counter electrode (CE) consisted of a gold wire (diameter 0.5 mm) which was melted in a glass grinding.

3.2.2. Potentiostats

Cyclic voltammetry experiments and galvanostatic pulse measurments were performed with a software controlled potentiostat/galvanostat either HEKA PG 310 (HEKA Elektronik Dr. Schulze GmbH) with the data acquisition software PotPulse v. 8.77 or an Autolab PGSTAT 30 (Metrohm Autolab B. V., Netherlands) with the data acquisition software GPES. A potentiostat maintains the applied potential to the working electrode in an electrochemical cell with respect to the reference electrode. Changes in the electrochemical conditions cause a current flow between the working electrode and the counter electrode in order to keep the potential constant. Vice versa a galvanostat keeps the current between working electrode and counter electrode constant by adjusting the necessary potential of the working electrode.

3.3. Electrochemical SPM Techniques

3.3.1. Setup EC SPMs

In this thesis two different electrochemical scanning probe microscopes (SPM) were used. One EC-STM was a homebuilt setup consisting of a Nanoscope IIIA controller (Veeco Instruments Inc., USA) and a PicoSPM STM base (Agilent Technologies former Molecular Imaging) together with an EC-Tec bipotentiostat/galvanostat BP600 and an EC-Tec bi-scangenerator SG600. The STM data were recorded with the computer software Nanoscope v 4.43r6 whereas electrochemical data were recorded with a labview program BP600 or a digital phosphor oscilloscope Tektronix TDS5034B (Tektronix, USA). In this setup the tip is attached to the scanner (so called tip-scanner) and scans above the sample which is fixed in position (Fig. 3.8).

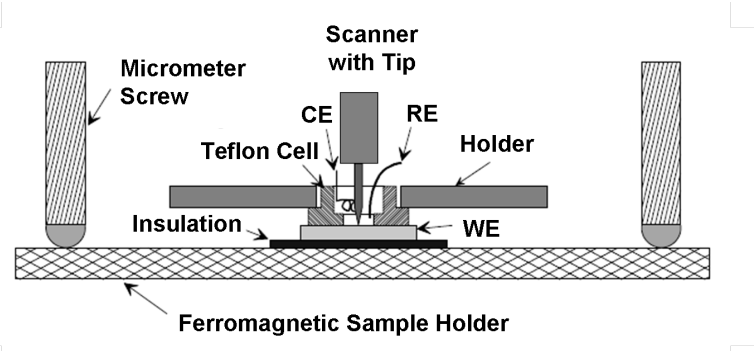

Figure 3.8. Schematic representation of the electrochemical STM cell, based on [192].

The sample, i.e. the working electrode is mounted to a minituarized EC cell made up of Teflon© with a diameter of 5 mm and an electrolyte volume of 500 μl. The cell sits on a ferromagnetic sample holder which is magnetically connected via three micrometer screws with the STM base below the scanner. Two screws serve for a first manual approach of the STM tip to the sample surface. The third screw is computer controlled by a stepper motor and is therefore responsible for the fine adjustment and the final approach of the tip. After each step the measured tunneling current is compared to the setpoint value. As long as the measured current is lower than the chosen setpoint value the z-piezo continues extending until the tunneling conditions selected in the software are established. The scanner had a maximum scan range of 5 μm $\times$ 5 μm in xy-direction and 2 μm in z-direction. The current to voltage converter used has a nominal maximum sensitivity of 10 nA/V.

The other SPM was a commercial combined in situ EC-AFM/EC-STM/SECPM instrument consisting of an electrochemical Veeco Multimode system with the Veeco universal bipotentiostat, optional a combined STM/SECPM head or an AFM head, a Nanoscope IIID Controller and the Nanoscope 5.31r2 software which provides SPM and EC data acquisition. In this setup the tip is fixed in position. It is placed above the sample which sits on top of the scanner, i.e. the sample scans in xyz-direction, so called sample-scanner (Fig. 3.9). The working electrode is positioned

between a ferromagnetic plate and a Teflon© cell (diameter 5 mm, electrolyte volume 100 μl). Throughout the experiments a scanner type E with a range of (10 μm × 10 μm × 2.5 μm) in xyz-direction was utilized.

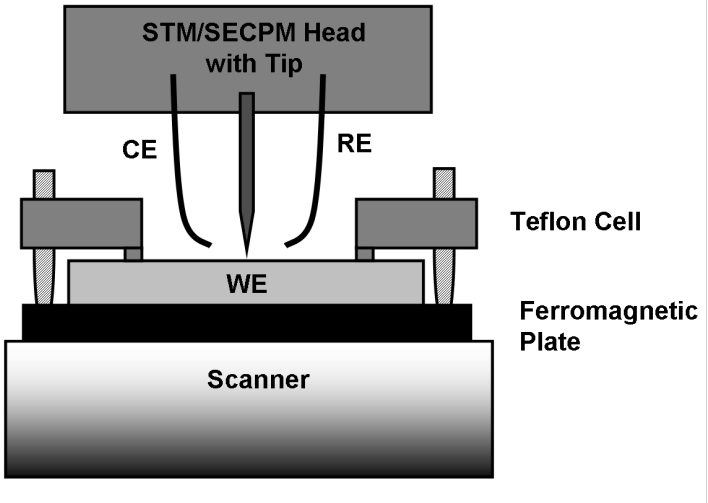

Figure 3.9. Schematic representation of the EC Veeco Multimode system in EC-STM/SECPM configuration.

The SECPM head amplifies the measured potential difference between the potential controlled substrate electrode and a tip which is at open-circuit with four gain values (1, 10, 50, 100) and a leakage current of only a few fA. In STM mode the tunneling current is amplified by a factor of 10^8, i.e. the current to voltage converter also has a nominal maximum sensitivity of 10 nA/V.

3.3.2. Tip preparation

The shape of the SPM tip is of great importance for the qualitiy of the recorded images. Atomic resolution is only achieved with very sharp tips. In the ideal case the apex of the tip consists of only one single atom. Furthermore, in order to benefit from a large potential range in electrochemical investigations SPM tips are usually made of metals that are electrochemically inert over a large potential range such as gold, platinum or palladium. Due to their catalytic activity platinum or palladium are often used to detect hydrogen-related reactions.

3.3.2.1. SPM tip etching

The SPM tips used in this thesis were produced by electrochemical etching (Fig. 3.10). The etching procedure was done with the lamella technique where the setup consists of three electrodes: the etching electrode, the cleaning electrode and a wire of the tip material. The etching electrode has the shape of a ring with a diameter of approximately 10 mm and was made up of platinum wire (thickness 0.5 mm). The wire (0.25 mm) to be etched was pulled through

the center of the etching ring. A precise positioning of the wire in the middle of the ring was important to provide homogenous etching in order to obtain tips witch a symmetrical apex. A lamella of the etching electrolyte was formed in the platinum ring by dipping the ring electrode into a beaker filled with electrolyte. Then a voltage between the etching electrode and the wire in its center was applied until the tip, i.e. the lower part of the wire fell down in the tip catcher and the etching stopped.

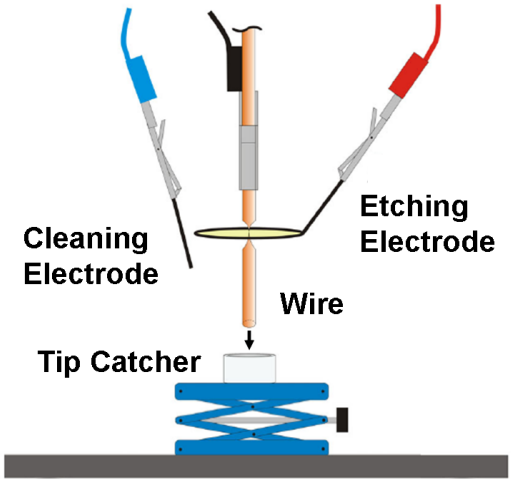

Figure 3.10. Sechematic drawing of the setup for electrochemical SPM tip etching, taken from [146].

Gold and palladium tips were anodically etched in concentrated hydrochloric acid (HCl, 32%) applying a voltage of 1.65 V dc. The etching process of the gold tips lasts approximately 2 minutes whereas the palladium wire took approximately 5 minutes. The tips had a typical apex diameter of 30-40 nm as can be seen in scanning electron microscope (SEM) images (Fig. 3.11 and Fig. 3.12). Freshly etched tips were immediately stored in hot Milli-Q water to remove oxides, metal residues and other contaminations. Before use the shape of the tip was checked in an optical microscope. After each etching process the etching electrode is electrochemically cleaned with the aid of the cleaning electrode which is also made up of platinum wire. To this end, both eletrodes were immersed in a beaker with HCl and a voltage of 4 V was applied between the etching electrode and the cleaning electrode.

3.3.2.2. Tip insulation

Using SPM techniques in electrochemical environments where both electrodes the working electrode and the tip are under potential control, the probe has to be insulated in order to reduce Faradaic leakage currents during the measurements. The ideal tip for electrochemical studies should have a chemically and electrochemically inert insulation except for the very end of the

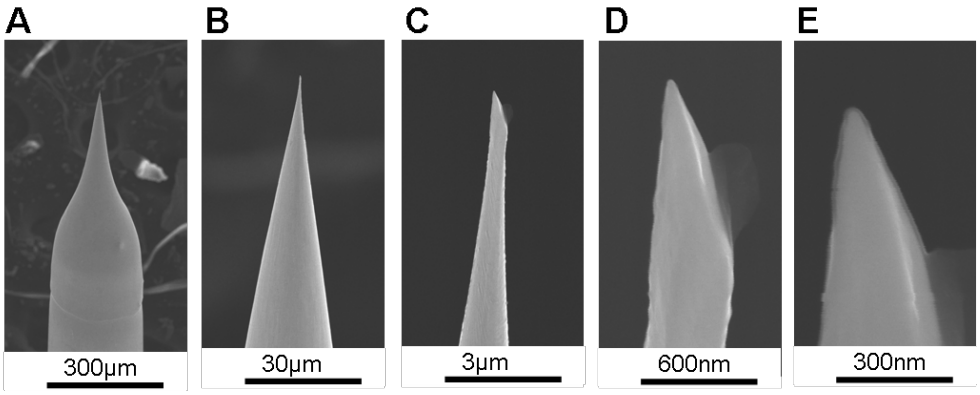

Figure 3.11. SEM pictures of a typical etched Au tip with different magnifications between A) 100 and E) 100000.

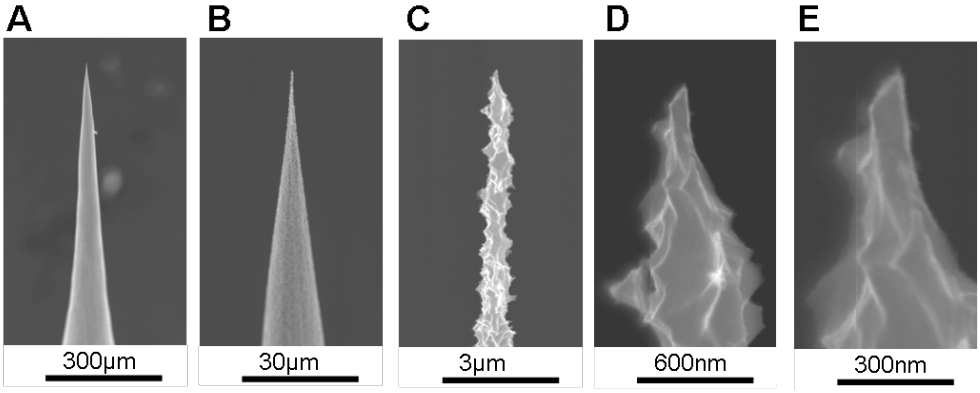

Figure 3.12. SEM pictures of a typical etched Pd tip with different magnifications between A) 100 and E) 100000.

tip. Different techniques for insulating tips: Apiezon wax [193], epoxy glue [151], glass coating, nail polish, electrophoretic paint are commonly used. Since Apiezon wax is inert in most electrolytes and, moreover, is less fragile than e.g. glass, all tips were insulated with Apiezon wax (Plano, Germany). The tip was inserted, with its etched end facing upwards, into a vertically mounted tube attached to a micromanipulator. The Apiezon wax was melted on a notched soldering iron at 190 ° C. Using the micromanipulator the middle of the tip is positioned in the notch of the soldering iron, then the tube was lowered until the whole upper half of the tip was covered with wax. Finally, the tube was shifted upwards again to its original position and the tip was removed from the soldering iron in order to leave the wax for hardening. During the hardening the wax breaks due to the curvature of the tip apex and only a small electrochemically active area gets free [193]. With this procedure the Faradaic leakage current could be reduced to a maximum of 100 pA.

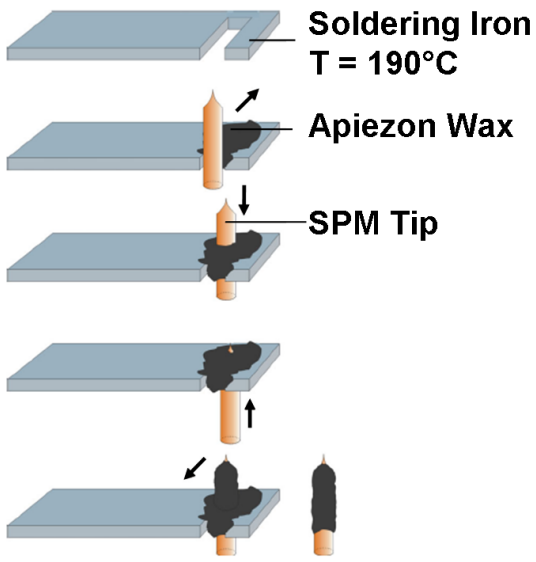

Figure 3.13. Schematic drawing of the tip insulation using Apiezon wax on top of a temperature controlled soldering iron, taken from [146].

3.3.2.3. Preparation and Characterization of Hydrogen loaded Pd

Polycrystalline palladium electrodes were loaded with hydrogen in oxygen-free 1 M $NaClO_4$ containing 0.1 M $HClO_4$ or 1 M $HClO_4$ by applying galvanostatic pulses between -100 μA and -500 μA for different time intervalls. In order to check the potential stability of the produced H/Pd electrodes OCP measurements were performe dover several hours. The pH sensitivity

was investigated by titration experiments. Starting at almost neutral pH values in 1M $NaClO_4$ the pH was decreased by adding stepwise $HClO_4$ of different concentrations and volumes to the electrolyte and meanwhile measuring the OCP.

3.3.3. Reference Electrode

Due to the limited space available in the SPM setups quasi-reference electrodes are required. For all EC SPM measurements gold/gold oxide wire electrodes were used as reference electrodes. Before and after each experiment the potential of the gold/gold oxide electrode was measured for potential stability. For all experiments which were performed in acidic electrolyte the gold/gold oxide electrode was measured versus a mercury/mercury sulfate electrode stored in 0.1 M H_2SO_4, for the enzyme experiments which were performed in neutral buffer solution the gold/gold oxide electrode was measured versus a mercury/mercury sulfate electrode stored in saturated K_2SO_4. The gold/gold oxide reference electrode showed a stable equilibrium potential behavior in acidic as well as in neutral electrolytes. However, one has to keep in mind that the potential behavior of the gold/gold oxide reference electrode is pH sensitive. The equilibrium potential of the gold/gold oxide electrode was measured versus a commercial mercury/mercury sulfate electrode in different concentrations of $HClO_4$ using a salt bridge which minimizes diffusion potentials. Thereby, $NaClO_4$ was added to the electrolytes in order to keep the ionic strength of the solution constant. In Figure 3.14 the potential response (left axis, squares) and the electrolyte concentration (right axis, triangles) are plotted versus the measured pH. The black line represents the linear fit to the obtained U_0(pH) values resulting in a slope of 58 mV per pH and an equilibrium potential U_{00} = 1.32 V vs. NHE, which is in good agreement with the Nernst equation and the literature data of the equilibrium potential of the Au^{+3}/Au^{+2} redox couple U_{00} = 1.36 V vs. NHE [194].

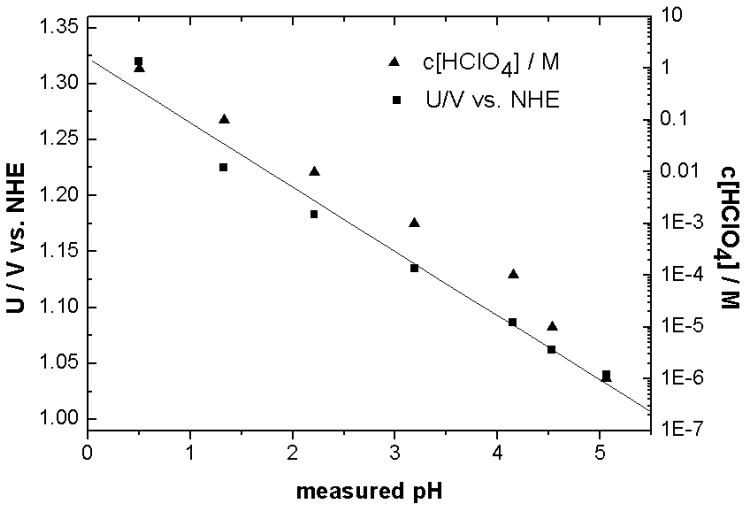

Figure 3.14. Response of the equilibrium potential of the gold/gold oxide reference electrode (left axis, squares) in different concentrations of $HClO_4$ (right axis, triangles) plotted versus the measured pH of the $HClO_4$ electrolyte.

3.4. Electrodes and Electrode Preparation

3.4.1. Au(111) single crystal

Au(111) single crystals were purchased from MaTeck GmbH (Jülich, Germany) with a diameter of 10 mm and a thickness of 1 mm. Before each experiment the Au(111) single crystal was cleaned by an oxidation process in 1 M H_2SO_4. For this purpose, the potential was swept several times up to 1.8 V vs. NHE with a scan rate of 100 mVs^{-1}. Then the electrode was stored for about 30 s in HCl to remove the formed gold oxides and other contaminations. After the crystal was thoroughly rinsed with Milli-Q water an annealing process [195] in a butane flame followed and the crystal was cooled down in an argon atmosphere. The electrode was immediately transferred either into the electrochemical glass cell or to a polytetrafluoroethylene (PTFE) SPM cell with a droplet of ultrapure water protecting the surface from contamination. To confirm that the electrochemical response obtained is characteristic of the Au(111) face, cyclic voltammograms for Au(111) in 1 M H_2SO_4 were collected and found to be in good agreement with literature reports [196].

3.4.2. Highly Oriented Pyrolytic Graphite

Highly oriented pyrolytic graphite (HOPG) is a form of high purity sp^2 hybridized carbon and is characterized by the highest degree of three-dimensional ordering. The density, parameters of the crystal lattice, preferable orientation in a plane (0001) and anisotropy of the physical properties are close to those for natural graphite material. Graphite and in particular HOPG consist of

a lamellar structure and are composed of stacked planes. Carbon atoms within a single plane interact much stronger than with those from adjacent planes, a two-dimensional single-atom thick plane is called graphene. The lattice of graphene consists of two equivalent interpenetrating triangular carbon sublattices A and B (Fig. 3.15A). Within a plane each carbon atom has three nearest neighbors forming a network with a honeycomb structure. Atomic resolution STM images of HOPG normally show a close packed array where each atom is surrounded by six nearest neighbors (see Fig. 3.15B). The distance between two atoms is 0.246 nm. However, under ideal conditions the true structure of graphene (superimposed structure in Fig. 3.15B) the hexagonal rings with an atomic distance of 0.1415 nm can be resolved.

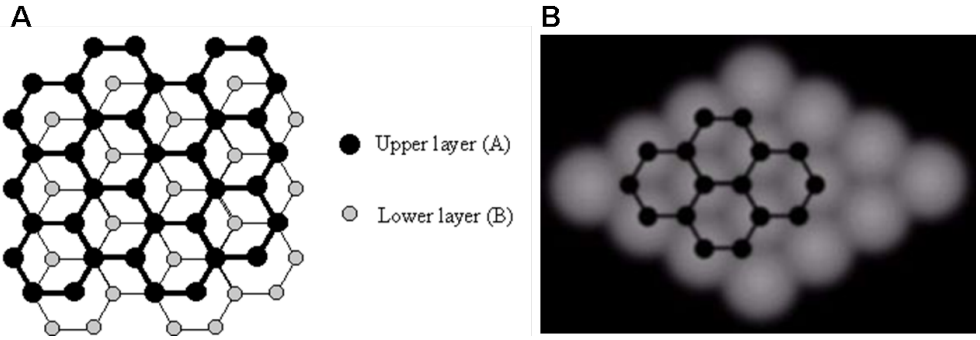

Figure 3.15. Layered structure of HOPG. A) Two identical graphene planes A and B. The HOPG structure can be described as an alternate succession of these layers (ABABAB...). B) Typical high resolution STM image of HOPG showing a close packed array superimposed by a corresponding fragment of the graphene structure, taken from http://www.spmtips.com/hopg.

HOPG can serve as an ideal atomically flat surface to be used as a substrate or calibration grid for SPM investigations. The higher the quality, the less the roughness of the surface and the smaller the number of steps and defect sites. Thereby, the mosaic spread angle obtained from X-ray crystallography gives the disorientation of graphene layers with respect to each other. The higher the quality, the smaller the angle. The electrodes used in this thesis were obtained from Mikromash (USA) and are of ZYB grade, i.e. the mosaic spread is less than 1.2°.

HOPG possesses a low capacitance, observed by Randin and Yaeger [197, 198] and Gerischer et al. [199] which was attributed to an internal space charge layer caused by a low density of states (DOS) at the Fermi level. The capacitance increases with defect density on the surface, as such sites produce localized electronic states [200, 201]

Prior to each experiment, the surface of the HOPG electrode was cleaved with an adhesive tape. All experiments were performed at the basal plane of the HOPG surface. In order to have a well-defined surface area and to avoid the involvement of the edge plane in electrochemical experiments, the electrode was partly covered with Teflon© tape (CMC Klebetechnik, Germany) exposing a geometric surface area of 0.2 cm^2 to the electrolyte.

3.4.3. Functionalized HOPG as Protein Electrodes

3.4.3.1. Adsorption

Freshly cleaved HOPG offers only few active sites for protein binding as its surface is hydrophobic. In order to create binding sites for the biomolecules, the HOPG was electrochemically oxidized in 0.1 M $HClO_4$ by applying three potential sweeps from 0.2 to 2.1 V vs. NHE with a scan rate of 200 mVs^{-1} [15, 16]. This treatment forms oxygen-containing groups on the surface such as carboxyl, hydroxyl and carbonyl [10, 11] (see Fig. 4.1.1) and produces surface defects which improve the electron transfer between protein and electrode [12, 202] probably due to a lowered potential barrier. It is well known that the adsorption of polar molecules is promoted on glassy carbon (GC) and defected HOPG by the oxygenated surface, which creates strong dipole-dipole or ion-dipole interactions with the adsorbates [13]. Afterwards, the rinsed HOPG electrode was immersed into a fresh protein solution (about 0.1 $mgml^{-1}$) in 10 mM PBS (pH 7). The amine groups of the protein polypeptide react with the carboxylic groups on the surface [14]. After an immersion time of 2 h the electrode was immediately rinsed with PBS to remove weakly adsorbed molecules.

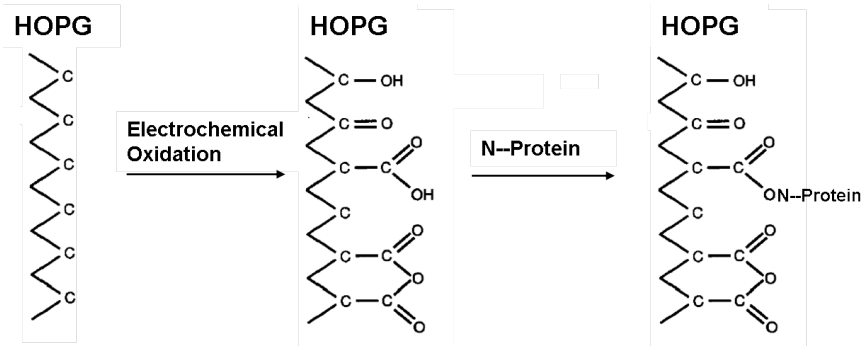

Figure 3.16. Formation of oxygen containing groups on the HOPG surface by electrochemical oxidation and subsequent binding of proteins.

3.4.3.2. Covalent Immobilization

The production of stable functional layers on electrode surfaces by the electroreduction of aryl diazonium salts is of great interest in order to covalently bind redox complexes [50, 203], proteins and even enzymes [22] to carbon [204], semiconductors [205, 207] and metals [206]. This kind of surface derivatization exhibits high potential for possible applications in chemical sensing [208], biosensing [22, 209, 210], molecular electronics [205] and also corrosion protection [211]. For covalent immobilization of proteins or enzymes onto freshly cleaved HOPG the electrode surface was modified with 4-carboxyphenyl diazonium tetrafluoroborate (4-CP). The electrochemical reduction of diazonium salts is a well known method to modify carbon electrode surfaces. Thereby, the covalent attachment of the aryl groups is assigned to the binding of the aryl radicals produced

upon one-electron reduction of the diazonium salt to the carbon surface. Since the beginning of the 1990s the modification of carbon fibers by 4-nitrophenyl radicals was described in several articles [20, 212]. Diazonium salt modified glassy carbon and HOPG electrodes were characterized via Raman spectroscopy [213]. This kind of electrode modification was used e.g. for the immobilization of glucose oxidase [212] and the electrochemical differentiation of dopamine and ascorbic acid [214]. Further experiments of Allongue et al. [21] showed that this method is also suitable for a wide variety of unsubstituted or substituted aromatic radicals in order to functionalize carbon surfaces. The synthesis of the 4-carboxyphenyl diazonium tetrafluoroborate used here was described in Section 3.1.5.1. The HOPG electrode was immersed into a diazonium salt solution made of 5 mM 4-carboxyphenyl diazonium tetrafluoroborate and 0.1 M tetrabutylammonium tetrafluoroborate (Bu_4NBF_4) solved in acetonitrile. The solution was deaerated with argon for at least 15 minutes. The surface derivatization was performed by applying three potential sweeps from + 0.45 V to −0.2 V vs. NHE with a scan rate of 100 mVs^{-1}. Thereby, the electrochemical reduction of the diazonium cations led to the formation of a covalent carbon-carbon bond on the graphite surface [212] (see Fig. 3.17).

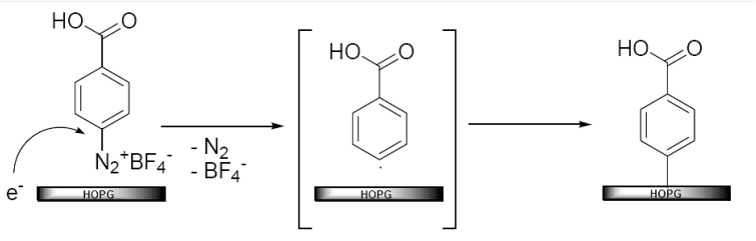

Figure 3.17. Electrochemical reduction of 4-carboxyphenyl diazonium tetrafluoroborate at the HOPG electrode surface via cyclic voltammetry.

The 4-carboxyphenyl modified HOPG (4-CP/HOPG) was thoroughly rinsed with acetonitrile and Milli-Q water. In order to activate the surface for covalent immobilization of proteins, the electrode was incubated into an aqueous solution containing 40 mM N-ethyl-(3-dimethylaminopropyl)-N′-carbodiimide hydrochloride (EDC) and 10 mM *N*-hydroxysuccinimide (NHS) for 1 h [215]. After rinsing with Milli-Q water, the activated electrode was immediately immersed in protein solution (0.1 $mgml^{-1}$ or 1 $mgml^{-1}$) or solution containing the ferrocene affinity label, both with pH 8 at 4°C over night (12 h) (see scheme in Fig. 3.18).

3.4.4. Diamond

Electrode materials most often used in electrochemistry (e.g. for electroanalysis, energy storage and conversion devices, electrosynthesis) are platinum, gold and various forms of sp^2-bonded carbon such as glassy carbon (GC), carbon fibers and HOPG. sp^3-bonded diamond is a promising candidate for electrode materials offering several advantages for electrochemical measurements, as compared to other carbon and metal supports. Beside a large electrochemical potential window,

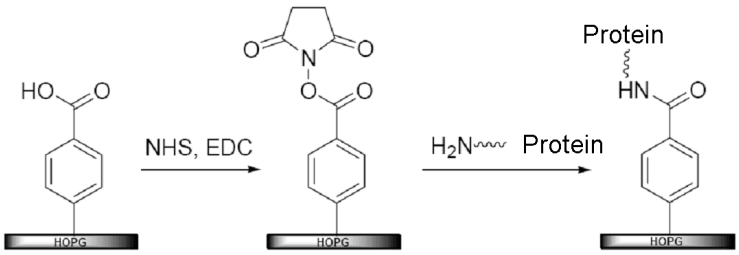

Figure 3.18. Formation of an active NHS-ester for covalent immobilization of proteins onto the HOPG surface

which is due to the large overpotentials for oxygen and hydrogen evolution, diamond provides chemical inertness, fouling resistance and low background current compared to other materials.

Electrochemical studies of diamond started only twenty years ago [216] since such studies were essentially impeded by two factors: the preparation of single crystal diamond is expensive as it requires high pressure and high temperature (HPHT) and furthermore, diamond is an insulator. Upon the invention of growing diamond by chemical vapor deposition (CVD) an effective and economical method for fabricating polycrystalline, nanocrystalline and ultrananocrystalline diamond films on different substrates, as well as large single crystals were developed [217]. Boron doping of diamond leads to the required conductivity necessary for an electrically active material possessing electronic properties ranging from semiconduting to semimetallic [13, 216] and opened a new area for diamond electrodes in electrochemistry. Diamond surfaces can be hydrogen- or oxygen-terminated. Hydrogen-terminated surfaces are hydrophobic. Because dangling bonds at the surface are passivated by the hydrogen atoms, these surfaces are relatively passive. Oxidized diamond surfaces carry oxygen-containing groups and are therefore hydrophilic. By chemically modifying the molecular structures present at the free surface, it is possible to provide diamond with specific biomolecular recognition properties and to control specific and nonspecific binding of proteins to the surface [51, 52, 218]. Due to its unique electrochemical properties, its good biocompatibility and the possibility to immobilize biomolecules by surface termination, diamond is especially suited for biological, environmental and medical science, especially biosensor applications from DNA [219] over enzymes [51, 220] to living cells [221].

Boron doped oxygen-terminated diamond electrodes (obtained from Dr. Denisenko, University of Ulm, Institute for Electronic Devices and Circuits) were tested as potential enzyme electrode material. Electroactive proteins such as azurin and FcAL@papain were adsorbed (2 h, 0.1 $mgml^{-1}$ in 10 mM PBS, pH 7) onto these oxygen-modified diamond surfaces and investigated performing cyclic voltammetry (100 mVs^{-1}) in 10 mM PBS (pH 7), in order to study the direct electron transfer between protein and electrode. The results are compared to data obtained for oxidized HOPG electrode surfaces. Similar to HOPG diamond possesses a reduced excess surface charge due to a low density of states and a low charge carrier concentration [13].

Single-crystalline diamond layers were grown on homoepitaxial (100) HPHT substrates (Sumitomo) by microwave-assisted chemical vapor deposition (MWCVD) in a hydrogen/methane at-

mosphere [222]. A solid doping source technique [223] lead to a boron doping concentration in the range of 10^{20} cm^{-3} [222]. Nanocrystalline diamond (NCD) films were grown on silicon substrates by hot-filament chemical vapor deposition (HFCVD) in a hydrogen/methane atmosphere with a trimethyl borate (TMB) gas source for boron doping with a concentration of 10^{20} cm^{-3} [224]. Three different oxidation procedures were applied to the electrodes in order to create oxygen-containing groups on the surface.

1. O_2 plasma / μ-etch: The termination by oxygen plasma was performed at 100 mTorr pressure at 100 W under ambient temperature in a radiofrequency barrel reactor for 2 minutes. The diamond samples were placed onto the ground electrode to reduce the plasma-induced damage to a minimum (no DC self-bias).

2. Wet chemical oxidation (WC): The wet chemical oxidation process was performed at 80°C in chromium acid for 10 minutes and subsequent incubation in hot caroic acid $H_2O_2 : H_2SO_4$ (1:2) for 10 minutes. Afterwards the electrode was thoroughly rinsed with Milli-Q water.

3. Reactive ion etching (RIE): The electrode was first exposed to a Ar/O_2 plasma at 50 mTorr and 25 W for 40 s with a self-bias of 100 V, followed by the wet chemical oxidation, described above, to remove surface graphite.

In order to have a well-defined surface area in electrochemical experiments, the electrode was partly covered with Teflon© tape (CMC Klebetechnik, Germany).

3.5. Papain Labeling for Electrochemical Detection

3.5.1. Labeling in Solution

Commercially available papain stock solution contains inactive papain molecules, i.e. their active sites contain beside Cys-25 a second cysteine which is connected to Cys-25 by a disulfide bridge and blocks their peptide breaking functionality. An activation reagent such as tris(2-carboxyethyl)phosphine (TCEP) has to be used in order to reduce the disulfide linkage between the two cysteines and thus to activate Cys-25 by deprotonation (Fig. 3.19). For this purpose, 0.11 μM of the papain stock solution and 2.5 μM TCEP were incubated in 10 mM phosphate buffer solution for 1 h.

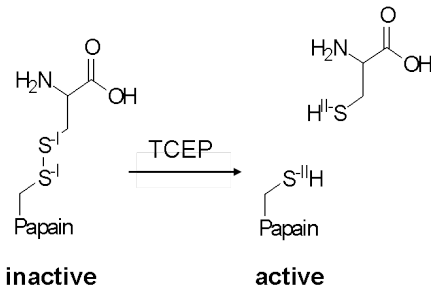

Figure 3.19. Activation of the active site of papain by deprotonation using tris(2-carboxyethyl)phosphine (TCEP)

After the activation of Cys-25 1 mg of the according ferrocene affinity label (1.1 μM) was added to the solution and incubated for 3 h. The excess label was removed by ultracentrifugation through a centrifugal filter with 5000 NMWL (nominal molecular weight limit) resulting in prelabeled FcAL@papain molecules. The FcAL@papain molecules were investigated and characterized by MALDI-TOF mass spectrometry as well as electrochemical measurement techniques such as cyclic voltammetry and EC-STM in order to confirm successful labeling. Figure 3.20 shows schematic drawings of the labeled papain with the ferrocene moiety outside (Fe(Cp)(η-C_5H_4-CH_2-CH(NH_2)-CO-Lys-Ahx-Tyr-Leu-Epx-COOEt), FcAL (out), Fig. 3.20A) and inside the active site (Fe(Cp)(η-C_5H_4-CH_2-NH-CO-Epx-Leu-Tyr-Ahx-Lys), FcAL(in), Fig. 3.20B), i.e. attached to the N-terminus or the carboxyl-terminus of the label, respectively.

Furthermore, in order to study in-situ the binding process of the ferrocene affinity label FcAL(in) to the active site of the papain molecules, both dissolved in solution, cyclic voltammetry at an HOPG electrode was performed in 10 mM PBS (pH 7) containing 0.5 μM FcAL(in) and different concentrations of activated papain molecules.

3.5.2. In-situ Labeling on the Electrode Surface

To get a better understanding of the labeling process, further approaches to electrochemically monitor the binding between FcAL and activated papain was aspired. In contrast to the previous

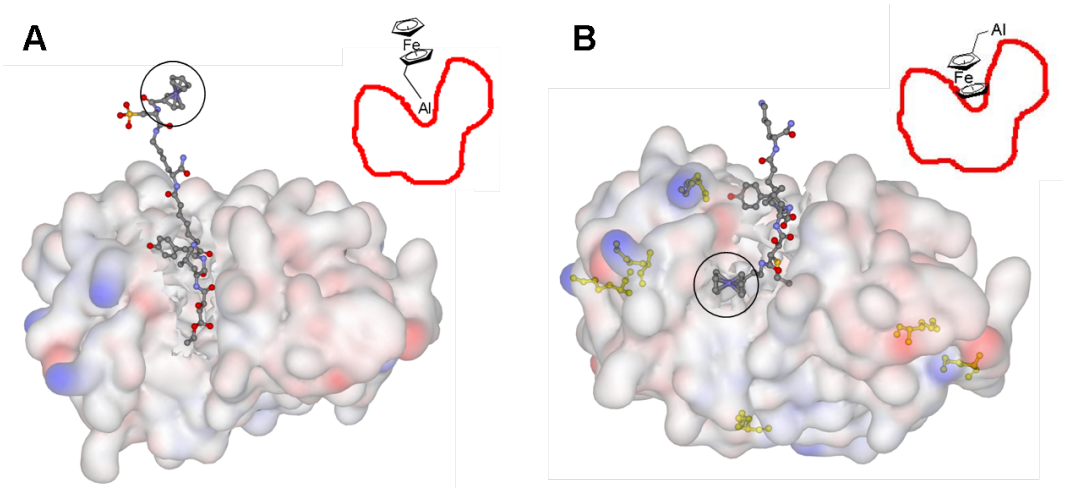

Figure 3.20. Scheme of papain molecules with the A) FcAL(out) where the ferrocene moiety is attached to a linker outside the protein shell and B) FcAL(in) where the ferrocene moiety is in the active site of the enzyme. The ferrocene moiety is marked by a black circle. The insets show cartoons of the two different FcAL@papain molecules to point out the different positions of the ferrocene moiety.

Section 3.5.1, here, one of the reagents, i.e. either the ferrocene label (Fig. 3.21) or the activated papain molecules (Fig. 3.22) were covalently immobilized onto the 4-CP/HOPG electrode and the other compound was added to the electrolyte.

In the first approach, the FcAL(in) (Fe(Cp)(η-C_5H_4-CH_2-NH-CO-Epx-Leu-Tyr-Ahx-Lys)) was coupled to 4-CP/HOPG by EDC and NHS over night at 4 °C. Figure 3.21 shows a scheme of the electrode surface. After thoroughly rinsing the FcAL/4-CP/HOPG electrode was incubated in 10 mM PBS and 230 μl activated papain (0.1 $mgml^{-1}$) was added. Cyclic voltammograms were recorded in different time intervalls in order to investigate changes in the electrochemical behavior of the electrode in the presence of enzymes.

In the second approach, complementary to the first, the papain molecules were covalently immobilized on 4-CP/HOPG and FcAL(in) was added to the electrolyte. This approach also enabled the investigation of the enzymatic activity of papain. Figure 3.22 shows each step of the multilevel procedure to label the papain molecules of the papain/4-CP/HOPG electrode in order to study the binding process of the label to the enzyme. First an active NHS-ester monolayer was formed on the 4-CP/HOPG surface (described in Section 3.4.3.2) to covalently immobilize the papain molecules on the elecrode surface. In order to avoid binding of the dissolved label to activated free NHS-ester groups later on, these groups were blocked by immersing the electrode in 1 M ethanolamine (C_2H_7NO) for 15 minutes (indicated by the blue dots in Fig. 3.22) and then thouroghly rinsed with Milli-Q water. The active sites of the immobilized papain molecules were activated with TCEP for 1 h (indicated by the green stars in Fig. 3.22) and afterwards again rinsed with water. Depending on the experiment the electrode was either immersed in the electrochemical cell for activity measurements or investigated by CV and EC-STM. After the

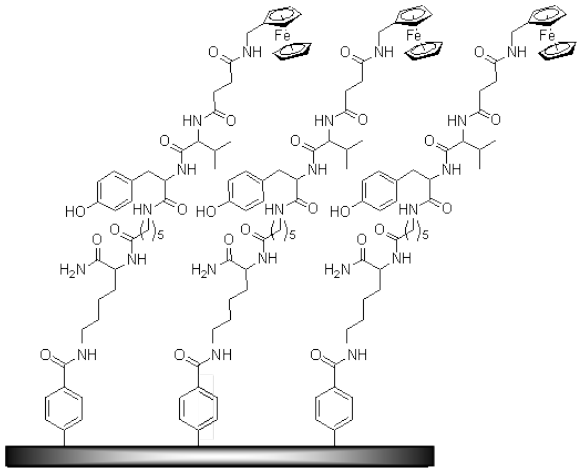

Figure 3.21. Scheme of the ferrocene affinity label FcAL(in) covalently immobilized on the 4-CP/HOPG electrode surface by EDC/NHS coupling.

electrochemical characterization the electrode was incubated in a solution containing ferrocene affinity label dissolved in 10 mM PBS.

The electrode incubated in the FcAL solution was stored over night at 4 °C. Before EC-STM investigations the prepared electrode was rinsed with water, put in the ultrasonic bath for about one minute to remove loosely bound enzymes and label and again thoroughly rinsed with water.

For activity measurements the activated papain/4-CP/HOPG electrode was investigated in an electrochemical glass cell performing continuous cyclic voltammetry in the presence of different concentrations of the ferrocence affinity label, as well as in the presence of reversible and irreversible inhibitors. From the electric charge under the redox peaks, the amount of formed FcAL-enzyme complexes with time can be evaluated. Based on this correlation, it is possible to obtain the kinetic enzymatic behavior of the immobilized papain molecules.

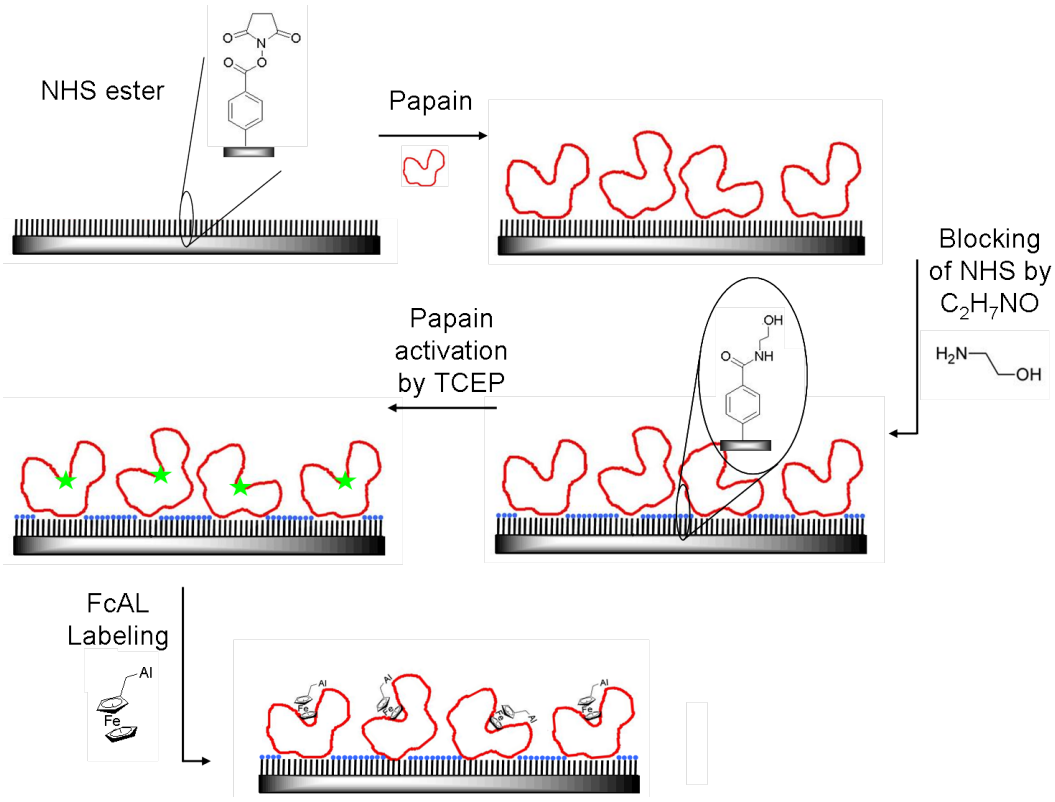

Figure 3.22. Scheme of papain labeling on the papain/4-CP/HOPG electrode surface.

4. Results

The focus of this work was the electrochemical investigation of biomolecules at the solid-liquid interface. Obtaining new information about the structure-function relation of redox active biomolecules such as proteins and enzymes would possibly allow to gain a fundamental understanding of biological systems and therefore, to biomimic these systems for innovative technical applications. However, to really achieve fundamental understanding of biomolecular function, investigations on a single molecule level are necessary. Therefore, several issues have to be taken into account. Beside providing a fast electron transfer between the biomolecule and the electrode, an adequate smooth electrode surface has to be used and a suitable high-resolution investigation tool must be available.

This chapter presents the results of the new experimental approaches that has been realized to accomplish these issues. As a model electrode for single biomolecule studies HOPG was chosen due to its atomically flat surface. In order to enhance the electron transfer between the HOPG surface and the biomolecules, the biomolecules were covalently immobilized on the basal plane by electrochemical grafting. This new approach is described and investigated by cyclic voltammetry and EC-STM using the metalloprotein azurin as testprotein in Section 4.1. Since we are not only interested in the behavior of naturally redox active biomolecules, but also in electroinactive enzymes such as proteases, a bottom-up approach was developed in Section 4.2 to electrochemically detect redox inactive enzymes using ferrocene affinity labels (FcAL). The labeling process and the electrochemical behavior of unlabeled and FcAL labeled enzymes is investigated down to a single molecule level using EC-STM (Section 4.3). Although up to now EC-STM is the method of choice for studying electrochemical properties of single biomolecules, the new EC SPM modification, the scanning electrochemical potential microscopy (SECPM) is used in Section 4.4.2 to investigate adsorbed biomolecules and to check whether it is possible, using SECPM, to gain further insights into their structure-function relation. Since diamond is a promising electrode material for applications in biosensor technology, first experimental results of biomolecules adsorbed on oxygen-terminated boron-doped diamond are presented in Section 4.5. Thereby, different oxidation procedures are investigated and compared oxidized HOPG in order to yield optimized surface conditions for biomolecule-electrode interactions.

4.1. Functionalization of the HOPG surface

Fundamental research in the field of bioelectrochemistry is of great importance for the development of innovative functional devices in biosensor technology, bioelectronics and bioelectrochemical fuel cells. An inalienable requirement of any bioelectrochemical system is the existence of

electronic coupling, i.e. the charge transfer between the electrode and the biomolecules [1]. The verification of undisturbed electrical communication is one of the main challenges in successful realization of biomelecular-electronic hybrid systems. Thereby, one of the key components is a surface-immobilization chemistry that stably anchors the biomolecules to the electrode surface, at the same time provides interfacial charge transfer and furthermore, maintains the activity of the biomolecule. Since proteins easily tends to denaturate when they are in contact with metallic surfaces a sp^2-bonded carbon substrate, highly oriented pyrolytic graphite (HOPG), was chosen here as electrode material for the immobilization of the biomolecules. This chapter describes two possible ways to functionalize the HOPG surface in order to optimize the surface properties for biomolecule immobilization and their electrochemical investigation via cyclic voltammetry and in-situ SPM. Especially, in-situ EC-STM has opened new perspectives for addressing the electronic properties of adsorbed proteins and enzymes in their natural functional aqueous medium down to a single molecule level [225]. Since immobilization of protein and enzyme molecules providing conductivity and stability are fundamental challenges for STM measurements with high resolution, two different methods to bind the metalloprotein azurin onto the HOPG surface are described and discussed. One possible way which has widely been approved to be effective to fix biomolecules to a carbon support is the electrochemical oxidation of the HOPG surface [14–16]. The other approach is to covalently immobilize proteins and enzymes to an HOPG surface modified with aromatic 4-carboxyphenyl groups [21]. This technique has recently also been realized to successfully bind heme proteins onto a glassy carbon (GC) electrode and to investigate their electrochemical behavior [226] and should now be adopted to the graphite surface which is more suitable for SPM studies than GC. Therefore, the metalloprotein azurin from *Pseudomonas aeruginosa* was adsorbed onto oxidized HOPG electrodes by chemisorption and covalently immobilized onto 4-carboxyphenyl modified HOPG by EDC/NHS coupling. Both immobilization mechanisms will be compared regarding the apparent interfacial electron transfer rate k_{app} and the electrode surface coverage Γ.

4.1.1. Electrochemical oxidation

The electrochemical oxidation of the HOPG surface was performed in 0.1 M $HClO_4$ using cyclic voltammetry. The electrode potential was varied between 0.45 V and 2.1 V vs. NHE with a scan rate of 200 mVs^{-1}, resulting in a CV showing a characteristic oxidation current at 2.1 V and a slightly diminished reduction peak at 1.8 V vs. NHE (Fig. 4.1). The oxidation is attributed to a combination of graphite oxidation and the intercalation of anions such as ClO_4^- into the graphite lattice [12]. Therefore, the reduction peak can be attributed partially to the deintercalation of the anions and partially to the reduction of the formed oxygen containing groups at the graphite surface. However, the oxidation of the graphite is not fully reversible, thus, surface bonds are broken and the graphite structure is thought to be disturbed during the oxidation process leading to a residual oxide layer.

EC-STM (U_{Bias} = 100 mV, I_T = 1nA) was used in order to investigate the oxidized HOPG surface. Figure 4.2 shows typical STM images of a bare (Fig. 4.2A) and oxidized HOPG surface

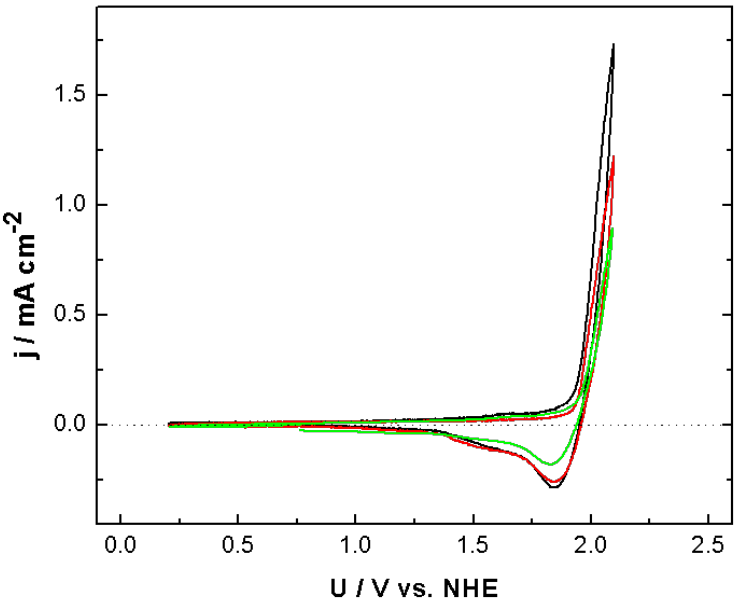

Figure 4.1. CV of the electrochemical oxidation of HOPG by three potential sweeps (black: first cycle, red: second cycle, green: third cycle) between 0.45 V and 2.1 V vs. NHE obtained at a scan rate of 200 mVs^{-1} in 0.1 M $HClO_4$.

(Fig. 4.2B) and C)). The bare HOPG is characterized by an atomically flat surface over large areas (1 μm × 1 μm) with only a few step edges, whereas the oxidized HOPG surface contains an increased step density and amount of defect sites within an area of 500 nm × 500 nm. The formation of the oxide groups occurs according to a nucleation and growth mechanism [12] where the oxidation, i.e. the irreversible breaking of the C-C bonds starts initially at step and defect sites, and proceeds along step and ridge sites and only to a lower extend also into the basal plane. However, areas with undefined surface structures were also found, as can be seen in Fig. 4.2C (400 nm × 400 nm). These structures might be huge agglomerates probably of oxidized carbon or caused by blister formation due to the intercalation of ClO_4^- [227, 228].

Furthermore, the electrochemical treatment forms active sites on the surface, e.g. oxygen containing groups such as carboxyl, hydroxyl and carbonyl [10, 11]. By performing in-situ EC-STM studies Gewirth and Bard [12] found that the tunneling barrier height through the oxide overlayer is significantly lower than that for the bare HOPG surface; it decreased from 0.9 eV to 0.25 eV in 0.1 M H_2SO_4. This indicates that the oxidation process also enhances the electron transfer between the electrode surface and surface bound species, making it suitable for electrochemical investigation of enyzme/electrode architectures.

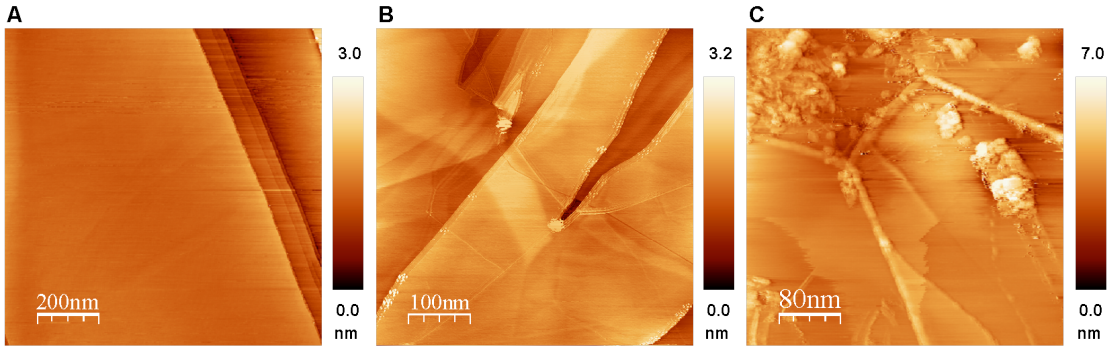

Figure 4.2. STM images of A) bare and B) and C) electrochemically oxidized HOPG surfaces.

4.1.2. Modification with 4-Carboxyphenyl Diazonium Tetrafluoroborate

The production of stable functional layers on electrode surfaces by the electroreduction of aryl diazonium salts has obtained heightened interest in order to covalently bind redox complexes [50, 203], proteins and even enzymes [22] to carbon [204], semiconductors [205], metals [206] and silicon [207]. This kind of surface derivatization inhibits high potential for possible applications in chemical sensing [208], biosensing [22, 209, 210], molecular electronics [205] and also corrosion protection [211].

The HOPG surface was functionalized with a carboxyphenyl layer via electrochemical reduction of 4-carboxyphenyl diazonium tetrafluoroborate (4-CP) using cyclic voltammetry performed in acetonitrile containing 1 mM of the diazonium salt and 0.1 M Bu_4NBF_4. The cyclic voltammogram of the electrochemical reduction is shown in Figure 4.3. The electrode potential was cycled three times between 0.45 V and -0.2 V vs. NHE with a scan rate of 100 mVs^{-1} starting at 0.45 V. In the first cycle an irreversible reduction peak with a peak potential of approximately 40 mV vs. NHE can be observed. This peak can be attributed to the reduction of the diazonium salt on the HOPG generating aryl radicals that couple, through carbon-carbon bond formation, to the HOPG surface [204]. Based on the integration of the charge passed under the reduction peak on the first scan the surface coverage of 4-carboxyphenyl moieties was calculated to be 1.41 $nMcm^{-2}$ of the geometric area of the HOPG electrode. This surface coverage is close to the theoretical value for a close-packed monolayer of phenyl rings of 1.35 $nMcm^{-2}$, which was calculated by Pinson and Podvorica [19]. During the second and the third cycle the current of the reduction peak decreases and finally disappears due to the passivation of the electrode surface.

In order to investigate the passivation of the active HOPG surface area by aromatic groups, cyclic voltammetry was performed at a scan rate of 100 mVs^{-1} in 10 mM PBS containing 1 mM ferrocene monocarboxylic acid (FCMA). Figure 4.4 shows typical CVs for the oxidation and reduction of FCMA at the bare (black line) and carboxyphenyl modified (red line) HOPG (4-CP/HOPG) surface. At the bare HOPG the characteristic redox peaks of the FCMA with a redox potential of 0.55 V vs. NHE occured. At the 4-CP/HOPG surface no redox behavior

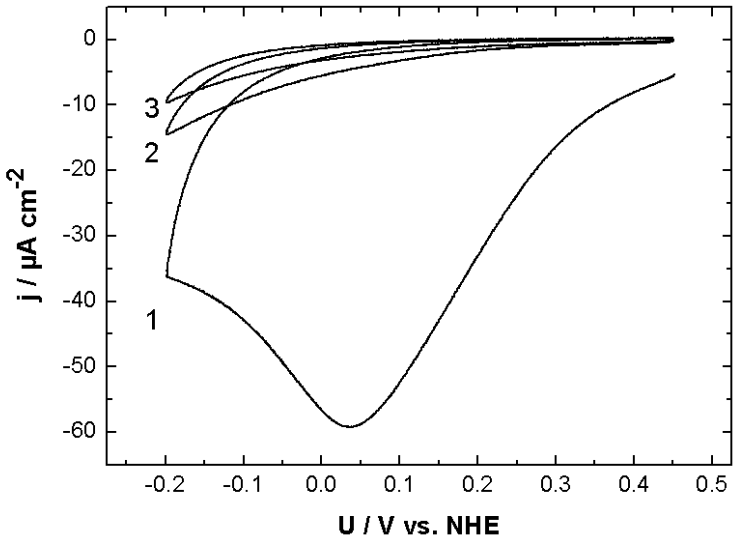

Figure 4.3. Electrochemical reduction of 4-carboxyphenyl diazonium tetrafluoroborate at the HOPG electrode surface via cyclic voltammetry, performed at a scan rate of 100 mVs^{-1} in acetonitrile + 0.1 M Bu_4NBF_4.

could be observed, giving evidence that the HOPG surface is successfully covalently grafted with phenyl groups that block the access of the FCMA to the electrode.

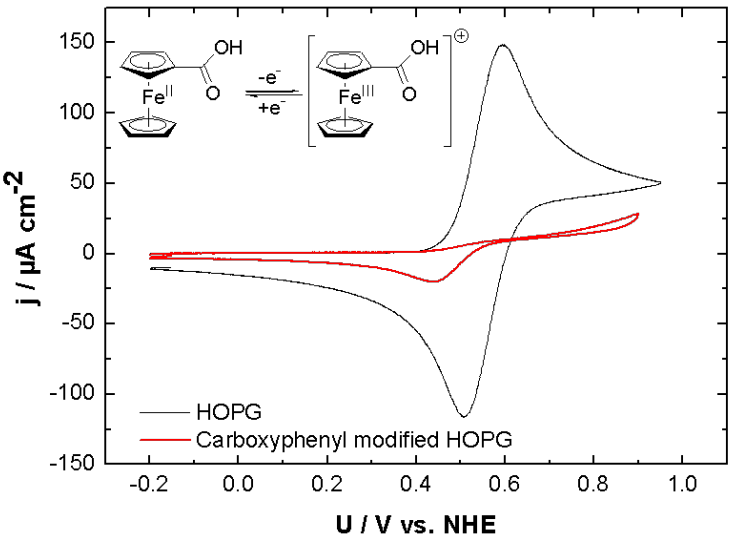

Figure 4.4. CVs of bare HOPG (black line) and 4-carboxyphenyl modified HOPG (red line) in 10 mM PBS + 1 mM FCMA at a scan rate of 100 mVs^{-1}.

4.1.3. Immobilization of Azurin

The copper containing metalloprotein azurin from *Pseudomonas aeruginosa* was adsorbed on HOPG electrodes by chemisorption and covalent immobilization via diazonium salts as described above. In this section these two immobilization mechanisms should be compared regarding the interfacial electron transfer and the electrode coverage.

4.1.3.1. Electrochemical Characterization

The electrochemical behavior of azurin electrodes, i.e. azurin chemisorbed on oxidized HOPG (azurin/HOPGox) and covalently immobilized on 4-CP modified HOPG using EDC/NHS coupling (azurin/4-CP/HOPG) was investigated by cyclic voltammetry in 10 mM phosphate buffer solution (pH 7). CVs obtained for both electrode architectures show observable redox peaks (see Fig. 4.5) indicating that in both cases a direct electron transfer (DET) between the surface bound azurin molecules and the HOPG electrode is possible. However, the redox behavior of the two different electrode types shows significant differences. The redox potential, assumed as the midpoint potential between oxidation and reduction peak [226], was found to be around 215 mV vs. NHE for azurin/HOPGox (black curve in Fig. 4.5) and around 50 mV vs. NHE for azurin/4-CP/HOPG (red line in Fig. 4.5). Depending on substrate material and immobilization technique, the redox potential of azurin reported in the literature is around 300 mV vs. NHE normally measured in NH_4Ac at a pH 4.6. Larver et al. [229] proposed that the redox potential of *Pseudomonas aeruginosa* azurin increases by 60-70 mV upon decreasing the pH from 8 to 5 since the protonation of the two conserved histidines, His-35 and His-83, increases the Cu(II)/Cu(I) potential. Therefore, the redox potential of the azurin/HOPGox electrode can be explained by pH dependence. The reason for the even lower redox potential of the azurin/4-CP/HOPG electrode is not clear, however, one might assume that the covalent immobilization leads to conformational changes in the vicinity of the copper atom that affect the redox potential.

Performing cyclic voltammetry at various scan rates, a linear behavior of the peak current density (corrected for double layer capacitance) with increasing applied scan rate was found for both types of azurin electrodes (Fig. 4.6), indicating that in both cases the azurin molecules are stably bound to the HOPG electrode surface and the electron transfer process is not diffusion controlled.

Furthermore, Figure 4.6 clearly shows that the peak current density is much higher for the covalently immobilized azurin molecules (squares) than for the azurin molecules only adsorbed (triangles) to the HOPG surface, indicating that a higher surface coverage Γ of electroactive azurin molecules can be obtained by the covalent immobilization. From the charge under the redox peaks the amount of redox active surface bound azurin can be determined assuming a one electron transfer. Since the ratio of anodic to cathodic charge (q_{ap}:q_{cp}) is close to unity, the surface coverage Γ was calculated by the mean of both charges. According to Laviron [73], the apparent interfacial electrochemical rate constants for the electron transfer k_{app} can be calculated from the variation in peak separation of the anodic and cathodic peaks with increasing scan rate. These results are summarized in Table 4.1.

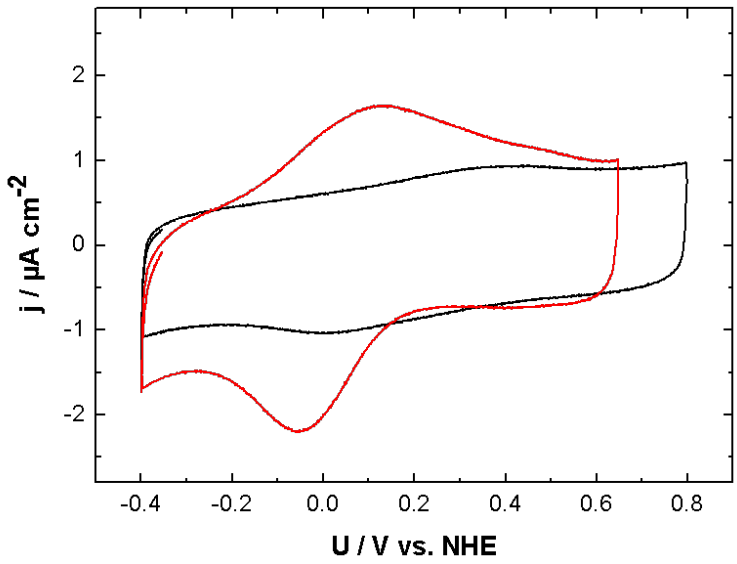

Figure 4.5. CVs of azurin adsorbed on oxidized HOPG (black line) and covalently immobilized on 4-carboxyphenyl modified HOPG (red line) in 10 mM PBS at a scan rate of 100 mVs^{-1}.

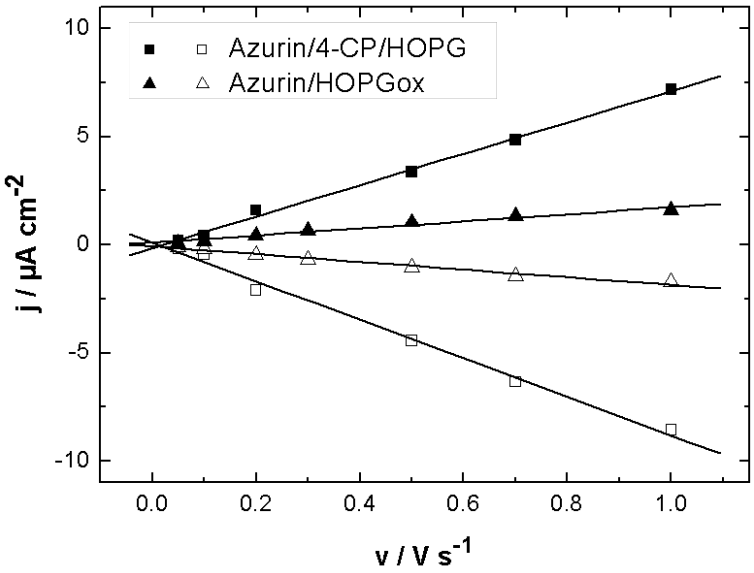

Figure 4.6. Faradaic peak current densities of the oxidation (full symbols) and the reduction (open symbols) peak plotted versus increasing scan rate between 0.05 and 1 Vs^{-1} for the azurin/HOPGox (triangles) and the azurin/4-CP/HOPG (squares) electrode, respectively.

azurin/	$\mathbf{U_0}$	$\mathbf{q_{ap}}$	$\mathbf{q_{cp}}$	$\mathbf{\lvert q_{ap}{:}q_{cp}\rvert}$	Γ	$\mathbf{k_{app}}$
	mV vs. NHE	μ**Ccm**$^{-2}$	μ**Ccm**$^{-2}$		**pMcm**$^{-2}$	**s**$^{-1}$
HOPGox	215	0.492	-0.497	0.99	5.13	0.43
4-CP/HOPG	50	2.463	-2.456	0.96	25.49	48.26

Table 4.1. Some parameters of azurin covalently immobilized on 4-CP modified HOPG and adsorbed on electrochemically oxidized HOPG: Redox potential U_0, charge density of the oxidation q_{ap} and the reduction q_{cp} peak evaluated from the CVs shown in Fig. 4.5, the ratio of q_{ap}:q_{cp}, surface coverage Γ and apparent electron transfer rate constant k_{app}.

The results show that the surface coverage of azurin molecules that are able to undergo DET with the HOPG surface is by a factor of 5 higher for covalent immobilization than for adsorption. The surface coverage for a complete azurin monolayer is calculated to be 30.64 pMcm^{-2} assuming that the molecules have a mean diameter of 2.5 nm and are arranged in a two dimensional closely packed hexagonal lattice on the HOPG surface. According to Faraday's law (Equation 2.15) this surface coverage is equal to a maximum charge densitiy of 2.9 μCcm^{-2} per monolayer. Therefore, the amount of azurin molecules electrochemically detected on the azurin/4-CP/HOPG electrode corresponds to more than 80% of a protein monolayer, whereas the molecules detected on the azurin/HOPGox corresponds only to approximately 16% of a monolayer. Furthermore, the electron transfer rate constant evaluated by the Laviron theory is two orders of magnitude higher for azurin covalently immobilized than just adsorbed on defect sites of the oxidized HOPG. According to the Marcus theory, electron transfer mainly depends on the distance between electron donor and electron acceptor, i.e. in this case between the copper center and the HOPG electrode surface. While it is not clear so far how proteins bind to the oxidized HOPG surface, we know that azurin is coupled via a lysine group to the 4-CP/HOPG electrode. However, this binding is unspecific, since there are 11 lysine groups located at the protein surface with distances between 8Å and 30 Å to the copper center. Therefore, it is not clear to which lysine chain the molecule is attached and the electron transfer rate only represents an average value. However, a rate constant of 48 s^{-1} is in good agreement with literature data obtained for similar systems where azurin is bound to an electrode surface [17, 229]. Chi et al. [230] found an interfacial electron transfer rate constant of approximately 30 s^{-1} for azurin adsorbed on Au(111) and of approximately 500 s^{-1} when azurin is wired by an octanethiol monolayer self-assembled on the Au(111) surface [17], both obtained in 50 mM NH_4Ac (pH 4.6). These results can be explained by different orientation and the different adsorption modes of the protein molecules. The adsorbed molecules self-assemble through the surface disulfide Cys-3 Cys-26 group resulting in a molecule orientation where the copper center is opposite to the electrode surface with a distance of 26Å, whereas the molecular wiring establishes effective electronic coupling directly between the copper center and the Au(111) surface, leading to a fast and reversible interfacial electron transfer. Beside possible pathways for the interfacial electron transfer also the intramolecular electron pathway of azurin has to be taken into account. Especially when the copper center is located opposite to the electrode surface, the electron transfer within the molecule might play

an essential role. Farver et al. [229] found the intramolecular electron transfer rate to be 44 s^{-1} at room temperature and pH 7. Therefore, the electron transfer between the electrode surface and the copper ion found for the azurin/4-CP/HOPG electrode might also be limited by the intramolecular ET rate. Furthermore, one has to keep in mind that the different material of the electrode might also have an impact on the electron transfer rate [50].

4.1.3.2. Characterization using EC-STM

In order to study the surface coverage for both immobilization techniques, azurin/HOPG electrodes were characterized by EC-STM applying a bias voltage of 100 mV and tunneling currents between 0.2 nA and 0.5 nA. Figure 4.7 shows typical STM images of both electrode types with an area of 300 nm × 300 nm. In Fig. 4.7A the azurin/HOPGox electrode shows only six azurin molecules (highlighted by black circles) visibly adsorbed on the $9 \cdot 10^{-10}$ cm^{-2} surface area which corresponds to a surface coverage of 0.011 $pMcm^{-2}$. Compared to the surface coverage obtained by the Faradaic charge of the CV, the coverage found by EC-STM is more than two orders of magnitude lower. A possible explanation could be that the adsorption of the molecules is too weak to resist interactions between the STM tip and the electrode surface occuring in the STM setup, so that a huge amount of molecules is just irreversibly removed from the surface while scanning. Covalent immobilization on the 4-CP groups yields high density submonolayers of azurin molecules on the HOPG surface (see Fig. 4.7B). The immobilized molecules are stable also when the surface area is scanned several times indicating that the covalent binding of the protein to the 4-CP via EDC/NHS coupling as well as the carbon-carbon bonding between the HOPG electrode surface and the carboxyphenyl group is strong enough to resist tip-sample interaction in the STM.

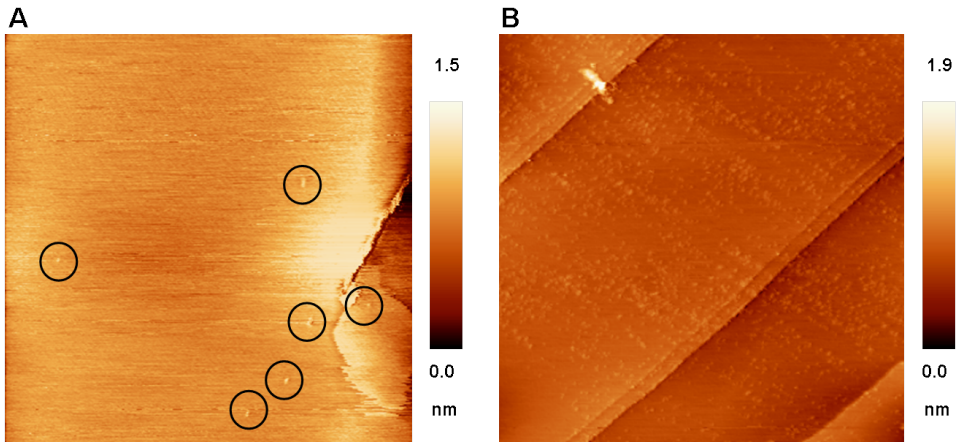

Figure 4.7. EC-STM images A) of the azurin/HOPGox and B) the azurin/4-CP/HOPG electrode showing the differences in surface coverage, both images were obtained in 10 mM PBS (pH 7), 300 nm × 300 nm).

4.1.3.3. Tip-induced Nanostructuring of Azurin Electrodes

SPM techniques are suitable tools for patterning electrode surfaces on the nanoscale. Especially, nanografting using contact mode AFM has been successfully applied e.g. for the formation of two-dimensional patterns within inorganic, organic or biological materials [161]. An increasing interest is also coming up in building biomolecular structures on surfaces via nanografting for the purpose of biosensor fabrication or investigating their electrical properties. The STM tip was used as a tool for local nanostructuring of the azurin/4-CP/HOPG electrode surface, i.e. selected azurin molecules were removed from the electrode surface. For this purpose, the tunneling current was increased in order to decrease the distance and thus, to increase the interaction between tip and electrode surface. Figure 4.8 shows the three steps of the nanostructuring procedure. First an electrode surface area was imaged under soft conditions, i.e. a small tunneling current 0.2 nA and a bias voltage of 100 mV (Fig. 4.8A). Then a selected area was scanned with a high tunneling current of 3 nA in order to remove the molecules of this area (Fig. 4.8B, 140 nm x 140 nm). The higher tunneling current (at constant bias voltage) causes the tip to approach closer to the surface. In the last step, the initially scanned surface area was imaged again and the tunneling current was readjusted to 0.2 nA. The area that was imaged with the high tunneling current (Fig. 4.8B) is clearly recognizable in Figure 4.8C, showing no immobilized protein molecules on the HOPG surface. However, so far it is not clear whether only the protein molecules were removed, i.e. the covalent binding between protein and NHS-ester was destroyed or whether also the carboxyphenyl layer was destroyed. In order to clarify this issue high resolution EC-STM images or scanning tunneling spectroscopy could be helpful.

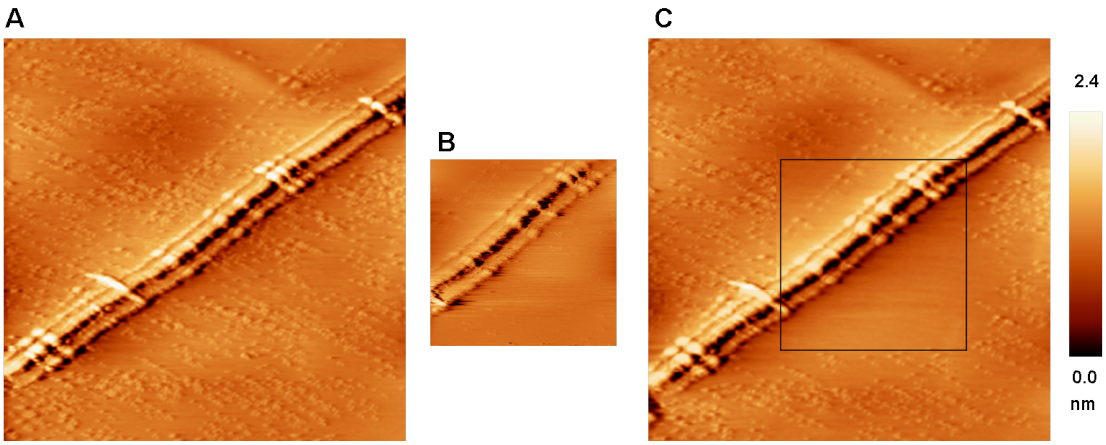

Figure 4.8. EC-STM images of azurin/4-CP/HOPG electrode A)300 nm × 300 nm before, B) 140 nm × 140 nm and C) 300 nm × 300 nm after the removal .

Preparing azurin/4-CP/HOPG electrodes with a small surface coverage (Fig. 4.9A), it was also possible to remove single protein molecules (Fig. 4.9B, indicated by the black square).

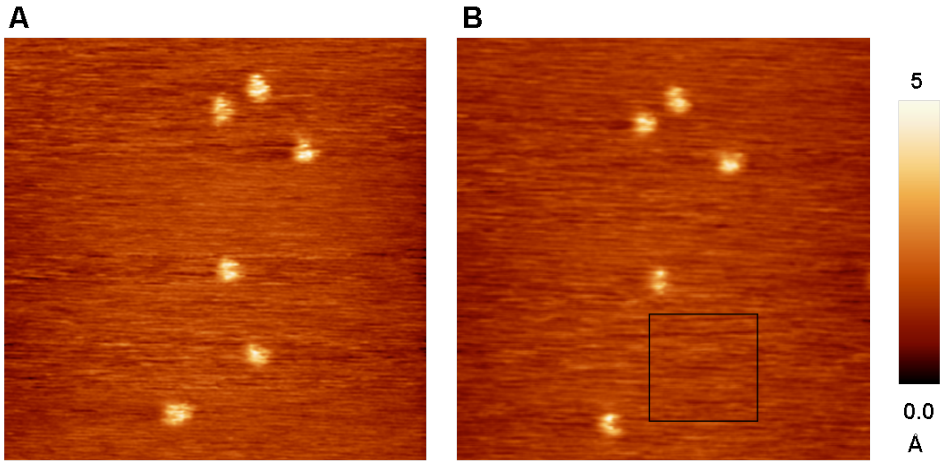

Figure 4.9. EC-STM images (25 nm × 25 nm) of azurin/4-CP/HOPG electrode A) before and B) after the removal of a single molecule using the STM tip as nanostructuring tool.

4.2. Two Ferrocene Affinity Labels for Papain-like Cysteine Proteases

Nowadays, the electrochemical investigation of biomolecules as well as electrochemical biosensing is mainly based on redox active enzymes or proteins. However, a lot of enzymes playing important roles in physiological reactions are naturally redox inactive. Among these redox inactive enzymes proteases represent a large group. Proteases are enzymes that conduct proteolysis, i.e. protein break down, by hydrolysis of the peptide bonds and are involved in reactions such as food digestion, the blood-clotting cascade, apoptosis pathways, but also in the reproductive cycle of cancer cells and infection of viruses, e.g. HIV and Hepatitis C. Understanding the reaction mechanism of these proteases and being able to design suitable inhibitors is of great interest in the field of medical and pharmaceutical research. Succeeding in adopting the affinity label concept from optical detection methods to electrochemical detection methods would open up new ways in bioelectrochemical analysis and fundamental research. This section reports the characterization of two watersoluble redox active ferrocene affinity labels (FcAL), Fe(Cp)(η-C_5H_4-CH_2-CH(NH_2)-CO-Lys-Ahx-Tyr-Leu-Epx-COOEt) (FcAL(out)) and Fe(Cp)(η-C_5H_4-CH_2-NH-CO-Epx-Leu-Tyr-Ahx-Lys) (FcAL(in)), for cysteine proteases such as papain. The FcALs were synthesized based on the motive of E-64, a well known irreversible inhibitor for papain-like cysteine protease which has been already used for fluorescent affinity labels and the optical detection of the cysteine protease papain [29]. The two FcALs differ only in the position and composition of the ferrocene moiety which is located either inside the enzyme, i.e. directly attached to its active site or outside the enzyme coupled to the N-terminus of a linker molecule. A first characterization of the labels and their binding to the enzymes was performed by mass spectrometry. The investigation of their functionality regarding electroactivity was studied by cyclic voltammetry which is a suitable tool to get started with a new system.

4.2.1. Characterization by Mass Spectrometry

Both conformations of the synthesized ferrocene affinity label Fe(Cp)(η-C_5H_4-CH_2-CH(NH_2)-CO-Lys-Ahx-Tyr-Leu-Epx-COOEt) and Fe(Cp)(η-C_5H_4-CH_2-NH-CO-Epx-Leu-Tyr-Ahx-Lys) were characterized in the Chemistry Department of the TUM by using electrospray ionization mass spectrometry (ESI MS). The mass spectrum of FcAL(out) shows a basis peak for the fragment $[M+H]^+$ with m/z = 932.3 Th (1 Thomson = 1 Da/e) and for the FcAL(in) m/z = 846.2 Th. Using TCEP, Cys-25 in the active site of the papain molecules was activated and the papain molecules were labeled with both FcALs. In order to verify a successful labeling of the cysteine protease papain with both possible FcALs matrix-assisted laser desorption/ionization time-of-flight mass spectrometry (MALDI-TOF MS) was performed. This technique is a soft ionization technique since the investigated biomolecules are embedded in a matrix and therefore, are protected from being destroyed by the direct laser beam. Figures 4.10 shows the MALDI-TOF spectra of labeled (red curve) and for comparison unlabeled (blue curve) papain molecules for both FcALs with the ferrocene group attached to the amine terminus (Fig. 4.10A) and the

carboxyl terminus (Fig. 4.10B), respectively.

Figure 4.10A shows that the binding of FcAL(out) to the papain molecule increases the molecular mass from 23430 Th to 24333 Th. The difference of 903 Th is in the range of the measured molecular weight of the FcAL itself using ESI MS (see above). As can be clearly seen in Fig.4.10B the binding of Fe(Cp)(η-C_5H_4-CH_2-NH-COt-Epx-Leu-Tyr-Ahx-Lys) to the papain molecule leads to an increase in the molecular weight from 23430 Th to 24275 Th. The mass difference of about 845 Th agrees with the molecular mass found for the FcAL itself and indicates that also the FcAL(in) is accepted in the active site of the papain molecule.

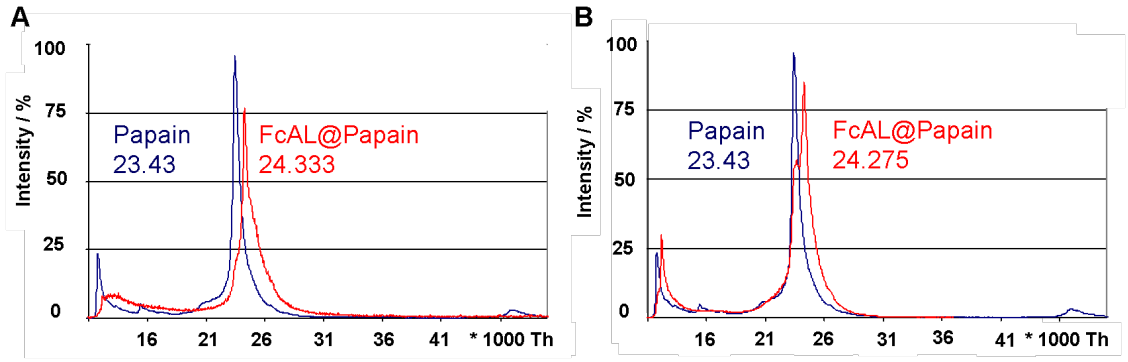

Figure 4.10. MALDI-TOF mass spectra of unlabeled (blue curve) and FcAL labeled (red curve) papain molecules A) FcAL(out) Fe(Cp)(η-C_5H_4-CH_2-$CH(NH_2)$-CO-Lys-Ahx-Tyr-Leu-Epx-COOEt) and B) FcAL(in) Fe(Cp)(η-C_5H_4-CH_2-NH-CO-Epx-Leu-Tyr-Ahx-Lys).

4.2.2. Electrochemical Behavior of the Ferrocene Affinity Labels

Both synthesized ferrocene affinity labels were investigated electrochemically by cyclic voltammetry in a three electrode arrangement with HOPG as the working electrode: 500 nM of the ferrocene affinity labels were dissolved in 50 ml 10 mM PBS (pH 7) and cyclic voltammograms between 0.2 V and 0.8 V vs. NHE were obtained at a scan rate of 100 mVs^{-1}. Figure 4.11 shows the CVs of the HOPG electrode immersed in pure 10 mM PBS (pH 7) (black line), PBS containing 500 nM of the FcAL(out) (red line) and FcAL(in) (green line), respectively.

The FcAL with the ferrocene moiety outside the molecule (Fe(Cp)(η-C_5H_4-CH_2-$CH(NH_2)$-CO-Lys-Ahx-Tyr-Leu-Epx-COOEt)) shows an irreversible redox behavior with only a distinct oxidation peak in the first sweep located at U_{ox} = 635 mV vs. NHE and an initial charge density of 3.23 μCcm^{-2}, which decreases to 0.59 μCcm^{-2} (minus 82%)in the second and 0.38 μCcm^{-2} (minus 88% compared to the first) in the third scan. However, no reduction peak could be observed. This behavior leads to the assumption that the FcAL is not stable and destroyed by the oxidation process. The FcAL with the ferrocene moiety inside the molecule (Fe(Cp)(η-C_5H_4-CH_2-NH-CO-Epx-Leu-Tyr-Ahx-Lys)) shows a reversible redox behavior with a redox potential of 613 mV vs. NHE. The charge density evaluated from the oxidation and reduction peak is

3.74 μCcm^{-2} and 3.72 μCcm^{-2}, respectively. The redox behavior is stable for several sweeps (Fig. 4.11 only shows the first three cycles) and the transferred charge within the oxidation and reduction process changes by less than 1%.

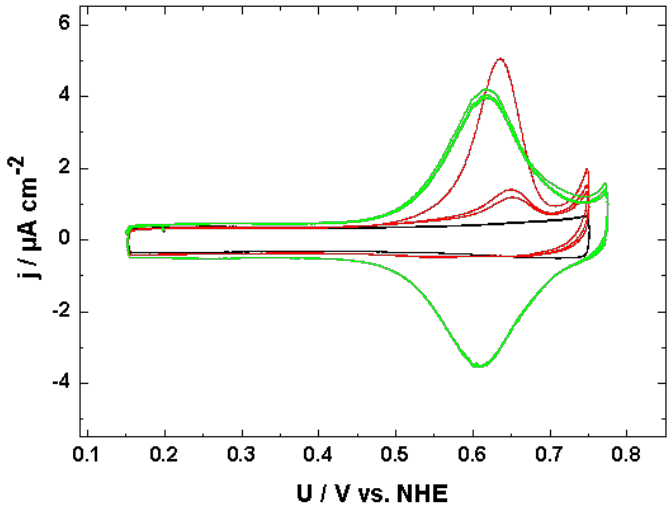

Figure 4.11. Cyclic voltammograms (100 mVs^{-1}) of HOPG in pure 10 mM PBS (black line), PBS containing 500 nM of the ferrocene affinity label with the ferrocene moiety at the N-terminus (FcAL(out), red line) and at the carboxyl terminus (FcAL(in), green line), respectively.

4.2.3. Electrochemical Behavior of Papain labeled with the Ferrocene Affinity Labels

MALDI-TOF mass spectrometry has already shown that the incubation of the activated papain molecules with both FcALs leads to an irreversible enzyme-FcAL complex (Fig. 4.10A and B). However, to prove the concept of the electroactive affinity labels, it is necessary that the inhibition of the papain by the FcAL also leads to a detectable electrochemical signal. Therefore, papain molecules unlabeled and labeled with both FcALs were adsorbed onto oxidized HOPG electrodes (0.1 mgml^{-1} enzyme PBS solution, 2 h incubation time). Their electrochemical behavior was investigated performing cyclic voltammetry in 10 mM PBS (pH 7) with a scan rate of 100 mVs^{-1}, whereas the unlabeled papain electrode serves as reference electrode. In Figure 4.12A and 4.12B the CVs obtained for the three different papain electrodes are shown. As expected, unlabeled papain adsorbed to the HOPG electrode (blue line in 4.12A and B) shows no electroactivity, whereas for papain modified with both FcALs (red line in 4.12A) and B)) a distinct redox behavior can be observed. The redox behavior of papain labeled with the FcAL where the ferrocene group is attached to the N-terminus is undefined, i.e. the oxidation and reduction peaks are very broad ranging from 0.4 to 0.65 V vs. NHE for the oxidation process and from 0.6 to 0.35 V vs. NHE for the reduction process. Therefore, the redox potential can only be roughly estimated from the midpoint between oxidation and reduction peak to around 500 mV

vs. NHE (red line in 4.12A). The Faradaic charge was determined to be 0.22 μCcm^{-2} and the surface coverage was 2.29 pMcm^{-2}. Labeled papain where the ferrocene is located in the active site results in significant redox peaks according to the electrochemical oxidation and reduction of the ferrocene group with a defined redox potential of 550 mV vs. NHE (red line in 4.12B). The mean Faradaic charge evaluated from the symmetrical redox peaks is 0.52 μCcm^{-2}, which corresponds to a surface coverage of 5.41 pMcm^{-2} assuming a one electron transfer process.

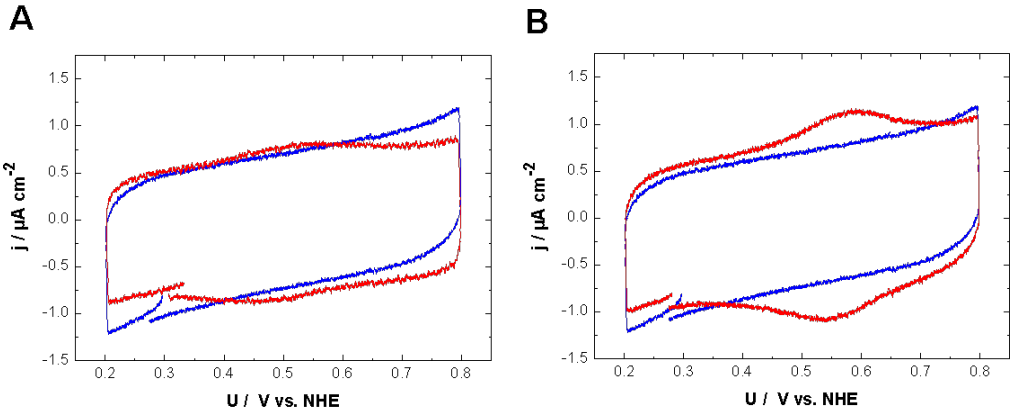

Figure 4.12. Cyclic voltammograms of unlabeled (blue line) and ferrocene labeled papain (red line) adsorbed on electrochemically oxidized HOPG in 10 mM PBS (100 mVs^{-1}). The ferrocene moiety is A) attached to the N-terminus of the AL, i.e. it is located outside the protein shell and B) attached to the carboxyl terminus of the AL, i.e. it is located in the active site of papain.

4.2.4. Validation of the Concept

Two watersoluble ferrocene affinity labels for the electrochemical detection of cysteine proteases such as papain have been synthesized. Both FcALs consists of the same affinity label which is based on the E-64 motive, the only difference in their structure is the conjugation site to which the ferrocene moiety is coupled. The FcALs as well as labeled papain were characterized via mass spectrometry and cyclic voltammetry. The results have shown that both FcAL conformations are able to successfully and irreversibly bind to the papain molecule, forming an irreversible FcAL-enzyme complex leading to an electrochemically detectable redox signal. In this respect, the proof-of-principle was provided for both synthesized FcALs. However, both FcALs and also the FcAL labeled papain molecules showed significant differences in their electrochemical behavior. For FcAL(in) a completly reversible redox behavior with well-defined redox peaks was observed, also when incorporated into the papain protein structure. On the contrary, FcAL(out) dissolved in PBS could only be oxidized once without further redox behavior, indicating that the label might be decomposed in solution or during the oxidation process. However, bound to the papain molecule the FcAL caused reversible and recognizable, but only weak and undefined redox peaks. The width of the peaks might be due to the fact that the ferrocene group is attached to the N-

terminus of the affinity label located outside the protein shell and is therefore attached to a flexible linker. Depending on the bending of the linker, the ferrocene group can be located in different positions with variable distances to the electrode surface, i.e. either completly free and exposed to the electrolyte, in contact with another enzyme or directly attached to the electrode surface (Fig. 4.13A). These different environmental conditions refer to different energy states and result in an energy dispersion and, accordingly, in broad redox peaks. For comparison, when the ferrocene group is bound to the active site in the protein pocket its position is always fixed in the same chemical surrounding. Although the enzyme itself can be oriented in different ways, the distance between the ferrocene moiety and the electrode surface does not significantly change (Fig. 4.13B).

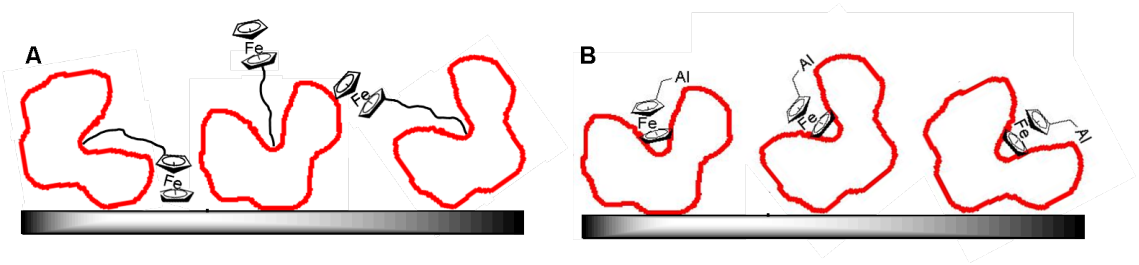

Figure 4.13. Scheme of papain orientation adsorbed on the oxidized HOPG surface and possible positions of the FcAL with respect to the electrode surface when the ferrocene group is A) attached to the N-terminus at the end of a flexible linker or B) incorporated in the active site.

Furthermore, the ferrocene moiety being located in the vicinity of the active site is similar to the structure of natural redox proteins or enzymes, where the active site in the protein pocket often contains metal species such as Fe or Cu. Therefore, FcAL@papain can be in principle considered as a redox enzyme and its electrochemical behavior when immobilized on electrode surfaces should be comparable to other enzyme electrode studies. The more promising candidate for the realization of an electroactive enzyme marker for electrochemical biosensing of papain molecules was FcAL(in) Fe(Cp)(η-C_5H_4-CH_2-NH-CO-Epx-Leu-Tyr-Ahx-Lys), and further studies were continued only with this FcAL.

4.3. Electrochemical Detection of Papain Using Fe(Cp)(η-C_5H_4-CH_2-NH-CO-Epx-Leu-Tyr-Ahx-Lys)

According to the results described in Section 4.2 the focus of the following studies rests upon the investigation of the ferrocene affinity label Fe(Cp)(η-C_5H_4-CH_2-NH-CO-Epx-Leu-Tyr-Ahx-Lys) where ferrocene methylamine is attached to the C-terminus of the affinity label and the ferrocene moiety is located directly in the active site of the papain molecule. For simplicity this ferrocene label will be in the following only named FcAL. This section is an overview of the electrochemical investigation of the FcAL and the FcAL@papain molecule adsorbed on the HOPG surface using cyclic voltammetry and EC-STM. Both immobilization techniques presented in Section 4.1 are applied in order to elucidate the more promising electrode architecture not only for electrochemical measurements, but also for investigations by SPM. Furthermore, the electrode characterization includes electron transfer studies and also the in-situ visualization of the labeling process. Thereby, EC-STM is used to investigate the structure-function relation of the FcAL and the papain molecules down to a single molecule level. Finally, it is shown that the electrochemical detection of the binding process can be used to study the enzymatic activity of the papain molecules in the presence and absence of inhibitors which is very important for possible future applications in electrochemical biosensors.

4.3.1. Electrochemical Characterization

4.3.1.1. Fe(Cp)(η-C_5H_4-CH_2-NH-CO-Epx-Leu-Tyr-Ahx-Lys)

The electrochemical behavior of the FcAL Fe(Cp)(η-C_5H_4-CH_2-NH-CO-Epx-Leu-Tyr-Ahx-Lys) was studied under different conditions: dissolved in 10 mM PBS (pH 7), adsorbed to an oxidized HOPG surface (FcAL/HOPGox) and covalently immobilized on carboxyphenyl modified HOPG (FcAL/4-CP/HOPG) (Fig. 4.14A). Cyclic voltammetry was performed in 10 mM PBS (pH 7) with a scan rate of 100 mVs^{-1}. The CVs of the three systems (see color coding in Fig. 4.14A) show a reversible redox behavior, as can be seen in Figure 4.14B, however, the redox potentials and the peak maxima are different.

For FcAL in solution a redox potential of 619 mV vs. NHE and a peak potential difference of 0 mV was found. The Faradaic charge of the redox peaks was calculated to 5.33 μCcm^{-2} (Fig. 4.14B, black curve). Usually, for a redox species in solution that undergoes a single electron transfer reaction with the electrode surface, a redox peak shift of 60 mV is expected due to diffusion. Since no potential shift between the oxidation and the reduction peak is visible for the FcAL dissolved in the PBS, it is assumed that the FcAL immediately adsorbs to the electrode surface when injected into the electrolyte and thus behave like adsorbed species. For the FcAL/HOPGox electrode the redox potential was 610 mV and the Faradaic charge was calculated to be 4.23 μCcm^{-2}, which corresponds to a surface coverage of 43.8 $pMcm^{-2}$ (red curve). For the FcAL/4-CP/HOPG electrode the redox potential was significantly lower, 545 mV vs. NHE with a Faradaic charge of 8.57 μCcm^{-2}, which corresponds to a surface coverage of 88.9 $pMcm^{-2}$ (green curve). These results show that the amount of electrochemically active FcAL that is in electronic

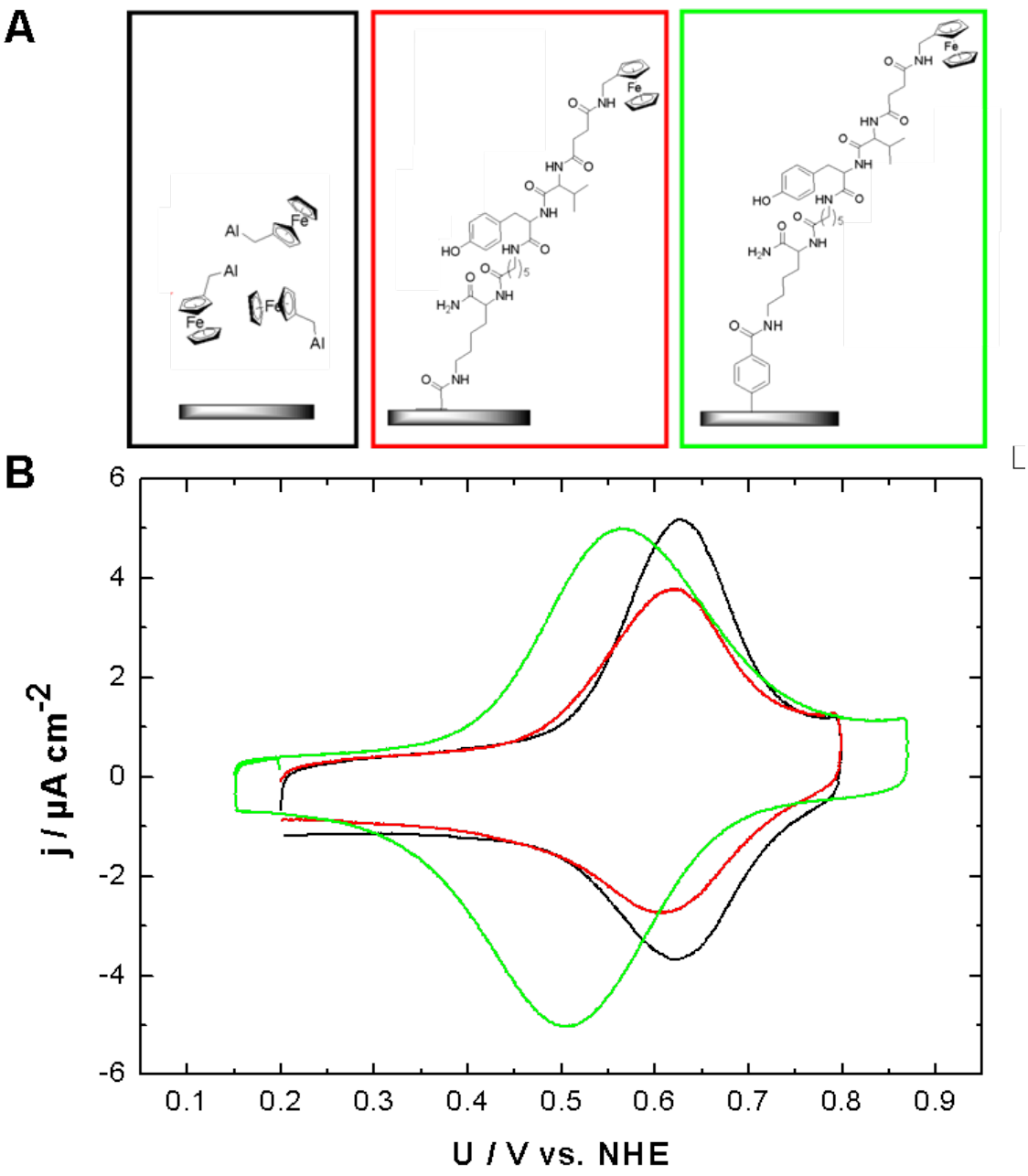

Figure 4.14. A) Schematic views and B) CVs of FcAL in solution (2 μM, black curve), preadsorbed on oxidized HOPG (red curve) and covalently immobilized on HOPG (green curve) measured in 10 mM PBS (pH 7) and at a scan rate of 100 mVs^{-1}.

contact with the electrode surface is by a factor of 2 higher for the covalent immobilization than for the adsorption. However, assuming a complete monolayer of carboxyphenyl groups with a surface coverage of 1.35 nMcm^{-2} on the HOPG surface, only 7% of the surface is covered by FcAL. Furthermore, the FcAL/4-CP/HOPG electrode shows a peak separation of approximately 60 mV (see green curve in Fig. 4.14B). In order to check whether the FcAL was really tightly bound to the carboxyphenyl groups on the HOPG surface, cyclic voltammetry with different scan rates was performed. Figure 4.15A shows the cyclic voltammograms of the FcAL/4-CP/HOPG electrode in 10 mM PBS (pH 7) at scan rates between 10 mVs^{-1} and 100 mVs^{-1}.

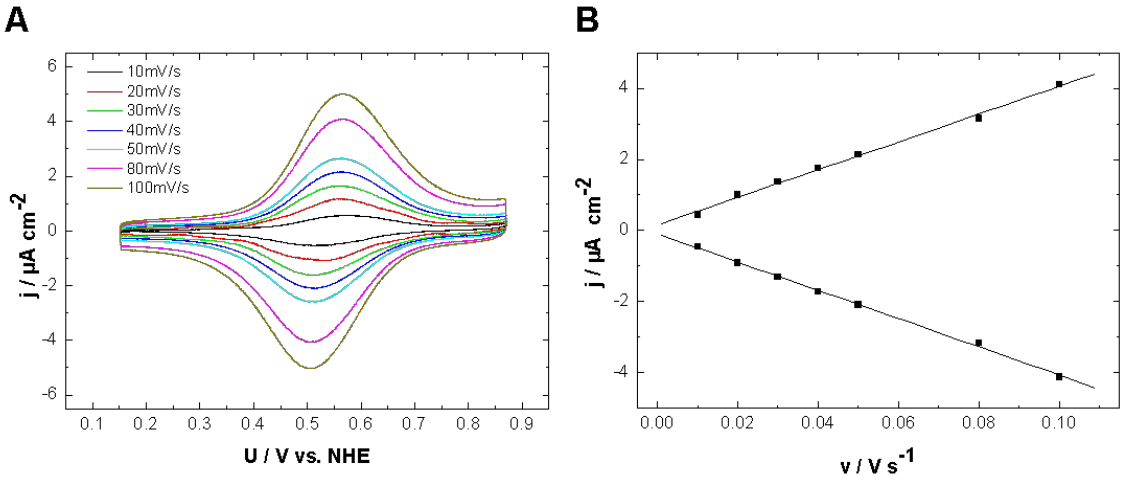

Figure 4.15. A) CVs of FcAL covalently immobilized on HOPG in 10 mM PBS (pH 7) obtained at scan rates between 10 mVs^{-1} and 100 mVs^{-1}, B) Peak current density of the oxidation and the reduction peak plotted versus the scan rate.

The peak current density of the oxidation and the reduction peak increases linearly with increasing scan rate, indicating that the FcAL is surface bound (Fig. 4.15B). The solid lines represent the linear fit to the measured values. However, applying scan rates higher than 300 mVs^{-1}, the linear dependence between peak current density and scan rate becomes more and more diffusion controlled, i.e. the peak current density gets constrained to the square root of the scan rate. The black lines in Fig. 4.16A represent the fit to the measured values. The anodic peak potentials could be fitted by $v^{0.65}$ and the cathodic peak potentials by $v^{0.63}$. Furthermore, the peak potentials of the oxidation and the reduction peak shift to more positive and more negative potential values, respectively. Plotting the peak potentials versus the logarithm of the scan rate yields the so called trumpet plots (Fig. 4.16B), which show that the oxidative and the reductive peaks separate as the scan rate increases and the reversibility of the reaction declines. From the peak separation $\triangle U_P = U_{AP} - U_{CP}$ plotted versus the scan rate, the apparent interfacial electron transfer rate constant k_{app} was calculated to 4.65 s^{-1} according to the Butler-Volmer model developed by Laviron for electron transfer between an electrode and a redox active film [73].

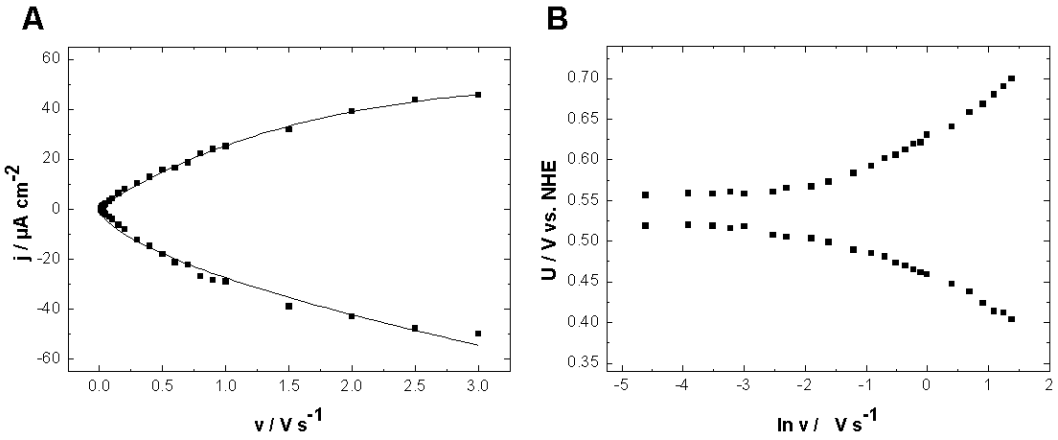

Figure 4.16. A) Peak current densities of the oxidation and the reduction peak in dependence of the CV scan rates between 10 mVs^{-1} and 3 Vs^{-1}, B) Trumpet Plot: Potential of the oxidation and the reduction peak plotted versus the logarithm of the scan rate.

Liu et al. [50] performed similar experiments: they coupled ferrocenemethylamine directly to a 4-CP monolayer on glassy carbon (GC) (Fig. 4.17) and investigated the electrodes in aqueous phosphate buffer solution (50 mM, pH 7) via cyclic voltammetry. The CVs they obtained also showed non-ideal behavior with regards to peak separation (79 mV) at slow scan rates. This behavior was attributed to the ferrocene molecules being located in a range of environments with a range of formal electrode potentials U_0. Formal potential dispersion is often cited as a potential cause for the peak broadening. They found a surface coverage of 73 $pMcm^{-2}$ which is similar to the detected FcAL amount on the FcAL/4-CP/HOPG electrode. Using the Butler-Volmer model and the Marcus theory for electron transfer [231–233], the interfacial electron transfer k_{app} was determined to 17 s^{-1}, which is by a factor of 3.7 higher than the rate constant observed for the FcAL. However, assuming an electrode configuration as shown in Figure 4.14 (green box) the lower rate constant can be explained by a larger distance between electrode and the ferrocene group, since the rate of electron transfer decays exponentially with distance [65].

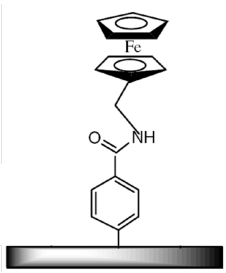

Figure 4.17. Ferrocenemethylamine coupled to a 4-CP/CG electrode, taken from [50].

4.3.1.2. Prelabeled Papain adsorbed on HOPG

The electrochemical behavior of prelabeled FcAL@papain adsorbed on the HOPG electrode surface was also studied using cyclic voltammetry. For this purpose, both immobilization techniques, the oxidation of the HOPG surface and the functionalization using 4-carboxyphenyl groups were investigated (Scheme in Fig. 4.18A). Figure 4.18B shows the CVs of the FcAL@papain/HOPGox (black line) and FcAL@papain/4-CP/HOPG (red and green line) electrodes obtained in 10 mM PBS (pH 7) with a scan rate of 100 mVs^{-1}.

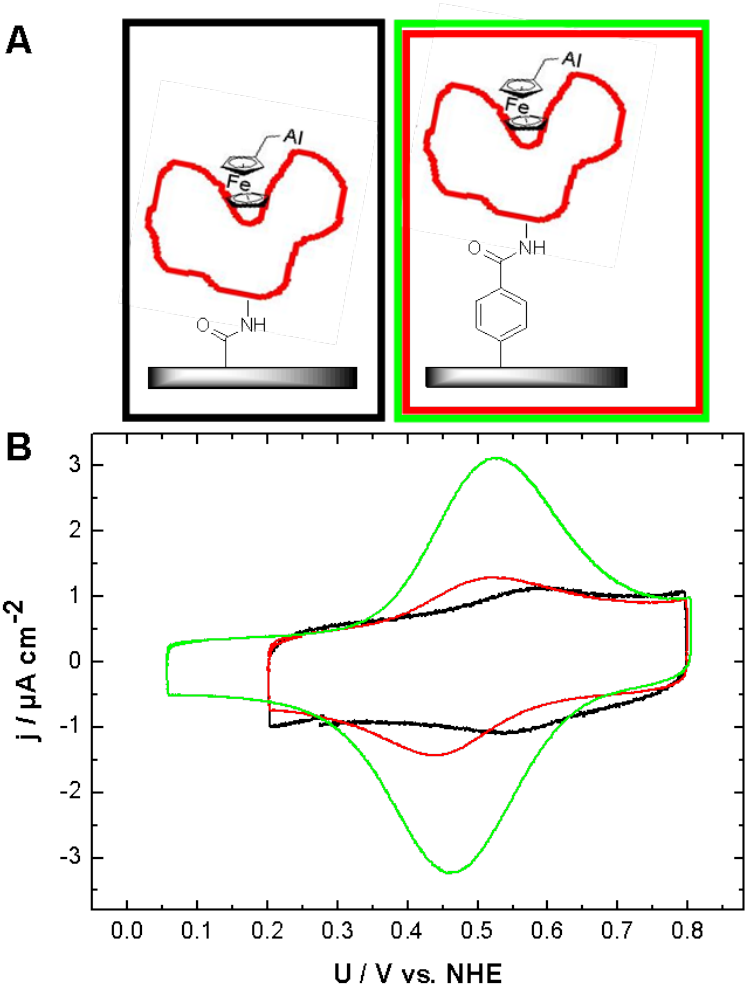

Figure 4.18. A) Schemes and B) CVs of FcAL@papain preadsorbed on oxidized HOPG (black curve) and covalently immobilized on HOPG (red and green curve) measured in 10 mM PBS (pH 7) obtained at a scan rate of 100 mVs^{-1}.

The black and red curves were obtained for electrodes which were incubated in an enzyme solution containing 0.1 $mgml^{-1}$ FcAL@papain, the green curve for an electrode incubated in a solution containing 1 $mgml^{-1}$ FcAL@papain. All electrodes showed a reversible redox behavior

with distinct oxidation and reduction peaks. For the FcAL@papain/HOPGox electrode, a redox potential of 555 mV vs. NHE was found, the Faradaic charge was 0.49 μCcm^{-2}, corresponding to a surface coverage of 5.1 pMcm^{-2} (Fig. 4.18, black curve). For both FcAL@papain/4-CP/HOPG electrodes the redox potential was significantly lower, 490 mV vs. NHE, the Faradaic charge was 0.99 μCcm^{-2}, which corresponds to a surface coverage of 10 pMcm^{-2} (red curve) and 4.0 μCcm^{-2} corresponding to a surface coverage of 42 pMcm^{-2} (green curve). Assuming an average protein diameter of 35 Å and a hexagonal closely packed papain layer on the 4-CP/HOPG surface, a monolayer would refer to a surface coverage of 17.32 pMcm^{-2} and a charge density of 1.67 μCcm^{-2}. This means that on the oxidized HOPG surface one can obtain approximately 29% of a monolayer, on the 4-CP/HOPG depending on the concentration of the enzyme solution between 59% of a monolayer and more than two monolayers. However, one has to keep in mind that the detected charge was only referred to the geometric area. Although HOPG possesses an atomically smooth surface the active area might be slightly larger than the geometric area. Therefore, surface coverages might be systematically overestimated. Furthermore, using an enzyme solution with a concentration of 1 mgml^{-1} might lead to protein agglomeration in solution and also on the electrode surface, resulting in slightly higher charge densities.

From electrochemical bulk measurements so far we know that the ferrocene moiety in the FcAL Fe(Cp)(η-C_5H_4-CH_2-NH-CO-Epx-Leu-Tyr-Ahx-Lys) has different redox potentials depending on whether it is adsorbed or covalently immobilized to an HOPG surface and also whether it is bound to papain molecules, which themselves can be bound in different ways to the electrode surface. In Table 4.2 all redox potentials of the FcAL and FcAL@papain found for different conditions are listed. Additionally, the redox potentials of ferrocene and different ferrocene derivatives are given.

Redox System	**U_0 / mV vs. NHE**
Ferrocene, according to [140]	400
Ferrocene monocarboxylic acid in solution	550
Ferrocenylalanine in solution	480
FcAL in solution	619
Ferrocenemethylamine/4-CP/GC [50]	464
FcAL/HOPGox	610
FcAL/4-CP/HOPG	545
FcAL@Papain/HOPGox	555
FcAL@Papain/4-CP/HOPG	490

Table 4.2. Redox potentials of ferrocene derivatives and the FcAL in different conformations, when not other stated obtained in 10 mM PBS (pH 7).

Table 4.2 shows that the immobilization of FcAL or FcAL@papain by covalent binding to the 4-carboxypenhyl layer resulted in a redox potential shift of 65 mV to more negative potentials compared to chemisorption onto oxidized HOPG.

4.3.1.3. In-situ Labeling

From Table 4.2 it is obvious that significant differences in the redox potentials exist depending on the state of the FcAL, i.e. whether it is immobilized on the surface or bound to the enzyme. Therefore, the question arises whether it is possible to electrochemically detect the labeling of FcAL to the activated papain. In order to study this issue, 500 nM FcAL Fe(Cp)(η-C_5H_4-CH_2-NH-CO-Epx-Leu-Tyr-Ahx-Lys) was dissolved in 10 mM phosphate buffer (pH 7). The cyclic voltammetry performed at the bare HOPG surface with a scan rate of 100 mVs^{-1} shows the already well known electrochemical behavior of the FcAL with a redox potential of 617 mV vs. NHE (Fig. 4.19, black line). Then, activated papain molecules were added. The papain concentration was increased stepwise from 10 nM to a final concentration of 200 nM (Fig. 4.19 from the red to the purple curve). With increasing papain concentration the peak current density decreased from 4.3 μAcm^{-2} to 1.28 μAcm^{-2}. Furthermore, with increasing papain concentration the redox potential shifted towards more negative potentials.

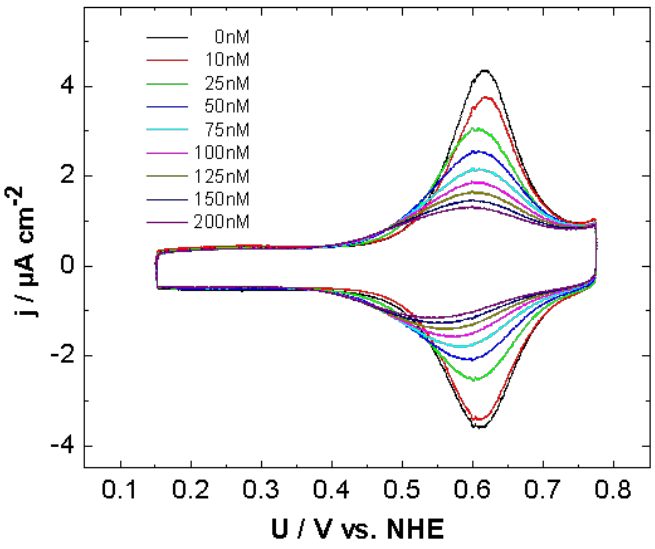

Figure 4.19. CVs of 500 nM FcAL and increasing concentration of activated Papain molecules (10 nM to 200 nM) in solution, obtained at 100 mVs^{-1}.

This potential shift is illustrated in Fig. 4.20 by plotting U_0 vs. NHE as a function of the papain concentration in solution. A nearly linear relationship between enzyme concentration and potential shift can be observed. Starting at 617 mV vs. NHE, which is the redox potential for the FcAL (Fig. 4.20B), i.e. 0 nM papain, U_0 decreases towards 565 mV vs. NHE for 200 nM papain in solution. That means U_0 converges towards the redox potential of prelabeled papain chemisorbed on HOPG (see Fig. 4.20C) which was already found and described in Section 4.2.3.

As already mentioned above, the CV of the FcAL in solution shows no peak shift of 60 mV typical for a one electron tranfer process where the redox species is in solution. Therefore, we

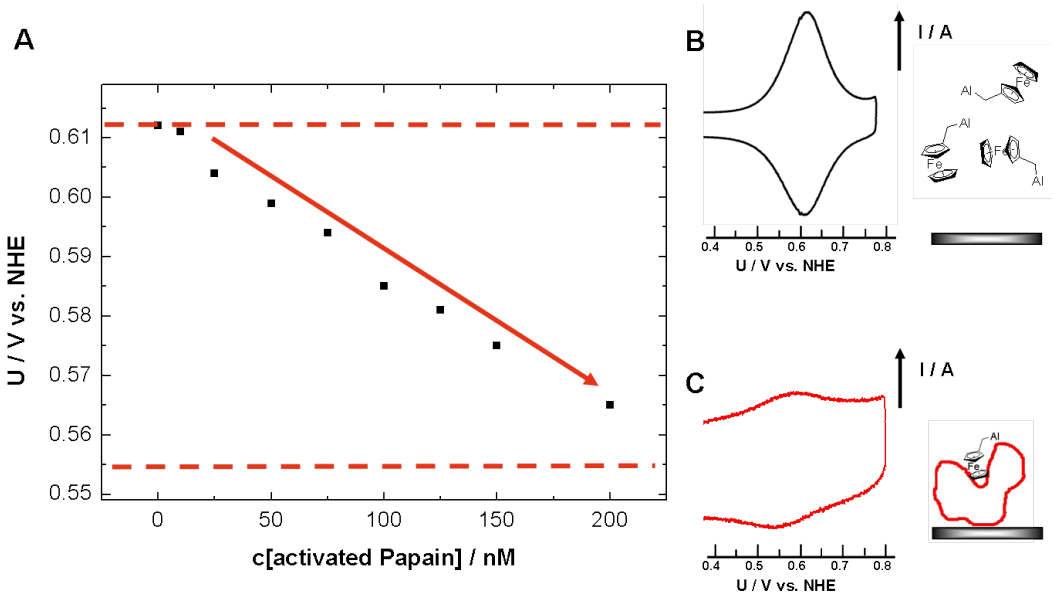

Figure 4.20. A) Measured redox potential U_0 in dependence of the concentration of activated papain in solution. B) CV of FcAL in solution. C) CV of FcAL@papain chemisorbed on HOPG.

assume that the dissolved FcAL immediately adsorbs to the HOPG surface. When the activated papain is added to the electrolyte, the FcAL desorbs from the surface and reacts with the active site of the papain due to the high affinity forming the irreversible FcAL@papain complex. This complex then might adsorb to the HOPG surface and the measured potential is equal to the redox potential of FcAL@papain/HOPG. That means that the now ferrocene labeled enzymes displace the adsorbed FcAL on the electrode surface, i.e. the charge density decreases due to the fact that the papain molecules are larger than the FcAL resulting in the decay of the peak current density. Compared to the free FcAL an inhibited electron transfer between the ferrocene group of FcAL@papain and the electrode can also not be excluded.

Furthermore, to verify the detection of the in-situ labeling process (shown in Fig. 4.19) another experiment with modified initial conditions was performed. Therefore, the FcAL was immobilized onto a 4-CP/HOPG electrode surface and investigated using cyclic voltammetry (100 mVs^{-1}). As already observed earlier, the CV shows a redox behavior with a redox potential of 550 mV vs. NHE (Fig. 4.21, black curve). Then activated papain molecules were added to the electrolyte and CVs were recorded continuously. Immediately after the injection, the CV shows no significant difference compared to the FcAL/4-CP/HOPG electrode, however, after ten minutes the peak current density decreased by more than 15% from 4.76 μAcm^{-2} to 3.85 μAcm^{-2} (Fig. 4.21, outer red curve). The red curves were obtained in time intervalls of 10 minutes up to 1 h after adding the papain molecules, the green curve was recorded after 2 h, the blue curve after 5 h, the turquoise curve after 10 h and the magenta curve after 15 h, respectively. After 15 h the peak current density decreased to 1.69 $\mu A\ cm^{-2}$ and the redox potential shifted to a more positive

value of 565 mV vs. NHE. Considering that the FcAL molecules are tightly bound to the 4-CP/HOPG surface they are not able to release the surface in order to bind to the active site of the dissolved enzymes. Therefore, the activated papain molecules can only simply adsorb on top of the FcAL layer blocking the access of the electrolyte to the FcAL. As a result the current density decreases, the peak potentials shifts and the redox potential increases due to a higher required overpotential. The peak potential separation of 60 mV might now be attributed to diffusion controlled processes, e.g. diffusion of the electrolyte through the enzyme overlayer to the redox active FcAL on the electrode surface.

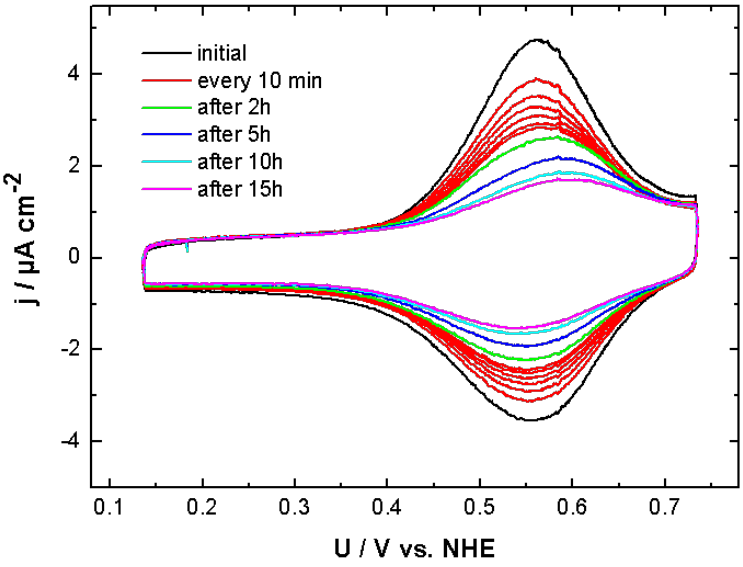

Figure 4.21. CVs of FcAL/4-CP/HOPG electrode obtained in 10 mM PBS (pH 7) containing activated papain.

4.3.2. Nanoscale Read-out by EC-STM

Electrochemical properties investigated by bulk measurement techniques such as cyclic voltammetry display only an average over the whole active area of the electrode surface. However, EC-STM allows to study electrodes on the nanoscale and probe single molecules under full potential control. The first experimental EC-STM study of electron tunneling via a redox active molecule was performed by Tao [36], who investigated the electron transfer through Fe(III)-protoporphyrin (FePP) compared to a reference sample protoporphyrin(PP), both adsorbed on HOPG. When the substrate potential was held near the redox potential of FePP (-0.24 V vs. NHE) the molecular species containing Fe appeared brighter than the reference. This imaging contrast depending on the substrate potential was due to the redox level made available by the Fe ion. This section shows that this technique can also be applied for papain and FcAL@papain molecules. In order to elucidate the electron transport through ferrocene labeled and unlabeled

papain molecules down to a single enzyme level, in-situ EC-STM and scanning tunneling spectroscopy (STS) were performed.

4.3.2.1. Single Labeled Papain Molecules

FcAL@papain was covalently immobilized on 4-CP modified HOPG using EDC/NHS coupling and investigated with different modes of the EC-STM. All EC-STM experiments were performed in 10 mM phosphate buffer solution (PBS, pH 7).

Constant Current Mode EC-STM

Constant current mode EC-STM was performed applying a constant tunneling current of I_T= 0.2 nA and a bias voltage of U_{Bias} = 100 mV. The initial substrate potential was set to U_S = 490 mV vs. NHE equal to the redox potential U_0 of the FcAL@papain/4-CP/HOPG electrode (see Table 4.2). Figure 4.22 shows typical EC-STM images of papain/4-CP/HOPG (Fig. 4.22A) and FcAL@papain/4-CP/HOPG (Fig. 4.22B) electrode surfaces.

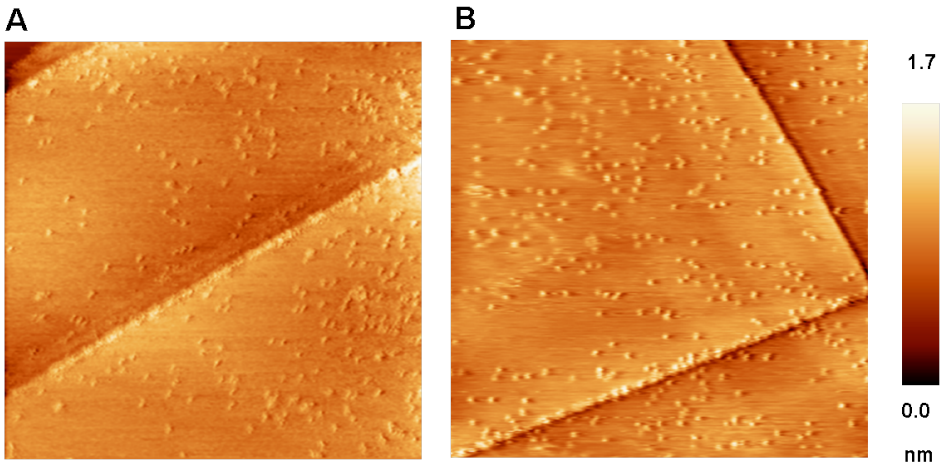

Figure 4.22. In-situ EC-STM images of A) papain/4-CP/HOPG and B) FcAL@papain/4-CP/HOPG electrode surface, obtained in constant current mode (I_T = 0.2nA) in 10 mM PBS (pH 7) at a substrate potential U_S = U_0 = 490 mV vs. NHE (150 nm x 150 nm).

From line scan analysis of several molecules (> 20), the average size of the enzymes observed in EC-STM was measured to be (30 × 23 × 2.3) Å^3 for papain/4-CP/HOPG and (31 × 25 × 6.1) Å^3 for FcAL@papain/4-CP/HOPG, which is significantly smaller than the crystallographic data of papain. However, one has to keep in mind that STM images always show a convolution of the surface topography and its electronic properties, such as conductivity, apart from further possible tip induced image artefacts. Therefore, in STM experiments the electron transfer pathway is a crucial point for mapping the topography of protein structures. If only the amide skeleton is involved in the tunneling process and not all the sidechains, the enzyme appears smaller in the STM image than it is in reality [234]. An inhibited electron transfer between the STM tip and

the electrode also impairs the resolution of the protein structure, as could be observed in the combined EC-STM/SECPM study of HRP/HOPGox electrodes in Section 4.4. Another point that might be responsible for the mismatch of apparent morphology and crystallographic data is the fact that STMs are normally calibrated against a monoatomically high Au(111) step in z-direction and against the atomic structure of HOPG in x-y-direction, not against a protein calibration standard which would be more suitable due to the different conductivity. However such calibration standards are not available. Therefore, absolute values should not be overrated. Measured dimensions only describe the apparent topography, which is a convolution of electronic and morphological properties. The reason for the difference in the average apparent height of labeled and unlabeled papain molecules will be discussed in more detail in the following sections.

In order to study the potential dependence of the apparent morphology of the ferrocene-labeled papain molecules, two single enzyme molecules were imaged for different applied substrate potentials. STM imaging started with the substrate potential set to the equilibrium redox potential of FcAL@papain/4-CP/HOPG, i.e. at $U_S = U_0 = 490$ mV vs. NHE. During continous imaging ($I_T = 0.2$ nA, $U_{Bias} = 100$ mV) the substrate potential and simultaneously the tip potential to keep the bias voltage constant were changed in steps of 50 mV towards either more positive or more negative values, i.e. the absolute value of the overpotential $|\eta| = |U_S - U_0|$ with respect to the redox potential was increased. As a result, a series of EC-STM images has been acquired at different overpotentials, which are presented in Figure 4.23. For substrate potentials close to the redox potential (Fig. 4.23A) the STM image has the highest image contrast as compared to STM images obtained at different overpotentials, indicating that the tunneling current through the FcAl@papain and thus its conductivity is strongly enhanced for $U_S = U_0 = 490$ mV vs. NHE. With increasing overpotential the image contrast is decreasing independent whether the substrate potential is more positive or more negative than the redox potential (Fig. 4.23B-J).

From the evaluation of the apparent height of the FcAL@papain molecules Figure 4.24 is derived. According to the image contrast, the apparent height of both FcAL@papain molecules was highest at the redox potential with an apparent height of 7 Å relative to the HOPG surface. With increasing overpotentials, positive and negative, the apparent height decreased to 2.8 Å for η = -200 mV (Fig. 4.23E) and to 2.4 Å for η = +400 mV (Fig. 4.23J). When the redox potential (Fig. 4.23A) is restored, the molecules reappeared with the same image contrast and thus, with the same apparent height of 7 Å, illustrating the reversibility of the effect. Within this experiment all experimental parameters other than substrate and tip potentials remained unchanged.

The same potential-dependent experiment was performed for unlabeled papain covalently immobilized on HOPG (Fig. 4.25). The experimental parameters; $U_{Bias} = 100$ mV and $I_T = 0.2$ nA, were exactly the same as mentioned above. EC-STM images were first obtained at a substrate potential of 490 mV vs. NHE, which is equal to the redox potential of the FcAL@papain/4-CP/HOPG electrode (see Fig. 4.25B). Then images were recorded for different overpotentials in 50 mV steps. Figure 4.25 A) and C) representatively show images obtained at overpotentials of -200 mV (A) and 200 mV (C). Over the whole potential range that was investigated, no change in the image contrast was visible. The analysis of the apparent height of 54 papain molecules

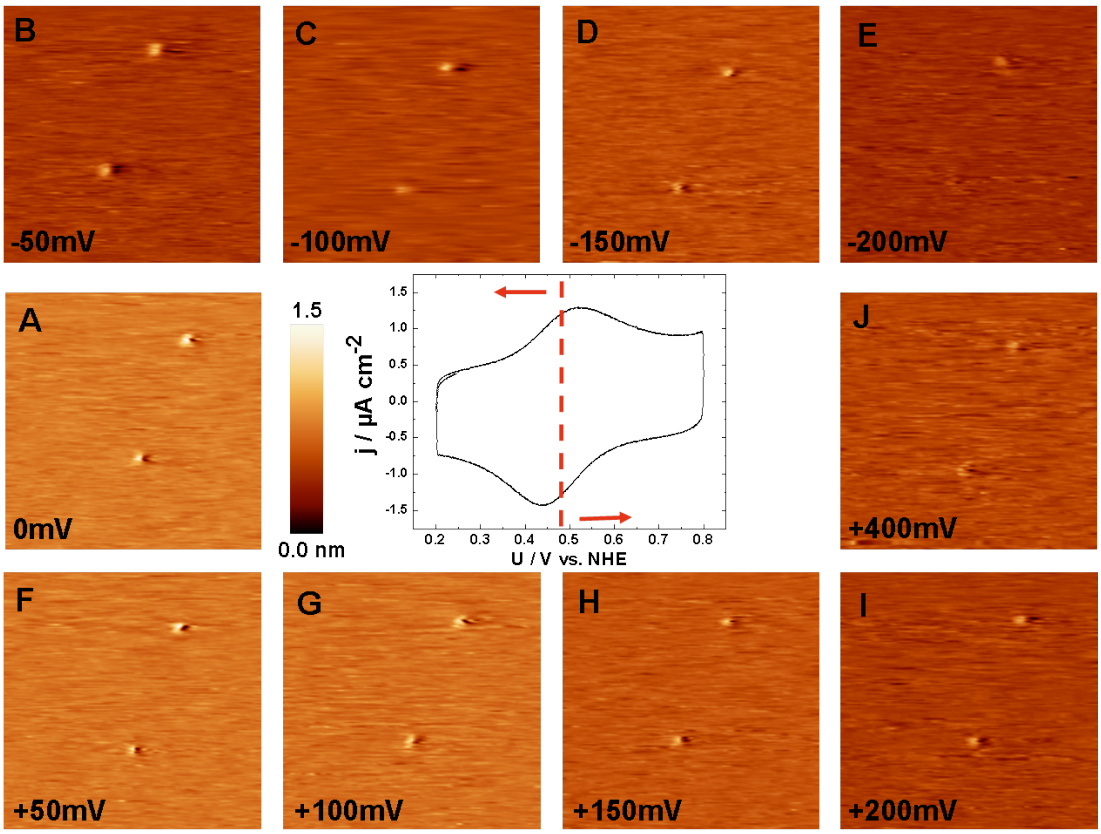

Figure 4.23. Series of EC-STM images (35 nm x 35 nm) of FcAL labeled papain covalently immobilized on 4-carboxyphenyl modified HOPG obtained in constant current mode (I_T = 0.2nA, U_{Bias} = 100mV) at different overpotentials η starting at U_0 = 490 mV vs. NHE, i.e. η =0 (A). The overpotential is stated in the images. The inset shows the CV of the FcAL@papain/4-CP/HOPG electrode obtained in 10 mM PBS (pH 7) at a scan rate of 100 mVs^{-1}.

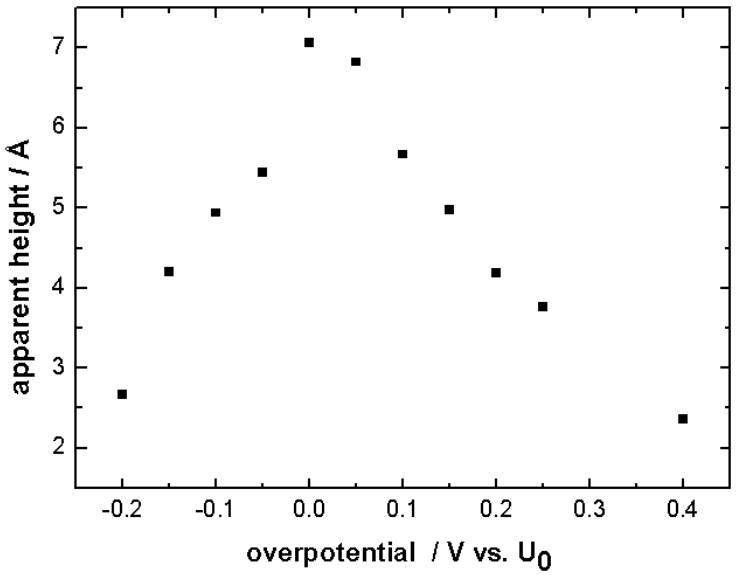

Figure 4.24. Apparent height of the ferrocene-labeled papain molecules shown in Fig. 4.23 in dependence of the applied overpotential $\eta = U_S - U_0$.

yielded an average apparent height of (2.3 ± 0.3) Å independent of the applied substrate potential (dashed line in Fig. 4.25D). The open circles in Figure 4.25D represent the average apparent height of the molecules shown in Figure 4.25A - C.

Constant Height Mode EC-STM

The FcAL@papain/4-CP/HOPG electrode surface was investigated also in constant height mode EC-STM in order to achieve direct access to the tunneling current that is flowing without feedback control. The current response coming from the labeled molecules was mapped in dependence of the applied substrate potential in 10 mM PBS (pH 7). The tip was approached to a setpoint current of 0.2 nA inside the tunneling range at a constant bias voltage of 100 mV. The feedback loop was then switched off and the surface area was scanned continuously and relatively fast with a frequency of 30 Hz to minimize lateral and vertical drift. The initial potential applied to the substrate was equal to the equilibrium redox potential of FcAL@papain/4-CP/HOPG, i.e. $U_S = U_0 = 490$ mV vs. NHE (Fig. 4.26). The surface area of 20 nm x 20 nm shows the tunneling current flowing through four FcAL@papain molecules (Fig. 4.26A) with a maximum current of 100 pA, as can be seen in the line scan in Figure 4.26B. The same surface area was scanned with unchanged parameters several times to assure that the system is running stable although the feedback is switched off.

Only when reproducible images were obtained an overpotential was applied to the HOPG electrode. Within continous imaging, tip and substrate potential were carefully adjusted in order to keep the bias voltage constant. In constant height mode it is essential that both potentials are

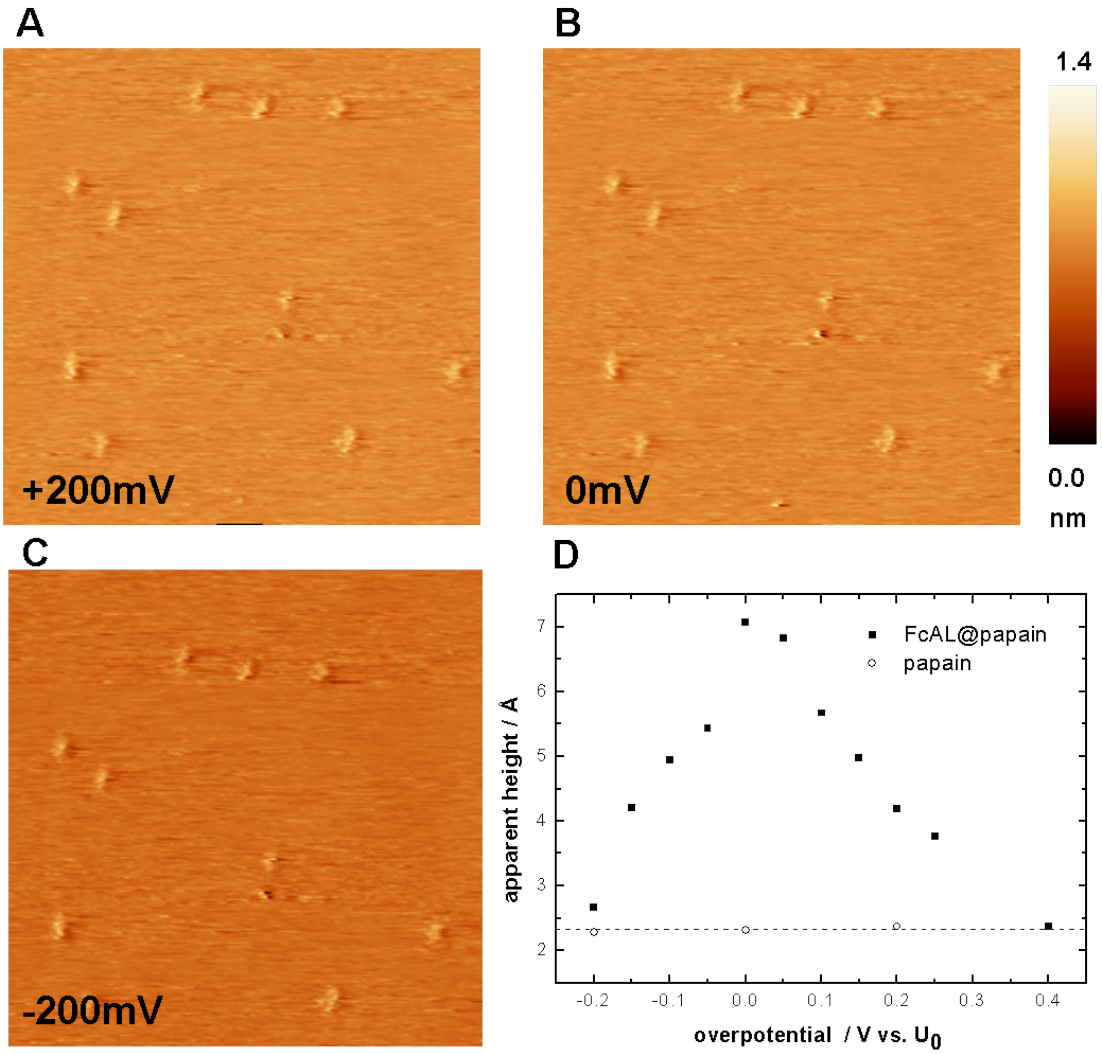

Figure 4.25. EC-STM images of unlabeled papain molecules obtained in constant current mode at different applied substrate potentials (45 nm x 45 nm). The overpotentials given here are stated with respect to the redox potential of FcAL@papain/4-CP/HOPG, i.e. the substrate potentials are U_S = A) 290 mV vs. NHE, B) 490 mV vs. NHE and C) 690 mV vs. NHE. D) Fig. 4.24 supplemented with the apparent height found for unlabeled papain molecules at different applied substrate potentials (dashed line).

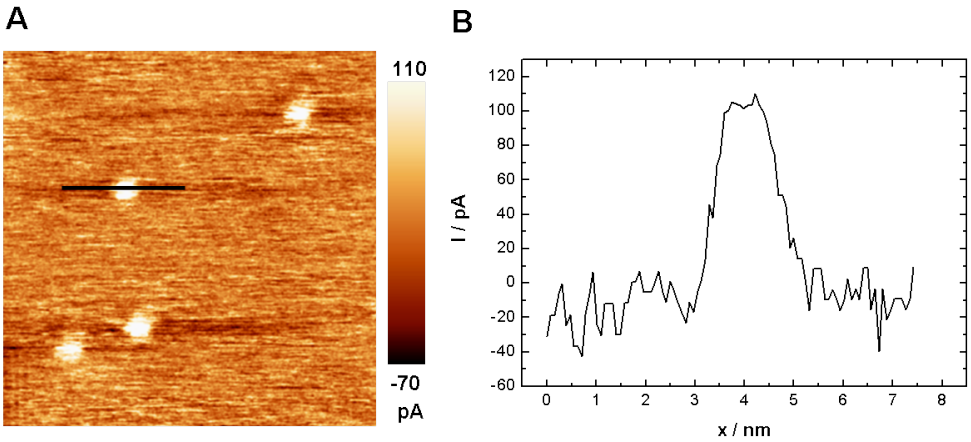

Figure 4.26. A) (20 nm × 20 nm) EC-STM image of FcAL@papain/4-CP/HOPG obtained in constant height mode at $U_S = U_0$= 490 mV vs. NHE showing four FcAL@papain molecules. B) Line scan of the tunneling current through a single labeled molecule (indicated by the black line in 4.26A) yielding a maximum current of 100 pA.

changed simultaneously since the tip, while scanning without feedback control, might react to already small parameter changes by crashing into the substrate or leaving the tunneling regime. In those cases the experiment had to be aborted.

The potential-dependent EC-STM images of the series shown in Figure 4.27 were recorded one after the other, the scan direction is represented by the arrow in the upper or lower right corner. Starting with the scan shown in Figure 4.26A (equal to 4.27A), $U_S = U_0 = 490$ mV vs. NHE, an overpotential of η = -200 mV (U_S = 290 mV vs. NHE) was applied to the substrate potential while imaging Fig. 4.27B. The dashed line indicates the simultaneous change of U_S and U_{Tip}, keeping the bias U_{Bias} = 100 mV constant. The overpotential immediately induces a decrease in the tunneling current through the FcAL@papain molecules; both molecules in the upper part of the image were "switched off", i.e. they disappear in the constant height STM image. Holding the potentials the (20 nm x 20 nm) surface area was imaged subsequently in Figure 4.27C showing no molecules. When the substrate potential was readjusted to U_S = 490 mV vs. NHE the molecules were "switched on" again, i.e. they reappear (Fig. 4.27D). The effect was reproducible several times (Fig. 4.27E + F). The slight differences in image contrast before and after changing the working electrode potential to 0.29 V vs. NHE (compare Fig. 4.27A and Fig. 4.27F) might be, in spite of the fast scanning, due to a small vertical drift of the STM piezos.

As already mentioned, constant height mode EC-STM is extremely sensitive to parameter changes. Therefore, it was not possible to perform this experiment for the whole range of overpotentials shown in Figure 4.23.

Scanning Tunneling Spectroscopy

In order to quantitativly assess the current response depending on the applied substrate potential

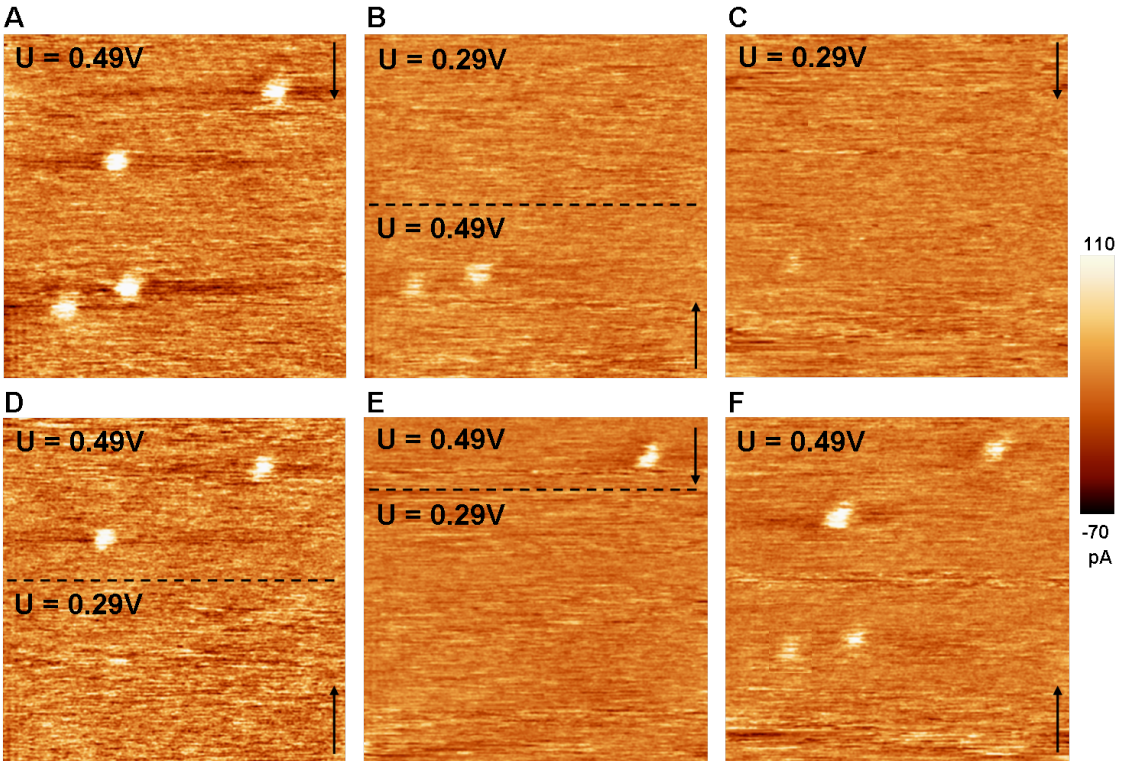

Figure 4.27. Series of EC-STM images in constant height mode obtained at two different applied substrate electrode potentials (20 nm × 20 nm).

scanning tunneling spectroscopy (STS) measurements were performed on single FcAL@papain molecules. STS directly yields the tunneling current as a function of the applied bias voltage and overpotential. For this experiment the enzyme surface coverage was chosen to be relatively low, so that the average distance between the papain molecules on the surface is large and the interaction between single papain molecules could be neglected. After having modified the HOPG electrode surface with an activated NHS-ester the electrode was incubated over night at 4 °C in a 10 mM PBS (pH 8) enzyme solution containing only 0.1 mgml^{-1} papain. The FcAL@papain/4-CP/HOPG electrode surface was characterized via constant current mode EC-STM (U_S = 490 mV vs. NHE, I_T = 0.2 nA, U_{Bias} = 100 mV) in order to check the suitability of the surface coverage and the stability of the immobilized enzymes. A region where only few molecules were located was chosen for the STS experiment. From STM imaging prior to STS, lateral drift can be estimated. Only when the system was running stably the STS measurement could be performed on a single FcAL labeled papain molecule (see Fig. 4.28 A).

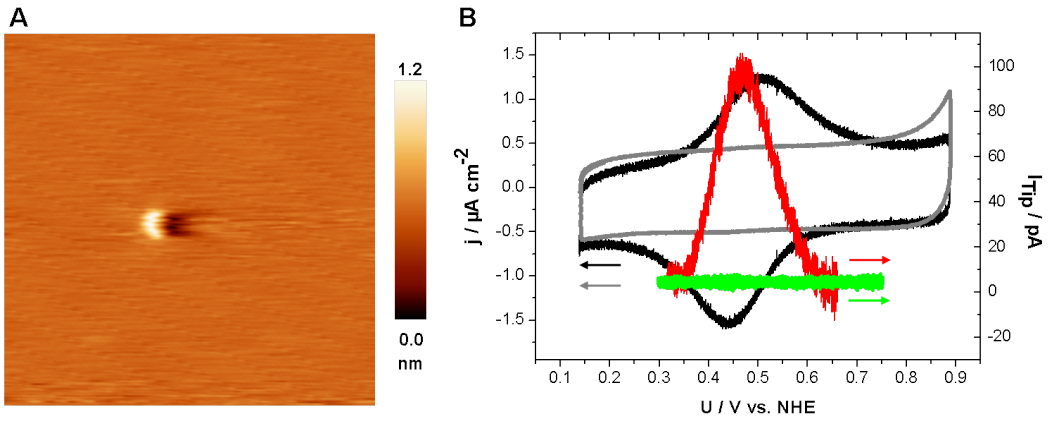

Figure 4.28. A) Constant current mode EC-STM image of a single FcAL@papain molecule on the FcAL@papain/4-CP/HOPG electrode on which the STS experiment is performed, obtained at a tunneling current of 0.2 nA and a bias voltage of 100 mV (25 nm × 25 nm). B) Cyclic voltammogram of the FcAL@papain/4-CP/HOPG electrode (black curve, left ordinate, scan rate 100 mVs^{-1}) and STS tip current (right ordinate, red curve) of the FcAL@papain molecule in 10 mM PBS (pH 7) with U_{Bias} = 100 mV. The green curve shows STS data obtained for an unlabeled papain molecule under same experimental conditions with the corresponding cyclic voltammogram of the papain/4-CP/HOPG electrode shown in grey.

Since this enzyme was the only molecule located within a surface area of 25 nm x 25 nm the contribution of molecules positioned further away from the tip apex could be considered negligible. The tip was approached to a setpoint current of I_{set} = 0.2 nA inside the tunneling range. A constant bias voltage of 100 mV with an initial potential U_i suitably remote from the redox potential was applied to the working electrode. Initial parameters such as the current setpoint and the bias voltage were always the same for all tip approaches in order to yield the same tip-sample distance for all sweeps. The feedback loop was then switched off and the substrate potential U_S and the tip potential U_{Tip} were cycled between 0.1 V and 0.9 V vs. NHE to scan over the equilibrium redox potential of the FcAL@papain/4-CP/HOPG. Both electrode

potentials were changed with a scan rate of 100 mVs^{-1} in parallel, i.e. the bias voltage between tip and sample was kept constant. With the feedback control switched off, the tunneling current through a single molecule is locally probed by the EC-STM tip as a function of the substrate potential.

In Figure 4.28B the current response detected at the tip (right ordinate) above the FcAL@papain (red curve, Fig. 4.28 B) and for comparison above an unlabeled papain molecule (green curve) are plotted together with the CVs obtained at the working electrode (black curve for FcAL@papain/4-CP/HOPG and grey curve for papain/4-CP/HOPG, both left ordinate) in 10 mM PBS (pH 7). I_{Tip} is baseline corrected by a background signal of 0.2 nA. For the FcAL@papain molecule a significant enhancement of the tunneling current could be detected with a distinct maximum close to the redox potential U_0 of FcAL@papain/4-CP/HOPG, whereas the same experiment performed on top of an unlabeled papain molecule showed no current enhancement, indicating that the redox level of the ferrocene moiety incorporated in the FcAL@papain molecule is involved in the tunneling process through the nanogap.

The measurements reported in Figure 4.28 were repeated for several fixed bias voltages between 50 mV and 300 mV in 50 mV steps, as shown in Figure 4.29 in order to evaluate the dependence of the tunneling current on the applied bias voltage across the hybrid junction. As can be seen, the tunneling current through the FcAL@papain molecule measured at the tip increases with increasing bias voltage, wheras the maximum peak potential shifts towards more negative substrate potentials U_S.

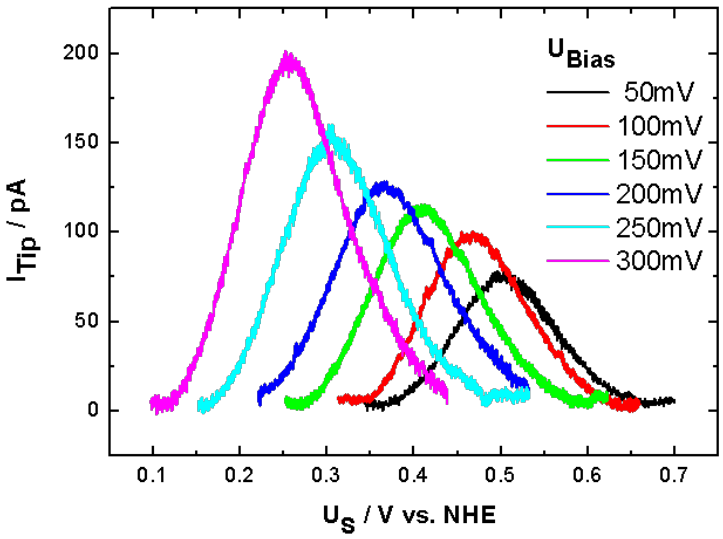

Figure 4.29. STS tunneling current/substrate potential correlations for different bias voltages between 50 mV and 300 mV in 50 mV steps.

Explanation by a Two-step Electron Transfer

The results of the single FcAL@papain molecule study obtained by different modes of EC-STM can be explained by a two-step electron transfer mechanism where the electrons have to tunnel from the tip via the redox state of the FcAL@papain to the substrate (or vice versa, depending on the sign of the bias voltage). Thereby, the appearance of the maximum in the tunneling current will be rationalized as follows [40, 44]: In general, the configuration tip - redox molecule - substrate, or Au(Tip) - FcAL@papain - 4-CP/HOPG present in these experiments, implies that a molecule with discrete electronic levels is located in the gap between substrate and tip electrode, both representing continous distributions of electronic levels. Figure 4.30 shows a scheme of the potential dependent in-situ EC-STM tunneling current and the corresponding energy diagrams (Fig. 4.30A-C) to illustrate the correlation between tunneling current and the relative energy levels of substrate, tip and redox active species located in the nanogap [40].

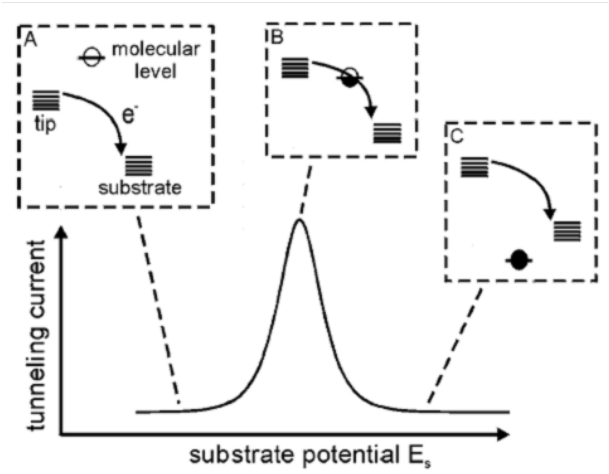

Figure 4.30. Scheme of potential-dependent in-situ EC-STM tunneling current through a redox-active molecule located in the nanogap between substrate and tip at a fixed bias voltage, taken from [40].

The localized electronic states are broadend by possible interactions of the redox-center with the surrounding electrolyte and with the substrate [3, 109]. Variation of the overpotential at fixed bias voltages (U_{Bias} - U_{Tip}) is equivalent to a parallel shift of the Fermi levels of tip and substrate. Figure 4.30A shows the case where the redox level is empty and located above the Fermi levels. This level, initially vacant, constitutes a lower tunneling barrier, i.e. as the redox level approaches one of the Fermi levels an amplifying current channel opens and the current rises (see Fig. 4.30B). Further increase leads to redox level occupation and to level trapping below the Fermi level (Fig. 4.30C). Theoretically, this behavior can be desribed by a sequential two-step electron transfer mechansim developed by Ulstrup and Kuznetsov et al. [40, 44, 153–155] that predicts the following correlation between the tunneling current and the applied bias voltage:

$$I_T \propto (\mathrm{eU_{Bias}}) \exp\left(-\frac{\lambda + \mathrm{eU_{Bias}}}{4k_BT}\right)\left\{\cosh\left[\frac{(0.5-\gamma)\mathrm{eU_{Bias}} - \xi e\eta}{2k_BT}\right]\right\}^{-1} \tag{4.1}$$

The nuclear reorganization free energy λ represents the electronic-vibrational coupling, ξ and γ are the fractions of the overpotential and bias voltage, respectively, at the site of the redox center, e the electronic charge, k_B Boltzmann's constant, and T the temperature. This theory has recently been applied to redox-active proteins and metal transition complexes [3, 40, 41, 44, 235].

Figure 4.31 shows the linear correlation between the substrate potential where the maximum of the tunneling resonance is achieved in dependence on the applied bias voltage, which supports the validity of the two-step ET model. The potential dependent image contrast of FcAL@papain obtained in constant current and constant height mode qualitatively supports the interpretation of the STS data as a tunneling process involving the redox level of the ferrocene moiety incorporated in the papain protein shell. Similar results for potential-dependent constant current mode EC-STM were already found for redox molecules [36, 41], the metalloprotein azurin [3, 17, 43, 110] and the redox enzyme glucose oxidase [15, 16]. All the papers report about gating the tunneling current by the redox level of the redox species [236], i.e. one could use the incorporation of the ferrocene group to "gate" the interfacial charge transport across the papain molecule to the electrode surface.

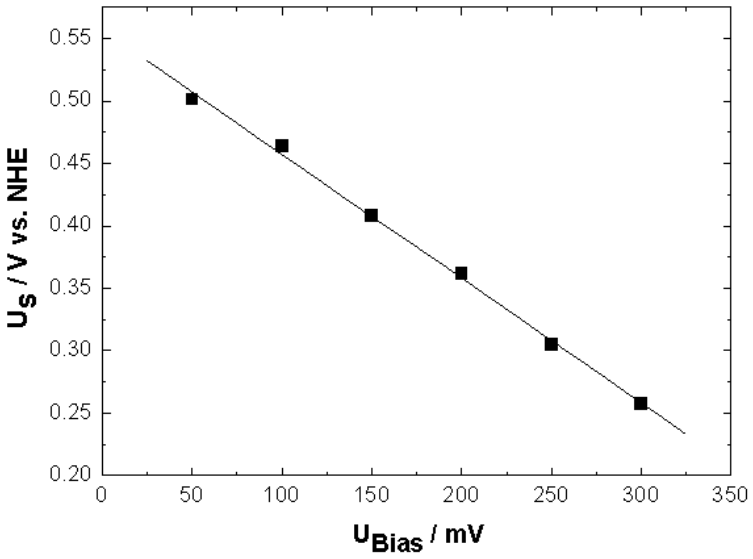

Figure 4.31. Dependence of the peak potentials on the applied bias voltage for bias voltages between 50 mV and 300 mV (see data in Fig. 4.29)

4.3.2.2. Submonolayers of mixed Labeled and Unlabeled Papain

Based on the results discussed so far, electrodes with a submonolayer of labeled and unlabeled papain molecules were studied with in-situ EC-STM. These electrodes were prepared as usual by incubating the NHS-ester modified 4-CP/HOPG electrode over night at 4°C this time into a solution containing a mixture of crude papain and FcAL@papain (1:1, 0.1 $mgml^{-1}$ in 10 mM PBS, pH 8). The exact composition of labeled and unlabeled molecules can only be estimated since every

charge of FcAL@papain also contained some unlabeled molecules. After thoroughly rinsing with Milli-Q water the electrode surface was investigated in 10 mM PBS (pH 7) in constant current mode EC-STM with a tunneling current of 0.2 nA and a bias voltage of 100 mV. The potential applied to the working electrode again was equal to the redox potential of FcAL@papain/4-CP/HOPG electrodes, $U_S = U_0 = 490$ mV vs. NHE. Figure 4.32 shows typical surface areas (A) 150 nm × 150 nm, B) 100 nm × 100 nm) with submonolayer coverage. Imaging smaller surface areas with higher resolution 20 nm × 20 nm, enzyme molecules with two different image contrasts, i.e. different apparent heights were observed (Fig. 4.33).

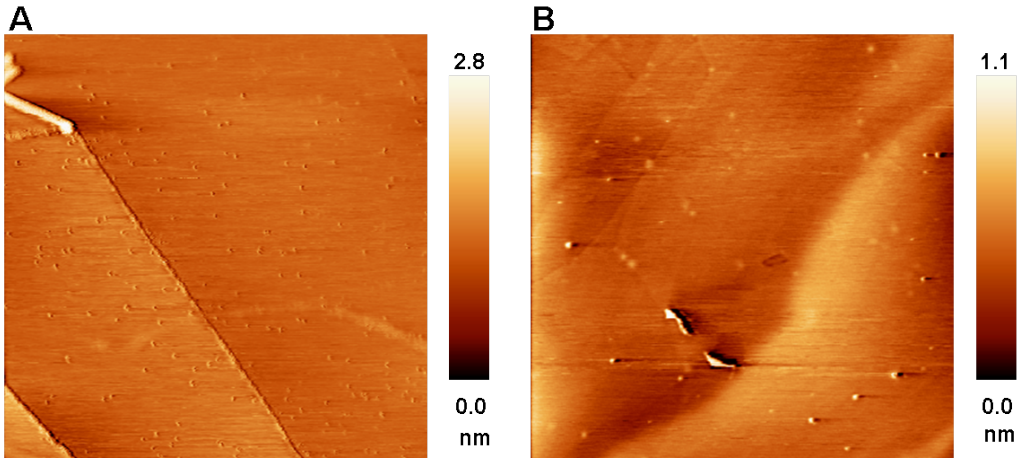

Figure 4.32. EC-STM images of papain electrodes with unlabeled and FcAL@papain molecules with submonolayer coverages: A) 150 nm × 150 nm, B) 100 nm × 100 nm. Obtained at $U_S = U_0 = 490$ mV vs. NHE with $U_{Bias} = 100$ mV and $I_T = 0.2$ nA.

The apparent height of the molecules was investigated performing a line scan analysis. The papain molecules with the lower image contrast had an apparent height between 2 Å and 3 Å (see blue line scan in Fig. 4.33), whereas the papain molecules with the high image contrast had an apparent height of approximately 6 Å to 7 Å(see green line scan in Fig. 4.33). Similar values for single FcAL labeled and unlabeled papain molecules were also found before. Therefore, we assume that the single molecule with low image contrast is an unlabeled papain molecule, whereas the two molecules showing high image contrast are FcAL@papain molecules.

4.3.2.3. On-chip Labeling

In Section 4.3.1.3 was already shown that it is possible to detect the labeling process of the ferrocene affinity label to the activated papain molecule in-situ by cyclic voltammetry. Furthermore, the investigations at the nanoscale using in-situ EC-STM enables one to differentiate between single ferrocene-labeled and unlabeled papain molecules. In this section it will be discussed whether EC-STM also provides the detection of the labeling process directly on-chip, i.e. whether the binding of the electroactive ferrocene species to immobilized papain molecules can

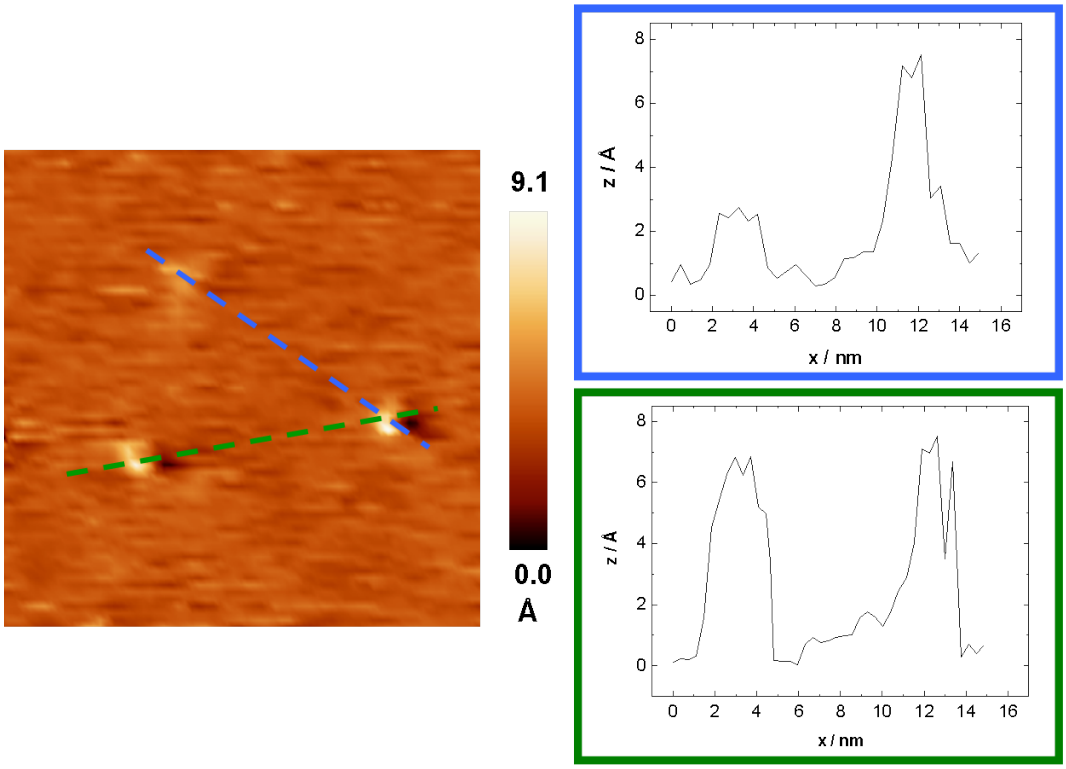

Figure 4.33. High resolution EC-STM image of papain molecules showing different image contrasts (20 nm × 20 nm). The apparent height can be evaluated from the corresponding line scan analysis (color coded).

be monitored. Unlabeled papain molecules were covalently immobilized on the active NHS-ester of a 4-CP/HOPG electrode. In order to obtain a high surface coverage, an enzyme solution containing a papain concentration of 1 $mgml^{-1}$ was pipetted onto the functionalized HOPG surface and stored over night at 4 °C. The electrode was then thoroughly rinsed with water and characterized by cyclic voltammetry and in-situ EC-STM. Figure 4.34 represents the papain/4-CP/HOPG electrode surface showing that the molecules are arranged in a hexagonal close-packed lattice over large areas (150 nm × 150 nm). Furthermore, a potential-dependent EC-STM study was performed, verifying that the apparent height of unlabeled papain molecules is not affected by the applied substrate potential (comparable to Section 4.3.2.1).

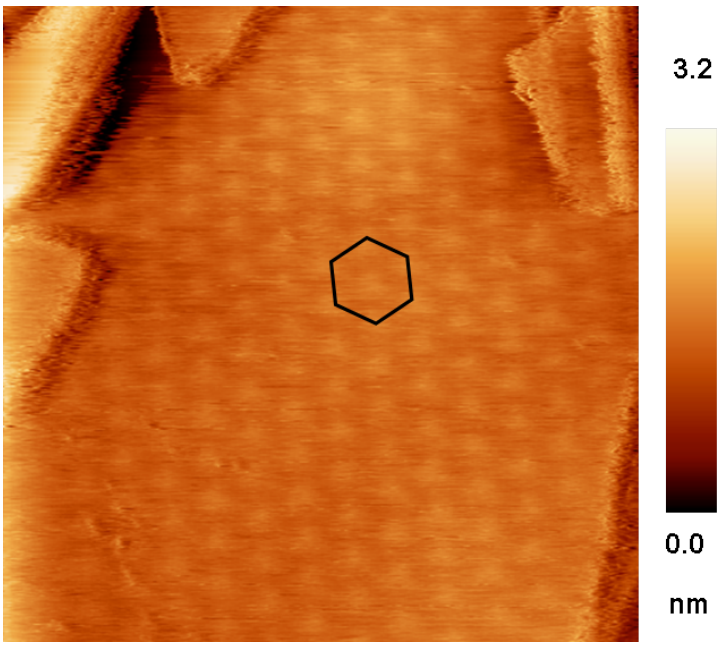

Figure 4.34. In-situ EC-STM image of papain molecules immobilized on 4-CP/HOPG arranged in a hexagonal close-packed lattice (150 nm × 150 nm, U_S = 490 mV vs. NHE, I_T =0.5 nA, U_{Bias} = 80 mV).

After the electrochemical characterization, the free NHS-ester groups on the surface were blocked with ethanolamine and the papain molecules were activated with TCEP (detailed description of the electrode preparation procedure in Section 3.5.2). 70 μl of phosphate buffer solution (10 mM, pH 8) containing 1 μM FcAL were dropped onto the surface and the electrode was again stored over night at 4 °C. The electrode was then thoroughly rinsed with Milli-Q water, put in the ultrasonic bath for 30 s to remove loosely bound FcAL, rinsed again with Milli-Q water and finally characterized by cyclic voltammetry and in-situ EC-STM.

Figure 4.35 shows the cyclic voltammograms and an in-situ EC-STM images of the papain electrode surface before and after the FcAL labeling. As expected, the CV of the papain/4-CP/HOPG electrode (Fig. 4.35A1) showed no redox active behavior, however, after incubation in the FcAL containing solution a distinct redox behavior with a redox potential of 490 mV vs.

NHE could be observed (Fig. 4.35B1). Therefore, the redox potential was equal to the redox potential found for FcAL@papain/4-CP/HOPG electrodes in previous studies. Furthermore, the apparent morphology observed by EC-STM applying a substrate potential of 490 mV vs. NHE changed significantly. While unlabeled papain molecules exhibit an apparent height of approximately 2.4 Å their apparent height increased by a factor of four, up to 10 Å after the labeling procedure (compare Fig. 4.35A2 and B2).

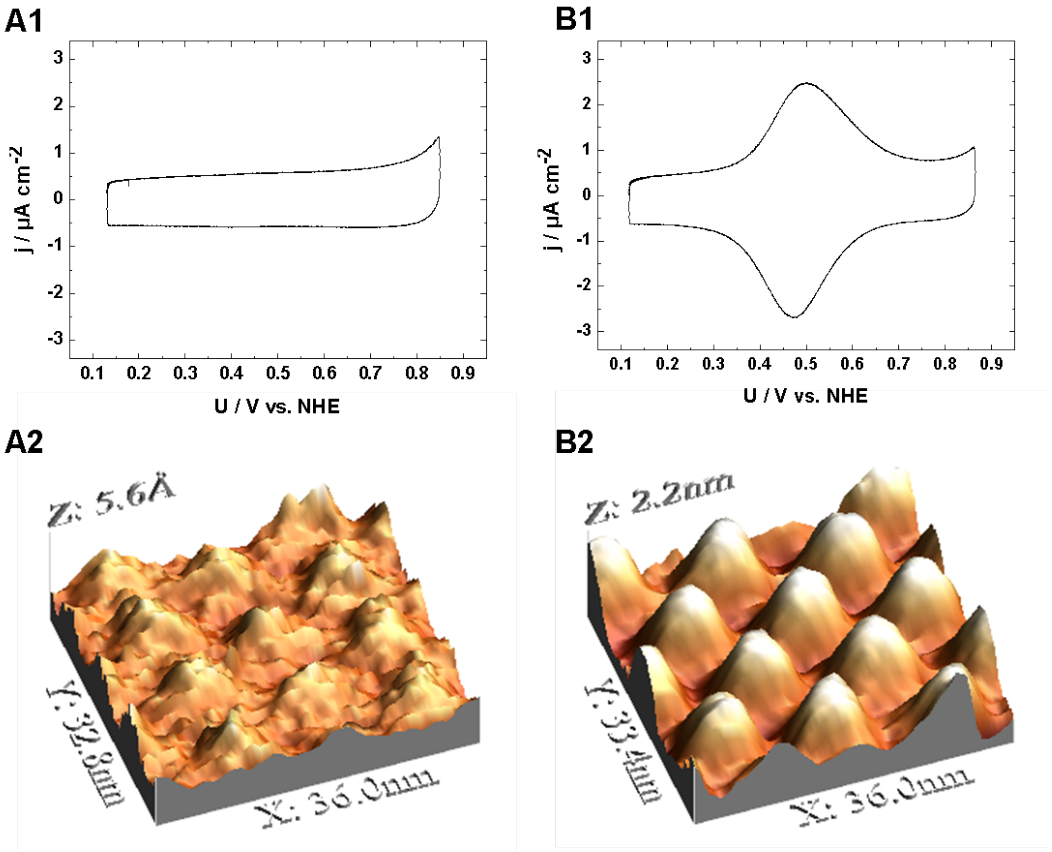

Figure 4.35. CVs (1) and in-situ EC-STM images (2) of an array of papain molecules A) before FcAL labeling and B) after FcAL labeling. Both images were obtained at I_T = 0.5 nA and U_{Bias} = 80 mV at an applied substrate potential 490 mV vs. NHE

These results already indicate that the FcAL bound to the immobilized papain molecules on the HOPG surface. However, after the FcAL labeling the electrode surface was imaged again at different applied substrate potentials 240 mV $\leq U_S \leq$ 890 mV in steps of 50 mV in order to investigate the potential-dependent apparent height of the molecules (Fig. 4.36). Figure 4.36A shows the cyclic voltammogram of the papain/4-CP/HOPG electrode obtained after the labeling process, the letters within highlight the applied substrate potential and refer to the corresponding EC-STM images (36 nm × 33 nm). The CV reveals a redox potential of 490 mV vs. NHE equal

to the redox potential found for prelabeled FcAL@papain immobilized on 4-CP/HOPG. Figure 4.36B shows the EC-STM image obtained at U_0 = 490 mV vs. NHE. Figure 4.36C, D and E correspond to positive overpotentials of 100 mV, 200 mV and 350 mV, whereas Figure 4.36F and G correspond to negative overpotentials of -100 mV and -200 mV, respectively. Again, with increasing overpotential, positive or negative, the image contrast of the papain molecules decreased.

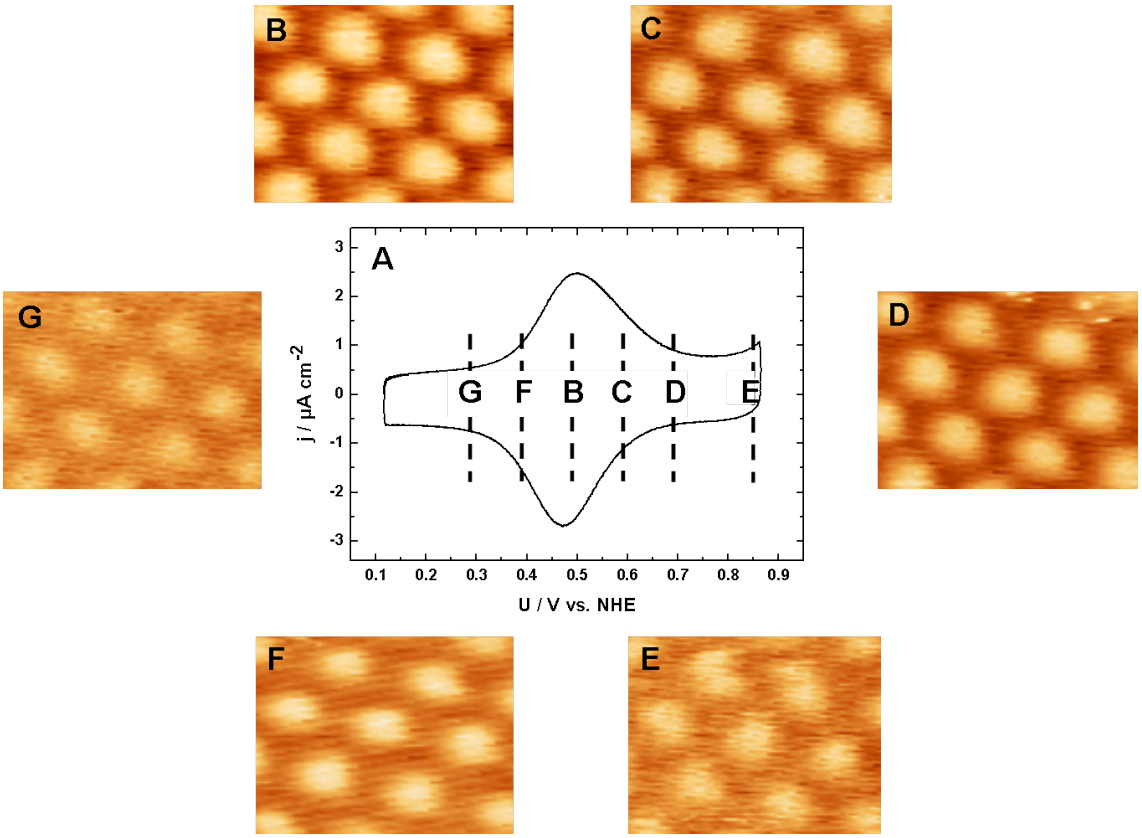

Figure 4.36. Series of in-situ EC-STM images of the labeled papain array obtained at different applied electrode potentials indicated in the corresponding CV (A). The letters B) - G) highlight the applied substrate potential and refer to the corresponding EC-STM image. Parameters for all images: I_T = 0.5 nA and U_{Bias} = 80 mV, 36 nm × 33 nm

The analysis of the apparent height depending on the applied overpotential is shown in Figure 4.37. The dashed line represents the apparent height found for the papain molecules before the labeling procedure being approximately 2.4 Å. After the FcAL incubation the apparent height exhibits a maximum of 10 Å when the redox potential U_0 = 490 mV vs. NHE was applied, i.e. the overpotential was zero, and decreased to 2.4 Å for an overpotential of -250 mV and to 5 Å for an overpotential of 350 mV. In order to check the reversibility of the effect, the substrate potential was switched several times to the redox potential, U_0 = 490 mV vs. NHE, where the

molecules reappeared with the same height of 10 Å as before.

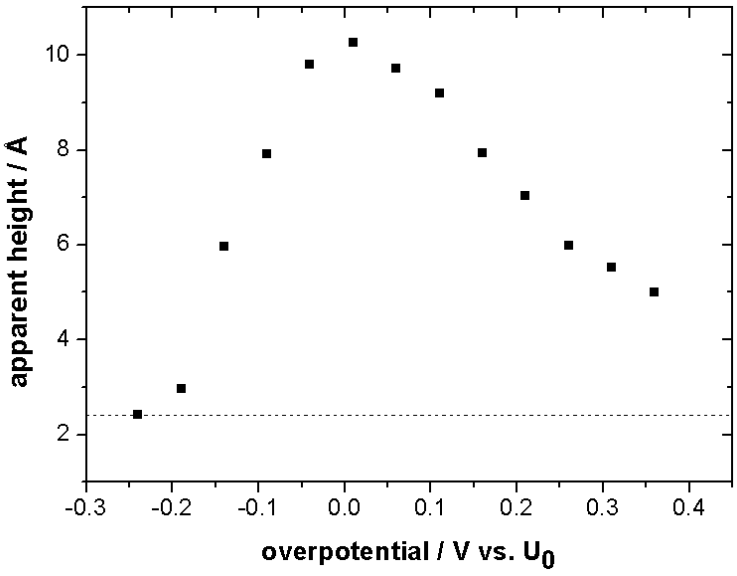

Figure 4.37. Apparent height of the papain molecules before (dashed line) and after the incubation in FcAL solution (squares) in dependence on the applied substrate potential given as overpotential with respect to U_0 = 490 mV vs. NHE.

Comparing the potential dependence of the apparent height observed in Figure 4.37 with the apparent height of the prelabeled FcAL@papain molecules presented in Figure 4.24 a similar behavior can be observed. Although the maximum apparent height of the immobilized papain molecules after the labeling procedure is slightly higher than for the FcAL@papain complex, it is assumed that the on-chip labeling of the papain molecules was successful. Possible explanations for the differences in the apparent height will be discussed in the following.

Single Molecule vs. Molecule Array

As already mentioned, it was observed that the maximum apparent height of the immobilized, on-chip labeled papain molecules is higher than for the prelabeled FcAL@papain complex immobilized on 4-CP/HOPG. Assuming a successful ferrocene labeling, the only differences between these two cases are the amount and the arrangement of the enzymes on the surface, thus, the enzymes will be distinguished between arrayed and single FcAL@papain molecules.

In Figure 4.38 the potential dependence of the apparent height of single (circles) and arrayed (squares) FcAL@papain molecules is presented in one graph for direct comparison. Both data sets show a similar, almost parallel behavior with an apparent height of 2.4 Å at negative overpotentials, which is equal to the height of unlabeled single and arrayed papain molecules. Furthermore, a maximum height is observed when the redox potential U_0 = 490 mV vs. NHE

of FcAL@papain/4-CP/HOPG is applied. However, the averaged maximum height of 10 Å for an enzyme located in the array is about 40% higher than for a single enzyme with an apparent height of 7 Å. Since EC-STM images represent a convolution of morphology and the electronic properties of the molecules, where brighter contrasts represent regions of high-tunneling probability, an enhanced electron tranfer in the enzyme array is proposed. Beside the apparent height also the apparent width of the molecules will be compared.

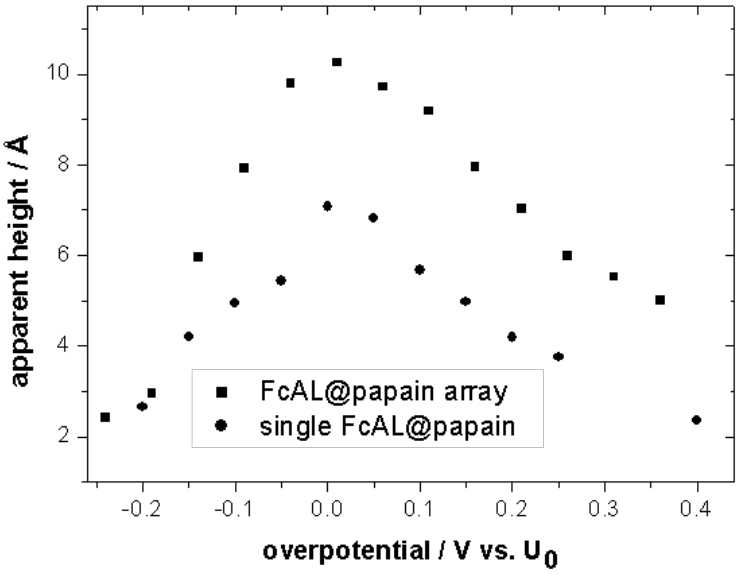

Figure 4.38. Apparent height of the papain molecules arranged in hexagonel close-packed layer after the incubation in FcAL solution (squares) in comparison with the apparent height of single FcAL@papain (circles) molecules, plotted as a function of the applied overpotential vs. U_0 = 490 mV vs. NHE.

The apparent width of the FcAL@papain molecules in dependence on the applied substrate potential was evaluated and is shown in Figure 4.39. The dashed and dotted line represent the average molecule width found for unlabeled arrayed (5.4 nm) and single (2.5 nm) papain, respectively. Both conformations, arrayed and single FcAL@papain molecules showed an increased apparent width when the redox potential U_0 = 490 mV vs. NHE of FcAL@papain/4-CP/HOPG is applied. While the width of a single FcAL@papain molecule increased from 2.5 nm to 3 nm (15%), the width of the arrayed enzyme was already about 5.4 nm initially, i.e. much larger than the width of a single molecule and increased up to 6.5 nm (20%).

Again it is noteworthy to mention that EC-STM visualizes the tunneling probability of electrons through the nanogap between tip and electrode. The more electrons flow, the higher is the image contrast and the apparent height of the feature under study. We assume that beside the one-dimensional electron transfer pathway from the tip through the FcAL@papain molecule directly to the elctrode surface, another two-dimensional pathway from the tip and across the enzyme array might exist, i.e. the electrons might propagate also in x-y direction. Thereby, the

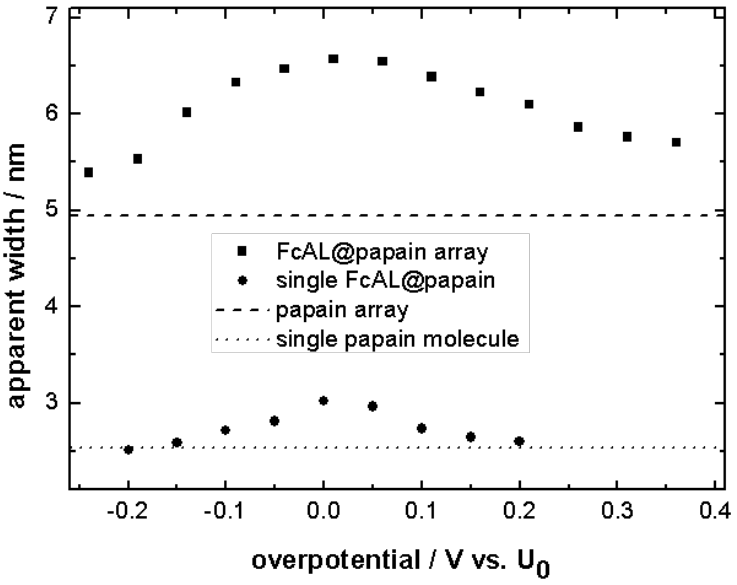

Figure 4.39. Apparent width of the papain molecules arranged in an hexagonel close-packed layer before (dashed line) and after the incubation in FcAL solution (squares) in comparison to the apparent width of single unlabeled papain (dotted line) and FcAL@papain molecules (dots), plotted in dependence on the applied overpotential vs. U_0 = 490 mV vs. NHE.

2D electron transfer migth be provided and enhanced either by the underlying 4-carboxyphenyl layer or by the N-terminated residue amino acid chain of the FcAL that is flexibly located outside the papain protein shell or even both. Especially, features observed at the edge of an hexagonal close-packed enzyme array support this assumption. Figure 4.40A shows an 55 nm × 55 nm EC-STM image obtained at the redox potential of the FcAL@papain/4-CP/HOPG electrode of edge and centered FcAL@papain molecules.

Within the array all molecules appear rather homogenously and with a spherical shape, whereas the molecules located at the edge (bottom row) are asymmetric and show an enhanced image contrast at the rim of the array. The line scan analysis in Figure 4.40B shows the profile of a centered and an edge molecule (indicated by the black line in Fig. 4.40). It is obvious that the FcAL@papain molecule located in the center of the array possesses a homogenous profile with an average apparent width of 6.3 nm, while the FcAL@papain molecule at the edge has a decreased apparent width of only 4.5 nm. Furthermore, the cross section of the edge molecule is asymmetric, showing an increased apparent height with a steep trailing edge towards the rim of the array. The shape of the molecule might indicate that the electron transfer in the direction of the enzyme array is present, but inhibited towards the edge, probably due to the fact that there are no neighbours. Therefore, the electron transfer is limited in this direction, the electrons have to follow the pathway in z-direction directly to the surface leading to an slightly increased apparent height. Performing EC-STM images of azurin on Au(111), Friis et al. [109] observed a higher

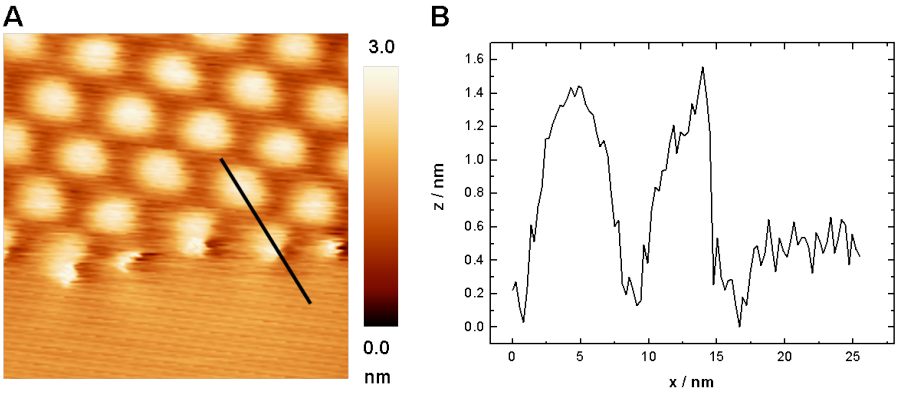

Figure 4.40. A) EC-STM image of the edge of an enzyme array (U_0 = 490 mV vs. NHE, 55 nm × 55 nm) and B) corresponging line scan across two enzymes, one sitting in the center and the other sitting at the edge of the hexagonal close-packed array.

apparent height within the azurin molecule at the position of the copper atom visualizing ideal electron tunneling routes through the metalloprotein. Since single FcAL@papain molecules have no neighboring molecules, the electron transfer is limited to the z-direction. The probability for electrons to propagate in x-y direction is not existing. Therefore, the apparent width of single FcAL@papain molecules is much smaller than that of arrayed molecules. Furthermore, the absolute value of electrons tunneling from the tip through the enzyme to the electrode is confined by the electron transfer rate which might be even higher for the hexagonal close-packed enzyme array.

4.3.2.4. Summary

Electrochemical scanning tunneling microscopy (EC-STM) and spectroscopy (STS) was used to elucidate the mechanism of the electron transport through ferrocene-modified papain molecules down to a single enzyme level. The enhancement of the electron transfer around the redox potential of the FcAL@papain complex is reflected both in the EC-STM imaging contrast and directly in the tunneling current observed in constant height and STS mode. Since EC-STM shows a convolution of the topography of the papain molecules and their electronic properties, single labeled and unlabeled papain molecules could be distinguished. Furthermore, EC-STM imaging enabled one to monitor the labeling process directly on the surface by detecting the changes in the nanoscopic electrochemical properties of the immobilized papain molecules due to the incorporation of a ferrocene moiety.

4.3.3. Investigation of the Enzymatic Activity of Papain using Fe(Cp)(η-C_5H_4-CH_2-NH-CO-Epx-Leu-Tyr-Ahx-Lys)

In the previous section it was shown that the labeling process of the FcAL Fe(Cp)(η-C_5H_4-CH_2-NH-CO-Epx-Leu-Tyr-Ahx-Lys) to the active site of the papain molecule can be electrochemically detected "on-chip" by cyclic voltammetry and in-situ EC-STM. In this section, we report about the kinetic approach to also electrochemically determine the enzymatic activity of papain "on-chip" via cyclic voltammetry. The approach uses the intrinsic property of the FcAL to efficiently and specifically react with the enzyme in an activity-dependent manner, forming the irreversible FcAL@papain complex. The successful realization of such a system requires, as a key component, a surface-immobilization chemistry that besides facilitating the electron transfer to the electrode also maintains the activity of the papain. The results obtained in Section 4.3.2.3 provide evidence that the covalent immobilization of papain onto a 4-carboxyphenyl modified HOPG surface by EDC/NHS coupling fulfills these requirements.

4.3.3.1. Papain Activity

Commercial, i.e. inactive papain was covalently immobilized onto the 4-CP/HOPG electrode surface. In order to yield a complete monolayer of papain molecules on the surface, a high concentrated enzyme solution 1 $mgml^{-1}$ was used. The remaining, unconverted functionalities on the electrode surface were blocked with ethanolamine to avoid FcAL binding. Then, the active site of the papain molecules was activated with TCEP. Prior to the activity measurements, the papain/4-CP/HOPG electrode was checked in 10 mM PBS (pH 7) using cyclic voltammetry (100 mVs^{-1}). The CV is shown in Figure 4.41 indicated by t_0, showing no redox behavior. Finally FcAL was added to the electrolyte and cyclic voltammograms (100 mVs^{-1}) were recorded continuously. Figure 4.41 shows a significant increase in the oxidation and reduction peak current densities with time due to the binding of FcAL to the papain/4-CP/HOPG electrode.

Assuming that only FcAL bound to the enzyme contributes to the redox signal, the amount of the reaction product, i.e. of the irreversible enzyme-AL-complex FcAL@papain, can be calculated from the Faradaic charge of the redox peaks. The experiment was performed for different concentrations of FcAL in solution. Figure 4.42 shows the amount of produced FcAL@papain with time for FcAL concentrations of 100 nM, 250 nM, 500 nM and 1 μM following typical Michaelis-Menten kinetics, where the product formation, i.e. the amount of produced FcAL@papain, is dependent on the concentration of the substrate, in this case, the FcAL.

After the injection of the FcAL the amount of produced FcAL@papain increases with increasing FcAL concentration. Since the amount of active papain on the surface is limited and both, papain and FcAL are consumed within the reaction, the amount of FcAL@papain approaches a saturation level with time. Thereby, ideally the saturation level is equal to a complete FcAL@papain monolayer of 17.32 $pMcm^{-2}$. After 60 minutes the injection of 100 nM only reached 6.98 $pMcm^{-2}$, probably indicating that there are still free active papain molecules on the surface and that the fast binding processes are limited by diffusion of the FcAL to the active site of the papain molecules [29]. The addition of 250 nM and 500 nM FcAL already yielded

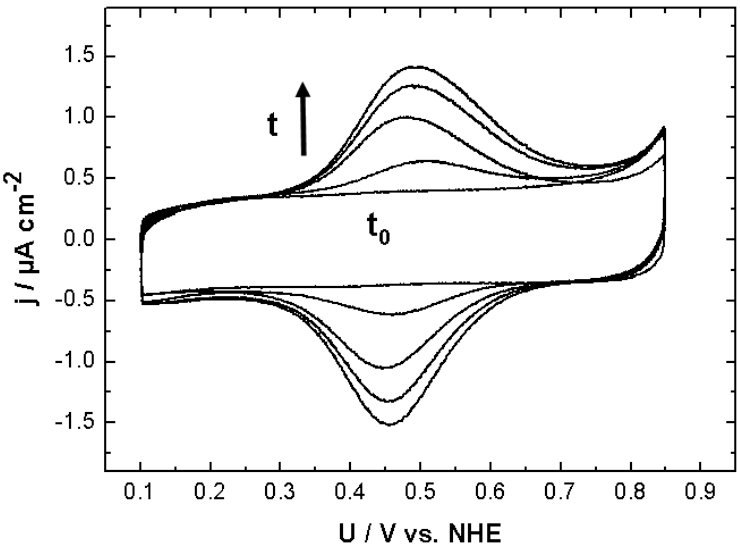

Figure 4.41. Cyclic voltammograms of the papain/4-CP/HOPG electrode detected before (t_0) and continously after the FcAL (500 nM) was added to the electrolyte (10 mM PBS, pH 7)

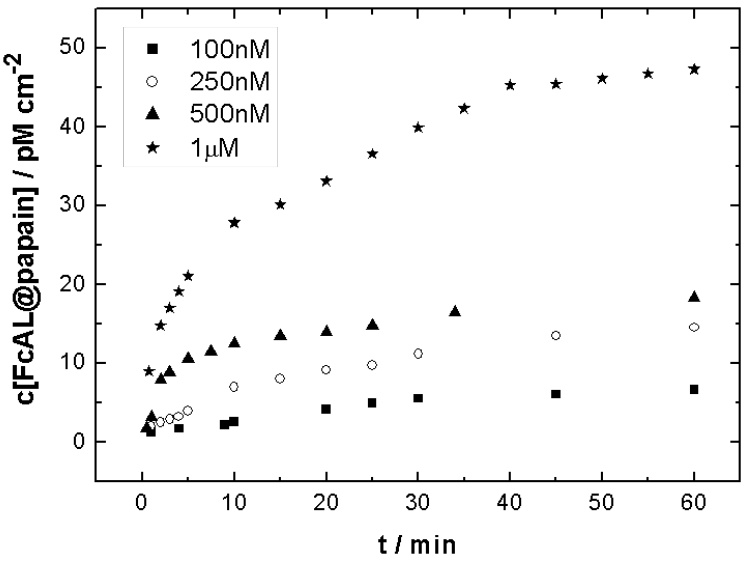

Figure 4.42. Amount of irreversibly formed FcAL@papain complex plotted versus time for different FcAL concentrations in the electrolyte: 100 nM (squares), 250 nM (circles), 500 nM (triangles) and 1 μM (stars).

concentrations of 14.64 pMcm^{-2} and 18.45 pMcm^{-2}, which are both close to the full monolayer. However, the amount of FcAL@papain produced after 60 minutes when 1 μM FcAL was added is 46.76 pMcm^{-2}, which corresponds to 2.7 monolayers. This observation could be explained by agglomeration effects and/or possible diffusion of the FcAL through the carboxyphenyl groups to the electrode, providing direct electron transfer between the ferrocene moiety and the HOPG surface.
Since the FcAL irreversibly binds to the active site of papain, [ES] is equal to [P] and Equation 2.37 can be simplified

$$E + S \overset{k_{cat}}{\rightarrow} P \tag{4.2}$$

Being at least three orders of magnitude higher than the enzyme concentration on the surface (∼pMcm^{-2}) the substrate concentration c[FcAL] (∼nMcm^{-2}) can be considered constant throughout the reaction. Therefore, the initial reaction rate v_0 can be determined from the slope of the initial rise in FcAL@papain concentration according to equation 2.38 (Fig. 4.43).

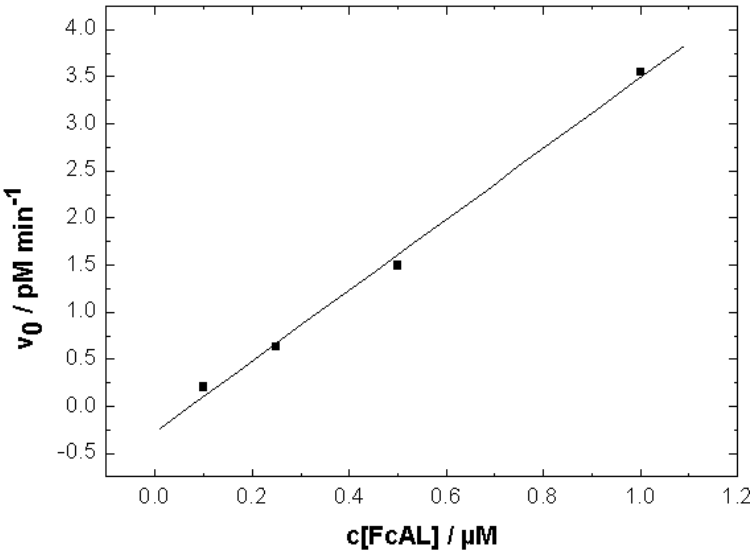

Figure 4.43. Initial reaction rate v_0 plotted versus the concentration of injected FcAL.

However, for further quantitative conclusions an adequate kinetic model is required considering also possible diffusion-controlled reversible side reactions between the FcAL and the electrode.

4.3.3.2. Influence of Inhibitors

In order to demonstrate that this method can also be used for the development and characterization of inhibitors, activity measurements were performed in the presence of papain inhibitors. Leupeptin, a well-known competitive cysteine protease inhibitor and the synthesized affinity label

(AL) (without the ferrocene moiety) were used as reversible and irreversible inhibitors, respectively. While leupeptin can be replaced by the FcAL with time, the affinitiy label completly inhibits the reaction between papain and the FcAL. The inhibitors were preinjected, i.e. before 500 nM FcAL was added, and incubated for various times. The reversible inhibitor leupeptin was added two hours before FcAL injection, whereas the affinity label was incubated over night. The transients for FcAL@papain formation in the presence and absence of inhibitors are shown in Figure 4.44. The addition of leupeptin slows down the reaction between the FcAL and the active enzyme in a concentration-dependent manner, i.e. the higher the leupeptin concentration in the solution the slower the reaction of FcAL and papain. When 500 nM leupeptin were preinjected the addition of 500 nM FcAL resulted in 16.06 pMcm^{-2} FcAL@papain after 60 minutes. This value is already close to the saturation level of the reaction, indicating that reversibly bound leupeptin is replaced by the FcAL which binds irreversibly. For 5 μM and 10 μM leupeptin preinjection concentrations of only 11.66 pMcm^{-2} and 9.29 pMcm^{-2} were determined after 60 minutes. Furthermore, the incubation of the irreversible inhibitor, the affinity label (AL), resulted in a FcAL@papain concentration below 2.5 pMcm^{-2}. This fact clearly shows that, by irreversibly binding to the papain, the AL really blocks the active enzyme and successfully inhibits the reaction with the FcAL. Therefore, the charge measured via CV, can also be attributed to side reactions such as direct interaction beteween the FcAL and the electrode surface, already mentioned above.

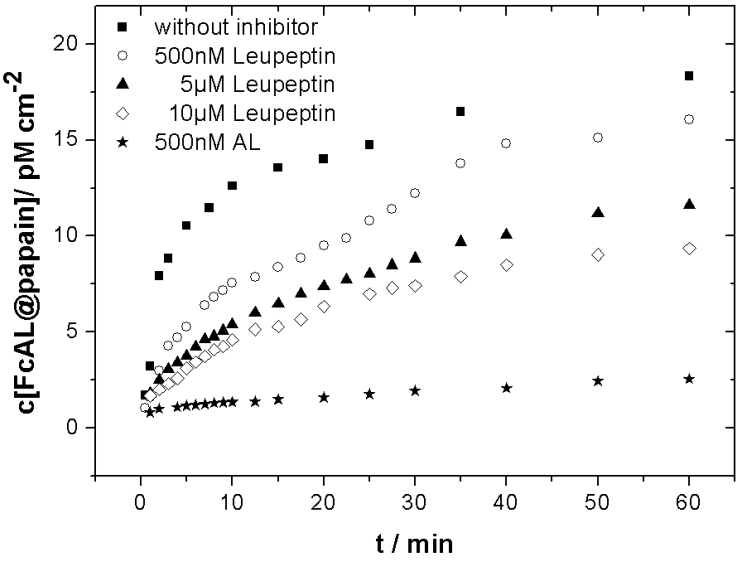

Figure 4.44. Amount of irreversibly formed FcAL@papain complex plotted versus time for 500 nM FcAL in the absence and presence of reversible and irreversible inhibitors. Squares: without inhibitor, circles: 500 nM leupeptin, 5 μM leupeptin, triangles: 10 μM leupeptin, stars: 500 nM affinity label.

Estimated reaction velocities v_0 for 500 nM FcAL in the presence and absence of reversible and irreversible inhibitors are shown in Table 4.3, providing evidence that the catalytic activity

of papain is decreased in the presence of inhibitors.

500 nM FcAL	**c[FcAL@papain](60 min)/pMcm^{-2}**	**v$_0$/pM min^{-1}**
without inhibitors	18.45	1.49
500 nM leupeptin	16.06	0.66
5 μM leupeptin	11.66	0.38
10 μM leupeptin	9.29	0.32
500 nM AL	2.48	0.004

Table 4.3. Parameters of the catalytic reaction between the FcAL and the active papain immbolized on HOPG, obtained in 10 mM PBS (pH 7) in the presence and absence of inhibitors. The concentration of formed FcAL@papain is measured after 60 minutes. The reaction velocity v_0 is estimated from the slope of the initial rise in FcAL@papain concentration observed in the transients in Figure 4.44.

4.3.4. Summary

It was shown that the synthesized FcAL can in principle be used in order to electrochemically detect the enzymatic activity of immobilized papain. The method is also suitable for qualitative investigations of enzyme inhibitors. The results show that one can distinguish between reversible and irreversible inhibition. However, in order to develop an appropriate quantitative model for the evaluation of, both, kinetic and inhibition constants, detailed studies of possible side reactions are required.

4.4. Scanning Electrochemcial Potential Microscopy

The scanning electrochemical potential microscopy (SECPM) is a modification of the electrochemical SPM techniques. Its experimental setup is based on the EC-STM. However, instead of a current preamplifier that enables measuring nA tunneling currents a high impedance voltage amplifier allows to detect the potential difference between the electrode surface and the SECPM tip. Therefore, the SECPM tip can be used as local potential probe. The long-term aim of the scanning electrochemical potential microscopy (SECPM) is to monitor surface potentials at the solid-liquid interface due to ion distribution in the electrochemical double layer or adsorbates at the electrode surface. If this could be achieved any type of charged surface could be studied and the limitations of EC-STM to conductors or semi-conductors would disappear. Since in SECPM no current flows between the tip and the sample surface SECPM seems to be a suitable tool for the investigation of biomolecules under electrochemical conditions. In this chapter first results of the constant potential mode SECPM applied to typical electrochemical support materials such as Au(111) and HOPG are presented and the approach to map single enzyme molecules under in-situ conditions is discussed. For direct comparison and in order to get a better understanding of the SECPM imaging technique combined EC-STM/SECPM studies of the same surface area were performed. Furthermore, potential profiles were measured on Au(111) and preliminary results are shown. Finally, a possbile application using the potentiometric tip of the SECPM as local pH sensor is introduced.

4.4.1. Mapping Electrode Surfaces

4.4.1.1. Au(111)

A comparison of both techniques, EC-STM and SECPM, operating in constant current mode and constant potential mode, respectively, is shown in order to evaluate the possibilities of the SECPM method. The Au(111) surface was first imaged in constant current mode EC-STM in 0.1 M $HClO_4$, then the system was switched to SECPM and the same surface area was scanned in constant potential mode. Obtained data can be compared to existing EC-STM literature reports where the structure of the Au(111) surface could be resolved with atomic resolution using EC-STM [237].

Figure 4.45 A1 shows a typical in-situ EC-STM image of an Au(111) single crystal in 0.1 M $HClO_4$ taken at a substrate potential U_S of 500 mV vs. NHE. The image was obtained in constant current mode applying a bias voltage between the tip and the substrate $U_Bias = U_{Tip} - U_S = 100$ mV and a tunneling current $I_T = 1$ nA . The scanned area of the gold surface shows atomically flat (111) terraces separated by well-defined steps. A line scan analysis of the EC-STM image (4.45 A2) reveals that the gold steps are of monoatomic height. The step height h is approximately 2.5 Å which is in good agreement with the theoretical value of 2.35 Å which is calculated from the lattice constant $a = 4.0786$ Å and $h = 3^{-1/2}a$. Furthermore, the angle of the Au(111) terrace edge in the middle of the picture is 59°; 120/60° step edges are characteristic of the Au(111) orientation. These results were compared with scanning electrochemical potential microscopy

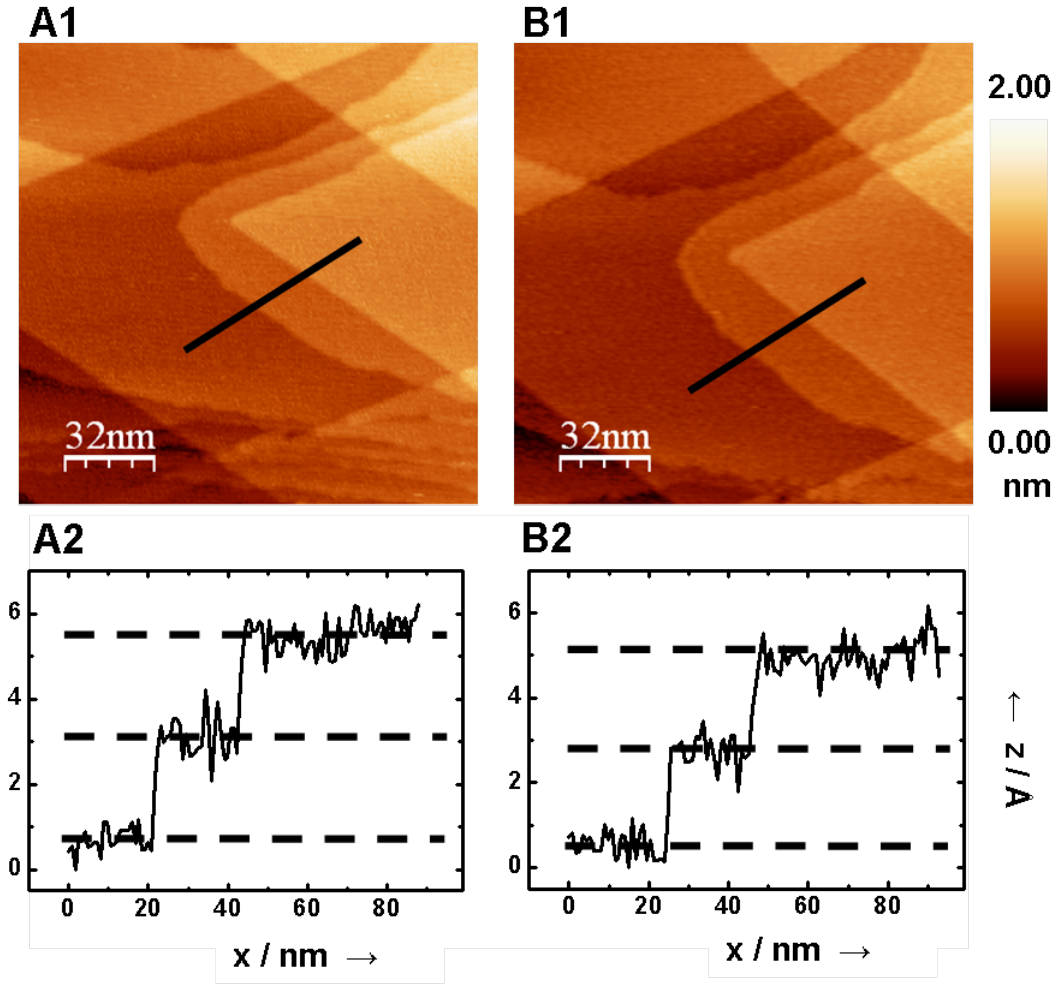

Figure 4.45. EC-STM and SECPM of Au(111) single crystal electrode: A, In situ EC-STM image (1) and corresponding line scan (2) of Au(111) single crystal electrode in 0.1 M $HClO_4$, I_T = 1 nA, U_{Bias} = 100 mV, U_S = 500 mV vs. NHE; B, In situ SECPM image (1) and corresponding line scan (2) of Au(111) single-crystal electrode in 0.1 M $HClO_4$, U_S = 500 mV vs. NHE, $\triangle U$ = 5 mV.

(SECPM). The same area was scanned in constant potential mode applying a potential difference of 5 mV between the tip and the Au(111) single crystal electrode. The potential applied to the single crystal was 500 mV vs. NHE. As can be seen in Figure 4.45 B1, no significant differences between the STM and the SECPM image are observed. The angle of the gold terrace is 61.2° and the line scan in Figure 4.45 B2 reveals a step height between 2.3 and 2.4 Å. These results show that the lateral resolution of SECPM in these dimensions is comparable to STM.

4.4.1.2. Highly Oriented Pyrolytic Graphite

Highly oriented pyrolytic graphite (0001) (HOPG) has been the support of choice for many STM experiments, as it provides atomically flat areas, good mechanical stability and electronic conductivity. Its atomic topography usually shows a hexagonal lattice with a lattice constant of 0.246 nm [238]. Due to the fact that the atomic resolution can easily be obtained HOPG is often used as a calibration grid for the piezos in xy-direction in SPM . Figure 4.46 shows a combined EC-STM and SECPM study of a freshly cleaved HOPG surface obtained in 0.1 M $HClO_4$ at a substrate potential U_S = 300 mV vs. NHE. The constant current mode EC-STM images (Fig. 4.46A1 and Fig. 4.46A2) show the characteristic atomically flat HOPG surface and a typical step edge across the section. The SECPM also maps a smooth surface (Fig. 4.46B1 and Fig. 4.46B2) indicating a homogenous potential distribution. However, the step edges show a much higher image contrast and appear much broader than observed in STM. This result suggests a significant change in the electrochemical properties, probably in the electrochemical surface potential at the step edge.

In the past, intensive studies have shown that defect sites on basal plane HOPG play an important role especially in influencing and controlling the electrochemcial behavior of the basal plane [197, 198, 200, 201]. The anisotropy of HOPG leads to several problems when examining parameters such as adsorption, capacitance and electron transfer kinetics which often vary with the proportions of edge and basal plane on the exposed surface. Based on $Fe(CN)_6^{-3/-4}$ studies, Rice and McCreery [239] found a 1000 times larger electron transfer rate for the basal plane when only 0.1 % of edge defects, with a transfer rate of 0.1 cms^{-1}, are present on the basal plane, with a transfer rate of 10^{-7} cms^{-1}. Furthermore, defect sites such as steps and edges have dangling bonds, giving rise to charged functional groups and reactive sites. Such disordered structures have a locally increased density of states due to the variety of energy levels created by defects, functional groups and local dipoles [240]. Whereas macroscopic techniques such as differential capacitance measurements only yield a spatially averaged response over the whole surface, SECPM is able to map the local potential distribution. Therefore, SECPM enables one to image structural heterogeneities of the basal plane with high spatial resolution and is a promising tool for further investigations of the electrochemical properties and the surface chemistry of HOPG defect sites. However, so far it is not clear why the HOPG step edges appear with a much higher image contrast than the Au(111) steps.

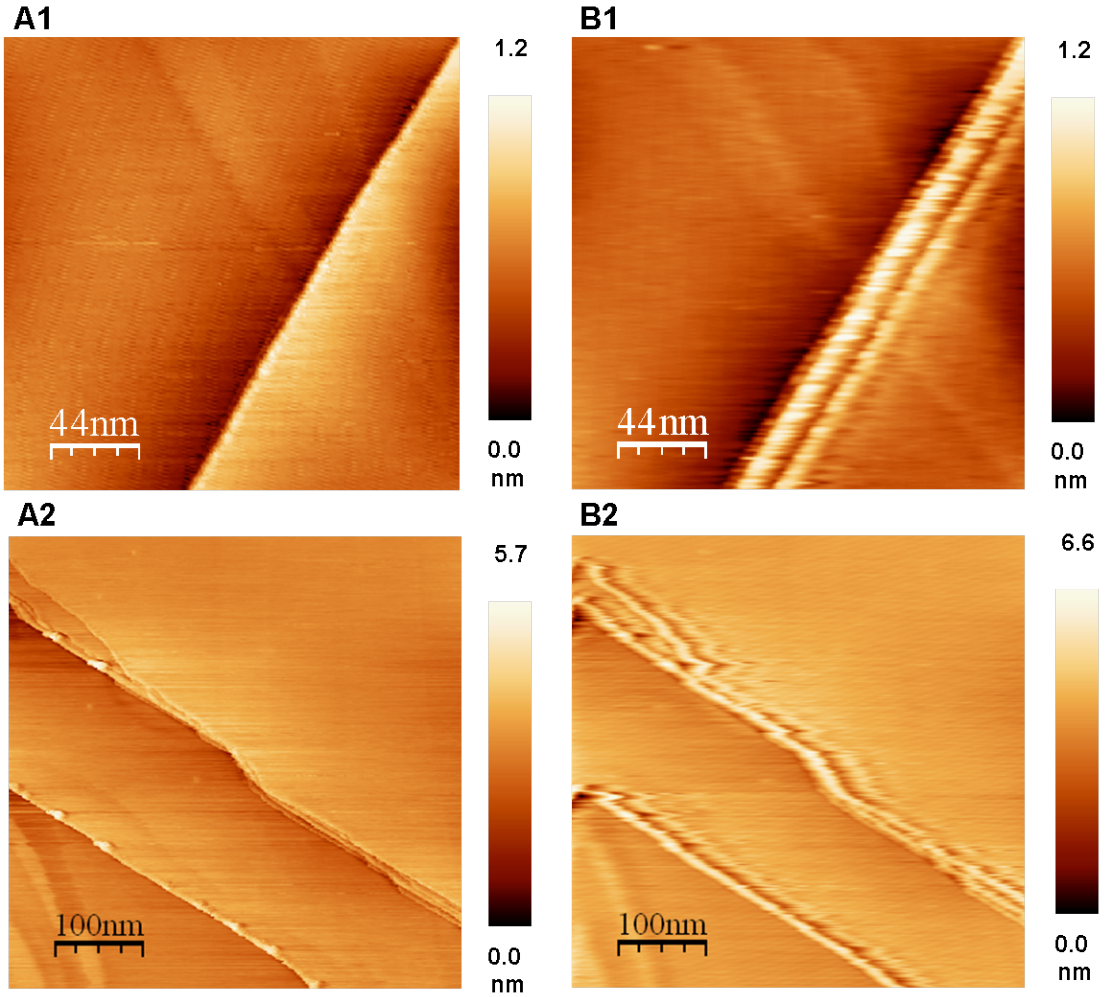

Figure 4.46. Combined A) EC-STM (I_T = 1 nA, U_{Bias} = 100 mV) and B) SECPM ($\triangle U$ = 5 mV) study of the basal plane HOPG surface, obtained in 0.1 M $HClO_4$, U_S = 300 mV vs. NHE. A1 and B1: 220 nm x 220 nm, A2 and B2: 500 nm × 500 nm.

4.4.2. Imaging Enzymes adsorbed on HOPG

Nowadays, imaging of enzymes adsorbed on electrode surfaces is usually performed using AFM. Due to weak interaction forces between the oscillating AFM tip and the soft protein structure tapping mode AFM (TM AFM) is the method of choice to investigate all kind of soft biomolecules: DNA, enzymes or even living cells [241, 242]. However, to gain information about the electronic properties of these biomolecules, STM is indispensable. Especially the electrochemical behavior of redox enzymes is of great interest in biosensor technology, biofuel cell research and bioelectronics. However, the interaction of the STM tip and the biological material, as well as a possible harm caused by the tunneling current are questions of dispute. Combining soft surface imaging and mapping of electronic properties SECPM would be an excellent alternative for both TM AFM and EC-STM. Therefore, SECPM has the potential to become a suitable tool for electrochemical in-situ SPM investigations of biomolecules.

HOPG was chosen as substrate material since performing EC-STM experiments of biological samples requires a flat conducting, inert and structureless electrode. These conditions are satisfied by HOPG which was already used in 1985 by Baro et al. [225] who for the first time performed a STM study of a biological specimen. In this section constant current mode EC-STM and constant potential mode SECPM imaging of enzymes adsorbed on oxidized HOPG is discussed.

4.4.2.1. Ferritin and Apoferritin

Due to its spherical shape the iron storage protein ferritin was chosen as an ideal candidate to test SECPM imaging of enzyme electrodes. Ferritin and its iron free conformation apoferritin have a symmetrical 3D structure consisting of 24 subunits which form a spherical protein shell with a diameter of 12 nm. While each ferritin can store about 4500 Fe(III) ions as $8FeO(OH) \cdot FeO(H_2PO_3)$ crystallites in a core with a diameter of up to 8 nm [86], apoferritin only consists of the hollow protein shell [87]. Although they have the same protein structure ferritin and apoferritin are supposed to have different electronic properties due to the presence and absence of the metal core.

First, ferritin was adsorbed onto oxidized HOPG (HOPGox) and studied using cyclic voltammetry and in-situ EC-STM in 10 mM PBS (pH 7) (Fig. 4.47).

Figure 4.47A shows the CV of the ferritin/HOPGox electrode recorded with a scan rate of 100 mVs^{-1}. The observable redox behavior indicates a direct electron transfer between the ferritin molecules and the graphite electrode. The cathodic peak appears at 160 mV vs. NHE and the anodic peak at 240 mV vs. NHE, giving a mean redox potential of 200 mV vs. NHE (indicated by the dashed line) which can be attributed to the electroactivity of the iron in the core of ferritin [89, 243]. EC-STM images were obtained at a substrate potential $U_S = 300$ mV vs. NHE, applying a bias voltage of 100 mV and a tunneling current of 0.5 nA. A typical EC-STM image of the ferritin/HOPGox electrode show ferritin molecules attached to the HOPG surface (Fig. 4.47B). Single ferritin molecules with a diameter of approximately 8 nm could be observed (see Fig. 4.47C and corresponding line scan in Fig. 4.47D).

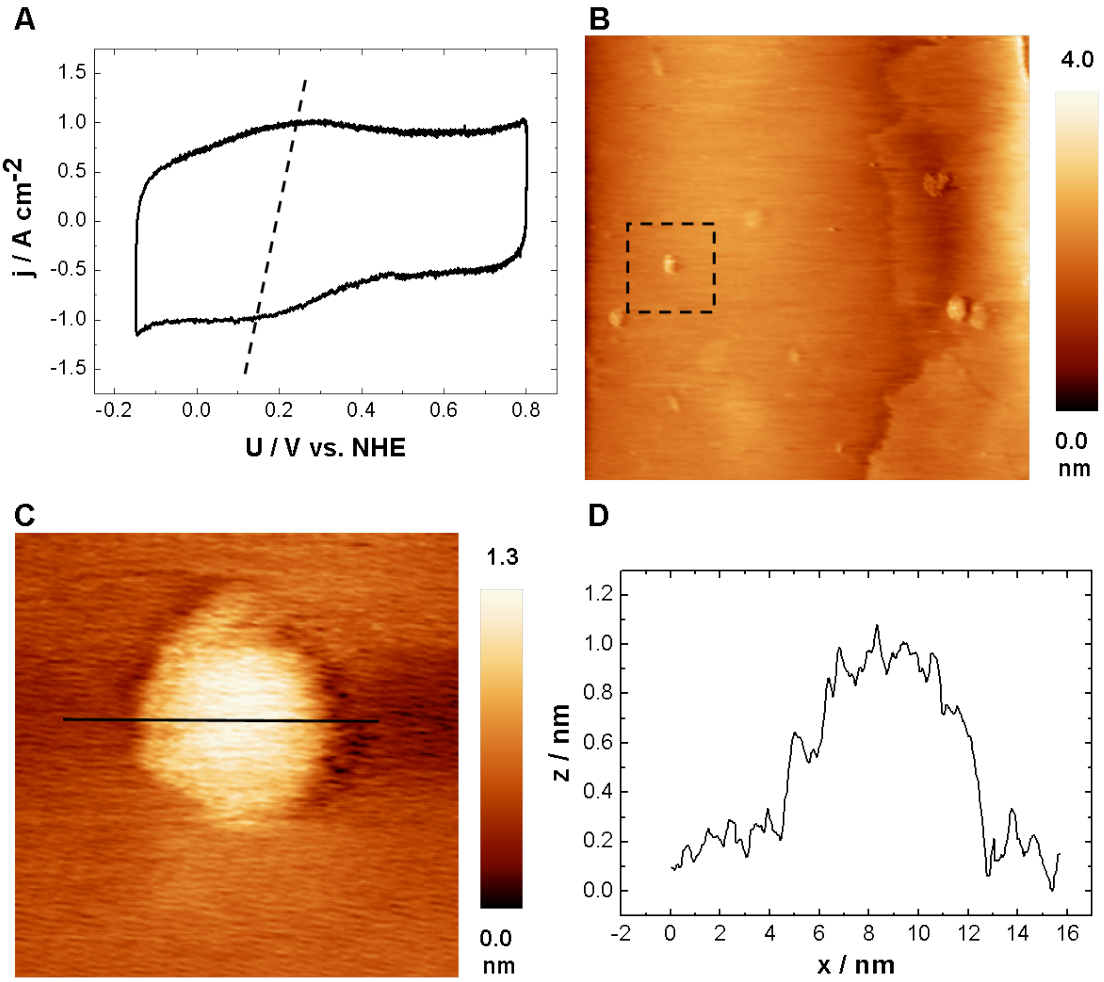

Figure 4.47. A) Cyclic voltammogram (100 mVs^{-1}) and B) EC-STM image of the ferritin/HOPGox electrode in 10 mM PBS (pH 7) (180 nm × 180 nm). C) Single ferritin molecule (19 nm × 19 nm), with D) corresponding line scan analysis showing a molecule diameter of 8 nm).

Then a combined EC-STM/SECPM study was performed, i.e. a defined surface area was first imaged in constant current mode EC-STM and subsequently in constant potential mode SECPM, in order to study the possibilities of both techniques regarding in-situ imaging of biomolecules.

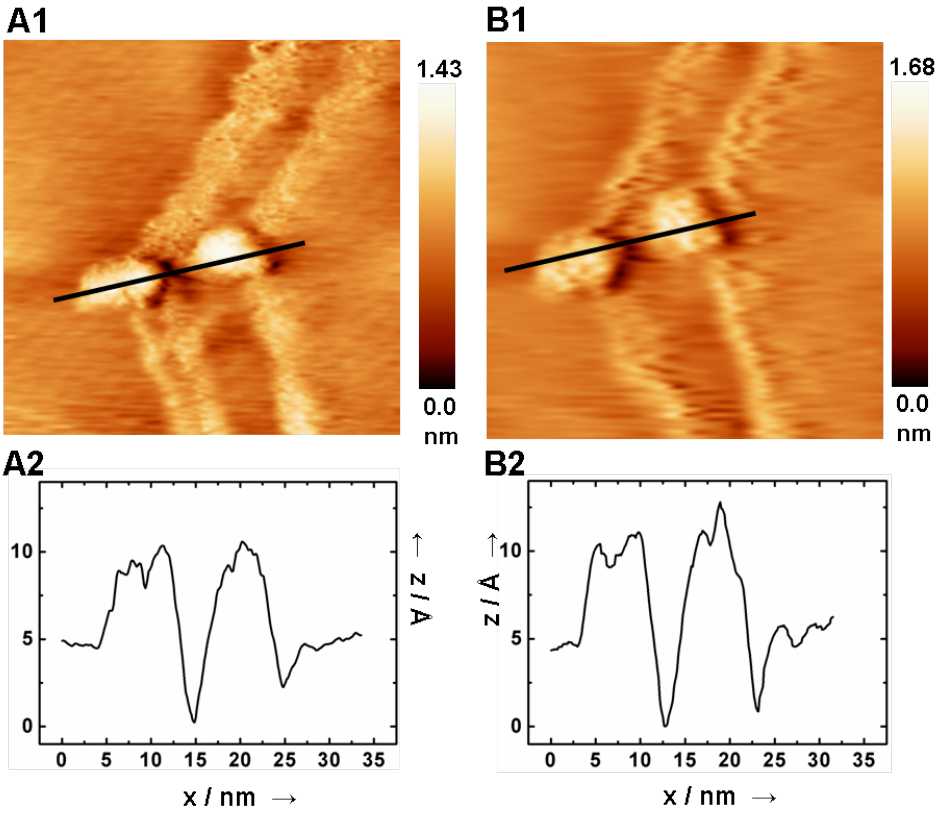

Figure 4.48. A1) EC-STM image and B1) SECPM image of ferritin/HOPGox electrode (40 nm × 40 nm) with corresponding line scans A2) and B2).

Figure 4.48 shows two ferritin molecules adsorbed on line defects of an oxidized HOPG surface imaged in 10 mM PBS using EC-STM (U_{Bias} = 0.1 V, I_T = 0.5 nA) (Fig. 4.48 A1) and SECPM ($\triangle$U = 5 mV) (Fig. 4.48 B1). Both images show a similar shape of the molecules with a diameter of 7.5 nm (left enzyme) and 6.9 nm (right enzyme) and a height of 5 Å relative to the HOPG flat surface (line scans in Fig. 4.48 A2, B2). During STM measurements artifacts may arise from tip-electrode interactions, especially when enzymes are located at HOPG step edges, as can be seen in Fig. 4.49A), or when agglomerates of molecules are imaged. The same electrode area can be imaged in SECPM mode without any disturbance (Fig. 4.49B).
Furthermore, the iron free conformation apoferritin was examined under the same experimental conditions using SECPM and EC-STM. SECPM images resolve single molecules (Fig. 4.50 A) with a diameter of approximately 12 nm extracted from the line scan analysis seen in Fig. 4.50 B. The low image contrast might result from the homogeneous potential distribution of the

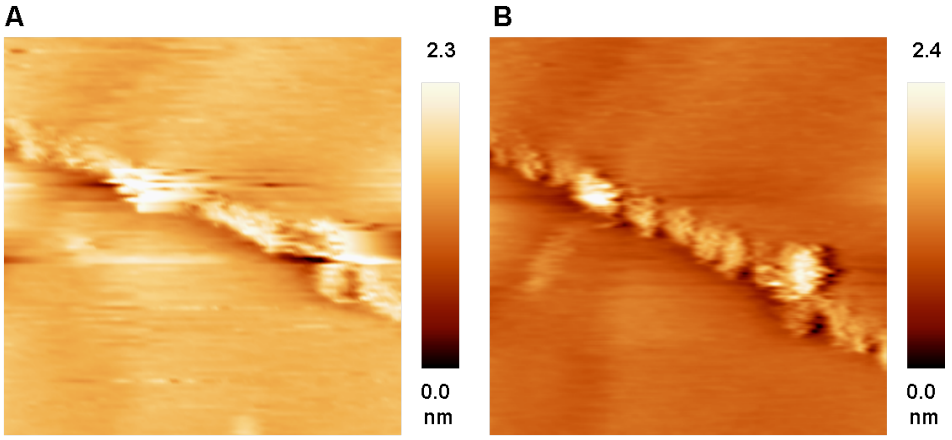

Figure 4.49. A) EC-STM and B) SECPM image of two ferritin molecules adsorbed on an HOPG step edge (U_S = 300 mV vs. NHE, 65 nm × 65 nm).

protein structure. It was not possible to image the apoferritin/HOPGox electrode via EC-STM, probably due to a low conductivity of the protein polypeptide. Therefore, it is assumed that the conductivity (EC-STM) and the potential distribution (SECPM) of the iron atoms inside the cavity of the ferritin molecule dominate in the imaging process and thus superimpose upon the properties of the protein shell and thus only the iron core with a diameter of 8 nm can be resolved in EC-STM and SECPM.

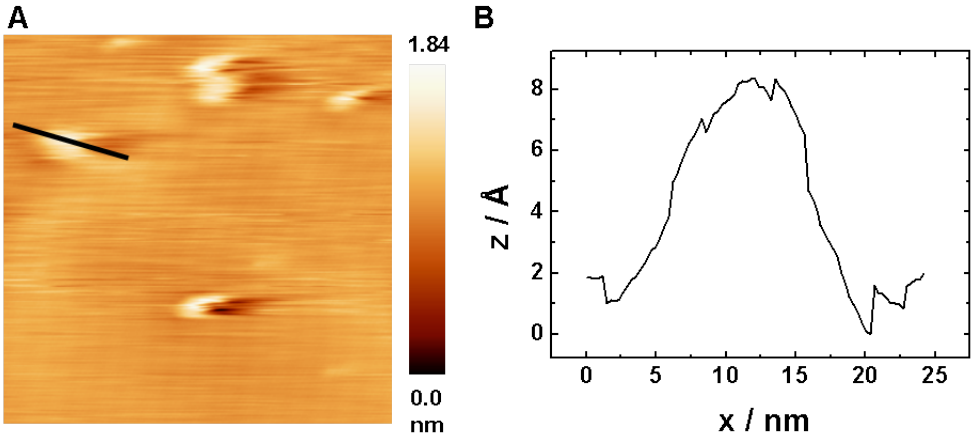

Figure 4.50. A) SECPM image of apoferritin/HOPGox electrode (90 nm × 90 nm) and B) corresponding line scan.

4.4.2.2. Horseradish Peroxidase

In contrast to ferritin, the redox enzyme horseradish peroxidase (HRP) contains only one iron atom located in the active site, the heme group [90]. Single HRP molecules adsorbed on oxidized HOPG were imaged in 10 mM PBS in EC-STM (Fig. 4.51A U_{Bias} = 0.1 V, I_T = 0.5 nA). The four homogeneous bright spots represent single molecules with dimensions of 43 × 34 × 2.4 Å^3. The same area was also imaged in SECPM mode (△U = 5 mV) (Fig. 4.51B). All five visible molecules exhibit an open-loop-shaped structure with mean dimensions of 54 × 52 × 3.2 Å^3. Comparing EC-STM and SECPM, the molecules could be resolved to a much greater extent in SECPM. Furthermore, in SECPM an additional HRP molecule in the upper part of the image (Fig. 4.51B black circle) can be observed which is not visible in STM. A poor electrical contact between enzyme and electrode may inhibit the electron transfer between tip and electrode and thus prevent imaging of the molecule. Since SECPM only maps the charge distribution of the molecule, no electron transfer is required and the molecule is observable.

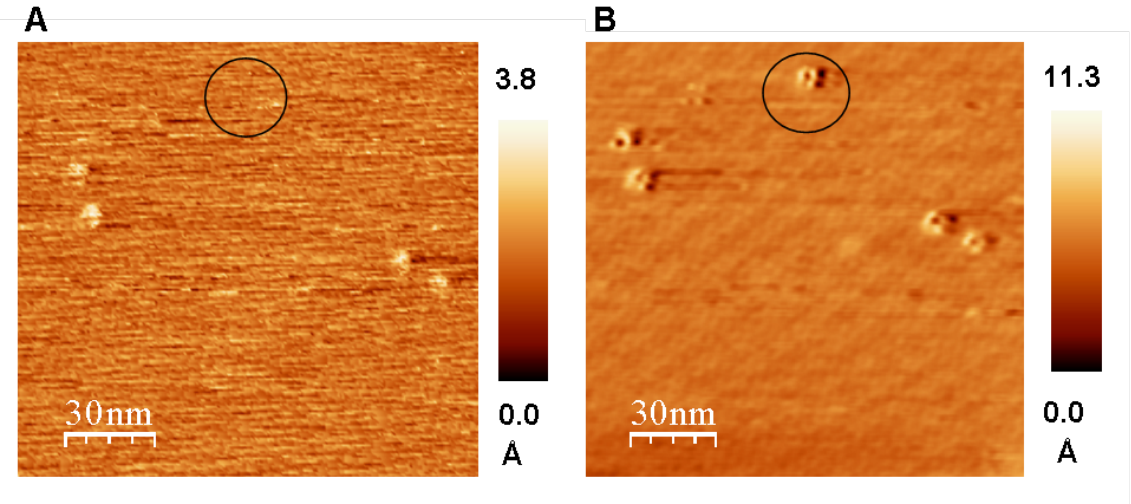

Figure 4.51. A) EC-STM image and B) SECPM image of HRP/HOPGox electrode in 10 mM PBS (pH 7).

In addition, the resolution of the biomolecules in the STM image is relatively low, especially the size of the molecules is smaller than reported by Zhang et al. [14] based on ex-situ (62 × 43 × 12 Å^3) and in situ (68 × 44 × 40 Å^3) STM studies performed on HOPG with I_T = 0.5-1.2 nA. A possible explanation for this observation may be again a poor contact of the enzymes with the substrate possibly impairing the STM image. Furthermore, contributions due to tip intrusion of the molecule moiety must be taken into account. One has to consider that applying a tunneling current of 0.5 nA in STM means that approximately 10^9 e^- per second flow through the molecule or, vice versa, one e^- passes every ns. This may have a negative effect not only on the image quality, but also on the protein structure.

In a 3D representation of the SECPM image (Fig. 4.52A) of two molecules the open-loop

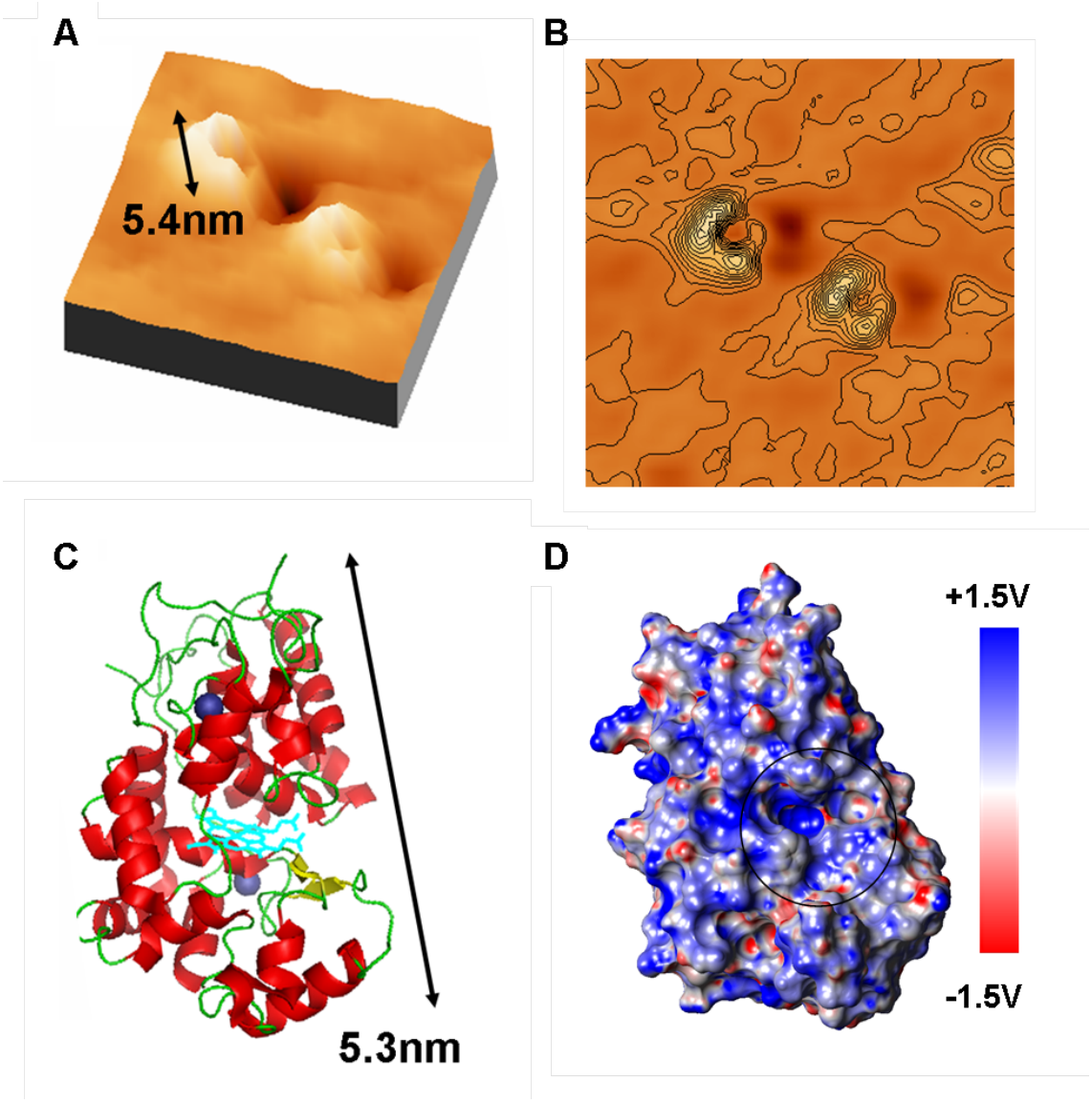

Figure 4.52. A) 3D SECPM image of HRP adsorbed on oxidized HOPG (Zoom in of Fig. 4.51B). B) Contour Plot of A, 45 nm × 45 nm, 10 intermediate contours with 0.27 Å nm^{-1}. C) 3D plot of the X-ray crystal structure of HRP. The heme is colored in turquoise, the calcium atoms are shown in blue, α-helical and β-sheet regions are shown in red and yellow (Plotted with PyMOL [82]), accession code 1w4w from PDB [83].). D) Surface potential of an HRP molecule in 10 mM PBS (pH 7) created by YASARA [244].

structure is clearly recognizable. Figure 4.52 B shows the corresponding contour plot of Figure 4.52A. The lines represent constant height slices with a constant height difference of 0.27 Å. From X-ray crystallographic data it is concluded that the heme is located in a pocket between the distal and the proximal domain of the molecule (Fig. 4.52C) [90]. Comparing the 3D image and the X-ray structure one could suggest that the open-loop seen in SECPM corresponds to the pocket in the protein shell where the active center of the enzyme is located. In order to compare the SECPM images with the charge distribution, the electrostatic surface potential of an HRP molecule immersed in 10 mM PBS (pH 7, T = 298 K) was simulated by YASARA (Fig. 4.52D) [244]. The potential map allows a qualitative comparison with the SECPM data. The position of the active site in the pocket of the protein shell can also be identified in the potential map (Fig. 4.52D black circle) as well as in the SECPM image (Fig. 4.52A and Fig. 4.52B). Compared to the ferritin study, the single Fe of the heme group does not superimpose the signal coming from the protein shell. The position of the metal ion can clearly be located in SECPM due to the potential distribution of the molecule. In order to confirm these findings one could repeat the experiment using Fe free HRP.

4.4.2.3. Remarks

The results show that SECPM is able to image biomolecules under in-situ conditions with an unprecedented resolution. SECPM seems to be a promising electrochemical SPM technique for mapping the charge distribution of adsorbed molecules. Comparing SECPM images with EC-STM images indicates that a potentiometric technique such as SECPM may clearly be advantageous for imaging enzymes at the solid-liquid interface and has the potential to investigate their dynamic behavior on the surface. Further studies e.g. potential dependent imaging or mapping active enzymes should reveal whether SECPM provides new insights into electrochemical properties of the active site of redox proteins and enzmyes.

4.4.3. Potential Profiling

The SECPM was initially designed to measure potential profiles in the electrochemical double layer (EDL) without significant perturbation by the probe [245]. The potential profile of the EDL is theoretically described by the Gouy-Chapman-Stern theory (see Section 2.1.1). Using the SECPM setup, Hurth et al. ([47, 246]) measured the potential profile on several surfaces using $Pt_{0.8}Ir_{0.2}$ tips in a dilute I-I electrolyte (KCl, 0.01 mM).
In this work the potential profiles of an Au(111) single crystal in $NaClO_4$ were investigated using an etched and insulated gold tip. Beside concentration effects, the dependence of the potential profiles on the applied working electrode potential was studied. Prior the SECPM experiments, the gold single crystal was prepared as described in Section 3.4. The profiles, the so called potential-separation plots (P-S plots) were obtained while the tip approached the surface. The potential of the tip was measured with respect to the working electrode potential. The P-S plots give the potential difference $\triangle$U between the substrate potential U_S and the tip potential U_{Tip} versus the distance between electrode and tip, i.e. $\triangle$U(z)-curves are obtained. Since the Au tip

itself is a metallic electrode in contact with the electrolyte, $\triangle$U(z) contains also contributions from the tip potential profile which will be discussed later. Although P-S plots can not be directly compared to theoretical EDL potential profiles of metal electrodes, at least trends of the potential distribution in the nanogap between tip and electrode are expected.

Effects of the Electrolyte Concentration

Since the potential distribution of the electrochemical double layer strongly depends on the concentration of the electrolyte, P-S plots were recorded in different concentrations of $NaClO_4$. The experiment was performed starting with the diluted electrolyte (1 μM) and increasing the concentration up to 1 M in order to avoid distortion by mixing effects. During the measurements the Au(111) single crystal was held at a constant potential of 800 mV vs. NHE. The P-S plots were measured while the tip approached (0.1 Hz for 3 μm) the Au(111) electrode starting 3 μm above the surface, far enough to avoid interactions between the EDLs of tip and substrate. Thereby, a typical etched and insulated gold tip as used in common EC-STM experiments served as potential probe. Figure 4.53 shows the potential profiles obtained in $NaClO_4$ with concentrations ranging between 1 μM and 1 M.

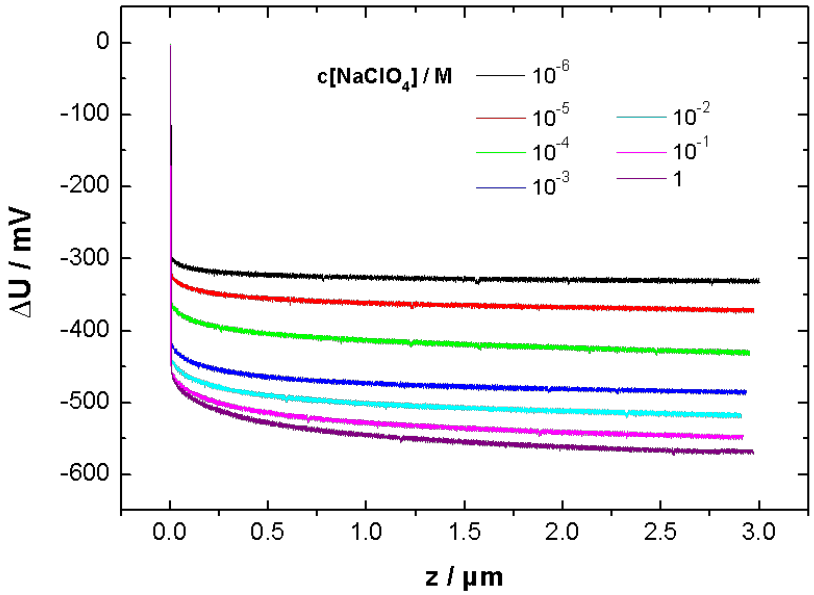

Figure 4.53. Potential-separation plots of an Au(111) surface in $NaClO_4$ (1 μM - 1 M) at an electrode potential of 800 mV vs. NHE, obtained with an etched and insulated Au tip.

Independent of the concentration of the electrolyte, all P-S plots show the same behavior. Far away (3 μm) from the Au(111) surface they all possess a constant potential. When the tip approaches the electrode surface, the potential difference decreases. For higher concentrations the decay starts earlier than for diluted electrolytes, e.g. the P-S plot for 1 M $NaClO_4$ (purple curve in Fig. 4.53) shows a decrease in the potential difference already at distances closer than

2 μm, whereas for the 1 μM $NaClO_4$ (black curve in Fig. 4.53) the decay starts not until 250 nm in front of the electrode. Actually, according to the Gouy-Chapman-Stern theory the opposite behavior would be expected as with increasing electrolyte concentration the Debye length decreases. Finally, when the tip is in the immediate vicinity of the Au(111) the potential difference drops to 5 mV, which is the smallest potential difference allowed by the feedback loop in order to avoid crashing the tip into the electrode surface. The potential difference $\triangle$U between the Au(111) at 800 mV vs. NHE and the gold tip, positioned 3 μm away from the Au(111) surface, is significantly different for different electrolyte concentrations. According to the Gouy-Chapman-Stern theory the potential in the bulk electrolyte, i.e. far away from the electrode is independent of the electrolyte concentration. Therefore, $\triangle$U(z = 3 μm) is expected to be constant for all concentrations, only depending on the OCP of the tip. However, Figure 4.53 shows: the more diluted the electrolyte, the smaller is $\triangle$U(z = 3 μm). So far it is not clear how to explain the observed behavior. Experimental difficulties to obtain the tip at the potential of zero charge (pzc) can not be excluded. The OCP of the tip could be disturbed due to adsorption and Faradaic perturbation from, e.g. dissolved oxygen. Further fundamental studies are required.

Dependence on the substrate potential

According to equation 2.9 the potential distribution of the EDL also depends on the potential that is applied to the electrode. Therefore, for different Au(111) electrode potentials P-S plots were recorded. The concentration of the electrolyte was chosen to be 1 mM, where the thickness of the diffuse double layer is about 10 nm [53]. In Figure 4.54 the P-S plots for U_S = 800 mV vs. NHE (black curve), 500 mV vs. NHE (red curve) and 300 mV vs. NHE (green curve) are shown.

Again the shape of all three P-S plots is similar. They run almost in parallel following the behavior described before. The potential difference $\triangle$U between the Au(111) and the gold tip positioned 3 μm away from the Au(111) surface is significantly different for different electrode potentials. The absolute value of the measured $\triangle$U(z=3 μm) is highest for an electrode potential of 800 mV vs. NHE, shows a minimum at 500 mV vs. NHE and increases again for smaller potentials such as 300 mV vs. NHE. This behavior might probably be explained by influences of the OCP of the Au(111) single crystal electrode which was measured to be 550 mV vs. NHE, i.e. close to the applied substrate potential of 500 mV vs. NHE. Since the tip is also made up of gold a similar OCP can be assumed. Therefore, the potential difference $\triangle$U between single crystal electrode and tip is expected to be smallest when substrate potentials close to the OCP are applied to the Au(111).

Remarks

The measured potential profiles obtained for an Au(111) in different concentrations of $NaClO_4$ and for different applied electrode potentials do not follow the potential distribution of an EDL predicted by the classical Gouy-Chapman-Stern theory, neither quantitatively nor qualitatively. It is known that the interaction between both EDLs influences the observed P-S plots. Thus, calculations are possibly required in order to substract the contribution of the tip electrode.

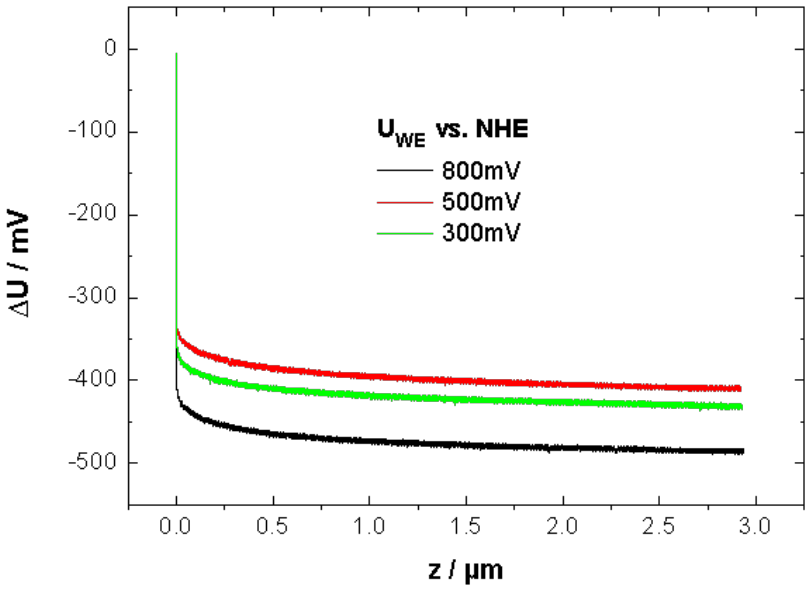

Figure 4.54. Potential-separation plots of an Au(111) surface in 1 mM $NaClO_4$ for different applied electrode potentials: black curve: 800 mV vs. NHE, red curve: 500 mV vs. NHE, green curve: 300 mV vs. NHE, obtained with an etched and insulated Au tip.

Furthermore, we assume that the extension and the shape of the metallic apex play an important role. Potential profiles reported by C. Hurth et al. [47] did also not fit the GCS theory (4.55), Figure 4.55 shows the normalized potential profiles as a function of the Pt foil surface potential in a 10 μM KCl solution (Fig. 4.55A) and for different electrolyte concentrations (Fig. 4.55B). Since all curves overlap, no dependence on the surface potential could be observed. Changing the electrolyte concentration resulted in a change of the decay length of the P-S curves, however for electrolyte concentrations higher than 0.1 mM no significant differences were observed. They suggested that the tip extension along the z-axis limits the smallest Debye length that can be resolved.

Therefore, future work has to reveal which kind of tip is perfectly suited for SECPM, not only regarding tip geometry, but also tip material and insulation, and to develop a procedure in order to reproducibly produce such tips. Additionally, it must be pointed out that further experimental challenges occur within the potential profiling experiment. It could be observed that the shape of the potential profiles significantly changes by applying different approach velocities. Especially at high frequencies the curves tend to be not reproducible, probably indicating that the potential detected at the tip is not at equilibrium and possibly affected by the movement of the tip. Therefore, the fundamental question of the response time of double layers to changes induced in the environment still remains. Furthermore, a reference electrode with a stable potential behavior, i.e. a fixed equlibrium potential is required. Assuming a reference electrode with only a slightly oscillating potential ($\pm$ 5 mV) might cause crashing the tip into the electrode surface

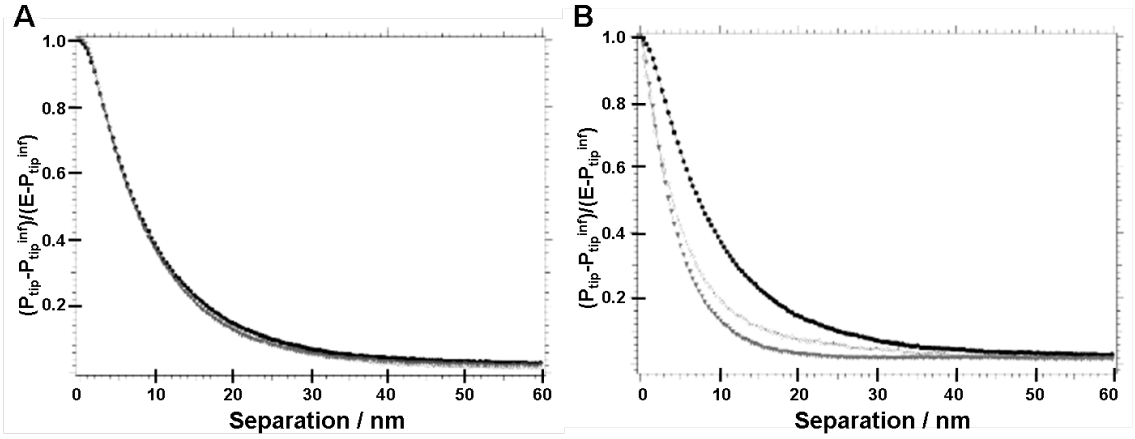

Figure 4.55. A) Potentiometric approach curves on the Pt foil surface held respectively at +400 mV (filled black circles), +300 mV (filled gray triangles), and +200 mV vs. a platinum polypyrrole reference electrode (PtPPy) (empty gray boxes) recorded at 20 nms^{-1}) in 10 μM KCl. B) Influence of the electrolyte concentration on the double-layer profile obtained by approaching the Pt foil surface held at +400 mV vs. PtPPy at 20 nms^{-1}) in 10 μM (filled black circles), 100 μM (filled gray triangles), and 1 mM (empty gray boxes) KCl. The curve corresponding to 1 mM KCl should decay faster than all others. However, in this case the typical electrode size falls within the value of the expected Debye length for a 1-1 electrolyte at 1 mM (9.6 nm). The curves are normalized to the applied surface potential, E, and the tip potential far away from the Pt foil surface, $P_{tip}^{inf} \approx$ 32 mV vs. PtPPy, adopted from [47].

leading to a deformation of the tip apex. As already mentioned the tip and its free apex seem to be crucial for potential profiling experiments as will be discussed in the following section.

4.4.4. The SECPM tip

As in all SPM techniques special care has to be taken for the tip preparation which has to be tailored to the specific needs of the technique, i.e. the shape of the tip, its free surface area, thus the tip insulation and the tip material have to be adjusted to the experimental conditions. Especially SPM imaging in x-y-direction yields always a convolution of the geometry of the tip and the topographical structure of the investigated surface. Furthermore, electronic effects of the tip such as influences caused by the EDL of the tip have to be taken into account.

4.4.4.1. Geometry of the tip

Since the change in the potential distribution perpendicular and parallel to the electrode surface is different, the tip geometry should be dependent on the scan mode. For this discussion the cases x-z profiling and x-y imaging have to be distinguished (Fig. 4.56).

For potential profiling in x-z direction (Fig. 4.56A), the required spatial resolution depends on the extension of the tip along the z-axis which has to be considerably smaller than the expected Debye length of the EDL. Due to its extension $\triangle z$, a thin tip can measure the potential

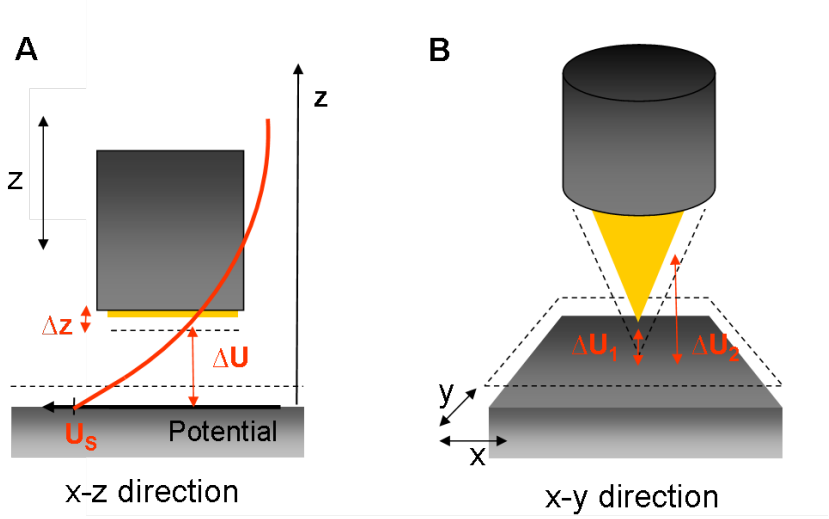

Figure 4.56. Scheme of the tip influence depending on SECPM operation mode: A, Potential profiling mode (x-z direction) and B, Constant potential mode (x-y direction)

distribution perpendicular to the electrode with a resolution given by $\frac{\triangle U}{\triangle z}$.
For scanning in x-y direction in constant potential mode (Fig. 4.56B) a sharp tip like in EC-STM is preferred. The free tip surface probes different potentials $\triangle U_1$ and $\triangle U_2$ (indicated by the red arrows in Fig. 4.56) at different positions of the apex. Since the decay of the EDL follows an exponential behavior, a change in the charge distribution at the surface would lead to a significant change in $\triangle U_1$, but would probably be negligible for $\triangle U_2$, assuming that the extension along the z-axis is larger than the expected Debye length (Fig. 4.56).

4.4.4.2. Overlapping double layers

Furthermore, the tip is a metal electrode with an EDL at the solid-liquid interface. As long as the tip is sufficiently far away from the electrode surface there is no interaction between the two EDLs (see Fig. 4.57A). However, when the tip approaches the electrode, the EDLs of both will overlap at close distances (Fig. 4.57B); such effects are already known from EC-STM studies [35, 247, 248]. Since the STM tip potential influences the local electrode potential underneath the tip apex, these effects have to be taken into account e.g. in in situ metal deposition and dissolution [249, 250].

In SECPM the presence of the EDL at the tip has a direct impact on the measuring signal, since the SECPM signal is a convolution of the EDLs of tip and electrode. However, for a discussion of the tip influences on SECPM measurements, again the x-z and the x-y mode have to be distinguished. While scanning in the x-z direction, the probed potential at the tip is a function of the distance relative to the surface $f(z)$ i.e. the effects of overlapping double layers increase with decreasing distance. In dilute electrolytes, following the Gouy-Chapman theory the effect can be calculated. Based on a symmetrical problem, one can deconvolute the potentials

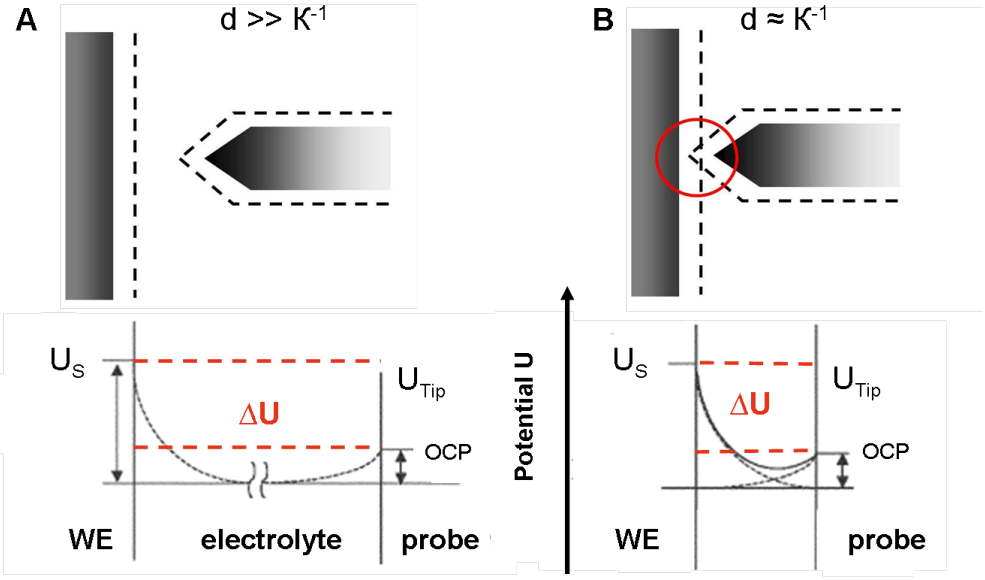

Figure 4.57. Scheme of the EDLs present at the tip and the electrode surface, based on [46]: A) When tip and electrode surface are far apart the two EDLs do not influence each other. B) When the tip approaches the surface the EDLs start overlapping.

and calculate the EDL of the electrode surface.

Woo et al. [46] suggested a simplified approach where the interfacial potential is represented as a linear superposition of two independent EDLs, assuming two planar surfaces and no interaction between the EDLs. However, Hurth et al. [47] claimed that a more complex situation with interacting double layers and a nanogap between a tip at OCP and a electrode at a fixed potential has to be considered. In x-y mode with a set $\triangle$U between the tip and the sample, the height of the tip will only slightly change in order to keep the potential difference constant. Therefore, the effects coming from the overlap of the EDLs can be considered being of small variation within the measurements. When the tip approaches the electrode both EDLs will overlap; again the x-z and the x-y mode have to be distinguished. For moving in the x-z direction towards the surface the potential measured at the tip is increasingly influenced by the overlapping EDLs. In the x-y mode, the influences of two overlapping EDLs can be considered as almost constant throughout the imaging since changes in height are negligible compared to the extension of the free area of the tip. With an adequate model of two overlapping EDLs at identical metals, both following the Gouy-Chapman-Stern theory it might be possible to deconvolute the potentials and to calculate the EDL at the electrode surface. However, one has to keep in mind that the GCS theory is only valid for diluted I-I electrolytes and furthermore, has to be adjusted to the nanogap geometry present in the SECPM setup.

4.4.4.3. Application as local pH sensor

In the past, it has been shown that the EC-STM tip can be used as a local sensor in order to measure the reactivity of single Pd [159, 160] or Pt nanoparticles [251]. Thereby, the tip probes the reaction products of a catalytic reaction occuring at the nanoparticle in the reverse process, e.g. hydrogen is evolved at the nanoparticle and will be oxidized at the unisolated STM tip apex yielding in an oxidation current. A second approach to measure the activity of nanoparticles or possibly even enzymes is to locally probe the change in proton concentration within the catalytic reaction using the SECPM tip as a potential sensor. Since a change in proton concentration changes the local pH causing a potential shift of 59 mV per pH value, hydrogen evolution or oxidation can be directly detected at the potentiometric SECPM tip by a shift of its OCP, presuming that the tip is pH sensitive. In order to have a pH sensitive Pd SECPM tip, palladium has to be loaded with hydrogen.

Hydrogen Loading
In order to form palladium hydride electrodes polycrystalline palladium was loaded with hydrogen by galvanostatic pulses in an electrochemical glass cell. This technique has already been introduced earlier [178]. Figure 4.58 shows typical potential transients obtained for three different applied current values (-100 μA, -300 μA, -500 μA) and a pulse length of 500 s. Before and after the pulse, the OCP was measured for 20 s and 100 s, respectively. The curves are recorded in 1 M $NaClO_4$ containing 0.01 M $HClO_4$ (pH 2.5). The time transients start at a high open circuit potential around 1 V vs. NHE, indicating the equilibrium potential of palladium oxide. Applying negative currents to the electrode, which means enforcing the adsorption, absorption and evolution of hydrogen, the potential subsequently drops below 0 mV vs. NHE. For small current values (-100 μA, black curve in Fig. 4.58) the potential stays constant within the pulse length of 500 s and the OCP detected after the hydrogen loading steadily increases. For higher currents (-300 μA and -500 μA, red and green curve, respectively) the measured potential further decays after some time to a second potential plateau with a value between -700 mV and -750 mV vs. NHE, where it stays constant for the rest of the pulse. After the galvanostatic pulse, the OCP of the electrodes reaches steady state with a equilibrium potential of -160 mV vs. NHE.

The transients can be explained as follows:
The inital potential drop includes double layer charging, hydrogen adsorption and α Pd hydride formation, while the first potential plateau is thought to represent the completion of the β hydride phase. The further potential decay and thus the increase in overpotential could be attributed to the hydrogen gas evolution. Similar results were found earlier for potentiometric measurements where Pd/H was formed by applying negative potentials and detecting the current transients [173].

However, measuring the OCP of these Pd/H electrodes for further 600 s revealed that the potential was not constant with time, independent of the current applied within the galvanostatic pulse (Fig. 4.59). The increase in potential indicates the diffusion of hydrogen into the electroyte, i.e. that the stable (α + β) phase of the palladium hydride has not been formed.

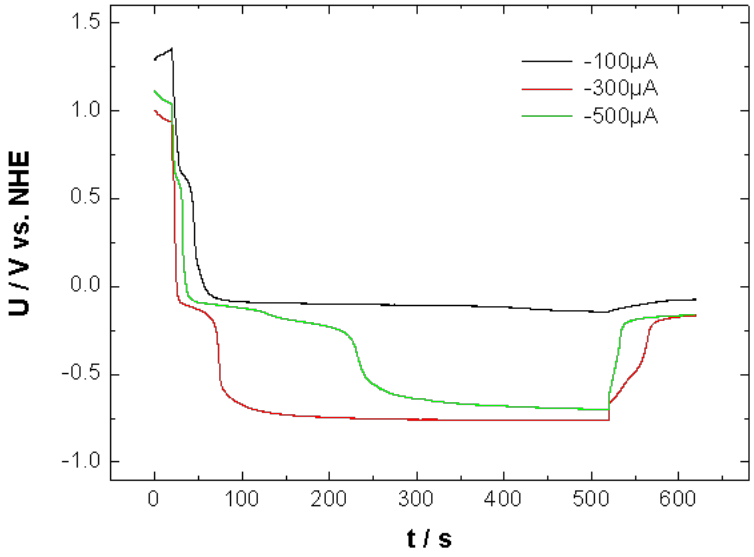

Figure 4.58. Formation of Pd/H electrodes by applying a galvanostatic pulses in 1 M $NaClO_4$ + 0.01 M $HClO_4$ (pH 2.5), pulse length 500 s, different applied current values: black curve: -100 μA, red curve: -300 μA, green curve: -500 μA.

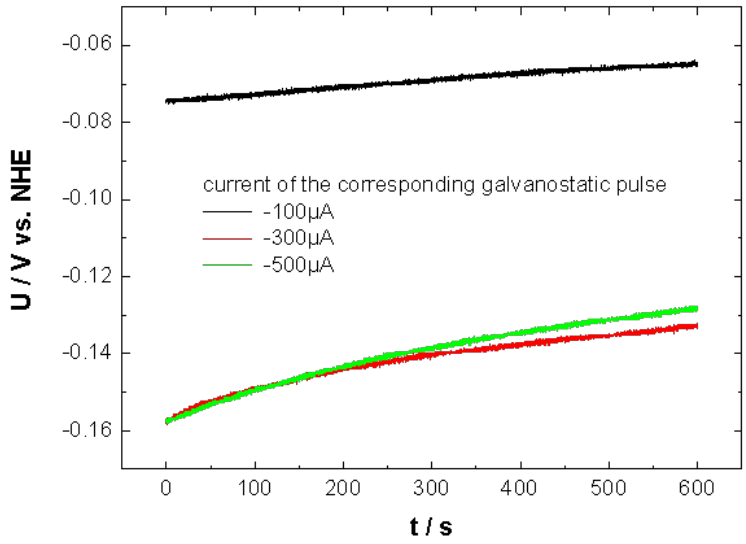

Figure 4.59. OCP measurements of the Pd/H electrodes formed by galvanostatic pulses shown in Fig. 4.58.

Flanagan and Lewis [252] found that the electrochemical loading of palladium electrodes can lead to a higher concentration of hydrogen at the surface than in the bulk, especially beyond the ratio H/Pd = 0.4. Therefore, an anodization procedure right after the electrolysis was applied to the Pd/H electrode in order to remove excess surface hydrogen and relieve concentration gradients [180]. Figure 4.60 shows the galvanostatic procedure for the stable Pd/H formation in the ($\alpha + \beta$) phase (red curve, right axis) and the corresponding potential transient (black curve, left axis) obtained in 1 M $HClO_4$. The galvanostatic process consists of 1. an OCP measurement for 10 s, 2. the H loading pulse with an applied current of -300 μA for 500 s, 3. an anodization pulse with an applied current of 200 μA for 20 s and 4. the final OCP measurement for 600 s. Again, with the beginning of the charging current, the potential response decays immediately from 780 mV vs. NHE down to -25 mV vs. NHE and stays constant according to the formation of the β hydride phase. Then the anodization pulse causes a potential increase up to 15 mV vs. NHE indicating the release of hydrogen from the Pd/H electrode by a hydrogen oxidation process. The following OCP measurement results in a stable potential of 0 mV vs. NHE indicating that the stable ($\alpha + \beta$) phase is obtained.

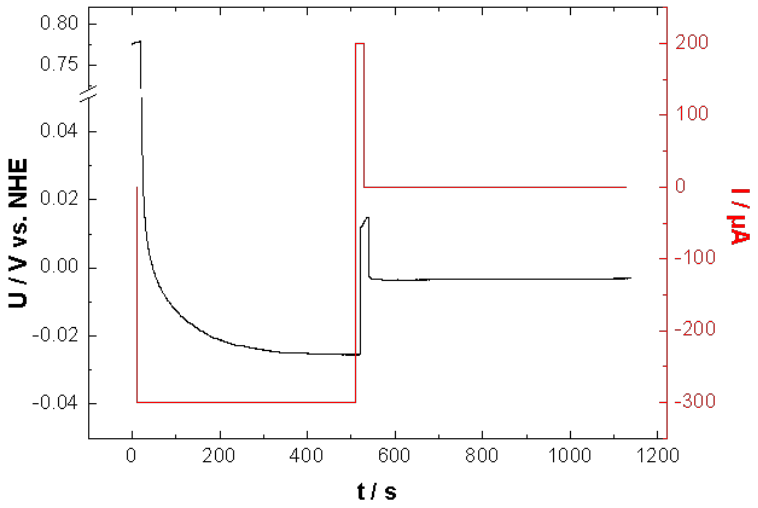

Figure 4.60. Formation of Pd/H electrodes by applying a galvanostatic pulse in 1 M $HClO_4$ (pH 0.8) and subsequent anodization procedure followed by OCP measurement. The potential transient is shown in black according to the left axis and the applied current of the galvanostatic pulse is shown in red according to the right axis.

pH Sensitivity

In order to investigate the pH sensitivity of the Pd/H electrodes, titration experiments were performed. A Pd/H electrode was prepared as described above in 1 M $HClO_4$ and transferred to 1 M $NaClO_4$. If necessary the preparation procedure was repeated in 1 M $NaClO_4$ until a stable OCP was achieved. Starting at a pH value of approximately 5 in 1 M $NaClO_4$ (80 ml) electrolyte the H^+ concentration was increased by adding stepwise $HClO_4$ in different concentrations. During

the whole experiment the OCP of the Pd/H electrode was recorded. Figure 4.61 shows the potential transient of the Pd/H electrode versus time. In the beginning, i.e. at higher pH values, only low amounts of diluted $HClO_4$ were added to the electrolyte since the pH is proportional to the logarithm of the H^+ concentration and thus, only small changes in the H^+ concentration strongly affect the pH. With decreasing pH the amount and the concentration of $HClO_4$ were increased (exact values see Fig. 4.61). At the end of the experiment the pH of the electrolyte was measured with a pH meter to be 0.79.

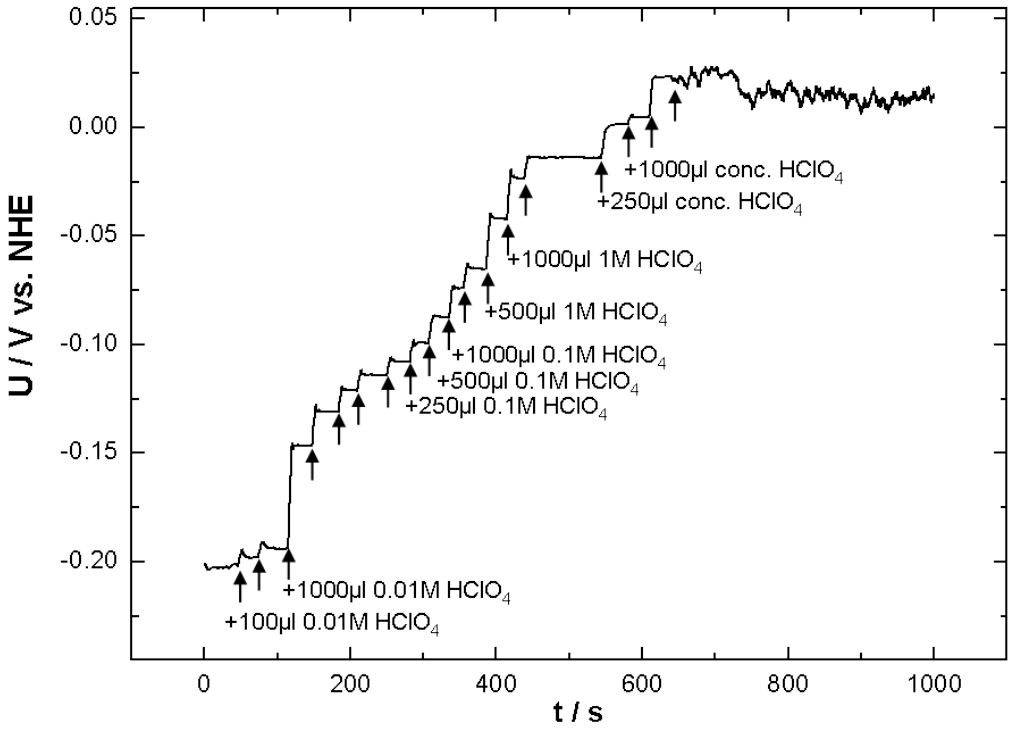

Figure 4.61. Titration curve: Potential response of a Pd/H electrode immersed in 1 M $NaClO_4$ when stepwise decreasing the pH value by adding different amounts and concentrations of $HClO_4$. The arrows indicate the injection of $HClO_4$. The amount and concentration of the injection is stated at the arrow.

From the amount and concentration of added $HClO_4$ the pH value of the electrolyte can be calculated after each step. The relation between the OCP of the Pd/H electrode and the pH value is presented in Figure 4.62. The black curve is the linear fit to the measured data points yielding a slope of -56 mV per pH value and an intersection point with the ordinate of 58 mV vs. NHE for pH 0. Within accuracy, these data are in good agreement with theoretical and literature data stating a slope of -59 mV per pH [53, 173] and an equilibrium potential of the (α + β) phase of 50 mV vs. NHE [180, 181]. These results show that the Pd/H electrode can be used as pH sensor.

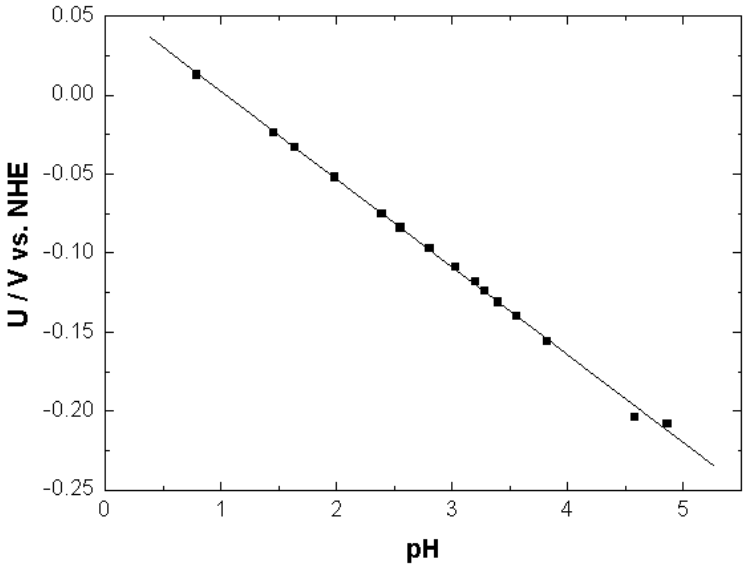

Figure 4.62. pH sensitivity of the Pd/H electrode OCP, evaluated from the titration curve shown in Figure 4.61

4.5. Oxygen-Terminated Diamond for Biomolecule Immobilization

So far, HOPG was used as electrode material for the immobilization and electrochemical investigation of biomolecules. Due to its smooth surface the basal plane of HOPG is a suitable model electrode which provides single molecule studies using SPM techniques. However, for technical applications e.g. in electrochemical biosensors or bioelectrochemical fuel cells, the use of HOPG is disadvantageous since HOPG is susceptible for corrosion. Therefore, biocompatible electrode materials with a higher electrochemical and mechanical stability are of great importance. Due to its unique properties regarding electrochemical inertness, stability and biocompatibility boron-doped diamond is a promising alternative carbon material for biomolecule immobilization and electrochemical characterization.
In this section oxygen-terminated synthetic boron-doped diamond electrodes are investigated concerning their suitability for electrochemical biosensing electrodes. Different oxidation procedures were applied to the diamond electrodes in order to form oxygen containing groups on the surface and improve immobilization of redox active biomolecules. Furthermore, electrodes with different morphology, i.e. nanocrystalline diamond films (NCD) and single crystal diamond (001) electrodes were used. The surface coverage and the direct electron transfer are studied by cyclic voltammetry.

4.5.1. Characterization in Phosphate Buffer Solution

Prior to enzyme adsorption the diamond electrodes were studied by cyclic voltammetry in the potential range between -0.15 V and 1 V vs. NHE in 10 mM PBS (pH 7). Figure 4.63 shows the CVs obtained at a scan rate of 100 mVs^{-1}. The red curve corresponds to the diamond terminated by oxygen plasma, also called μ-etch, the green curve to the wet chemical oxidation (WC), the blue curve to the reactive ion etching (RIE) and the black curve is an untreated, i.e. "as grown" and therefore hydrogen-terminated surface. Except for the electrode terminated by RIE all electrodes show a similar capacitive behavior in the phosphate buffer according to a double layer capacitance of approximately 4.5 μFcm^{-2}. This value is in good agreement with literature data obtained from electrochemical impedance spectroscopy [13]. The CV of the RIE treated diamond shows a positive current density starting at 0.3 V vs. NHE, steadily increasing up to 1 V vs. NHE when sweeping from negative to positive electrode potentials, and an increased negative current density between 1 V and 0.7 V vs. NHE when sweeping backwards from positive to negative potentials, respectively. This might indicate that an electrochemical process takes place at the electrode surface, which is only partially reversible. All other CVs show currents only determined by the double layer charging of the electrode due to the fact that the oxidized surfaces are electrochemically inert.

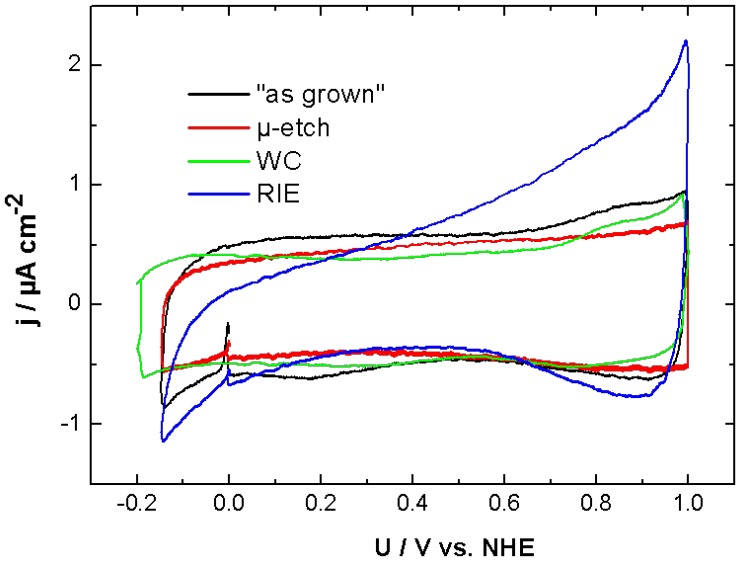

Figure 4.63. Cyclic voltammograms of diamond electrodes oxygen-terminated by different oxidation procedures, obtained in 10 mM PBS (pH 7) at a scan rate of 100 mVs^{-1}.

4.5.2. Ferrocene labeled Papain on Diamond

The nanocrystalline diamond (NCD) films were oxygen-terminated by the three different oxidation procedures described in Section 3.4.4 in order to immobilize and investigate the electroactive FcAL@papain molecules (studied in detail in Section 4.3.3). A NCD film without surface modification, i.e. "as grown", served as a reference electrode. For comparison FcAL@papain was also adsorbed on an oxidized HOPG electrode surface. All electrodes were freshly prepared, being exposed to one adsorption procedure (2 h incubation at room temperature) using the same enzyme solution (0.1 $mgml^{-1}$ in 10 mM PBS, pH 7).

Figure 4.64 shows the CVs (100 mVs^{-1}) obtained after the adsorption procedure. The color coding is given in the figure caption and is the same as the one for Figure 4.63. Additionally, the CV of the FcAL@papain/HOPGox electrode is shown in turquoise. The capacative background current of the oxidized HOPG electrode is by a factor of 2 larger than the background current of the NCD electrodes. The FcAL@papain/HOPGox electrode shows a significant redox behavior with a redox potential at 555 mV vs. NHE, as already known from chapter 4.3. In contrast, only for the NCDs which were oxygen terminated by wet chemical oxidation (green curve in Fig. 4.64) and by μ-etch (red curve in Fig. 4.64) redox peaks can be observed. From the CV of the NCD modified by the reactive ion etching (RIE) (blue curve in Fig. 4.64) a redox behavior can also be assumed in the range of 0.7 V vs. NHE. However, the oxidation and reduction peaks are superimposed by the background current which was already observed for the pure NCD RIE. The untreated NCD "as grown" shows no redox behavior (see black curve in Fig. 4.64). Untreated NCDs are usually hydrogen-terminated and thus, hydrophobic. The lack of chemically reactive

groups usually precludes the attachment of biomolecules to the surface [220], i.e. FcAL@papain molecules can not stably bind to the "as grown" NCD electrode and thus no direct electron transfer is visible in the cyclic voltammogram.

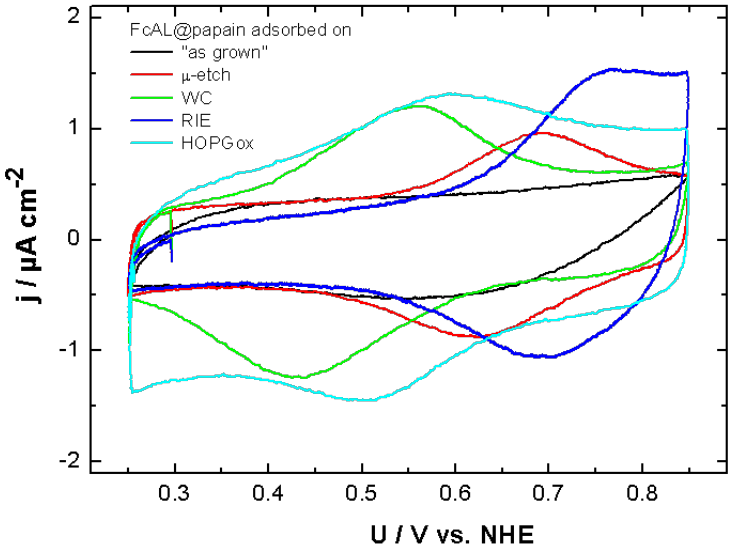

Figure 4.64. Cyclic voltammograms of FcAL@papain adsorbed on oxidized HOPG and differently treated diamond surfaces, obtained in 10 mM PBS (pH 7) at a scan rate of 100 mVs^{-1}.

Furthermore, the surface coverage and the redox potential of the FcAL@papain adsorbed on different electrodes is significantly different. For all electrodes, the redox potential, the charge densities evaluated from the oxidation peak (q_{ap}) and the reduction peak (q_{cp}), as well as their ratio q_{ap}:q_{cp} are given in Table 4.4. The lowest redox potential of 495 mV Vs. NHE was found for the NCD treated by wet chemical oxidation. The redox potential for μ-etched NCD is 160 mV more positive at 655 mV vs. NHE and the redox potential for the RIE NCD, although only assumed, is even higher at 720 mV vs. NHE. Due to the high background current the reactive ion etching procedure seems to be not suitable for biomolecule immobilization. XPS studies performed by Dr. Andrej Denisenko at the University in Ulm have shown that this oxidation technique roughens the surface and leads to C-O-C and C=O groups at the diamond surface with an underlying 3 nm to 6 nm thick insulating layer made up of amorphous diamond (α-sp^3). Therefore, further experiments and evaluation were focused on the WC and μ-etch diamond. According to the detected charge, nearly the same amount of FcAL@papain molecules were adsorbed onto the oxidized HOPG surface and the μ-etch diamond, while the NCD modified by the wet chemical oxidation shows a 50% higher surface coverage. However, since the charge densities are based on the geometric surface area of the electrodes it is hard to compare these absolute values without knowing the roughness factor of the different surfaces. The ratio of the charge densities q_{ap}:q_{cp} is for all electrodes close to unity, indicating a completly reversible electron transfer process independent of the surface modification.

FcAL@papain	U_0	q_{ap}	q_{cp}	q_{ap}:q_{cp}	Γ
adsorbed on	**mV vs. NHE**	μ**Ccm**$^{-2}$	μ**Ccm**$^{-2}$		**pMcm**$^{-2}$
HOPGox	555	0.806	0.798	1.01	8.29
diamond WC	495	1.196	1.225	0.98	12.5
diamond μ-etch	655	0.890	0.882	1.01	9.18
diamond RIE	720	-	-	-	-
diamond "as grown"	-	-	-	-	-

Table 4.4. Redox potential U_0, charge density of the oxidation (q_{ap}) and the reduction peak (q_{cp}) evaluated from the CVs shown in Figure 4.64, the ratio of q_{ap}:q_{cp} and the surface coverage Γ.

Cyclic voltammetry at different scan rates between 0.1 Vs^{-1} and 1 Vs^{-1} was performed for the electrodes FcAL@papain/diamond WC (triangles, Fig. 4.65A) and FcAL@papain/diamond μ-etch (squares, Fig. 4.65A). The redox peaks show a linear variation in the peak current density with increasing scan rate, indicating that the FcAL@papain molecules are surface bound and undergo direct electron transfer with the oxygen-terminated diamond electrode surfaces (Fig. 4.65A). For comparison, Figure 4.65B shows the linear increase in peak current density with increasing scan rate for the FcAL@papain/HOPGox electrode, showing also a direct electron transfer between the electrode and the redox-active ferrocene group of the FcAL@papain molecules.

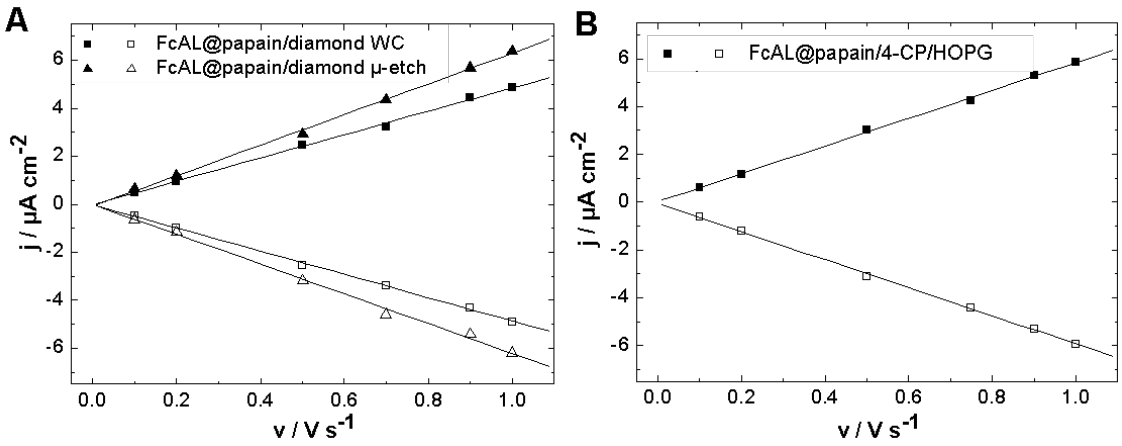

Figure 4.65. Peak current density j plotted versus the scan rate v obtained from CVs of A) FcAL@papain/diamond μ-etch (squares) and FcAL@papain/diamond WC (triangles) and B) FcAL@papain/HOPGox electrodes.

4.5.3. Azurin on Diamond

Electron transfer studies of the metalloprotein azurin covalently immobilized on carboxyphenyl modified HOPG and adsorbed onto oxidized HOPG surfaces have already been shown in Section 4.1.3 in order to compare and evaluate both immobilization techniques. Therefore, azurin will also be used here to investigate the interfacial electron transfer between a redox active biomolecule and oxygen-terminated diamond electrodes. Single crystal boron-doped CVD diamond (001) was used in order to have smooth surfaces with sub-nanometer roughness, i.e. the geometric area is almost equal to the active surface area, comparable to the HOPG. In the previous section it was shown that wet chemical oxidation and μ-etching provides the immobilization of biomolecules onto the diamond surface and enables a direct electron transfer. Therefore, the electrode surfaces were oxygen-terminated only by the wet chemical (WC) oxidation and the μ-etch procedure. For comparison azurin was also adsorbed on an oxidized HOPG electrode surface. All electrodes were freshly prepared, being exposed to one adsorption procedure (2 h incubation at room temperature) using the same enzyme solution (0.1 mgml^{-1} in 10 mM PBS, pH 7). In Figure 4.66 the cyclic voltammograms obtained for the azurin/diamondWC (black curve), azurin/diamond μ (red curve) and azurin/HOPGox (green curve) electrodes are shown.

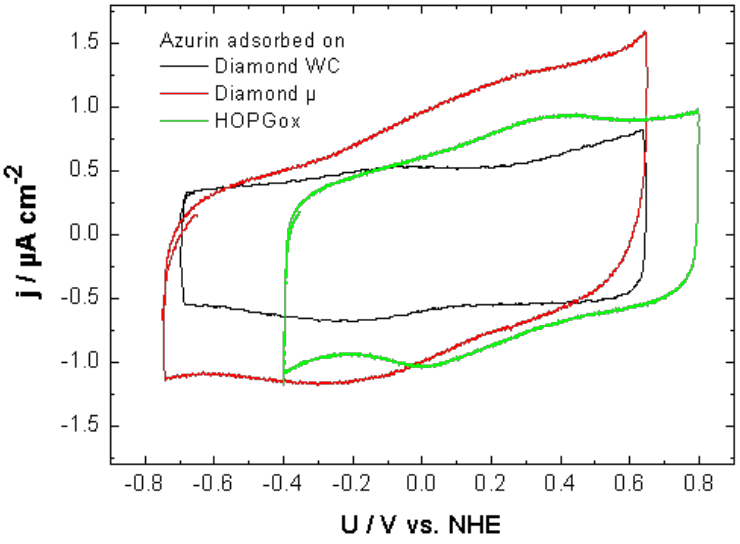

Figure 4.66. Cyclic voltammograms of azurin adsorbed on oxidized HOPG and single crystal diamond oxygen-terminated by two different approaches, obtained in 10 mM PBS (pH 7) at a scan rate of 100 mVs^{-1}.

All three electrodes show observable redox peaks, which can be attributed to the oxidation and the reduction of the adsorbed azurin on the surfaces. However, the redox behavior shows significant differences. Especially in the case of the azurin/diamond μ electrode, the redox peaks almost disappear in the background current. Therefore, the redox potential can only be roughly estimated. Furthermore, the redox potential, i.e. the midpoint potential differs between -150 mV vs. NHE for the azurin/diamondWC, approximately -60 mV vs. NHE for the azurin/diamond μ

and 215 mV vs. NHE for the azurin/HOPGox. These potential differences might be explained by the azurin molecules being located in different chemical compositions depending on the kind of the oxide overlayer. Due to the ligand effect, the redox potential of a molecule can vary [253]. Especially the protonation of the molecule plays an important role [229]. Table 4.5 shows that the redox potential of azurin significantly differs depending on the electrode material and the electrode pretreatment. Literature data [3, 230] obtained for azurin in NH_4Ac at a pH 4.6 lies around 300 mV vs. NHE, while the redox potential found for azurin adsorbed on oxidized HOPG is around 80 mV lower due to deprotonation effects of histidines within the molecule (see Section 4.1.3) the redox potential on the diamond electrodes can not be explained so far.

The surface coverage Γ, i.e. the number of redox-active azurin molecules attached to the electrode surface is determined from the charge passed under the Faradaic peaks assuming a one electron transfer process. Although the surface coverage obtained for the azurin/diamond μ is by a factor of 5 higher than for the azurin/diamond WC (Table 4.5) the redox peaks are broad and almost superimposed by the capacitive current originating from double layer charging of the electrode. The surface coverage on the μ-etch diamond is comparable to the coverage obtained for oxidized HOPG. For the diamond surface terminated by wet chemical oxidation, the surface coverage achieved only 25% of the coverage obtained for oxidized HOPG or μ-etch diamond. For both electrodes azurin/diamond μ and azurin/diamond WC, cyclic voltammetry at different scan rates was performed. However, due to the broad redox peaks the electron transfer rate could not be evaluated for the μ-etch diamond. The peak separation of approximately 400 mV indicates a sluggish electron transfer. The CVs obtained for the azurin/diamond WC showed a linear increase in peak current density with increasing scan rate, indicating that the azurin molecules are really surface bound. The rate constant for electron transfer was determined from the variation in peak position between the oxidation and the reduction peak as a function of the scan rate. The separation of the peak potentials was fitted according to the Laviron theory [73] yielding an electron transfer rate $k_{app} = 1.5\ s^{-1}$. The rate constant for the azurin/diamond WC electrode is also given in Table 4.5 together with the rate constant for the azurin/HOPGox electrode already evaluated in Section 4.1.3. The apparent electron transfer rate of azurin/diamond WC is by a factor of three higher than for the oxidized HOPG.

azurin on	$\mathbf{U_0}$	$\mathbf{q_{ap}}$	$\mathbf{q_{cp}}$	$\mathbf{q_{ap} : q_{cp}}$	$\mathbf{\Gamma}$	$\mathbf{k_{app}}$
	mV vs. NHE	$\mu\mathbf{Ccm^{-2}}$	$\mu\mathbf{Ccm^{-2}}$		$\mathbf{pMcm^{-2}}$	$\mathbf{s^{-1}}$
diamond WC	-150	0.115	0.124	0.93	1.24	1.50
diamond μ	-60	0.659	0.590	1.11	6.47	-
HOPGox	215	0.492	0.497	0.99	5.13	0.43

Table 4.5. Parameters of azurin adsorbed on diamond WC, diamond μ and HOPGox. Redox potential U_0, charge density of the oxidation q_{ap} and the reduction peak q_{cp} peak evaluated from the CVs shown in Figure 4.66, the ratio of q_{ap}:q_{cp}, surface coverage Γ and the apparent electron transfer rate constant k_{app}.

4.5.4. Summary and Remarks

Preliminary results of enzyme electrodes using oxygen-terminated diamond as support material were shown. While the NCD electrode surface is characterized by grain boundaries and powder like orientation without preferential direction, single crystal diamond electrodes have atomically flat surfaces and might also be used for EC SPM experiments. The results indicate that it is possible to directly adsorb metalloproteins and enzymes onto oxygen-terminated diamond surfaces similar to the immobilization of biomolecules onto oxidized HOPG. Thereby, the wet chemical oxidation procedure shows promising results providing a faster electron transfer than on oxidized HOPG. First XPS experiments revealed that the WC oxidation forms, besides C=O and C-O-C groups, also C-OH groups on the diamond surface which were also found on oxidized HOPG. However, so far it is not clear in which manner biomolecules adsorb or bind to the oxidized carbon surfaces. A detailed XPS study of oxygen-terminated diamond and oxidized HOPG is planned in order to reveal which oxygen groups on the carbon surface are responsible for the biomolecule binding and which oxidation treatment is best suited to realize these groups on the diamond surface.

5. Discussion

The scientific focus of this work was the electrochemical investigation of biomolecules at the solid-liquid interface in order to study their functional properties such as activity, stability and structure-function relation down to a single molecule level. Obtaining new insights into these properties and being able to systematically tune the biological and electronic function of such biomolecules, new possibilities in the field of biosensors [6], bioelectrochemical fuel cells [254, 255] and bioelectronics [1, 256] will open up. In the past a lot of work has been done to study these questions depending on the biomolecule-electrode interaction and therefore, the right electrode material, the optimized immobilization mechanism and the suitable investigation technique. Thereby, electrochemical investigations were mainly limited to naturally redox-active proteins and enzymes.
Beside electrode preparation and surface characterization, the investigation and improvement of direct electron transfer between the biomolecules and the electrode was one of the main issues. Thereby, different electrode preparation procedures were applied to achieve an optimized electrode architecture (surface coverage, stability) and to enhance electron transfer processes between the biomolecule and the electrode.
Moreover, it was shown that by transfering the affinity label concept to electrochemical detection methods, i.e. tagging the affinity labels with electroactive markers, redox-inactive enzymes could be studied electrochemically.
Well established electrochemical investigation techniques such as cyclic voltammetry for bulk measurments and EC-STM for single molecule studies have been mainly applied throughout this thesis in order to study these issues in detail. Furthermore, it was shown that the scanning electrochemical potential microscopy, although being still in its infancy, has high potential for electrochemical investigation of biological samples.

In this chapter the obtained results presented in chapter 4 will be discussed under the following aspects: (i) the improvement of the direct electron transfer between the biomolecules and the electrode by functionalization of carbon electrode surfaces, (ii) the investigation and characterization of protein electrodes with EC SPM techniques with special focus on the new opportunities offered by SECPM and (iii) the valuation of a new concept of electrochemical biosensing of naturally redox-inactive enzymes for possible medical applications using ferrocene affinity labels.

5.1. Interfacial Electron Transfer between Biomolecules and Electrodes

The study of the electron transfer behavior of molecules and biomolecules immobilized onto electrode surfaces represents an interesting and important task since it is intimately connected to the possibility of deeply understanding and tuning their functional properties. The electronic communication and thus the charge transfer across the solid-liquid interface is of great importance for all kinds of bioelectrochemical devices. However, usually the redox-active site of a biomolecule is encapsulated deep inside the protein structure, providing an effective barrier for electron transfer. The electronic communication between the molecule and the electrode is often achieved by mediators. Typical mediators are small charge carriers, i.e. redox-active molecules such as ferrocenemonocarboxylic acid (FCMA) acting as electron donor and electron acceptor, shuttling electrons between the active site of the biomolecule and the electrode surface [257]. Only under carefully controlled conditions, i.e. by anchoring the biomolecule to the electrode surface, maintaining their functionality and keeping the electrode-active site distance short enough, also direct electron transfer can proceed. Therefore, several surface techniques have been employed to study the molecular organization and the redox properties of metalloproteins immobilized onto electrode surfaces [258, 259]. It is well known that the electron transfer rate constants in electrode-contacted enzymes are often lower than those between the enzymes and their natural electron acceptors, e.g. O_2. This decrease can be attributed to an insufficient electronic contact between the biomolecule and the electrode or to the binding of the enzyme in a nonoptimal position and, thus, to the lack of alignment of the biomolecule to the electrode surface. Therefore, surface chemistry, i.e. the modification and functionalization of electrode surfaces in order to immobilize metalloproteins and -enzymes and to provide fast electron transfer between biomolecule and electrode, is a key parameter for the investigation of direct electron transfer phenomena [260, 261]. Thereby the immobilization has to be optimized to the used electrode material and also has to meet the experimental requirements, for example regarding obtained surface coverage and binding stability. In order to be able to perform EC SPM experiments on protein electrodes one has to take into account that the molecules have to be strongly bound to the electrode surface to resist occurring tip-molecule interactions (see section 4.1.3.2).
The choice of the electrode is another crucial point for EC SPM, since the surface to which the proteins are immobilized should be ideally atomically smooth so that also small single proteins or enzymes with a size of a few nanometers can be resolved with high resolution. Atomically planar surfaces of single crystal electrodes offer well-defined environments with large terraces and only few defect sites. Therefore, proteins and enzymes are often immobilized onto the Au(111) single crystal surface either via thiol groups which are present in the biomolecule itself (e.g. cysteine amino acids [99, 230]) or by thiolate self-assembled monolayers (SAM) [17, 262].
Within this work a first experimental attempt was also performed on Au(111) single crystals. However, using phosphate buffer solution as electrolyte, phosphate ion adsorption and desorption on the gold surface could be observed in cyclic voltammetry and electrochemical impedance spectroscopy experiments [100, 263, 264]. Phosphate ion adsorption is even stronger than the

known specific adsorption behavior of sulphate ions. Especially for enzyme electrodes with only small surface coverages the electroactivity of the enzymes was superimposed on the background current coming from electrochemical interaction between the phosphate ions and the gold surface occurring in a potential range between 0.4 V and 0.8 V vs. NHE. Therefore, carbon electrodes such as highly oriented pyrolytic graphite (HOPG) and diamond were preferred as electrode material. Especially using HOPG as model electrode has several advantages: (i) its smooth surface that makes it perfectly suitable for EC SPM investigations, (ii) being a biocompatible carbon material, not a metal, since proteins often denaturate when coming into contact with metal surfaces [8, 9], and (iii) due to its electrochemical inertness (HOPG has a larger potential window). However, binding of proteins and enzymes onto the initially hydrophobic HOPG electrode is challenging and requires an adequate pretreatment of the surface. Protein adsorption can be enhanced by the modification of the carbon material, forming active sites on the surface for example by oxidation techniques resulting in oxygen containing groups. The peripheral amino groups of the proteins and enzymes can bind to the formed CO groups on the oxidized carbon surface providing stable binding and a direct electron transfer [10, 11]. The redox activity of the metalloprotein azurin adsorbed on electrochemically oxidized HOPG and different oxygen-terminated diamond electrodes was investigated in Section 4.1 and Section 4.5, respectively. A reversible interfacial electron transfer between the Cu-ion of the protein and the electrode surface was confirmed for both modified electrode materials by cyclic voltammetry. The apparent electron transfer rate constants k_{app} were found to be 0.43 s^{-1} for azurin/HOPGox and 1.50 s^{-1} for azurin on single crystal diamond electrodes oxygen-terminated by the wet chemical procedure (see Table 4.5 in Section 4.5). While literature mainly reports about enzyme immobilization on oxygen-terminated diamond electrodes by an additonal functionalization using silane groups [52, 265] it was demonstrated here that azurin can also be directly adsorbed onto the diamond WC electrodes showing an enhanced direct electron transfer compared to azurin on oxidized HOPG. Therefore, due to its biocompatibility, its electrochemical inertness and stability, oxygen-terminated diamond seems to be a promising material for fundamental studies in bioelectrochemistry and for technical applications such as biosensor devices. However, the exact nature and number of oxygen-containing functional groups which are formed on the carbon surfaces during the oxidation procedures are difficult to ascertain and control. Furthermore, oxidation of carbon normally leads to a roughening of the surface (also shown in Section 4.1), which makes this functionalization technique disadvantageous for single molecule EC SPM experiments.
In 1992, Delamar et al. [20] introduced a promising alternative proposing the functionalization of carbon surfaces by electrochemical reduction of aryl diazonium ions consisting of an aromatic ring and a $N_2^+X^-$ group, where X can be an inorganic or organic anion. After elimination of dinitrogen the generated aryl radicals couple to the carbon support forming a robust covalent C-C bond [21]. In contrast to the oxidation procedures this technique does not roughen the carbon surface, but forms a monolayer of conductive linker molecules on the flat surface. When a biomolecule is covalently bound to the linker, the delocalized electron system of the Π electrons within the aromatic ring enables good conductivity through the chain and across the bioelectrochemical solid-liquid interface. This electrochemically assisted grafting method has several advantages compared to

common self-assembled monolayer (SAM) methods as known from thiol-Au surface chemistry. The formation of SAMs often needs several hours of incubation and usually becomes unstable at potentials higher than 0.9 V vs. NHE. Furthermore, the possibility to control the potential and/or the current within the reduction process allows an easy variation of the functionalization coverage between submonolayers and a full monolayer. Besides a strong binding of the linker molecule to the electrode surface, electrochemical grafting enables a fast surface modification which can be easily controlled by the grafting parameters. The formation of a saturated 4-CP monolayer generally required only a few seconds within the first potential sweep (Section 4.1.2) and offers an increased stability with a wider potential window for subsequent electrochemistry [50, 226, 266].

In Section 4.1.2 this covalent immobilization technique was transferred to the basal plane of HOPG and tested in 10 mM phosphate buffer solution (pH 7) using again the metalloprotein azurin. Although this protein immobilization technique was already used before for the modification of glassy carbon, a surface characterization via SPM methods and an investigation of the surface coverage have not been done before probably due to the roughness of the glassy carbon electrode. EC-STM studies on azurin/4-CP/HOPG electrodes showed surface coverages up to 80% of a monolayer, whereas varying the grafting parameters also coverages of about 10% could be achieved. By electrochemically grafting of the basal plane with the aryl 4-carboxyphenyl diazonium tetrafluoroborate and the subsequent protein anchoring by EDC/NHS-coupling, submonolayers and monolayers of azurin were successfully prepared. These electrodes were investigated by cyclic voltammetry and EC-STM and compared to protein adsorption on electrochemically oxidized HOPG (Section 4.1.3 and Section 4.3.1). Evaluating the apparent electron transfer rate constant k_{app} of azurin covalently immobilized on the 4-CP/HOPG electrode according to Laviron [73], k_{app} was found to be 48 s^{-1}. This quantitative analysis showed that k_{app} is two orders of magnitude higher for azurin/4-CP/HOPG compared to azurin/HOPGox (Section 4.1.3.1). Although it is known that defect sites on oxidized HOPG facilitate the electron transfer [12], the covalent binding onto the carboxyphenyl-modified HOPG provided a faster direct electron transfer process.

Furthermore, both immobilization techniques showed significant differences in the electrode surface coverage when characterized by EC-STM. The adsorption of electroactive species onto oxidized HOPG only yielded low surface coverages throughout the experiment (normally $< 30\%$), showing that only a small number of molecules are strongly bound to the surface and/or can undergo direct electron transfer with the electrode. Even if strongly bound a lack of direct electron transfer between biomolecules and the electrode surface could occur within the adsorption of proteins. This finding was also confirmed by EC SPM experiments presented in Section 4.4.2 where the combined EC-STM/SECPM study performed on HRP/HOPGox revealed that constant potential mode SECPM resolved an HRP molecule that was not visible in the EC-STM due to inhibited electron transfer.

Furthermore, all attempts to visualize the interfacial electron transfer through a single FcAL@papain molecule adsorbed on oxidized HOPG performing potential dependent EC-STM studies failed, probably also due to an insufficient electron transfer. However, performing the same experiments

on FcAL@papain/4-CP/HOPG electrodes, the enhanced interfacial electron transfer provided by the covalent binding to the carboxyphenyl monolayer enabled the visualization of the electron transfer process in constant height mode EC-STM, constant current mode EC-STM and STS (Section 4.3.2.1).

These results clearly show that the covalent anchoring of redox-active proteins onto 4-CP/HOPG enabled not only the preparation of electrodes with a high surface coverage, but also fast electron transfer between the biomolecule and the electrode was successfully achieved. A fast interfacial electron transfer is the prerequisite for fundamental studies on biomolecules and for bioelectrochemical devices ranging from biosensors to bioelectrochemical fuel cells.

5.2. EC SPM of Protein Electrodes

The interfacial electron transfer of redox enzymes and metalloproteins have long been addressed by voltammetric methods achieving patterns for protein-electrode interactions and molecular mechanisms [154, 267]. However, the so far obtained data such as redox potential and rate constants, are of average character since the whole electrode is investigated using integral measurement techniques like cyclic voltammetry or electrochemical impedance spectroscopy. Scanning probe microscopy techniques operating in aqueous solution allow to perform the investigation of proteins and enzymes on a single molecule level in their natural environment. Measuring different properties simultaneously can allow the structure–function relationship of biological samples to be investigated. Due to its soft imaging technique which provides to maintain the biomolecules in their native conformation and preserve its functionality atomic force microscopy (AFM) [39] is probably the most used SPM technique for biological samples. Extensive reviews can be found in literature [268–271]. Making the AFM tip and cantilever conductive, it is even possible to measure the current between a conductive sample and the tip along with its topography in the so called conductive atomic force microscopy (C-AFM) configuration [272]. Positioning a biological molecule between the tip and a conductive substrate allows the measurement of the modulation of the current due to the molecule [273, 274]. However, up to now it is not possible to extend such C-AFM experiments to a physiological environment due to the lack of suitable tips. Like in EC-STM the conductive AFM tips have to be insulated except for the very apex of the tip in order to avoid large Faradaic leakage currents. If such tips are available a great breakthrough would be reached because, with respect to other current sensitive techniques such as EC-STM, soft surface imaging without a current flowing and subsequent electrochemical characterization of biomolecular samples could be achieved independently. Moreover, such a set-up will allow to study the effect of mechanical forces on the molecular transport properties under full potentiostatic control. As long as such AFM tips are commercially not available the electrochemical scanning tunneling microscopy will be the method of choice to study the electrochemical behavior of individual biomolecules. In the recent past different STM works on redox molecules, metalloproteins and redox enzymes adsorbed onto atomically flat electrode surfaces have been carried out aiming at the investigation of the interfacial electron transfer through a single immobilized biomolecule. Thereby, it could be shown experimentally [3, 15, 16, 36, 40, 41, 43, 44, 235] and theoretically

[40, 44, 153–155] that the tunneling current which flows through the electrode/biomolecule/EC-STM tip hybrid junction can be significantly enhanced when the redox level of the biomolecule located within the nanogap is involved in the tunneling process. Combined with well-defined functionalized surfaces EC-STM has paved the way for true molecular-scale electrochemical nanotechnology e.g. demonstratiing single metalloprotein-based transistors [110] or operating individual nanoparticles as multistate switches [42].
In order to characterize the surface structure and the electronic properties of individual immobilized protein or enzyme molecules, two different electrochemical scanning probe microscopy techniques were applied here, the EC-STM and the SECPM. Since in-situ EC-STM rests on the electronic conductivity of the sample and not directly on the morphology of the surface, EC-STM images of protein electrodes show a convolution of both, the real topography and the density of electronic states. Taking advantage of this knowledge, the EC-STM was the method of choice to investigate whether the naturally electroinactive papain molecules can be made electrochemically detectable by incorporating the redox-active ferrocene affinity label (FcAL) into its active site. The differences in the electronic properties of unlabeled papain and FcAL@papain, as well as their potential dependence were shown in Section 4.3.2.1 via constant current mode EC-STM. The image contrast of the FcAL@papain molecule changed with changing electrode potential, reaching a maximum in contrast when its redox potential was applied and the tunneling current was enhanced due to the fact that the electrons could easily tunnel from the tip through the redox level of the FcAL@papain molecule to the electrode. As expected, the unlabeled redox-inactive papain molecules showed no change in the image contrast when the applied electrode potential was varied. These results were in good agreement with the data obtained for prelabeled bulk FcAL@papain/4-CP/HOPG electrodes by cyclic voltammery in Section 4.3.1.2 and verified the concept of electrochemical detection using FcAL down to a single molecule level. Performing similar potential dependent EC-STM studies on protoporphyrin IX with and without a Fe-ion inside the structure, Tao [36] could identify the different molecules by the image contrast. Alessandrini et al. [18] were able to distinguish between Cu containing azurin and Zn containing azurin molecules. Making use of this technique, we were able, for the first time, to show under in-situ conditions that it is possible to make a naturally redox-inactive enzyme electroactive. Showing that the EC-STM is also able to detect "on-chip" (see Section 4.3.2.3) the changes in the nanoscopic electrochemical properties of immobilized papain molecules due to the in-situ binding of the FcAL and the coherent change in the interfacial electron transfer properties, confirmed the quality and the opportunities of this new kind of electrochemical biosensing. At the same time it could be shown with this results that the structure and function of papain molecules will be maintained when the molecules are covalently immobilized on 4-CP/HOPG. Applying current-voltage spectroscopy on single FcAL labeled and unlabeled papain molecules (see Section 4.3.2.1) showed that in-situ EC-STM offers the possibility for bioelectronic devices working on the single molecule level, directly in their natural aqueous reaction media. In 2005 Alessandrini et al. [110] performed similar experiments; positioning an azurin molecule between two biased gold electrodes they demonstrated that a single redox protein wet biotransistor can be a promising step forward towards future biomolecular electronics.

Beside EC-STM the scanning electrochemical potential microscope (SECPM) was used for the first time to investigate and characterize enzymes adsorbed on electrode surfaces. Due to the fact that the SECPM works by scanning in the region of the EDL mapping the potential distribution of the surface without any current flowing, it is a suitable tool for non-invasive imaging of soft biomolecules. Section 4.4.2 showed that the SECPM enables one to visualize the differences in the electronic properties of the iron-containing ferritin and its iron-free conformation apoferritin. Although both molecules have the same spherical protein structure with a diameter of 12 nm, the obtained SECPM images showed different molecule sizes due to their different chemical composition and surface potential. Having a homogenous potential distribution on the surface the protein structure of the apoferritin could be resolved with a molecular diameter of 12 nm. The surface potential of the ferritin molecule mapped by constant potential mode SECPM could not resolve the protein structure since the potential distribution was dominated by the signal coming from the iron core inside the protein shell, which has a diameter of up to 8 nm. Therefore, the ferritin molecules appeared with diameters between 6 nm and 8 nm in the SECPM images.
The scanning probe microscope used here could easily be switched between EC-STM and SECPM mode by software control, i.e it was possible to successively image the same surface area with both techniques for direct comparison. Since SECPM maps the surface potential of proteins, a direct electron transfer between the protein and the electrode is not required, what allows SECPM to resolve protein molecules that are "invisible" for STM imaging as was shown in Figure 4.51 in Section 4.4.2, where SECPM resolved an additional HRP molecule. Comparing high resolution SECPM with the crystallographic data of HRP showed that the position of the heme group inside the protein pocket could be identified in the SECPM image, whereas in EC-STM the HRP molecules only appeared as tiny dots probably due to an insufficient electronic contact to the electrode.
Since it is able to map the electrode surfaces without significant perturbation by the probe electrode and no current flows between tip and substrate, SECPM is especially suited for the investigation of sensitive organic and biological molecules. New insights into structure-function relation of the active sites of enzymes and their interaction with the electrode surface could be obtained by performing potential-dependent imaging on a single molecule level. Further experiments have to show whether SECPM is comparably good also in other systems and if it is possible to achieve atomic resolution. Although providing great potential especially for biomolecular investigations, the principle of SECPM is still not completely understood. Especially the potential profiling experiments in Section 4.4.3 showed that mapping the electrochemical double layer of the working electrode in xz-direction does not yield potential profiles like they would be expected by the GCS theory. Influences coming from the electrochemical double layer of the tip have to be considered and the overlap of both EDLs has to be understood in more detail in order to evaluate measured $\triangle$U(z) data. Therefore, fundamental experimental and theoretical work regarding the investigation of the SECPM tip with respect to tip geometry, the tip material and the role of the free surface area of the tip apex is required.
Once a better understanding of the SECPM is achieved, the instrumental conditions providing the combination of EC-STM and SECPM will permit new possibilities to investigate biomolecules

making use of the advantages of both techniques. The enzyme electrode surface can first be imaged under soft SECPM mapping conditions, i.e. nearly without any tip-enzyme interactions, for characterizing the surface coverage and distribution of the molecules on the surface, then the electron transfer can be investigated on selected single molecules performing scanning tunneling spectroscopy. Potential-dependent EC-STM and SECPM studies on single redox enzymes would probably yield new insights into the electrochemical properties of the active site, comparing changes in the tunneling current and the potential map for different applied electrode potentials. Furthermore, it was shown that in-situ EC-STM can be successfully used to perform nanografting on protein electrodes made of proteins covalently coupled onto carboxyphenyl-modified HOPG by increasing the tunneling current (Section4.1.3.3). This technique opens an innovative route to locally produce enzyme arrays with a well defined number of molecules, subsequently image and investigate their electrochemical behavior by EC-STM and SECPM. Using then the EC-STM tip as local current sensor [159, 160] would possibly allow to study the electrocatalytic activity of enzyme arrays (assuming that the catalytic turnover rate is high enough). Succeeding in the preparation of pH sensitive Pd/H electrodes (Section 4.4.4.3) for application as SECPM tips one might also think about using the SECPM tip as local potential probe in order to detect pH changes above enzymes and enzyme arrays due to their catalytic activity.

5.3. Electrochemical Biosensing using Ferrocene Affinity Label

Electrochemical biosensors with biomolecule-electrode signal transduction based on interfacial electron transfer are often limited to the sensing of redox-active proteins or enzymes. Therefore, most of the current methods for the detection of enzymes and the investigation of the enyzmatic activity are based on optical detection using fluorescent probes and fluorogenic peptides or on radiolabeling although the electrochemical detection, for example via cyclic voltammetry, possesses considerable advantages such as low costs, simple application and high sensitivity. The combination of high-resolution bioelectrochemistry using nanotechnology (EC-STM) (shown in Section 4.3.2) with electrochemical surface functionalization by carboxyphenyl groups (introduced in Section 4.1) enabling bioelectronics, i.e. fast electron transfer between molecule and electrode, has revealed the possibility to develop and approve a new approach for the electrochemical biosensing of electroinactive enzymes using redox-active markers. Over the last years, the research field of ferrocene modified receptors in order to develop protein-sensitive electrochemical probes has been mainly promoted by the group of Kraatz [115, 275–278]. Inspired by his work two tailormade watersoluble ferrocene affinity labels, FcAL(in) and FcAL(out), for the electrochemical detection of the cysteine protease papain were synthesized which are able to bind in an activity-dependent manner to the active site of the papain molecule (Section4.2, [29]). Although the proof-of-principle could be adduced for both FcALs for extended papain electrodes using cyclic voltammetry (Section 4.3.1), the redox behavior of FcAL(out) was irreversible. A detailed investigation by EC-STM experiments down to a single molecule level (Section 4.3.2.1) was only

performed with the more promising affinity label FcAL(in). In Section 4.3.1.3 it was shown that the labeling process of the FcAL to active papain molecules can be observed directly in solution by a potential shift detected in the cyclic voltammogram. The two facts that cyclic voltammetry is a sensitive measurement technique and that no complex electrode preparation is required since both compounds are dissolved in solution, make the application of this electrochemical sensing technique for redox-inactive enzymes in commercial biosensors possible. However, biosensors are not only used for the detection of enzymes, but also for the investigation of the enzymatic activity and the invention of new enzyme inhibitors for drug development in pharmaceutical research. Therefore, the FcAL has also to fullfil the requirement to bind in an activity-dependent manner to the papain molecules. In order to investigate this issue, FcAL-concentration-dependent experiments were performed in the presence and absence of possible papain inhibitors (Section 4.3.3). Thereby the activated papain molecules were covalently immobilized on a 4-CP/HOPG electrode to control the amount of enzymes on the surface. The detected charge in dependence on time was referred to the amount of formed FcAL@papain and thus to the reaction velocity. Side reactions were neglected since in Section 4.1 it was shown that the carboxyphenyl layer on the HOPG surface provides not only fast electron transfer between the redox-active site of immobilized biomolecules, but also passivates the HOPG electrode, inhibiting possible side reactions. Potential-dependent EC-STM studies before and after the Fc labeling process (Section 4.3.2.3) showed that all molecules within an enzyme array are active and can bind the FcAL, i.e. despite the strong covalent immobilization the biological activity of the papain molecules was maintained. The fact that after the labeling process all FcAL@papain molecules within the hexagonal close-packed monolayer showed nearly the same changes in the image contrast when the applied electrode potential was varied, might lead to the assumption that the molecules were bound with the same orientation to the 4-CP/HOPG electrode surface. Since the EC-STM image contrast represents the electron tunneling propability between tip, redox level of the molecule and the electrode surface which is, according to the Marcus theory, related to the distance between them, all papain molecules must bind via the same lysine group to the surface. Although the covalent immobilization technique using EDC/NHS coupling is unspecific, i.e. the amino group of the protein structure can not be specifically defined, it is possible that the papain molecules bind via a preferential lysine group to the active NHS-ester. Therefore, the possible orientation of the papain molecules is discussed here. In case that the FcAL is able to reach and bind to the active site of the immobilized papain the molecule must be orientated on the surface in such a way, that the protein pocket provides free access. As already mentioned, the anchoring of the protein to the NHS-ester on the 4-CP/HOPG surface happens at the lysine amino acids of the protein structure. Figure 5.1 shows the lysine groups at the papain surface that might be considered as possible binding sites and their distance to the ferrocene moiety of the FcAL in the active site. Assuming a sufficiently fast intramolecular electron transfer, Lys-10 located opposite to the active site would be an ideal immobilization position for activity measurements providing undisturbed diffudion of the FcAL into the protein pocket.

The results obtained by the EC-STM experiments to investigate the "on-chip" labeling process enabled the approach to qualitatively measure the enzymatic activity of immobilized papain

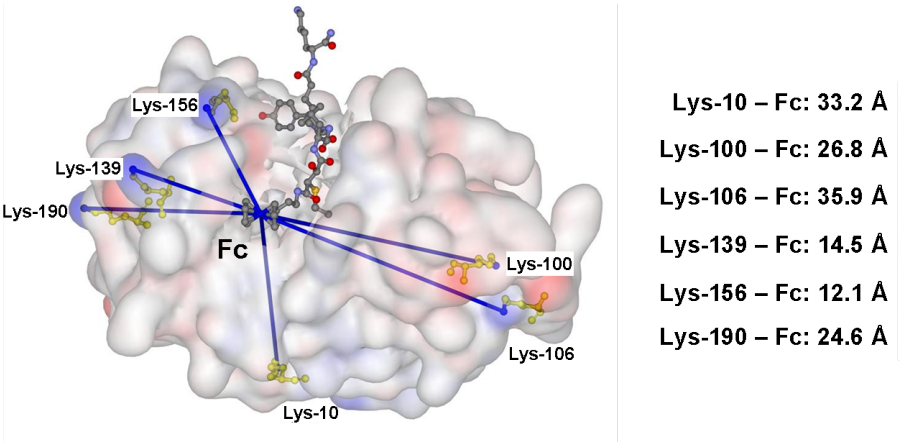

Figure 5.1. Scheme of the lysine amino acids within the papain protein structure and their distance to the ferrocene moiety (Fc) of the incorporated FcAL.

by detecting the binding process of the FcAL to the active site (Section 4.3.3). We have already performed first experiments with a synthesized ferrocene-tagged affinity label optimized for serine proteases such as trypsin. They have shown promising indication that it is possible to enlarge this concept of electrochemical detection also to other enzymes of the protease family ([33]). Therefore, ferrocene affinity labels combined with electrochemical detection techniques are promising systems for analytical devices in medical applications for diagnostics and health care.

Future appoaches to minituarize the electrodes forming microarrays in a chip format may enable fast and sensitive recording of the enzymatic activity, enabling high throughput screening (HTS). HTS allows rapid identification of enzyme inhibitors and antibodies, thus providing deeper understanding of biochemical processes and interactions and showing new ways of drug discovery.

6. Summary and Conclusion

The focus of this work was the electrochemical investigation of biomolecules. Thereby, one of the main issues was the investigation of the interfacial electron transfer between redox-active proteins and the chosen carbon electrode HOPG. Beside well established immobilization mechanisms such as anodic oxidation an adequate surface chemistry was found in order to enable a strong binding of the biomolecules to the electrode surface and to provide fast direct electron transfer between the protein and the electrode. It was shown that a covalent anchoring of the metalloprotein azurin to a carboxyphenyl-modified HOPG surface yielded an apparent electron transfer rate k_{app} that was two orders of magnitude higher compared to azurin only adsorbed onto electrochemically oxidized HOPG. EC SPM investigations also revealed protein electrodes with high surface coverages that could be varied up to a complete monolayer using this covalent immobilization technique. Thus, having found a suitable way to immobilize biomolecules onto the HOPG electrode surface allowing good electron transfer kinetics, a procedure was developed which enabled the electrochemical investigation of naturally redox-inactive enzmyes such as papain. Papain belongs to the family of proteases which play important roles in living organsims. This innovative biosensing approach was successfully achieved by incorporating ferrocene-containing affinity labels (FcAL) into the active site of the molecules which made the redox-inactive papain electroactive and therefore electrochemically addressable. Tracking the binding of the FcAL to the papain in-situ, it was also possible to study the kinetics of the enzymatic activity in the absence and presence of enzyme inhibitors.
Throughout the work electrochemical measurement techniques such as cyclic voltammetry and in-situ EC STM were used to characterize and investigate the electrochemical behavior of the biomolecules. Cyclic voltammetry was a useful method to study new electrochemical bulk systems such as the ferrocene labeled papain electrodes. The in-situ investigation of electron transfer processes through single biomolecules was enabled by high resolution EC-STM. In addition to the EC-STM the scanning electrochemical potential microscope (SECPM) was utilized the first time for the charcterization of electrode surfaces, revealing unexpected opportunities for the investigation of protein electrodes. The chosen HOPG substrate served as model carbon electrode and enabled single-molecule studies due to its unique surface properties. However, for commercial applications, e.g. as electrode material in electrochemical biosensors HOPG is not suited since it is sensitive to corrosion. First experiments showed promising results for using oxygen-terminated boron-doped diamond as substrate material for enzyme electrodes and biosensor technology.

In the first Section 4.1 two different techniques to functionalize the hydrophobic HOPG surface for successful protein and enzyme immobilization were introduced. HOPG was electrochemically

oxidized using cyclic voltammetry in order to form oxygen containing groups on the surface and thus, change the surface properties form hydrophobic to hydrophilic. The new approach was to covalently immobilize proteins by EDC/NHS coupling onto 4-carboxyphenyl-modified HOPG. For this purpose, diazonium tetrafluoroborate was electrochemically reduced. Both techniques were studied by EC-STM and cyclic voltammetry using the metalloprotein azurin as a redox-active species. These studies showed that the covalent immobilization results in an increased surface coverage and a higher electron transfer rate compared to the often used electrochemical oxidation treatment. Varying the concentration of the enzyme solution within the electrode preparation electrode surfaces with different coverages could be produced. Furthermore, applying high tunneling currents (3 nA) the EC-STM was successfully used to nanostructure the azurin/4-CP/HOPG surface. This technique opens up a new route to locally produce enzyme arrays with a well defined number of molecules, and to subsequently image and investigate their electrochemical behavior. Using then the EC-STM tip as local sensor would allow one to study the electrocatalytic activity of enzyme arrays.

Section 4.2 reported about the synthesis and the characterization of two ferrocene affinity labels for the electrochemical detection of redox-inactive enzymes such as the cysteine protease papain. Both FcALs are based on the structure of the E-64 motive, an irreversible inhibitor of papain that binds in an activity-dependent manner to the active site. The difference of the FcALs was the position of the ferrocene moiety which was either located directly in the active site of papain (FcAL(in)) or attached to a linker outside the protein shell (FcAL(out)). The successful binding of both FcALs to the papain molecule was verified by mass spectrometry and cyclic voltammetry. However, a detailed investigation of the electrochemical behavior of the FcALs and labeled papain molecules showed that FcAL(in) was more suitable for the electrochemical sensing of papain.

In Section 4.3 FcAL(in) was used for electrochemical biosensing of the naturally electroinactive papain. The FcAL, unlabeled papain and prelabeled FcAL@papain molecules adsorbed on oxidized HOPG and immobilized on 4-CP/HOPG were investigated in detail using cyclic voltammetry and in-situ EC-STM. Thereby, significant differences in the redox potential of the ferrocene moiety were found depending on the chemical surrounding of the FcAL, i.e. whether it was dissolved in solution, bound to oxidized HOPG or immobilized on 4-CP/HOPG. Different redox potentials were also found when FcAL was incorporated in the electroinactive protein shell of the enzyme forming FcAL@papain, which was then either adsorbed or covalently immobilized on HOPG. These potential differences enabled us to observe the labeling process, i.e. the binding of the FcAL to the active site of papain in solution via cyclic voltammetry. Furthermore, in situ EC-STM imaging enabled us to distinguish between FcAL-labeled and unlabeled papain molecules due to different image contrasts of the molecules caused by their different electronic properties. Thereby, the interfacial electron transfer between the ferrocene moiety incorporated in the electroinactive protein shell and the electrode surface could be resolved on a single molecule level by constant current and constant height EC-STM, as well as by scanning tunneling spectroscopy (STS). The tunneling current through the nanogap between the STM tip and the

electrode surface could be gated by the redox level of the FcAL in the active site of the papain molecule by applying different electrode potentials and different bias voltages. The observed behavior can be explained by a two-step electron transfer process. Furthermore, a potential dependent EC-STM study before and after the labeling demonstrated successful binding of the FcAL to immobilized papain molecules directly "on-chip". This evidence served as a prerequisite to investigate also the enzymatic activity of papain on the 4-CP/HOPG electrode surface in the presence and absence of inhibitors. While the reversible inhibitor slows down the binding kinetics of the FcAL to the papain, the irreversible inhibitor blocks the active site and avoids the binding completely. However, for a quantitative analysis and the determination of kinetics and inhibition constants further experiments and an appropriate theoretical model are necessary.

Section 4.4 showed experimental results obtained in constant potential and potential profiling mode of the scanning electrochemical potential microscope (SECPM). It could be shown that the SECPM is a suitable tool for the in-situ investigation of different electrode surfaces under full potential control. The potential distribution of typical support materials often used in electrochemistry such as Au(111) and HOPG have been imaged and compared to EC-STM images to verify the quality of the SECPM technique. SECPM was able to resolve the monoatomic height of the step edges and the 120/60° angles of the terrace edges of the Au(111) surface with the same resolution as EC-STM. However, HOPG step edges appeared with a higher image contrast probably due to their inhomogeneous potential distribution. SECPM revealed high potential in the investigation of soft biomolecular samples. It was demonstrated that SECPM is ideally suited to image the surface potential of enzymes such as apoferritin, ferritin and horseradish peroxidase adsorbed onto oxidized HOPG electrodes:

- SECPM is able to visualize the protein structure of the hollow apoferritin with a diameter of 12 nm, while EC-STM is not;
- EC-STM and SECPM can resolve ferritin molecules with comparable resolution. The measured diameter, however, is much smaller than that of apoferritin;
- SECPM images HRP molecules which are not visible in EC-STM;
- SECPM is able to resolve the protein pocket and the active site of the HRP molecule.

In future studies, one might investigate whether the potential map, obtained by SECPM imaging, changes by changing the electrode potential or within biological activity of the enzyme.

Potential profiles of the Au(111) surface were measured in different concentrations of $NaClO_4$ in order to study the dependence of the electrochemical double layer on the electrolyte concentration. Furthermore, the applied electrode potential was changed to investigate potential effects on the EDL. However, the potential-distance plots were not in agreement with the theoretical Gouy-Chapman-Stern theory. It is necessary to understand in more detail, experimentally and theoretically, the role of the SECPM tip to be able to prepare reproducible probe electrodes, which are tailormade for the requirements of SECPM. Detailed studies in order to clarify fundamental questions on the relaxation time of the double layers and the response of the probe

electrode to changes in its environment are required. It was shown that the potentiometric SECPM tip can in principle be used to detect local pH changes by a shift of the OCP value of the tip. A first approach to prepare pH sensitive SECPM tips by loading polycrystalline palladium electrodes with hydrogen has been performed. The pH response of the Pd/H electrode showed an OCP shift of 56 mV per pH, which is in good agreement with the theoretical value of 59 mV according to the Nernst equation.

In Section 4.5 oxygen-terminated diamond was used and studied as alternative substrate material for biomolecule immobilization. Three different termination procedures to form functional oxygen-containing groups on the sp^3 carbon surface were applied: O_2 plasma (μ-etch), wet chemical oxidation (WC) and reactive ion etching (RIE). First experiments using FcAL@papain and azurin as redox-active biomolecules showed that the wet chemical oxidation process is most promising the electrochemical investigation of biomolecules. However, futher studies are required. To conclude, the results obtained in this work brought a new progress in the investigation of the electrochemical behavior of biomolecules. We are now able to prepare protein/enzyme electrodes with high surface coverage providing fast electron transfer between the active site of the protein and the electrode allowing a detailed investigation of the electrochemical behavior of the biomolecules. Therefore, the presented electrode architecture can be used for future fundamental research in bioelectrocatalysis and possibly also technical applications in electrochemcial biosensors or bioelectrochemical fuel cells. For technical applications oxygen-terminated diamond electrodes seem to be suitable as substrate material due to their unique stability and biocompatibility. The concept of using electroactive ferrocene affinity labels for the development of a new electrochemical biosensor introduced here, opens up new ways for pharmaceutical and medical devices especially in the research field of drug development allowing HTS by microarray technology. Furthermore, it was found that SECPM has high potential for the investigation of biomolecular electrodes. In addition to EC-STM it might provide new insights into biomolecule-electrode-interactions with an unprecedented resolution of the protein structure paving the way for future enzymatic structure-function studies.

A. Attachment

A.1. Abbreviations and Symbols

a	Lattice Constant [m]
a_i(I)	Ativity of the Ion Species i in the Liquid Phase I
A	Electrochemically Active Surface Area [cm^2]
α	Transfer Coefficient
α_a	Transfer Coefficient for the anodic Reaction
α_c	Transfer Coefficient for the cathodic Reaction
α_S	Electron Transfer Coefficient between Tip and Redox Center
α_{Tip}	Electron Transfer Coefficient Redox Center
AFM	Atomic Force Microscope
AL	Affinity Label
Au	Gold
BOP	Benzotriazolyloxytris(dimethylamino)phosphonium Hexafluorophosphate
Bu_4NBF_4	Tetrabutylammoniumtetrafluoroborate
c	Concentration [Ml^{-1}]
c^*	Concentration of the Bulk $z:z$ Electrolyte [Ml^{-1}]
C-AFM	Conductive Atomic Force Microscopy
C_d	Differential Capacitance [Fcm^{-2}]
C_D	Capacitance of the diffuse Layer [Fcm^{-2}]
C_H	Capacitance of the Helmholtz Layer [Fcm^{-2}]
CE	Counter Electrode
CV	Cyclic Voltammetry
CVD	Chemical Vapor Deposition
4-CP	4-Carboxyphenyl
4-CP/HOPG	4-Carboxyphenyl modified HOPG
d_0	Width of the Tunneling Potential Barrier Height [m]
D	Diffusion Coefficient [cms^{-1}]
DCC	Dicyclohexylcarbodiimide

DCM	Dichlormethane
DIC	Diisopropylcarbodiimide
D_{ox}	Density of Oxidized States
DMF	Dimethylformamide
DOS	Density of States
e	Electron Charge = Elementary Charge Value ($1.602 \cdot 10^{-19}$C)
ε	Dielectric Constant
ε_0	Permittivity of Free Space ($8.854 \cdot 10^{-12}$ Fm^{-1})
$\triangle E_{eff}$	Effective Tunneling Barrier Height [eV]
E_F	Fermi Level [eV]
$E_{F,S}$	Fermi Level of the STM Tip [eV]
$E_{F,Tip}$	Fermi Level of the Sample [eV]
E_{Vac}	Vacuum Energy Level [eV]
EC	Electrochemical
EC SPM	Electrochemical Scanning Probe Microscope
EC-STM	Electrochemical Scanning Tunneling Microscope
EDC	N-Ethyl-(3-Dimethylaminopropyl)-N′-Carbodiimide Hydrochloride
EDL	Electrochemical Double Layer
EIS	Electrochemical Impedance Spectroscopy
ESI	Electronspray Ionization
η	Overpotential [V]
F	Faraday Constant (96 485 CM^{-1})
f_{H_2}	Fugacity of Hydrogen
FAL	Fluorescence Affinity Label
Fc	Ferrocene
FcAL	Ferrocene Affinity Label
FcAL(in)	Fe(Cp)(η-C_5H_4-CH_2-NH-CO-Epx-Leu-Tyr-Ahx-Lys) with Ferrocene group inside the active site of the papain molecule
FcAL(out)	Fe(Cp)(η-C_5H_4-CH_2-CH(NH_2)-CO-Lys-Ahx-Tyr-Leu-Epx-COOEt) with the Ferrocene group outside the papain molecule
FCMA	Ferrocenemonocarboxylic Acid
Fmoc	9H-Fluoren-9-ylmethoxycarbonyl
$\triangle$ G^0	Standard Gibbs Free Energy Change in a Chemical Process [kJM^{-1}]
$\triangle$ $G^{\ddagger}$	Standard Gibbs Free Energy of Activation [kJM^{-1}]
Γ	Surface Coverage [Mcm^{-2}]
γ	Fraction of the Bias Voltage Drop at the Redox Center
GCS theory	Gouy-Chapman-Stern Theory
GOx	Glucose Oxidase

h	Planck Constant ($6.626 \cdot 10^{-34}$ Js)
$\hbar$	Reduced Planck Constant $\frac{h}{2\pi}$
h	Step Height [m]
H	Hydrogen
HFCVD	Hot-Filament Chemical Vapor Deposition
HOMO	Highest Occupied Molecular Orbital
HOPG	Highly Oriented Pyrolytic Graphite
HOPGox	Electrochemically Oxidized HOPG
HPHT	High Pressure High Temperature
HPLC	High-Performance Liquid Chromatography
HRP	Horseradish Peroxidase
HTS	High Throughput Screening
I	Current [A]
I_{ap}	Current of the Anodic Peak of a Redox Reaction [A]
I_{cp}	Current of the Cathodic Peak of a Redox Reaction [A]
I_T	Tunneling Current [A]
I_{Tip}	Tip Current [A]
IHP	Inner Helmholtz Plane
j	Current Density [Acm^{-2}]
k	Rate Constant [s^{-1}]
k_{app}	Apparent Electron Transfer Rate [s^{-1}]
$k^{o/r}$	Electron Transfer Rate between STM Tip and Redox Center [s^{-1}]
$k^{r/o}$	Electron Transfer Rate between Redox Center and Substrate [s^{-1}]
k_B	Boltzmann's constant ($1.380 \cdot 10^{-23}$ JK^{-1})
κ^{-1}	Debye-Hückel Length
κ_{el}	Electronic Transmission Coefficient
$\kappa_{el,S}$	Electronic Transmission Coefficient between Redox Center and Substrate
$\kappa_{el,Tip}$	Electronic Transmission Coefficient between Tip and Redox Center
λ	Solvent Reorganization Energy [eV]
LDOS	Local Density of States
LSV	Linear Sweep Voltammetrey
LUMO	Lowest Unoccupied Molecular Orbital
m	Mole Number
MALDI-TOF	Matrix Assisted Laser Desorption/Ionization Time of Flight
MS	Mass Spectrometry

MWCVD	Microwave-Assisted Chemical Vapor Deposition
n	Number of Electrons transferred in an Electrochemical Reaction
n_i^0	Number Concentration of the Ion i in the Bulk Electrolyte [cm^{-3}]
n_{sample}	Number of States of the Sample
n_{tip}	Number of States of the STM Tip
ν	Reaction Rate [$Ms^{-1}m^{-2}$]
NHE	Normal Hydrogen Electrode
NHS	N-Hydroxysuccinimide
NMR	Nuclear Magnetic Resonance
O	Oxidized Species
OCP	Open Circuit Potential
OHP	Outer Helmholtz Plane
PBS	Phosphate Buffer Solution
Pd	Palladium
ϕ	Electrostatic Potential of the Electrode
φ_0	Potential of the Electrode
φ_{bulk}	Potential of the Bulk Electrolyte
Φ_S	Work Function of the Sample [eV]
Φ_{Tip}	Work Function of the STM Tip [eV]
Pt	Palladium
PZC	Point of Zero Charge [V]
q	Charge Density [Ccm^{-2}]
q_{ap}	Charge Density of the Anodic Peak [Ccm^{-2}]
q_{cp}	Charge Density of the Cathodic Peak [Ccm^{-2}]
Q	Charge [C]
R	Gas Constant (8.314 $JK^{-1}M^{-1}$)
R	Reduced Species
RE	Reference Electrode
RIE	Reactive Ion Etching
R_T	Effective Tunneling Resistance [Ω]
ρ_S	Electronic Level Density of the Substrate
ρ_{Tip}	Electronic Level Density of the Tip
SAM	Self-assembled Monolayer
SECPM	Scanning Electrochemical Potential Microscope
SEM	Scanning Electron Microscope

σ_M	Surface Charge Density [Ccm^{-2}]
SOMO	Single Occupied Molecular Orbital
SPM	Scanning Probe Microscope
SPPS	Solid-Phase Peptide Synthesis
STM	Scanning Tunneling Microscope
t	Time [s]
t_R	HPLC Retention Time = time between injection and maximum detected response
T	Absolute Temperature [K]
Th	Thomson, unit of m/z = 1 ue^{-1} = 1 Dae^{-1}
$T_S(E)$	Electronic Coupling between Redox Center and Substrate
$T_{Tip}(E)$	Electronic Coupling between Tip and Redox Center
t-Boc	tert-Butyloxycarbonyl
TCEP	Tris(2-Carboxyethyl)Phosphine
TFA	Trifluoroacetic Acid
TMB	Trimethyl Borate
TOC	Total Organic Carbon
Θ	Represents Double-Layer Effects and Tunneling Barrier-Overpotential Dependencies
u_i(I)	Ion Mobility of the Ion Species i in the liquid phase I [m^{2}V^{-1}s^{-1}]
U	Potential [V]
U_{ap}	Potential of the Anodic Peak of a Redox Reaction [V]
U_{cp}	Potential of the Cathodic Peak of a Redox Reaction [V]
U_{Bias}	Bias Voltage [V]
$\triangle U_{diff}$	Diffusion Potential [V]
U_S	Potential of the Working Electrode in the EC SPM setup [V]
U_{tip}	Tip Potential of the Tip in the EC SPM setup [V]
z	Voltage at Piezo [V]
U_0	Redox Potential [V]
U_{00}	Formal Potential of a Redox Couple [V]
UHV	Ultra High Vacuum
v	Sweep Rate [Vs^{-1}]
v_0	Initial Reaction Velocity
ω_{eff}	Effective Nuclear Vibrational Frequency [s^{-1}]
WC	Wet Chemical, Treatment for Producing Oxygen-terminated Diamond
WE	Working Electrode
WKB	Wentzel-Kramer-Brillouin
ξ	Fraction of Substrate-Solution Drop at the Redox Center

$z_i(\mathrm{I})$	Charge of the Ion Species i in the Liquid Phase I

A.2. Publications

Part of this work has been published

- C. Baier and U. Stimming. Imaging single enzyme molecules under in situ conditions, *Angewandte Chemie International Edition* **48** (2009) 5542.
- C. Baier and U. Stimming. In-situ Abbildung einzelner Enzym–Moleküle unter elektrochemischen Bedingungen *Angewandte Chemie* **121** (2009) 5650.
- H. Wolfschmidt, C. Baier, S. Gsell, M. Fischer, M. Schreck, U. Stimming. STM, SECPM, AFM and Electrochemistry on Single Crystalline Surfaces, *Materials* **3** (2010) 4196.
- C. Baier, H. Sternschulte, A. Denisenko, A. Schlichtiger, U. Stimming. Electrochemical Response of Biomolecules on Carbon Substrates: Comparison between Oxidized HOPG and O Terminated Boron-Doped CVD Diamond, *NATO ASI Series, Springer* (2010) *accepted.*

... or will be published soon:

- A. Schlichtiger, C. Baier, A. Frank, H. Kessler, U. Stimming, J. Eppinger. Synthesis and application of watersoluble ferrocene affinity labels for cysteine proteases. (2010) *in preparation.*
- C. Baier, A. Schlichtiger, J. Eppinger, U. Stimming. Covalent immobilization of proteins onto highly oriented pyrolytic graphite (HOPG) for in-situ EC-STM studies. (2010) *in preparation.*
- C. Baier, A. Schlichtiger, J. Eppinger, U. Stimming. Electrochemical biosensing of the cysteine protease papain using a ferrocene affinity label. (2010) *in preparation.*

A.3. Conference Contributions

Posters:

1. C. Baier, H. Wolfschmidt, J. Meier, U. Stimming, Probing of single particle reactivity via EC-STM: Dependence of reactivity on particle size, From Physical Understanding to Novel Architectures of Fuel Cells, Trieste, Italy, 21.05.-24.05.2007

2. M. Wang, C. Baier, U. Stimming, Charge Transfer between Redox Enzymes and Electrodes, International Conference on Electrified Interfaces (ICEI), Hokkaido, Japan, 24.06.-29.06.2007

3. C. Baier, S. Bugarski, U. Stimming, Electrochemical Investigation of Redox Enzymes, Marie Curie Summer School on Modern Concepts for Creating and Analysing Surfaces and Nanoscale Materials, Sant Feliu de Guixols, Spain, 12.05.-16.05.2008

4. C. Baier, S. Bugarski, U. Stimming, Electrochemical Investigation of Redox Enzymes, 1st Joint Nano Workshop, TU München, Germany, 10.06.-11.06.2008

5. A. Schlichtiger, C. Baier, D. Funeriu, J. Eppinger, U. Stimming, Towards an Electrochemical Detection on Enzyme Microarrays, 1st Joint Nano Workshop, TU München, Germany, 10.06.-11.06.2008

6. S.Ghodbane, H.Sternschulte, C. Baier, H.Wolfschmidt, S.Q. Lud, W.Goriwoda, C.Cordioli, M.Rasse, U.Stimming, J.A. Garrido, D.Steinmüller-Nethl, Corrosion resistance of pure and NCD-coated titanium endosseous implants, 19th European Conference on Diamond, Diamond-like Materials, Carbon Nanotubes, and Nitrides, Sitges, Spain, 07.09.-11.09.2008

7. C. Baier, U. Stimming, Investigation of Immobilized Redox Enzymes on HOPG, GDCh - Electrochemisty - Crossing boundaries, Gießen, Germany, 06.-08.10.2008

8. A. Schlichtiger, C. Baier, D. Funeriu, J. Eppinger, U. Stimming, Towards an Electrochemical Detection on Enzyme Microarrays, Tagung der Wöhler Gesellschaft, Chemie Department, TU München, Germany, 09.10.2008

9. C. Baier, A. Schlichtiger, J. Eppinger, U. Stimming, Ferrocene Affinity Label for the Electrochemical Detection of Enzymes, Chemical Nanotechnology Talks IX, "Bio meets Nano", Frankfurt am Main, Germany, 03.11.-04.11.2008

10. C. Baier, U. Stimming, Probing of Enzyme Reactivity using in-situ EC-STM, 7th ISE Spring Meeting, Szczyrk, Poland, 22.03.-25.03.2009

11. C. Baier, A. Schlichtiger, J. Eppinger, U. Stimming, In-situ Electrochemical Detection of Enzymes using Ferrocene Affinity Label, 2. Joint Nanoworkshop NanoDay 2009, Lyngby Denmark, 06.05.2009

12. C. Baier, U. Stimming, SPM Techniques in Electrochemical Surface Science, 5th Kurt Schwabe Symposium, Erlangen, Germany, 24.05.-28.05.2009, **Poster Award for the Scientific Poster KSCS 2009**

13. C. Baier, A. Schlichtiger, J. Eppinger, U. Stimming, In-situ Electrochemical Detection of Enzymes using Ferrocene Affinity Label, 11th Fischer Symposium on Microscopy in Electrochemistry, Benediktbeuern, Germany, 26.07.-31.07.2009

14. C. Baier, U. Stimming, SPM Techniques in Electrochemical Surface Science, 11th Fischer Symposium on Microscopy in Electrochemistry, Benediktbeuern, Germany, 26.07.-31.07.2009

15. C. Baier, A. Schlichtiger, J. Eppinger, U. Stimming, Ferrocene Affinity Label for the Electrochemical Detection of Enzymes Down to a Single Molecule Level, 60th Annual Meeting of the International Society of Electrochemistry, Beijing, China, 16.08.-21.08.2009

16. C. Baier, A. Schlichtiger, U. Stimming, Electrochemistry and SECPM on Biomolecules, ELECTROCHEMISTRY 2010 - From microscopic understanding to global impact, Bochum, Germany, 13.09.-15.09.2010 **Metrohm/Autolab best poster prize**

17. C. Baier, A. Schlichtiger, U. Stimming, New ways in bioelectronics: Detecting redox-modified enzymes down to a single molecule level using EC-STM, Seeing at the Nanoscale VIII, Basel, Switzerland, 30.08.-01.09.2010

18. H. Wolfschmidt, C. Baier, U. Stimming, STM, SECPM, AFM and Electrochemistry on Single Crystalline Surfaces, Seeing at the Nanoscale VIII, Basel, Switzerland, 30.08.-01.09.2010

19. C.Baier, H.Wolfschmidt, A. Schlichtiger, U.Stimming, Towards new electrochemical biosensors: Modification of enzymes with redox-active affinity labels, 61st Annual Meeting of the International Society of Electrochemistry, Nice, France, 26.09.-01.10.2010

Talks:

1. C. Baier, U. Stimming, Structure and activity of enzymes and metal clusters on a molecular scale, Winterschool of the International Graduate School of Materials and Complex Interfaces (CompInt), Antholz, Italy,17.03.-19.03.2007

2. C. Baier, U. Stimming, Charge Transfer and Catalytic Properties of adsorbed Redox Enzymes, Winterschool of the International Graduate School of Materials and Complex Interfaces (CompInt), Antholz, Italy, 01.03.-03.03.2008

3. C. Baier, U. Stimming, Investigation of Enzyme Electrodes using Electrochemical Techniques, Bio-Nano-Workshop, E19 TU München, Garching, Germany, 25.04.2008

4. C. Baier, H. Wolfschmidt, U. Stimming, Scanning Electrochemical Potential Microscopy (SECPM) for the Investigation of Electrode Surfaces, Seeing at the Nanoscale VI - Exploring the Future of Nanotechnology Using SPM and Related Techniques, Berlin, Germany, 09.-11.06.2008

5. C. Baier, U. Stimming, Combined Electrochemical Scanning Tunneling Microscopy (EC-STM) / Scanning Electrochemical Potential Microscopy (SECPM) Study of Electrode Surfaces, 59th Annual Meeting of the International Society of Electrochemistry (ISE), Sevilla, Spain, 07.09.-12.09.2008

6. C. Baier, U. Stimming, Investigation of Electrode Surfaces using Scanning Electrochemical Potential Microscopy (SECPM), GDCh - Electrochemistry - Crossing boundaries, Gießen, Germany, 06.10.-08.10.2008

7. C. Baier, A. Schlichtiger, J. Eppinger, U. Stimming, Ferrocene Affinity Label for the Electrochemical Detection of Enzymes down to a Single Molecule Level, DPG Frühjahrstagung, Dresden, Germany, 22.03.-27.03.2009

8. C. Baier, P. Bele, U. Stimming, Fuel Cells using a Biological Fuel, International Workshop on Distributed Energy Systems: The Role of Chemical Sciences and Technologies, Milano, Italy, 06.04.2009

9. C. Baier, A. Schlichtiger, J. Eppinger, U. Stimming, Electrochemical Biosensing of Cystein Proteases using Ferrocene Affinity Labels, GDCh-Wissenschaftsforum Chemie 2009, Frankfurt am Main, Germany, 30.08.-02.09.2009

10. H. Sternschulte, C. Baier, S. Ghodbane, M. Fischer, D. Steinmüller-Nethl, M. Schreck, U. Stimming, SEM and AFM studies of short grown ultra nano crystalline diamond (UNCD) films: determination of scaling exponents, Diamond 2009, Athen, Greece, 06.09.-10.09.2009

11. C. Baier, A. Schlichtiger, J. Eppinger, U. Stimming, In-situ Electrochemical Detection of Enzymes using Ferrocene Affinity Label, 216th ECS Meeting, Vienna, Austria, 04.10.-09.10.2009

12. C. Baier, A. Schlichtiger, U. Stimming, In-situ Electrochemical Detection of Papain using Ferrocene Affinity Label, Walter-Schottky-Institute, TU München, Garching, Germany, 05.02.2010 **Invited talk**

13. H. Sternschulte, C. Baier, S. Ghodbane, M. Fischer, D. Steinmüller-Nethl, M. Schreck, U. Stimming, Surface growth kinetics of ultra nanocrystalline diamond films, DPG Frühjahrstagung, Regensburg, Germany, 21.-26.03.2010

14. C. Baier, A. Schlichtiger, J. Eppinger, U. Stimming, Enzymatic Activity of Papain Determined by Ferrocene Affinity Label Detection, 217th ECS Meeting, Vancouver, Canada, 25.04.-30.04.2010

15. C. Baier, A. Schlichtiger, U. Stimming, Electrochemical Biosensing using Nanotechnology, NATO Advanced Study Institute - Nanotechnological Basis of Advanced Sensors, Sozopol, Bulgaria, 30.05.–11.06.2010 **Invited talk**

16. H. Sternschulte, C. Baier, A. Denisenko, A. Schlichtiger, U. Stimming, Biomolecules on diamond: surface functionalisation and characterisation, NATO Advanced Study Institute - Nanotechnological Basis of Advanced Sensors, Sozopol, Bulgaria, 30.05.–11.06.2010 **Invited talk**

17. H. Wolfschmidt, C. Baier, U. Stimming, Scanning Probe Techniques (EC-STM, SECPM, AFM) and Electrochemistry on Single Crystalline Supports, Electrochemistry 2010 - From microscopic understanding to global impact 13.09.-15.09.2010, Bochum, Germany

18. H.Wolfschmidt, C.Baier, U.Stimming, STM, SECPM, AFM and Electrochemistry on Single Crystalline Surfaces, 61st Annual Meeting of the International Society of Electrochemistry, Nice, France, 26.09.-01.10.2010

Workshops, Summer Schools, Winterschools:

1. Winterschool of the International Graduate School of Materials Science of Complex Interfaces (CompInt), Antholz, Italy, 17.03.-19.03.2007

2. Winterschool of the International Graduate School of Materials Science of Complex Interfaces (CompInt), Antholz, Italy, 01.03.-03.03.2008

3. Bio-Nano-Workshop, E19 TU München, Garching, Germany, 25.04.2008

4. ψ_k Marie Curie Summer School on Modern Concepts for Creating and Analysing Surfaces and Nanoscale Materials, Sant Feliu de Guixols, Spain, 12.-16.05.2008

5. 1st Joint Nano Workshop, TU München, Germany, 10.-11.06.2008

6. Practical Workshop in Electrochemistry SPM, organized by E19 and Veeco Instruments, TU München, Germany, 26.09.2008

7. International Workshop on Computation in Catalysis, Catalysis Research Center, TU München, Germany, 07.01.-09.01.2009

8. 2. Joint Nanoworkshop NanoDay 2009, Lyngby, Denmark, 06.05.2009

9. Workshop Tsinghua University – TU München, Research related to Electromobility, Beijing, China, 13.03.-14.03.2010

10. Workshop Tsinghua University – TU München, Advanced Power Sources for Electric Vehicles, TU München, Germany, 23.09.-25.09.2010

A.4. Acknowledgement

- I would like to thank my supervisor Prof. Dr. Ulrich Stimming for his guidance during my research and the opportunity to work on such an intersting, interdisciplinary and innovative scientific field.
- I would also like to thank Prof. Dr. Martin Stutzmann for his supervision as my co-advisor, for the fruitful discussions and his support.
- I acknowledge Prof. Dr. Andreas Bausch and the International Graduate School Materials Science of Complex Interfaces (CompInt) in the Elite Network of Bavaria for funding.

I can not imagine that this work could have been realized without the following persons:

- M. Sc. Holger Wolfschmidt: Dear Holger, you are the best office colleague I can imagine, thank you so much for your support, your patient help, the regular discussions and last but not least the cheering up in the lab, when once again everything went wrong :) After all that we have been through together I hope we will stay in contact. All the best for you and your family!
- Dr. Alice Schlichtiger: Dear Alice, thank you so much for everything; for your help, your advice concerning chemical and biochemical issues, for sharing problems, but also for celebrating our great results. Our amicable and successful teamwork gave me motivation and inspired my work, making things thought being impossible possible.

Furthermore, I would like to thank ...

- Prof. Dr. Jörg Eppinger and his group for the collaboration, all the beneficial discussions and the support. I am looking forward to visit you at KAUST!
- Prof. Dr. Andreas Bund for the nice atmosphere at E19 within my last year and also for his endless engagement in saving the ISL!
- Eduard Putzer and Markus Hass, as well as all the other guys from the workshop for their help to realize our experimental setups.
- Dr. Rainer Bussar not only for the introduction to single crystal preparation and all the scientific discussions, but first of all for being a friend with whom one can talk about everything and anything.
- Dr. Hadwig Sternschulte for the fruitful and motivating discussions, all the brain-storming, and last but not least for the proof-reading of this thesis.
- Dr. Philipp Hugelmann for the introduction to the alchemical secrets of electrochemistry and the fascinating world of nanotechnology.

- Joana Figueiredo; with her amicability and a heart of gold she gave the scientific everyday life a human site.
- Dr. Andrej Denisenko from the University of Ulm for scientific discussions and the disposal and preparation of the diamond electrodes.
- the former ISL crew: M. Sc. Holger Wolfschmidt, Dipl. Phys. Daniel Weingarth, Dipl. Phys. Tine Brülle and Dipl. Phys. Cornelia Ostermayr for the familial and entertaining hours in the lab. It was a great time I will never forget!
- the former E19 members: Dipl. Chem. Alexander Racz, Dipl. Chem. Tanja Walter, Dipl. Ing. Johannes Schwärzler and Dr. Franziska Wolfschmidt. I hope we will manage to arrange a E19-get-together from time to time.
- all the colleagues from the chair E19 *Interfaces and Energy Conversion.*

Special thanks

- From the bottom of my heart I thank my family for their endless and unconditional love, their everlasting support and the steady encouragements from the first day of my life that gave me all the power and strength to realize my dreams. Without you I would never be there where I am today! Thank you so much, I love you!
- I thank the sun that stepped into my life, lightening the days of writing and waiting, filling my life with colors, showing me facettes I could not imagine. From the first day your warming light touched my soul, I finally felt secure and being arrived, knowing that what we have is something special that can last forever.

Bibliography

[1] I. Willner, E. Katz. *Bioelectronics.* Wiley-VCH Verlag GmbH Co. KGaA, Weinheim, (2005).

[2] J. J. Davis, H. A. O. Hill. *Chemical Communications* **5** (2002) 393.

[3] A. Alessandrini, S. Corni, P. Facci. *Physical Chemistry Chemical Physics* **8** (2006) 4383.

[4] *Bioelectrochemistry.* John Wiley Sons Ltd, Chichester, (2008).

[5] J. Wang. *Electroanalysis* **13** (2001) 983.

[6] D. Grieshaber, R. MacKenzie, J. Voeroes, E. Reimhult. *Sensors* **8** (2008) 1400.

[7] S. Cosnier. *Biosensors Bioelectronics* **14** (1999) 443.

[8] E. Ferapontova, E. Dominguez. *Bioelectrochemistry* **55** (2002) 127.

[9] D. M. Sun, C. X. Cai, X. G. Li, W. Xing, T. H. Lu. *Journal of Electroanalytical Chemistry* **566** (2004) 415.

[10] J. F. Evans, T. Kuwana, M. T. Henne, G. P. Royer. *Journal of Electroanalytical Chemistry* **80** (1977) 409.

[11] S. Karel. *Electroanalysis* **4** (1992) 829.

[12] A. A. Gewirth, A. J. Bard. *Journal of Physical Chemistry* **92** (1988) 5563.

[13] J. Xu, Q. Chen, G. M. Swain. *Analytical Chemistry* **70** (1998) 3146.

[14] J. D. Zhang, Q. J. Chi, S. J. Dong, E. K. Wang. *Bioelectrochemistry and Bioenergetics* **39** (1996) 267.

[15] M. Wang, S. Bugarski, U. Stimming. *Journal of Physical Chemistry C* **112** (2008) 5165.

[16] M. Wang, S. Bugarski, U. Stimming. *Small* **4** (2008) 1110.

[17] Q. J. Chi, O. Farver, J. Ulstrup. *Proceedings of the National Academy of Sciences of the United States of America* **102** (2005) 16203.

[18] A. Alessandrini, M. Gerunda, G. W. Canters, M. P. Verbeet, P. Facci. *Chemical Physics Letters* **376** (2003) 625.

[19] J. Pinson, F. Podvorica. *Chemical Society Reviews* **34** (2005) 429.

[20] M. Delamar, R. Hitmi, J. Pinson, J. M. Saveant. *Journal of the American Chemical Society* **114** (1992) 5883.

[21] P. Allongue, M. Delamar, B. Desbat, O. Fagebaume, R. Hitmi, J. Pinson, J. M. Saveant. *Journal of the American Chemical Society* **119** (1997) 201.

[22] C. Vaz-Dominguez, S. Campuzano, O. Rüdiger, M. Pita, M. Gorbacheva, S. Shleev, V. M. Fernandez, A. L. D. Lacey. *Biosensors and Bioelectronics* **24** (2008) 531.

[23] M. Mayer. *Clinical Biochemistry* **23** (1990) 197.

[24] N. A. Thornberry, Y. Lazebnik. *Science* **281** (1998) 1312.

[25] M. Gale, E. M. Foy. *Nature* **436** (2005) 939.

[26] A. Wlodawer, J. W. Erickson. *Annual Review of Biochemistry* **62** (1993) 543.

[27] J. Gills, J. L. Piccolo, J. Tsurutani, R. H. Shoemaker, C. J. M. Best, M. S. Abu-Asab, J. Borojerdi, N. A. Warfel, E. R. Gardner, M. Danish, M. C. Hollander, S. Kawabata, M. Tsokos, W. D. Figga, P. S. Steeg, P. A. Dennis. *Clinical Cancer Research* **13** (2007) 5183.

[28] P. Pyrko, A. Kardosh, W. Wang, W. Xiong, A. H. Schonthal, T. C. Chen. *Cancer Research* **67** (2007) 10920.

[29] J. Eppinger, D. P. Funeriu, M. Miyake, L. Denizot, J. Miyake. *Angewandte Chemie-International Edition* **43** (2004) 3806.

[30] D. P. Funeriu, J. Eppinger, L. Denizot, M. Miyake, J. Miyake. *Nature Biotechnology* **23** (2005) 622.

[31] N. J. Long. *Metallocenes-An Introduction to Sandwich Complexes.* Blackwell Scientific, Oxford, .K., (1998).

[32] Z. Li, Y. Liu, S. F. L. Mertens, I. V. Pobelov, T. Wandlowski. *J Am Chem Soc* **132** (2010) 8187.

[33] A. Schlichtiger. *Synthese und Anwendung von Affinitätsmarkern für die fluoreszenzbasierte und die elektrochemische Bestimmung von Enzymaktivitäten.* PhD thesis, Technische Universität München, (2009).

[34] W. Schmickler. *Interfacial Electrochemistry.* Oxford University Press, Inc., New York, (1996).

[35] W. Schmickler, D. Henderson. *J.Electroanal. Chem.* **290** (1990) 283.

[36] N. J. Tao. *Physical Review Letters* **76** (1996) 4066.

[37] G. Binnig, H. Rohrer, C. Gerber, E. Weibel. *Applied Physics Letters* **40** (1982) 178.

[38] G. Binnig, H. Rohrer, C. Gerber, E. Weibel. *Physical Review Letters* **49** (1982) 57.

[39] G. Binnig, C. F. Quate, C. Gerber. *Physical Review Letters* **56** (1986) 930.

[40] T. Albrecht, A. Guckian, J. Ulstrup, J. G. Vos. *Nano Letters* **5** (2005) 1451.

[41] T. Albrecht, A. Guckian, A. M. Kuznetsov, J. G. Vos, J. Ulstrup. *Journal of the American Chemical Society* **128** (2006) 17132.

[42] T. Albrecht, S. F. L. Mertens, J. Ulstrup. *Journal of the American Chemical Society* **129** (2007) 9162.

[43] P. Facci, D. Alliata, S. Cannistraro. *Ultramicroscopy* **89** (2001) 291.

[44] J. Zhang, Q. Chi, A. Kuznetsov, A. G. Hansen, H. Wackerbarth, H. E. M. Christensen, J. E. T. Andersen, J. Ulstrup. *Journal of Physical Chemistry B* **106** (2002) 1131.

[45] C. Z. Li, K. J. Kjoller. Scanning electrochemcial potential microscope, (2007).

[46] D. H. Woo, J. S. Yoo, S. M. Park, I. C. Jeon, H. Kang. *Bulletin of the Korean Chemical Society* **25** (2004) 577.

[47] C. Hurth, C. Z. Li, A. J. Bard. *Journal of Physical Chemistry C* **111** (2007) 4620.

[48] C. Corbella, E. Pascual, G. Oncins, C. Canal, J. L. Andujar, E. Bertran. *Thin Solid Films* **482** (2005) 293.

[49] C. Baier, U. Stimming. *Angewandte Chemie International Edition* **48** (2009) 5542.

[50] G. Z. Liu, J. Q. Liu, T. Bocking, P. K. Eggers, J. J. Gooding. *Chemical Physics* **319** (2005) 136.

[51] A. Hartl, E. Schmich, J. A. Garrido, J. Hernando, S. C. R. Catharino, S. Walter, P. Feulner, A. Kromka, D. Steinmuller, M. Stutzmann. *Nature Materials* **3** (2004) 736.

[52] J. Hernando, T. Pourrostami, J. A. Garrido, O. A. Williams, D. M. Gruen, A. Kromka, D. Steinmuller, M. Stutzmann. *Diamond and Related Materials* **16** (2007) 138.

[53] A. J. Bard, W. R. Faulkner. *Electrochemical Methods: Fundamentals and Applications.* Wiley, Weinheim, (2001).

[54] V. S. Bagotsky. *Fundamentals of Electrochemistry.* John Wiley Sons, Inc., Hoboken, New Jersey, second edition edition, (2006).

[55] D. C. Grahame. *Chemical Reviews* **41** (1947) 441.

[56] H. L. F. Helmholtz. *Annalen der Physik* **89** (1853) 211.

[57] G. Gouy. *Journal de Physique et Le Radium* **9** (1910) 457.

[58] G. Gouy. *Comptes Rendus* **149** (1910) 654.

[59] D. L. Chapman. *Philosophical Magazine* **25** (1913) 475.

[60] Z. Borkowska, U. Stimming. Structure formation in the double layer at the electrode-electrolyte interface. In P. Lipkowski, P. N. Ross, editors, *Structure of Electrified Interfaces, Frontiers of Electrochemistry*, 2. VCH, (1993).

[61] R. J. Marcus, B. J. Zwolinski, H. Eyring. *Journal of Physical Chemistry* **58** (1954) 432.

[62] V. G. Levich, R. R. Dogonadze. *Doklady Akademii Nauk Sssr* **133** (1960) 158.

[63] N. S. Hush. *Transactions of the Faraday Society* **57** (1961) 557.

[64] R. A. Marcus. *Annual Review of Physical Chemistry* **15** (1964) 155.

[65] R. A. Marcus, N. Sutin. *Biochimica et Biophysica Acta (BBA) - Reviews on Bioenergetics* **811** (1985) 265.

[66] R. A. Marcus. *Angew. Chem. Int. Ed.* **32** (1993) 1111.

[67] P. Zanello. *Inorganic Electrochemistry - Theory, Practice and Application.* The Royal Society of Chemistry, (2003).

[68] R. Greef, R. Peat, L. M. Peter, D. Pletcher, J. Robinson. *Instrumental Methods in Electrochemistry.* Ellis Horwood Series in Physical Chemistry. Southampton Electrochemsitry Group/Ellis Horwood Limited, Chichester, (1985).

[69] J. E. B. Randles. *Transactions of the Faraday Society* **44** (1948) 327.

[70] A. Sevcik. *Collection of Czechoslovak Chemical Communications* **13** (1948).

[71] E. Laviron. *Journal of Electroanalytical Chemistry* **52** (1974) 395.

[72] E. Laviron. *Journal of Electroanalytical Chemistry* **100** (1979) 263.

[73] E. Laviron. *Journal of Electroanalytical Chemistry* **101** (1979) 19.

[74] L. Stryer. *Biochemistry.* Freeman, San Francisco, (1995).

[75] J. M. Odom, R. Singleton. *The sulphate-reducing Bacteria: Contemporary Perspectives.* Springer-Verlag, New York, (1993).

[76] H. B. Gray, J. R. Winkler. *Quarterly Reviews of Biophysics* **36** (2003) 341.

[77] S. S. Isied, M. Y. Ogawa, J. F. Wishart. *Chem. Rev.* **92** (1992).

[78] C. A. Hasemann, R. G. Kurumbail, S. S. Boddupalli, J. A. Peterson, J. Deisenhofer. *Structure* **3** (1995) 41.

[79] M. R. Gunner, B. Honig. *Proceedings of the National Academy of Sciences of the United States of America* **88** (1991) 9151.

[80] A. Kuznetsov, J. Ulstrup. *Electron transfer in chemistry and biology - An introduction to theory.* Theoretical Chemistry. John Wiley Sons Ltd, Chichester, (1999).

[81] *http://www.neb.com/nebecomm/tech$_r$eference/images/amino.gif.*

[82] W. L. DeLano. *De Lano Scientific, Palo Alto, CA, USA* (2002).

[83] H. M. Berman, J. Westbrook, Z. Feng, G. Gilliland, T. N. Bhat, H. Weissig, I. N. Shindyalov, P. E. Bourne. *The Protein Data Bank, Nucleic Acid Research* **28** (2000) 235.

[84] A. Bianconi, A. Congiucastellano, M. Dellariccia, A. Giovannelli, E. Burattini, P. J. Durham. *Biochemical and Biophysical Research Communications* **131** (1985) 98.

[85] B. Halliwell. *Journal of Neurochemistry* **59** (1992) 1609.

[86] R. R. Crichton. *Angewandte Chemie* **2** (1973) 53.

[87] R. R. Crichton. *FEBS Letters* **34** (1973) 125.

[88] G. D. Watt, R. B. Frankel, D. Jacobs, H. Q. Huang. *Biochemistry* **31** (1992) 5672.

[89] Y. H. Wu, S. S. Hu. *Analytica Chimica Acta* **527** (2004) 37.

[90] N. C. Veitch. *Phytochemistry* **65** (2004) 249.

[91] A. Azevedo, V. Martins, D. Prazeres, V. Vojinovic, J. Cabral, L. Fonseca. *Biotechnology annual review* **9** (2003) 199.

[92] M. Hamid, R. K. ur. *Food Chemistry* **115** (2009) 1177.

[93] K. G. Welinder. *FEBS Letters* **72** (1976) 19.

[94] M. Gajhede, D. J. Schuller, A. Henriksen, A. T. Smith, T. L. Poulos. *Nature Stuctural Biology* **4** (1997) 1032.

[95] E. E. Ferapontova. *Electroanalysis* **16** (2004) 1101.

[96] Y. Zhang, G. S. Wilson. *Journal of Electroanalytical Chemistry* **345** (1993) 253.

[97] T. Ruzgas, L. Gorton, J. Emneus, G. Marko-Varga. *Journal of Electroanalytical Chemistry* **391** (1995) 41.

[98] E. Ferapontova, K. Schmengler, T. Borchers, T. Ruzgas, L. Gorton. *Biosensors and Bioelectronics* **17** (2002) 953.

[99] E. Ferapontova, L. Gorton. *Electroanalysis* **15** (2003) 484.

[100] S. Burgarski. *Untersuchung der Adsorptions- und Katalyseeigenschaften der Horseradish Peroxidase auf Au(111).* PhD thesis, Technische Universität München, (2009).

[101] S. Shleev, J. Tkac, A. Christenson, T. Ruzgas, A. I. Yaropolov, J. W. Whittaker, L. Gorton. *Biosensors and Bioelectronics* **20** (2005) 2517.

[102] E. T. Adman. *Advances in Protein Chemistry* **42** (1991) 145.

[103] E. T. Adman. *Topics in Molecular and Structural Biology: Metalloproteins.* Chemie Verlag, Weinheim, (1985).

[104] E. T. Adman, R. E. Stenkamp, L. C. Sieker, L. H. Jensen. *Journal of Molecular Biology* **123** (1978) 35.

[105] E. N. Baker. *Journal of Molecular Biology* **203** (1988) 1071.

[106] H. Nar, A. Messerschmidt, R. Huber, M. van de Kamp, G. W. Canters. *Journal of Molecular Biology* **218** (1991) 427.

[107] E. I. Solomon, M. J. Baldwin, M. D. Lowery. *Chemical Reviews* **92** (1992) 521.

[108] D. Pinho, S. Besson, C. D. Brondino, E. Pereira, B. de Castro, I. Moura. *Journal of Inorganic Biochemistry* **98** (2004) 276.

[109] E. P. Friis, J. E. T. Andersen, Y. I. Kharkats, A. M. Kuznetsov, R. J. Nichols, J. D. Zhang, J. Ulstrup. *Proceedings of the National Academy of Sciences of the United States of America* **96** (1999) 1379.

[110] A. Alessandrini, M. Salerno, S. Frabboni, P. Facci. *Applied Physics Letters* **86** (2005).

[111] I. G. Kamphuis, K. H. Kalk, M. B. A. Swarte, J. Drenth. *Journal of Molecular Biology* **179** (1984) 233.

[112] H.-H. Otto, T. Schirmeister. *Chemical Reviews* **97** (1992) 133.

[113] K. E. Dombrowski, J. E. Sheats, D. J. Prockop. *Biochemistry* **25** (1986) 4302.

[114] P. Haquette, M. Salmain, K. Svedlung, A. Martel, B. Rudolf, J. Zakrzewski, S. Cordier, T. Roisnel, C. Fosse, G. Jaouen. *Chembiochem* **8** (2007) 224.

[115] K. A. Mahmoud, H. B. Kraatz. *Chemistry-a European Journal* **13** (2007) 5885.

[116] A. Strecker. *Annalen der Chemie und Pharmacie* **75** (1850) 27.

[117] A. Strecker. *Annalen der Chemie und Pharmacie* **91** (1854) 349.

[118] J. McMurry. *Organic Chemistry.* Brooks/Cole Pub. Co., Pacific Grove, CA. USA, (1996).

[119] H. Ishitani, S. Komiyama, Y. i. Hasegawa, S. Kobayashi. *Journal of the American Chemical Society* **122** (2000) 762.

[120] S. Masumoto, H. Usuda, M. Suzuki, M. Kanai, M. Shibasaki. *Journal of the American Chemical Society* **125** (2003) 5634.

[121] J. Huang, E. J. Corey. *Organic Letters* **6** (2004) 5027.

[122] R. B. Merrifield. *Journal of the American Chemical Society* **85** (1963) 2149.

[123] M. Amblard, J. A. Fehrentz, J. Martinez, G. Subra. *Molecular Biotechnology* **33** (2006) 239.

[124] K. Yoshizawa-Kumagaye, Y. Nishiuchi, H. Nishio, T. Kimura. *Journal of Peptide Science* **11** (2005) 512.

[125] S. Y. Han, Y. A. Kim. *Tetrahedron* **60** (2004) 2447.

[126] V. Henri. *Zeitschrift Fur Elektrochemie Und Angewandte Physikalische Chemie* **11** (1905) 790.

[127] L. Michaelis, M. L. Menten. *Biochemische Zeitschrift* **49** (1913) 333.

[128] D. L. Nelson, M. M. Cox. *Lehninger Biochemie*. Springer-Verlag, Berlin Heidelberg New York, (2001).

[129] G. E. Briggs, J. B. S. Haldane. *Biochemical Journal* **19** (1925) 338.

[130] L. C. Clark, C. Lyons. *Annals of the New York Academy of Sciences* **102** (1962) 29.

[131] D. C. Greenbaum, W. D. Arnold, F. Lu, L. Hayrapetian, A. Baruch, J. Krumrine, S. Toba, K. Chehade, D. Bromme, I. D. Kuntz, M. Bogyo. *Chemistry and Biology* **9** (2002) 1085.

[132] R. Gamsjaeger, A. Johs, A. Gries, H. Gruber, C. Romanin, R. Prassl, P. Hinterdorfer. *Biochemical Journal* **389** (2005) 665.

[133] R. P. Haugland. *The Handbook A guide to fluorescent probes and labeling technologies*. Invitrogen Corporation, San Diego, 10 edition, (2005).

[134] A. P. Fang, H. T. Ng, S. F. Y. Li. *Biosensors and Bioelectronics* **19** (2003) 43.

[135] M. S. Wilson. *Analytical Chemistry* **77** (2005) 1496.

[136] P. D'Oranzio. *Clinica Chimica Acta* **334** (2003) 41.

[137] T. J. Kealy, P. L. Pauson. *Nature* **168** (1951) 1039.

[138] S. A. Miller, J. A. Tebboth, J. F. Tremaine. *Journal of the Chemical Society* (1952) 632.

[139] D. R. van Staveren, N. Metzler-Nolte. *Chemical Reviews* **104** (2004) 5931.

[140] H. M. Koepp, H. Wendt, H. Strehlow. *Zeitschrift fuer Elektrochemie* **64** (1960) 483.

[141] R. R. Gagne, C. A. Koval, G. C. Lisensky. *Inorganic Chemistry* **19** (1980) 2854.

[142] S. Lu, V. V. Strelets, M. F. Ryan, W. J. Pietro, A. B. P. Lever. *Inorganic Chemistry* **35** (1996) 1013.

[143] R. Sonnenfeld, P. K. Hansma. *Science* **232** (1986) 211.

[144] P. Lustenberger, H. Rohrer, R. Christoph, H. Siegenthaler. *Journal of Electroanalytical Chemistry* **243** (1988) 225.

[145] K. Itaya, E. Tomita. *Surface Science* **201** (1988) L507.

[146] P. Hugelmann. *Elektrochemische Herstellung und Charakterisierung von Nanostrukturen - Entwicklung ultrascharfer STM-Spitzen als Nanoelektroden.* PhD thesis, Universität Karlsruhe (TH), (2004).

[147] G. Binnig, N. Garcia, H. Rohrer, J. M. Soler, F. Flores. *Physical Review B* **30** (1984) 4816.

[148] G. E. Engelmann, J. C. Ziegler, D. M. Kolb. *Surface Science* **401** (1998) L420.

[149] J. Tersoff, D. R. Hamann. *Physical Review Letters* **50** (1983) 1998.

[150] J. Bardeen. *Physical Review Letters* **6** (1961) 57.

[151] R. Christoph, H. Siegenthaler, H. Rohrer, H. Wiese. *Electrochimica Acta* **34** (1989) 1011.

[152] W. Schmickler, C. Widrig. *Journal of Electroanalytical Chemistry* **336** (1992) 213.

[153] A. M. Kuznetsov, P. Sommerlarsen, J. Ulstrup. *Surface Science* **275** (1992) 52.

[154] E. P. Friis, J. E. T. Andersen, L. L. Madsen, P. Moller, R. J. Nichols, K. G. Olesen, J. Ulstrup. *Electrochimica Acta* **43** (1998) 2889.

[155] A. M. Kuznetsov, J. Ulstrup. *Electrochimica Acta* **45** (2000) 2339.

[156] D. M. Eigler, E. K. Schweizer. *Nature* **344** (1990) 524.

[157] D. M. Kolb, F. C. Simeone. *Electrochimica Acta* **50** (2005) 2989.

[158] D. Jung. *Nanostrukturierung von Substraten - Literaturrecherche und experimentelle Herstellung EC-STM induzierter Cluster-Arrays.* Thesis, Technische Universität München, (2004).

[159] J. Meier, K. A. Friedrich, U. Stimming. *Faraday Discussions* **121** (2002) 365.

[160] J. Meier, J. Schiotz, P. Liu, J. K. Norskov, U. Stimming. *Chemical Physics Letters* **390** (2004) 440.

[161] J. Liang, G. Scoles. *Langmuir* **23** (2007) 6142.

[162] D. H. Woo, H. Kang, S.-M. Park. *Analytical Chemistry* **75** (2003) 6732.

[163] J. Ghilane, P. Hapiot, A. J. Bard. *Analytical Chemistry* **78** (2006) 6868.

[164] H. Ohshima. *Colloid and Polymer Science* **252** (1974) 158.

[165] J. E. Sader, A. M. Lenhoff. *Journal of Colloid and Interface Science* **201** (1998) 233.

[166] J. E. Sader, D. Y. C. Chan. *Journal of Colloid and Interface Science* **218** (1999) 423.

[167] R. F. Hamou, P. U. Biedermann, M. Rohwerder, A. T. Blumenau. *Excerpt from the Proceedings of the COMSOL Conference 2008 Hannover* (2009).

[168] R. C. Wolfe, K. G. Weil, B. A. Shaw, H. W. Pickering. *Journal of the Electrochemical Society* **152** (2005) B82.

[169] A. R. Kucernak, P. B. Chowdhury, C. P. Wilde, G. H. Kelsall, Y. Y. Zhu, D. E. Williams. *Electrochimica Acta* **45** (2000) 4483.

[170] A. Roos, W. F. Boron. *Physiological Reviews* **61** (1981) 296.

[171] W. B. Busa, R. Nuccitelli. *American Journal of Physiology* **246** (1984) R409.

[172] G. Dagher, C. Sauterey. *Journal of Hypertension* **10** (1992) 969.

[173] T. Imokawa, K.-J. Williams, G. Denuault. *Analytical Chemistry* **78** (2006) 265.

[174] R. G. Bates, D. B. Cater, G. J. Hills, D. J. G. Ives, G. J. Janz, R. W. Laity, I. A. Silver, F. R. Smith. *Reference Electrodes - Theory and Practice.* Academic Press Inc., New York and London, (1961).

[175] G. J. Hills, D. J. G. Ives. *Reference Electrodes, Theory and Practice.* Janz, G. J. Academic Press, London, (1961).

[176] D. Midgley. *Talanta* **37** (1990) 767.

[177] T. B. Flanagan, F. A. Lewis. *Transactions of the Faraday Society* **55** (1959) 1400.

[178] S. Pandelov. *Investigation of the structure and reactivity of nanostructured surfaces.* PhD thesis, Technische Universität München, (2007).

[179] D. D. Macdonald, P. R. Wentrcek, A. C. Scott. *Journal of the Electrochemical Society* **127** (1980) 1745.

[180] M. J. Vasile, C. G. Enke. *Journal of the Electrochemical Society* **112** (1965) 865.

[181] S. Schuldiner, G. Castellan, J. P. Hoare. *Journal of Chemical Physics* **28** (1958) 16.

[182] H. McNab, L. C. Monahan. *Journal of the Chemical Society-Perkin Transactions 1* (1989) 419.

[183] K. A. H. Chehade, A. Baruch, H. L. Verhelst, M. Bogyo. *Synthesis* **2** (2005) 240.

[184] P. D. Beer, D. K. Smith. *Journal of the Chemical Society-Dalton Transactions* (1998) 417.

[185] A. S. Carlstrom, T. Frejd. *Journal of Organic Chemistry* **55** (1990) 4175.

[186] A. J. Barett, A. A. Kembhavi, M. A. Brown, H. Kirschke, C. G. Knight, M. Tamai, K. Handa. *Biochemical Journal* **201** (1982) 189.

[187] K. Hanada, M. Tamai, M. Yamagishi, S. Ohmura, J. Sawada, I. Tanaka. *Agricultural and Biological Chemistry* **42** (1978) 523.

[188] K. Hanada, M. Tamai, S. Ohmura, J. Sawada, T. Seki, I. Tanaka. *Agricultural and Biological Chemistry* **42** (1978) 529.

[189] H. U. Demuth. *Journal of Enzyme Inhibition* **3** (1990) 249.

[190] J. M. Osgerby, P. L. Pauson. *Journal of the Chemical Society* (1958) 656.

[191] C. H. Hamann, W. Vielstich. *Elektrochemie.* Wiley-VCH, Weinheim, (2005).

[192] J. Meier. *Herstellung, Charakterisierung und Reaktivität von Oberflächeninhomogenitäten an der Grenzfläche fest-flüssig.* PhD thesis, Technische Universität München, (2003).

[193] L. A. Nagahara, T. Thundat, S. M. Lindsay. *Review of Scientific Instruments* **60** (1989) 3128.

[194] A. J. Bard, R. Parsons, J. Jordan. *Standard potentials in aqueous solutuion.* Marcel Dekker, New York, (1985).

[195] J. Clavilier, R. Faure, G. Guinet, R. Durand. *Journal of Electroanalytical Chemistry* **107** (1980) 205.

[196] L. A. Kibler. *Preparation and characterization of noble metal single crystal electrode surfaces.* PhD thesis, (2003).

[197] J.-P. Randin, E. Yeager. *Journal of Electroanalytical Chemistry* **36** (1972) 257.

[198] J.-P. Randin, E. Yeager. *Journal of Electroanalytical Chemistry* **58** (1975) 313.

[199] H. Gerischer, R. McIntyre, D. A. Scherson, W. Storck. *Journal of Physical Chemistry* **91** (1987) 1930.

[200] M. T. McDermott, K. Kneten, R. L. McCreery. *Journal of Physical Chemistry* **96** (1992) 3124.

[201] K. K. Cline, M. T. McDermott, R. L. McCreery. *The Journal of Physical Chemistry* **98** (1994) 5314.

[202] R. Bowling, R. T. Packard, R. L. McCreery. *Langmuir* **5** (1989) 683.

[203] S. Boland, F. Barriere, D. Leech. *Langmuir* **24** (2008) 6351.

[204] A. J. Downard. *Electroanalysis* **12** (2000) 1085.

[205] D. Cahen, G. Hodes. *Advanced Materials* **14** (2002) 789.

[206] B. L. Hurley, R. L. McCreery. *Journal of the Electrochemical Society* **151** (2004) B252.

[207] P. Allongue, C. H. de Villeneuve, G. Cherouvrier, R. Cortes, M. C. Bernard. *Journal of Electroanalytical Chemistry* **550** (2003) 161.

[208] J. Lyskawa, F. L. Derf, E. Levillain, M. Mazari, M. Salle, L. Dubois, P. Viel, C. Bureau, S. Palacin. *Journal of the American Chemical Society* **126** (2004) 12194.

[209] B. D. Bath, H. B. Martin, R. M. Wightman, M. R. Anderson. *Langmuir* **17** (2001) 7032.

[210] A. E. Radi, V. Lates, J. L. Marty. *Electroanalysis* **20** (2008) 2557.

[211] P. Viel, C. Bureau, G. Deniau, G. Zalczer, G. Lecayon. *Journal of Electroanalytical Chemistry* **470** (1999) 14.

[212] C. Bourdillon, M. Delamar, C. Demaille, R. Hitmi, J. Moiroux, J. Pinson. *Journal of Electroanalytical Chemistry* **336** (1992) 113.

[213] Y. C. Liu, R. L. McCreery. *Journal of the American Chemical Society* **117** (1995) 11254.

[214] A. J. Downard, A. D. Roddick, A. M. Bond. *Analytica Chimica Acta* **317** (1995) 303.

[215] J. Q. Liu, J. J. Gooding, M. N. Paddon-Row. *Chemical Communications* (2005) 631.

[216] Y. V. Pleskov. *Russian Journal of Electrochemistry* **38** (2002) 1275.

[217] J. E. Butler, Y. A. Mankelevich, A. Cheesman, J. Ma, M. N. R. Ashfold. *Journal of Physics-Condensed Matter* **21** (2009) 364201.

[218] J. Wang, J. A. Carlisle. *Diamond and Related Materials* **15** (2006) 270.

[219] R. J. Hamers, J. E. Butler, T. Lasseter, B. M. Nichols, J. J. N. Russell, K.-Y. Tse, W. Yang. *Diamond and Related Materials* **14** (2005) 661.

[220] Y. L. Zhou, R. H. Tian, J. F. Zhi. *Biosensors and Bioelectronics* **22** (2007) 822.

[221] M. Dankerl, S. Eick, B. Hofmann, M. Hauf, S. Ingebrandt, A. OffenhÃusser, M. Stutzmann, J. A. Garrido. *Advanced Functional Materials* **19** (2009) 2915.

[222] C. Pietzka, A. Denisenko, L. A. Kibler, J. Scharpf, Y. Men, E. Kohn. *Diamond and Related Materials* **18** (2009) 816.

[223] M. Kunze, A. Vescan, G. Dollinger, A. Bermaier, E. Kohn. *Carbon* **37** (1999) 787.

[224] C. Pietzka, A. Denisenko, A. Romanyuk, P. J. SchÃfer, L. A. Kibler, J. Scharpf, E. Kohn. *Diamond and Related Materials* (2009) in press.

[225] A. M. Baro, R. Miranda, J. Alaman, N. Garcia, G. Binnig, H. Rohrer, C. Gerber, J. L. Carrascosa. *Nature* **315** (1985) 253.

[226] G. Liu, T. Böcking, J. J. Gooding. *Journal of Electroanalytical Chemistry* **600** (2007) 335.

[227] D. Alliata, R. Kotz, O. Haas, H. Siegenthaler. *Langmuir* **15** (1999) 8483.

[228] B. Schnyder, D. Alliata, R. Kötz, H. Siegenthaler. *Applied Surface Science* **173** (2001) 221.

[229] O. Farver, N. Bonander, L. K. Skov, I. Pecht. *Inorganica Chimica Acta* **243** (1996) 127.

[230] Q. J. Chi, J. D. Zhang, J. U. Nielsen, E. P. Friis, I. Chorkendorff, G. W. Canters, J. E. T. Andersen, J. Ulstrup. *Journal of the American Chemical Society* **122** (2000) 4047.

[231] K. S. Weber, S. E. Creager. *Journal of Electroanalytical Chemistry* **458** (1998) 17.

[232] L. Tender, M. T. Carter, R. W. Murray. *Analytical Chemistry* **66** (1994) 3173.

[233] A. M. Napper, H. Y. Liu, D. H. Waldeck. *Journal of Physical Chemistry B* **105** (2001) 7699.

[234] T. Albrecht. *Dynamik und Mechanismen der heterogenen Elektronentransferprozesse von synthetischen und natuerlichen Haemproteinen.* PhD thesis, Technische Universitaet Berlin, (2003).

[235] T. Albrecht, K. Moth-Poulsen, J. B. Christensen, A. Guckian, T. Bjornholm, J. G. Vos, J. Ulstrup. *Faraday Discussions* **131** (2006) 265.

[236] W. Haiss, T. Albrecht, H. van Zalinge, S. J. Higgins, D. Bethell, H. Hobenreich, D. J. Schiffrin, R. J. Nichols, A. M. Kuznetsov, J. Zhang, Q. Chi, J. Ulstrup. *Journal of Physical Chemistry B* **111** (2007) 6703.

[237] J. Wiechers, T. Twomey, D. M. Kolb, R. J. Behm. *Journal of Electroanalytical Chemistry* **248** (1988) 451.

[238] J. M. Soler, A. M. Baro, N. Garcia, H. Rohrer. *Physical Review Letters* **57** (1986) 444.

[239] R. J. Rice, R. L. McCreery. *Analytical Chemistry* **61** (1989) 1637.

[240] K. Ray, R. L. McCreery. *Analytical Chemistry* **69** (1997) 4680.

[241] C. Callies, P. Schoen, I. Liashkovich, C. Stock, K. Kusche-Vihrog, J. Fels, A. S. Staeter, H. Oberleithner. *Nanotechnology* **20** (2009) 175104.

[242] A. Engel, D. J. Muller. *Nature Structural Biology* **7** (2000) 715.

[243] D. C. Zapien, M. A. Johnson. *Journal of Electroanalytical Chemistry* **494** (2000) 114.

[244] E. Krieger, T. Darden, S. Nabuurs, A. Finkelstein, G. Vriend. *Proteins* **57** (2004) 678.

[245] C. Z. Li, B. Russel, B. Maringer, S. Kjoller. *US Patent pending* (2003).

[246] C. Hurth. *Scanning Probe Microscopy Studies of Active Enzymes at Solid Surfaces.* PhD thesis, University of Texas at Austin, (2005).

[247] R. Hiesgen, D. Meissner, W. Schmickler. *Surface Science* **479** (2001) 183.

[248] A. A. Kornyshev, A. M. Kumetsov. *Electrochemistry Communications* **8** (2006) 679.

[249] Z. X. Xie, D. M. Kolb. *Journal of Electroanalytical Chemistry* **481** (2000) 177.

[250] J. Divisek, B. Steffen, U. Stimming, W. Schmickler. *Journal of Electroanalytical Chemistry* **440** (1997) 169.

[251] D. Weingarth. *Reactivity measurements with the STM.* Diploma thesis, Technische Universität München, (2009).

[252] T. B. Flanagan, F. A. Lewis. *Transactions of the Faraday Society* **55** (1959) 1409.

[253] S. Behera, C. R. Raj. *Journal of Electroanalytical Chemistry* **619** (2008) 159.

[254] L. B. W. Jr, C. H. Shaw, J. F. Castner. *Enzyme and Microbial Technology* **4** (1982) 137.

[255] A. M. Kannan, V. Renugopalakrishnan, S. Filipek, P. Li, G. F. Audette, L. Munukutla. *Journal of Nanoscience and Nanotechnology* **9** (2009) 1665.

[256] I. Willner, B. Willner, E. Katz. *Bioelectrochemistry* **70** (2007) 2.

[257] P. N. Bartlett, P. Tebbutt, R. G. Whitaker. *Progress in Reaction Kinetics* **16** (1991) 55.

[258] F. A. Armstrong, P. A. Cox, H. A. O. Hill, V. J. Lowe, B. N. Oliver. *J. Electroanal. Chem.* **217** (1987) 331.

[259] B. Bonanni, L. Andolfi, A. R. Bizzarri, S. Cannistraro. *Journal of Physical Chemistry B* **111** (2007) 5062.

[260] J. D. Zhang, A. M. Kuznetsov, I. G. Medvedev, Q. J. Chi, T. Albrecht, P. S. Jensen, J. Ulstrup. *Chemical Reviews* **108** (2008) 2737.

[261] D. Evrard, F. Lambert, C. Policar, V. Balland, B. Limoges. *Chemistry-a European Journal* **14** (2008) 9286.

[262] H. Zimmermann, A. Lindgren, W. Schuhmann, L. Gorton. *Chemistry-a European Journal* **6** (2000) 592.

[263] F. Silva, A. Martins. *Electrochimica Acta* **44** (1998) 919.

[264] F. Silva, A. Martins. *Journal of Electroanalytical Chemistry* **467** (1999) 335.

[265] M. Stutzmann, J. A. Garrido, M. Eickhoff, M. S. Brandt. *Physica Status Solidi A* **203** (2006) 3423.

[266] R. Polsky, J. C. Harper, D. R. Wheeler, S. M. Dirk, D. C. Arango, S. M. Brozik. *Biosensors and Bioelectronics* **23** (2008) 757.

[267] F. A. Armstrong. *Current Opinion in Chemical Biology* **9** (2005) 110.

[268] P. K. Hansma, V. B. Elings, O. Marti, C. E. Bracker. *Science* **242** (1988) 209.

[269] H. G. Hansma, J. H. Hoh. *Annual Review of Biophysics and Biomolecular Structure* **23** (1994) 115.

[270] C. M. Niemeyer. *Angewandte Chemie-International Edition* **40** (2001) 4128.

[271] R. Garcia, R. Perez. *Surface Science Reports* **47** (2002) 197.

[272] G. Leatherman, E. N. Durantini, D. Gust, T. A. Moore, A. L. Moore, S. Stone, Z. Zhou, P. Rez, Y. Z. Liu, S. M. Lindsay. *Journal of Physical Chemistry B* **103** (1999) 4006.

[273] J. Zhao, J. J. Davis. *Nanotechnology* **14** (2003) 1023.

[274] J. Zhao, J. J. Davis, M. S. P. Sansom, A. Hung. *J. Am. Chem. Soc.* **126** (2004) 5601.

[275] H. B. Kraatz, M. Galka. *Probing of Proteins by Metal Ions and Their Low-Molecular-Weight Complexes* **38** (2001) 385.

[276] K. Plumb, H. B. Kraatz. *Bioconjugate Chemistry* **14** (2003) 601.

[277] K. Kerman, K. A. Mahmoud, H. B. Kraatz. *Chemical Communications* (2007) 3829.

[278] C. Drexler, M. Milne, E. Morgan, M. Jennings, H. B. Kraatz. *Dalton Trans* (2009) 4370.

"Phantasie ist wichtiger als Wissen, denn Wissen ist begrenzt."
(Albert Einstein, 14.03.1879 - 18.04.1955)